Search for single production of Vector Like Quarks using the LHC pp collision data at $\sqrt{s} = 13$ TeV collected with the ATLAS detector

Takuya Tashiro

Abstract

I report the results of a search for vector-like-quark(VLQ), a hypothetical quark whose left- and right-handed components transform in the same way under the weak SU(2). VLQ is predicted by some theories beyond the Standard Model to solve the hierarchy problem of the Higgs mass. The analysis utilizes the *pp* collision data recorded by the ATLAS detector at the Large Hadron Collider during 2015 and 2016, corresponding to the integrated luminosity of 36.1 fb^{-1} at the collision energy of 13 TeV. While VLQ can be produced via both single- and pair-production processes, the target of the analysis is the single production mechanism, whose production cross section explicitly depends on the mixing between VLQ and SM quarks as well as on the mass of VLQ. The analysis in this thesis is focused on the singly-produced VLQ with electric charge of +2/3(referred to as T) decaying into a Z boson and a top quark. A Z boson is reconstructed as a resonance of a pair of opposite-charge same-flavor leptons ($\mu^+\mu^-$ or e^+e^-) and a top quark is identified as a large-R jet tagged by the boosted-top-tagger algorithm. In the event selection procedure, events are first required to fulfill the loose preselection, and then the number of b-jets, top-jets, and forward jets are employed to classify the events into a signal region, two control regions, and a validation region. The contribution of the VLQ signal is estimated by fitting the distribution of the invariant mass of the system with reconstructed Z boson and the top quark in the signal and control regions. As a result, no significant excess over the background-only hypothesis is observed and the upper limits at 95% confidence level are set on the production cross section times branching ratio of $T \rightarrow Zt$ at each combination of the VLQ mass and the mixing angle. The excluded region of mass and mixing of T reaches up to 1200 GeV. This is the first result in ATLAS reporting the VLQ $\rightarrow Zt$ channel using the 13 TeV dataset. It successfully extend the Run1 results that excluded the VLQ of up to 800 GeV and excluded significant region where the Higgs hierarchy problem is naturally solved.

Contents

List of Figures

List of Tables

Chapter 1

Introduction

Since the ancient times, people have been trying to reveal what and how the universe is made of. In the 20th century, through the efforts of scientists around the world, the Standard Model (SM) of particle physics, which explains what elementary particles are and how they interact with each other, was constructed.

Higgs mechanism[1] is one of the important elements of SM. It successfully explains the origin of mass of fermions and weak bosons (W and Z) by spontaneous symmetry breaking, but there are still some remaining problems concerning the mechanism such as the hierarchy problem[2]. Some physics models beyond SM predict existence of vector like quarks (**VLQ**s) to solve such problems.

In this chapter, the concept of the Higgs mechanism is discussed in SM in Section 1.1, and then VLQ is explained in Section 1.2.

1.1 The Higgs mechanism

The Higgs mechanism first introduces a complex doublet field (Higgs doublet) Φ written as

$$\Phi = \left(\begin{array}{c} \Phi_A \\ \Phi_B \end{array} \right), \tag{1.1}$$

where Φ_A and Φ_B are complex fields. A global $SU(2)_L \times U(1)$ gauge invariant Lagrangian can be written as:

$$\mathcal{L}\left(\Phi\right) = \partial_\mu \Phi^\dagger \partial^\mu \Phi - V\left(\Phi^\dagger \Phi\right). \tag{1.2}$$

Local gauge invariance is achieved by replacing the partial derivative ∂_μ by a covariant derivative

$$\mathcal{D}_\mu = \partial_\mu + \frac{i}{2} g \sigma^a W_\mu^a + \frac{i}{2} g' B_\mu, \tag{1.3}$$

where σ^a are the Pauli matrices (a=1,2,3), W_μ^a and B_μ are the gauge fields, and g and g' are the coupling constants.

Assuming that the potential V is written as:

$$V\left(\Phi^\dagger \Phi\right) = \mu^2 \Phi^\dagger \Phi + \lambda \left(\Phi^\dagger \Phi\right)^2, \tag{1.4}$$

where the parameters $\mu^2 < 0$ and $\lambda > 0$, the minimum potential is realized with all the states satisfying $|\Phi^\dagger \Phi| = -\frac{\mu^2}{2\lambda} \equiv \frac{v^2}{2}$. Choosing the gauge condition such that Φ_A becomes 0 and Φ_B

becomes real, the ground and excited states are written as:

$$\Phi_{\text{ground}} = \begin{pmatrix} 0 \\ \frac{v}{\sqrt{2}} \end{pmatrix}, \tag{1.5}$$

$$\Phi = \begin{pmatrix} 0 \\ \frac{v}{\sqrt{2}} + \frac{h(x)}{\sqrt{2}} \end{pmatrix}, \tag{1.6}$$

where $h(x)$ is the real Higgs field. Equation 1.2, 1.3, and 1.6 lead to mass terms of vector bosons as:

$$\mathcal{L}_{mass} = \frac{g^2 v^2}{4} W_\mu^\dagger W^\mu + \frac{\left(g^2 + g'^2\right) v^2}{8} Z_\mu Z^\mu, \tag{1.7}$$

where

$$W_\mu = \frac{1}{\sqrt{2}} \left(W_\mu^1 + iW_\mu^2\right), \quad Z_\mu = \frac{gW_\mu^3 - g'B_\mu}{\sqrt{g^2 + g'^2}}. \tag{1.8}$$

A photon field A_μ, corresponding to the massless $U(1)$ gauge boson, can be written as the term orthogonal to Z_μ:

$$A_\mu = \frac{gW_\mu^3 + g'B_\mu}{\sqrt{g^2 + g'^2}}. \tag{1.9}$$

Considering that the kinetic term can be written as:

$$\begin{aligned} \mathcal{L}_{kin} &= -\frac{1}{4} W_\mu^a W^{\mu a} - \frac{1}{4} B_\mu B^\mu & (1.10) \\ &= -\frac{1}{2} W_\mu^\dagger W^\mu - \frac{1}{4} Z_\mu Z^\mu - \frac{1}{4} A_\mu A^\mu, & (1.11) \end{aligned}$$

the mass of W and Z are

$$m_W = \frac{gv}{2}, \quad m_Z = \frac{v}{2}\sqrt{(g^2 + g'^2)}. \tag{1.12}$$

With the procedure above, the original $SU(2)_L \times U(1)$ symmetry is broken spontaneously and the W and Z mass terms in Eq. 1.7, which do not appear in the original Lagrangian Eq. 1.2, have been successfully introduced.

Yukawa coupling

The Higgs doublet field couples to quarks and charged leptons as well as the gauge bosons. The coupling terms of the j-th generation down-type and up-type quarks are written as:

$$\begin{aligned} \text{Down-type} : \mathcal{L}(d_j) &= -y_{d_j} \bar{q}_{Lj} \Phi d_{Rj} + h.c. & (1.13) \\ \text{Up-type} : \mathcal{L}(u_j) &= -y_{u_j} \bar{q}_{Lj} \left(i\sigma^2 \Phi^*\right) u_{Rj} + h.c., & (1.14) \end{aligned}$$

where y_{d_j} and y_{u_j} are corresponding coupling constants and q_{Lj} is the left-handed SU(2) doublet of the quarks:

$$q_{Lj} = \begin{pmatrix} u_{Lj} \\ d_{Lj} \end{pmatrix}. \tag{1.15}$$

$u(d)_{Lj}$ and $u(d)_{Rj}$ are the left- and right-handed components of the j-th generation up(down) type quarks, respectively. After the symmetry breaking in Eq. 1.6, the mass terms appear in Eq. 1.13 and 1.14:

$$\begin{aligned}\mathcal{L}_{\text{mass}}(u_j) &= -\frac{y_{u_j}v}{\sqrt{2}}\left(\bar{u}_{Lj}u_{Rj}+\bar{u}_{Rj}u_{Lj}\right), && (1.16)\\ \mathcal{L}_{\text{mass}}(d_j) &= -\frac{y_{d_j}v}{\sqrt{2}}\left(\bar{d}_{Lj}d_{Rj}+\bar{d}_{Rj}d_{Lj}\right). && (1.17)\end{aligned}$$

Hence, the Higgs mechanism gives masses to quarks as well:

$$m_{u_j}=\frac{y_{u_j}v}{\sqrt{2}},\quad m_{d_j}=\frac{y_{d_j}v}{\sqrt{2}}. \tag{1.18}$$

The coupling terms of charged leptons appear in the similar way:

$$\mathcal{L}(e_j)=-y_{e_j}\bar{l}_{Lj}\Phi e_{Rj}+h.c., \tag{1.19}$$

$$l_{Lj}=\begin{pmatrix}\nu_{Lj}\\ e_{Lj}\end{pmatrix}, \tag{1.20}$$

where e_j, y_{e_j},e_{Rj}, e_{Lj}, and ν_{Lj} are the j-th generation charged lepton, its Yukawa coupling constant, its right- and left-handed components, and the left-handed component of the j-th generation neutrino, respectively. After the symmetry braking, these terms lead to mass terms:

$$\mathcal{L}_{\text{mass}}(e_j)=-\frac{y_{e_j}v}{\sqrt{2}}\left(\bar{e}_{Lj}e_{Rj}+\bar{e}_{Rj}e_{Lj}\right), \tag{1.21}$$

which gives masses to the charged leptons:

$$m_{e_j}=\frac{y_{e_j}v}{\sqrt{2}}. \tag{1.22}$$

The Higgs boson

Eq. 1.2, 1.4 and 1.6 lead to terms of Higgs boson h and its interaction with fermions, vector bosons, and Higgs boson itself:

$$\begin{aligned}\text{Higgs boson term : }\mathcal{L}_{\text{Higgs}} &= \frac{1}{2}\partial^{\mu}\partial_{\mu}h+\mu^2h^2, && (1.23)\\ \text{Interaction with fermions : }\mathcal{L}_f &= -\frac{y_f}{\sqrt{2}}h\bar{f}_Lf_R, && (1.24)\\ \text{Interaction with }W\text{: }\mathcal{L}_W &= g^2\left(\frac{1}{4}h^2+\frac{v}{2}h\right)W_{\mu}^{\dagger}W^{\mu}, && (1.25)\\ \text{Interaction with }Z\text{: }\mathcal{L}_Z &= \left(g^2+g'^2\right)\left(\frac{1}{8}h^2+\frac{v}{4}h\right)Z_{\mu}Z^{\mu}, && (1.26)\\ \text{Self-interaction : }\mathcal{L}_{\text{self}} &= -\frac{\lambda h^4}{4}-\lambda vh^3. && (1.27)\end{aligned}$$

While the mass of the Higgs boson at tree level is $\sqrt{-2\mu^2}$ as indicated in Eq. 1.23, it is affected by the radiative correction by Eq. 1.24-1.27 as shown in Fig. 1.1. The correction of each diagram is computed as:

$$\Delta m_h^2=-\frac{1}{4\pi^2}\frac{m_f^2}{v^2}\left(\Lambda^2-m_f^2\ln\frac{\Lambda^2+m_f^2}{m_f^2}\right), \tag{1.28}$$

$$\left(\Delta m_h^2\right)^2 = -\frac{3}{8\pi^2} y_t^2 \Lambda^2, \tag{1.29}$$

where Λ is a cut off. If the GUT scale (10^{16} GeV) is chosen at Λ, the correction is approximately 13 orders of magnitude larger than the real Higgs mass of 125 GeV, thus quite strict fine-tuning is required to realize the actual Higgs mass. This unnaturalness, often referred to as the “hierarchy problem”, is one of the remaining problems of the SM.

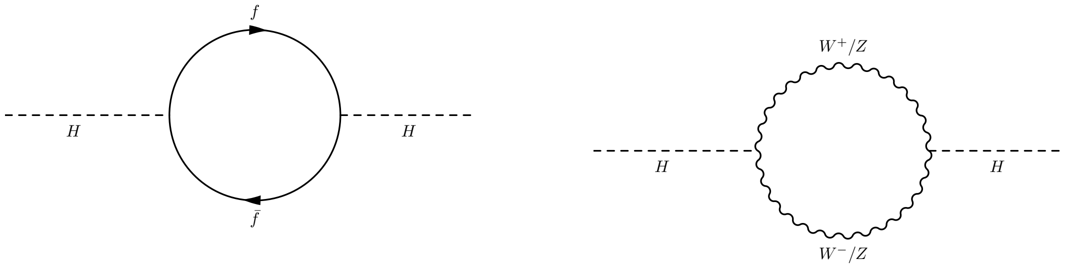

(a) A one-loop diagram of Higgs interacting with a pair of fermions, corresponding to the interaction term in Eq. 1.24 .

(b) A one-loop diagram of Higgs interacting with a pair of vector bosons, corresponding to the first terms in Eq. 1.25 and 1.26 .

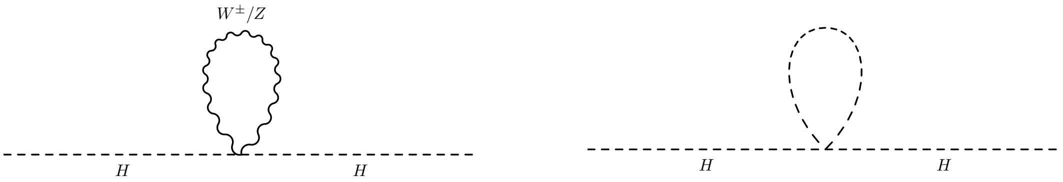

(c) A one-loop diagram of Higgs interacting with a vector boson, corresponding to the second terms in Eq. 1.25 and 1.26 .

(d) A one-loop diagram of Higgs self-interacting, corresponding to the first term in Eq. 1.27 .

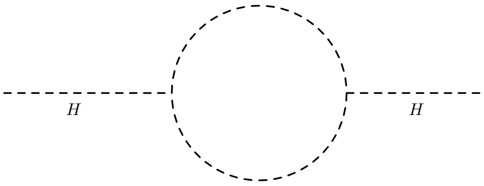

(e) A one-loop diagram of Higgs self-interacting, corresponding to the second term in Eq. 1.27 .

Figure 1.1: One-loop diagrams that contribute to the radiative correction of the mass of Higgs boson.

1.2 Vector Like Quark(VLQ)

VLQs are hypothetical quarks whose left- and right-handed components have the same electroweak quantum numbers. Their spin and color gauge groups are the same as the SM quarks. Since no stable VLQs are observed, all the VLQs are expected to decay into SM quarks via the weak interaction. Hence, only VLQs with the electric charge of +5/3, +2/3, -1/3, and -4/3 and the multiplets of singlet, doublet, and triplet are allowed. The allowed representations of VLQs are listed in Table 1.1.

Table 1.1: The allowed representations of VLQs. X, T, B, Y are the VLQs with the electric charge of +5/3, +2/3, -1/3, and -4/3, respectively.

	SM quarks			Singlets		Doublets			Triplets	
	$\begin{pmatrix} u \\ d \end{pmatrix}$	$\begin{pmatrix} c \\ s \end{pmatrix}$	$\begin{pmatrix} t \\ b \end{pmatrix}$	(T)	(B)	$\begin{pmatrix} X \\ T \end{pmatrix}$	$\begin{pmatrix} T \\ B \end{pmatrix}$	$\begin{pmatrix} B \\ Y \end{pmatrix}$	$\begin{pmatrix} X \\ T \\ B \end{pmatrix}$	$\begin{pmatrix} T \\ B \\ Y \end{pmatrix}$
$SU(2)_L$ multiplets	$q_L = 2$ $q_R = 1$			1		2			3	
$U(1)_Y$ hypercharge	$q_L = 1/6$ $u_R = 2/3$ $d_r = -1/3$			2/3	-1/3	7/6	1/6	-5/6	2/3	-1/3

VLQs receive a plenty of attention because they are the simplest additional quarks that are not ruled out by the existing experimental results and they are motivated by some models beyond SM. One of the most interesting models is the littlest Higgs model[3, 4], which solves the hierarchy problem by introducing VLQs with the mass of ~TeV. Details of the models are described in the following discussions.

1.2.1 Physics models predicting VLQ

Littlest Higgs Model

Littlest Higgs Model is one of the possible extensions of the SM which can explain the lightness of the Higgs boson without the fine-tuning. It introduces a global $SU(5)$ symmetry, which spontaneously breaks down to $SO(5)$. The symmetry breaking scale f is expected to be ~1 TeV to avoid the fine tuning. Since the number of $SU(5)$ generators is 24 and $SO(5)$ generators is 10, 14 Nambu Goldstone boson(NGB) fields $\pi^a(x)(a = 1, 2, \cdots, 14)$ appear in association with the symmetry breaking, and the matrix $\Pi(x)$ is defined as:

$$\Pi(x) = \sum_{a=1}^{14} \pi^a(x) X^a \ , \tag{1.30}$$

where X^a are the broken $SU(5)$ generators. The Higgs doublet field H in the SM is identified as a subset of the NGB fields, hence it appears as the context of the Π matrix. The Π matrix also contains additional fields of electroweak singlet and two doublets, referred to as η, ϕ and ω. Using these fields, Π can be explicitly written as:

$$\Pi(x) = \begin{pmatrix} -\frac{\omega^0}{2} - \frac{\eta}{\sqrt{20}} & -\frac{\omega^+}{\sqrt{2}} & \frac{H^+}{\sqrt{2}} & -i\phi^{++} & -i\frac{\phi^+}{\sqrt{2}} \\ -\frac{\omega^-}{\sqrt{2}} & \frac{\omega^0}{2} - \frac{\eta}{\sqrt{20}} & \frac{H^0}{\sqrt{2}} & -i\frac{\phi^+}{\sqrt{2}} & \frac{-i\phi^0+\phi^0_P}{\sqrt{2}} \\ \frac{H^-}{\sqrt{2}} & \frac{H^{0*}}{\sqrt{2}} & \sqrt{\frac{4}{5}}\eta & \frac{H^+}{\sqrt{2}} & \frac{H^0}{\sqrt{2}} \\ i\phi^{--} & i\frac{\phi^-}{\sqrt{2}} & \frac{H^-}{\sqrt{2}} & -\frac{\omega^0}{2} - \frac{\eta}{\sqrt{20}} & -\frac{\omega^-}{\sqrt{2}} \\ i\frac{\phi^-}{\sqrt{2}} & \frac{i\phi^0+\phi^0_P}{\sqrt{2}} & \frac{H^{0*}}{\sqrt{2}} & -\frac{\omega^+}{\sqrt{2}} & \frac{\omega^0}{2} - \frac{\eta}{\sqrt{20}} \end{pmatrix} . \tag{1.31}$$

In the littlest Higgs model, a is chosen to make the condensate proportional to

$$\Sigma_0 = \begin{pmatrix} 0 & 0 & \mathbb{1} \\ 0 & 1 & 0 \\ \mathbb{1} & 0 & 0 \end{pmatrix} , \tag{1.32}$$

where $\mathbb{1}$ is a unit 2 × 2 matrix, and the SU(5)/SO(5) sigma field can be written as:

$$\Sigma(x) = \exp\left(\frac{i\Pi}{f}\right) \Sigma_0 \exp\left(\frac{i\Pi^T}{f}\right) = \exp\left(\frac{2i\Pi}{f}\right) \Sigma_0 \ /. \tag{1.33}$$

While the Higgs is introduced as a NGB and no explicit mass term appears, the Higgs boson acquires the mass via the gauge and Yukawa interactions described in the following.

In terms of the gauge interaction, the model considers a gauge $[SU(2) \times U(1)]^2$ symmetry as a subgroup of the $SU(5)$. This gauge symmetry breaks down to $SU(2) \times U(1)$, which is identified as the electroweak $SU(2)_L \times U(1)$ gauge symmetry of the SM. This gauge group then breaks down to $U(1)$ at the scale of v.

To cancel the large one-loop contribution of Fig. 1.1, the Yukawa interaction term of the top quark is extended using the weak-singlet vector-like quark U with the electric charge of $+2/3$ in the following way.

$$\mathcal{L}_{top} = -\frac{\lambda_1}{2} f \chi^\dagger_{Li} \epsilon_{ijk} \epsilon_{mn} \Sigma_{jm} \Sigma_{kn} u_{3R} - \lambda_2 f U^\dagger_L U_R + \text{h.c.} \;, \tag{1.34}$$

where λ_1 and λ_2 are the coupling constants and

$$\chi_L = \begin{pmatrix} \sigma_2 \begin{pmatrix} u_{3L} \\ d_{3L} \end{pmatrix} \\ U_L \end{pmatrix} \tag{1.35}$$

where u_{3L} and d_{3L} are the up- and down-type of the third generation quark, respectively. In Eq. 1.34, the indices i, j, k run between 1 and 3, and m,n between 4 and 5. The two mass eigenstates t and T can be written as the mixing of u_3 and U as following:

$$t_L = u_L, \qquad t_R = \frac{\lambda_2 u_{3R} - \lambda_1 U_R}{\sqrt{\lambda_1^2 + \lambda_2^2}} \;, \tag{1.36}$$

$$T_L = U_L, \qquad T_R = \frac{\lambda_1 u_{3R} + \lambda_2 U_R}{\sqrt{\lambda_1^2 + \lambda_2^2}} \;, \tag{1.37}$$

resulting in t to be massless before the electroweak symmetry breaking, and the mass of T is written as

$$m_T = \sqrt{\lambda_1^2 + \lambda_2^2} f \;. \tag{1.38}$$

Using these eigenbases, the Higgs coupling terms in Eq. 1.34 up to quadratic order of H can be written as:

$$\begin{aligned} \lambda_1 & \left(\sqrt{2} q^\dagger_{3L} \tilde{H} t_R - \frac{1}{f} H^\dagger H U^\dagger_L \right) u_{3R} + \text{h.c.} \\ = & \; \lambda_t q^\dagger_L \tilde{H} t_R + \lambda_T q^\dagger_L \tilde{H} T_R - \frac{1}{\sqrt{2} f} \left(H^\dagger H \right) T^\dagger_L \left(\lambda_T T_R + \lambda_t t_R \right) + \text{h.c.} \;, \end{aligned} \tag{1.39}$$

where

$$\tilde{H} = i \sigma_2 H \;, \tag{1.40}$$

$$\lambda_t = \frac{\sqrt{2} \lambda_1 \lambda_2}{\sqrt{\lambda_1^2 + \lambda_2^2}}, \qquad \lambda_T = \frac{\sqrt{2} \lambda_1^2}{\sqrt{\lambda_1^2 + \lambda_2^2}} \;. \tag{1.41}$$

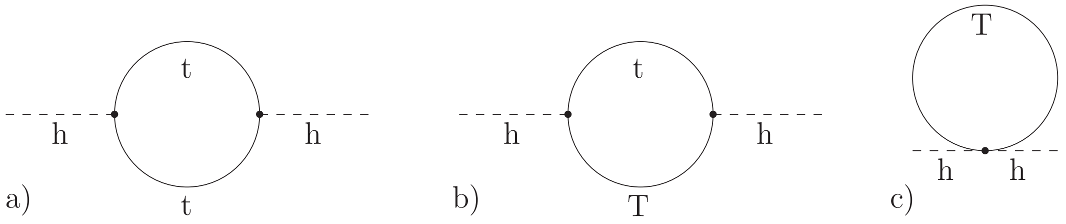

Figure 1.2: One-loop processes appearing in the top sector of the littlest Higgs model.[4]

Equation 1.39 lead to three processes of one-loop diagrams contributing to the Higgs mass as shown in Fig. 1.2 The contribution to the Higgs mass of each process are:

$$\begin{aligned}(a) &: -6\lambda_t^2 \int \frac{d^4k}{(2\pi)^4}\frac{1}{k^2} , \\ (b) &: -6\lambda_T^2 \int \frac{d^4k}{(2\pi)^4}\frac{1}{k^2-m_T^2} , \text{and} \\ (c) &: +6\frac{\sqrt{2}\lambda_T}{f} \int \frac{d^4k}{(2\pi)^4}\frac{m_T}{k^2-m_T^2} . \end{aligned} \tag{1.42}$$

Combining Eq. 1.38,1.41,1.42, the quadratic divergence of Eq. 1.29 is canceled out and the remaining contribution to the squared Higgs mass can be written as:

$$\Delta m^2 = -\frac{3\lambda_t^2 m_T^2}{8\pi^2}\ln\frac{\Lambda^2}{m_T^2} . \tag{1.43}$$

Composite Higgs model

The composite Higgs model[5, 6] is also one of the models predicting VLQs. It assumes that a global $SO(5)$ symmetry is broken spontaneously to $SO(4)$ at a scale of f. Using a real scalar quintet ϕ subject to a constraint $\phi^2 = f^2$, and with its first 4 components $\phi_1, \phi_2, \phi_3, \phi_4$, the usual $SU(2)$ Higgs doublet field H can be written as:

$$H = \frac{1}{\sqrt{2}}\begin{pmatrix}\phi_1 + i\phi_2 \\ \phi_3 + i\phi_4\end{pmatrix} . \tag{1.44}$$

To generate the $SO(5)$-symmetric quark-Higgs coupling terms, the third generation quark field is extended to

$$\Psi_L = \left(q^0, X^0, T^0\right)_L , t_R^0, b_R^0, X_R^0, T_R^0 ,$$

where q_L^0, X_L^0, X_R^0 are $SU(2)$-doublets whereas all the others are singlets. The gauge invariant mass term $\mathcal{L}_{\text{top}}$ is formed using the fields above as:

$$\mathcal{L}_{\text{top}} = \lambda_1\bar{\Psi}_L\phi t_R + \lambda_2 f\bar{T}_L T_R + \lambda_3 f\bar{T}_L t_R + M_X\bar{X}_L X_R + h.c. \tag{1.45}$$

The heavy and light mass eigenstates T and t are written as the mixture of T^0 and t^0 as:

$$T_R = T_R^0\cos\chi - t_R^0\sin\chi , \tag{1.46}$$

$$t_R = T_R^0\sin\chi + t_R^0\cos\chi , \tag{1.47}$$

thus Eq. 1.45 is rewritten as:

$$\mathcal{L}_{top} = \bar{q_L}H^c\left(\lambda_t t_R + \lambda_T T_R\right) + \bar{X_L}H\left(\lambda_t t_R + \lambda_T T_R\right) + m_T\bar{T}_L T_R + m_X\bar{X}_L X_R + h.c. , \tag{1.48}$$

where χ, λ_t, λ_T, and m_T are defined as:

$$\tan\chi = \frac{\lambda_1+\lambda_3}{\lambda_2} , \tag{1.49}$$

$$\lambda_t = \frac{\lambda_1\lambda_2}{\sqrt{\left(\lambda_1+\lambda_3\right)^2+\lambda_2^2}} , \tag{1.50}$$

$$\lambda_T = \frac{\lambda_1\left(\lambda_1+\lambda_3\right)}{\sqrt{\left(\lambda_1+\lambda_3\right)^2+\lambda_2^2}} , \text{and} \tag{1.51}$$

$$m_T = \sqrt{\left(\lambda_1+\lambda_3\right)^2+\lambda_2^2}f . \tag{1.52}$$

As a result of the one-loop corrections appearing in Eq. 1.48, the quadratic divergent term in Eq. 1.29 disappears and only the $\log\Lambda^2$ term remains.

1.2.2 Interaction between VLQs and SM particles

Since the theme of this thesis is a search for VLQ with the electric charge of +2/3 (T), this section is focused on the interaction of T. In all of the allowed multiplets, the covariant derivative D_μ of the local $SU(2) \times U(1)$ symmetry can be written as

$$D_\mu = \partial_\mu + \frac{ig}{2}\sigma^a W^a_\mu + \frac{ig_2}{2}B_\mu \ , \tag{1.53}$$

where g is the coupling constant same as the SM case and g_2 is a constant determined by the electric charge of the VLQs. W^a_μ terms do not appear in the singlet case.

If VLQs exist, new heavy mass eigenstates are formed as mixing of VLQs and the third generation quark. In the case with electric charge of +2/3, the heavy mass eigenstate T and light eigenstate t can be written as the mixing of the top quark(t^0) and the VLQ (T^0):

$$\begin{pmatrix} t_{L,R} \\ T_{L,R} \end{pmatrix} = \begin{pmatrix} \cos\theta^u_{L,R} & -\sin\theta^u_{L,R}e^{i\phi_u} \\ \sin\theta^u_{L,R}e^{-i\phi_u} & \cos\theta^u_{L,R} \end{pmatrix} \begin{pmatrix} t^0_{L,R} \\ T^0_{L,R} \end{pmatrix} \ , \tag{1.54}$$

where $t^0_{L,R}$ and $T^0_{L,R}$ are the left- and right-handed components of the weak eigenstate of top and vector-like quark. If B, a vector-like-quark with the electric charge of -1/3, exists, it can be written in the same format:

$$\begin{pmatrix} b_{L,R} \\ B_{L,R} \end{pmatrix} = \begin{pmatrix} \cos\theta^d_{L,R} & -\sin\theta^d_{L,R}e^{i\phi_d} \\ \sin\theta^d_{L,R}e^{-i\phi_d} & \cos\theta^d_{L,R} \end{pmatrix} \begin{pmatrix} b^0_{L,R} \\ B^0_{L,R} \end{pmatrix} \ . \tag{1.55}$$

Since both t^0 and T^0 interact with Higgs and the vector-bosons, the mixing in Eq. 1.54 results in three interaction terms $\mathcal{L}_W, \mathcal{L}_Z$, and $\mathcal{L}_H$, corresponding to T interaction with $W^\pm$, Z, and the Higgs boson, respectively.

$$\mathcal{L}_W = -\frac{g}{\sqrt{2}}\bar{T}\gamma^\mu \left(V^L_{Tb}\frac{1-\gamma_5}{2} + V^R_{Tb}\frac{1+\gamma_5}{2} \right) bW^+_\mu + \text{h.c.} \ , \tag{1.56}$$

$$\mathcal{L}_Z = -\frac{g}{\cos\theta_W}\bar{T}\gamma^\mu \left(X^L_{Tt}\frac{1-\gamma_5}{2} + X^R_{Tt}\frac{1+\gamma_5}{2} \right) tZ_\mu + \text{h.c.} \ , \tag{1.57}$$

$$\mathcal{L}_H = -\frac{gm_T}{2M_W}\bar{T} \left(Y^L_{Tt}\frac{1-\gamma_5}{2} + Y^R_{Tt}\frac{1+\gamma_5}{2} \right) tH + \text{h.c.} \ , \tag{1.58}$$

where θ_W is the Weinberg angle and M_W is the mass of the W boson. $V^{L,R}_{Tb}, X^{L,R}_{Tt}, Y^{L,R}_{Tt}$ are the coefficients depending on the mixing angle $\theta_{L,R}$, ϕ, and the multiplets summarized in the Table 1.2 and 1.3.

Table 1.2: Coupling of left-handed T to the bosons and the third-generation quarks.

Multiplets		V^L_{Tb}	X^L_{Tt}	Y^L_{Tt}
(T)	singlet	$\sin\theta^u_L e^{-i\phi_u}$	$\sin\theta^u_L \cos\theta^u_L e^{i\phi_u}$	$\frac{m_t}{m_T}\sin\theta^u_L \cos\theta^u_L e^{i\phi_u}$
(XT)	doublet	$\sin\theta^u_L e^{-i\phi_u}$	$2\sin\theta^u_L \cos\theta^u_L e^{i\phi_u}$	$\sin\theta^u_R \cos\theta^u_R e^{i\phi_u}$
(TB)	doublet	$\sin\theta^u_L \cos\theta^d_L e^{-i\phi_u} - \cos\theta^u_L \sin\theta^d_L e^{-i\phi_d}$	0	$\sin\theta^u_R \cos\theta^u_R e^{i\phi_u}$
(XTB)	triplet	$\left(\sin\theta^u_L \cos\theta^d_L - \sqrt{2}\cos\theta^u_L \sin\theta^d_L\right) e^{-i\phi}$	$\sin\theta^u_L \cos\theta^u_L e^{i\phi}$	$\frac{m_t}{m_T}\sin\theta^u_L \cos\theta^u_L e^{i\phi}$
(TBY)	triplet	$\left(\sin\theta^u_L \cos\theta^d_L - \sqrt{2}\cos\theta^u_L \sin\theta^d_L\right) e^{-i\phi}$	$-\sin\theta^u_L \cos\theta^u_L e^{i\phi}$	$\frac{m_t}{m_T}\sin\theta^u_L \cos\theta^u_L e^{i\phi}$

Table 1.3: Coupling of right-handed T to the bosons and the third-generation quarks.

Multiplets		V_{Tb}^R	X_{Tt}^R	Y_{Tt}^R
(T)	singlet	0	0	$\sin\theta_L^u \cos\theta_L^u e^{i\phi_u}$
(XT)	doublet	0	$\sin\theta_R^u \cos\theta_R^u e^{i\phi_u}$	$\frac{m_t}{m_T}\sin\theta_R^u \cos\theta_R^u e^{i\phi_u}$
(TB)	doublet	$-\cos\theta_R^u \sin\theta_R^d e^{-i\phi_d}$	$-\sin\theta_R^u \cos\theta_R^u e^{\phi_u}$	$\frac{m_t}{m_T}\sin\theta_R^u \cos\theta_R^u e^{i\phi_u}$
(XTB)	triplet	$-\sqrt{2}\cos\theta_R^u \sin\theta_R^d e^{-i\phi}$	0	$\sin\theta_L^u \cos\theta_L^d e^{i\phi}$
(TBY)	triplet	$-\sqrt{2}\cos\theta_R^u \sin\theta_R^d e^{-i\phi}$	$-2\sin\theta_R^u \cos\theta_R^u e^{i\phi}$	$\sin\theta_L^u \cos\theta_L^d e^{i\phi}$

The interaction terms in Eq. 1.56-1.58 result in three decay modes of T: $T \to W^+ b$, $T \to Zt$, and $T \to Ht$. The decay width of each process can be written as a function of the couplings and the mass of the relevant particles:

$$\begin{aligned}
\Gamma\left(T \to W^+ b\right) &= \frac{g^2}{64\pi}\frac{m_T}{M_W^2}\lambda\left(m_T, m_b, M_W\right)^{\frac{1}{2}}\left\{\left(|V_{Tb}^L|^2 + |V_{Tb}^R|^2\right)\right. \\
&\times \left.\left(1 + r_W^2 - 2r_b^2 - 2r_W^4 + r_b^4 + r_W^2 r_b^2\right) - 12 r_W^2 r_b Re\left(V_{Tb}^L V_{Tb}^{R*}\right)\right\}, \qquad (1.59) \\
\Gamma\left(T \to Zt\right) &= \frac{g}{128\cos^2\theta_W}\frac{m_T}{M_Z^2}\lambda\left(m_T, m_t, M_Z\right)^{\frac{1}{2}}\left\{\left(|X_{Tt}^L|^2 + |X_{Tt}^R|^2\right)\right. \\
&\times \left.\left(1 + r_Z^2 - 2r_t^2 - 2r_Z^4 + r_t^4 + r_Z^2 r_t^2\right) - 12 r_Z^2 r_t Re\left(X_{Tt}^L X_{Tt}^{R*}\right)\right\}, \qquad (1.60) \\
\Gamma\left(T \to Ht\right) &= \frac{g^2}{128\pi}\frac{m_T}{M_W^2}\lambda\left(m_T, m_t, M_H\right)^{\frac{1}{2}}\left(|Y_{Tt}^L|^2 + |Y_{Tt}^R|^2\right), \\
&\times \left(1 + 6r_t^2 - r_H^2 + r_t^4 - r_t^2 r_H^2\right), \qquad (1.61)
\end{aligned}$$

where $r_x = \frac{m_x}{m_T}$ and $\lambda\left(x, y, z\right) \equiv x^4 + y^4 + z^4 - 2x^3y^2 - 2y^2z^2 - 2z^2x^2$. The possible branching ratio of each multiplet is shown in Fig. 1.3.

In a more general and simple expression[8], the Lagrangian terms of the interactions between T and SM particles can be written as:

$$\begin{aligned}
\mathcal{L}_{T-SM} &= \frac{g}{2}\bar{T}\gamma^\mu\left(c_L^W\frac{1-\gamma_5}{2} + c_R^W\frac{1+\gamma_5}{2}\right)bW_\mu^+ \\
&+ \frac{g}{2}\bar{T}\gamma^\mu\left(c_L^Z\frac{1-\gamma_5}{2} + c_R^Z\frac{1+\gamma_5}{2}\right)tZ_\mu \\
&+ \frac{g}{2}\bar{T}\left(c_L^H\frac{1-\gamma_5}{2} + c_R^H\frac{1+\gamma_5}{2}\right)tH + h.c.\,, \qquad (1.62)
\end{aligned}$$

where c_L^V and c_R^V are the left- and right-handed couplings between T and boson V. The associated parameters defined as $c_V = \sqrt{(c_R^V)^2 + (c_L^V)^2}$ are useful to discuss the phenomenon of T because they are closely related to the production cross section and branching ratio of T.

In ATLAS, the Monte Carlo simulation samples of VLQ signals are generated based on the parametrization in the following[8]:

$$\mathcal{L} = \kappa_T\left\{\sqrt{\frac{\xi_W^T}{\Gamma_W^0}}\frac{g}{\sqrt{2}}[\bar{T}_{L/R}W_\mu^+\gamma^\mu b_{L/R}] + \sqrt{\frac{\xi_Z^T}{\Gamma_Z^0}}\frac{g}{2\cos\theta_W}[\bar{T}_{L/R}Z_\mu^+\gamma^\mu t_{L/R}] - \sqrt{\frac{\xi_H^T}{\Gamma_H^0}}\frac{M}{v}[\bar{T}_{R/L}Ht_{L/R}]\right\}, \qquad (1.63)$$

where Γ_V^0 are the partial decay width of $T \to Vq$ computed under an setting that q is massless and ξ_V^T are the branching ratio of $T \to Vq$ decay channel. In this convention, Γ_V^0 can be computed as functions of T mass and κ_T and ξ_V can be computed as functions of T mass and mixing, hence the T mass and κ_T are treated as the free parameters, and the latter is referred to as "coupling".

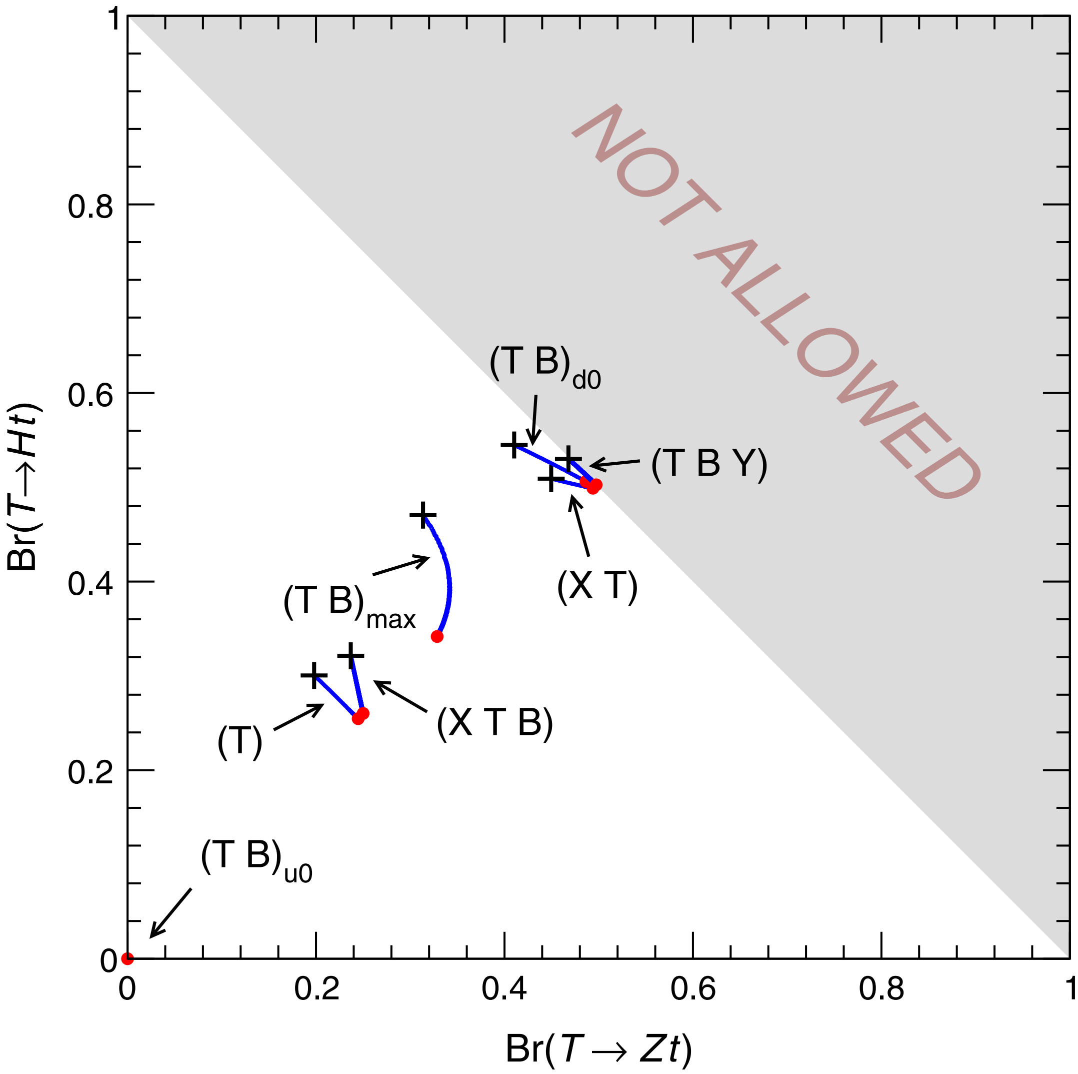

Figure 1.3: Possible branching ratio of T in each multiplet. In the (TB) doublet case, three special cases are considered: u_0 corresponding to $\theta_u = 0, \theta_d \neq 0$, d_0 corresponding to $\theta_u \neq 0, \theta_d = 0$, and "max" corresponding to the maximal mixing. [7]

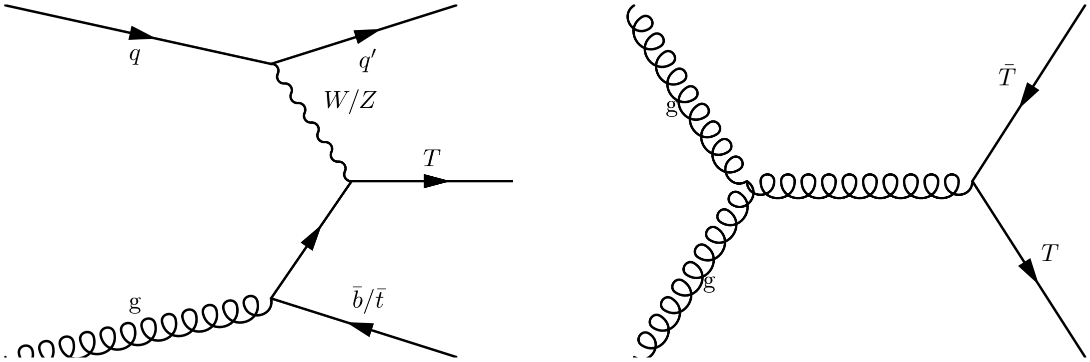

(a) (b)

Figure 1.4: Feynman diagrams of single(a) and pair(b) production mechanisms of T. q and q' indicate the light quarks.

1.2.3 VLQ production in LHC

T can be produced via the pp collisions in LHC at $\sqrt{s}$ =13 TeV in two main production mechanisms: (1) single production via the weak interaction and (2) pair production via the strong interaction, whose Feynman diagrams are shown in Fig. 1.4. Since T is coloured as the normal quarks, the pair-production cross section depends only on the mass of T whereas the single-production cross section depends on the coupling between T and SM particles as well. Fig. 1.5 shows the cross section of the pair production and maximum single production processes. The pair production is the dominant production channel in the low mass region because of the strong interaction while in the high mass (∼1 TeV) region the single production can be dominant because the required collision energy is smaller in the single production compared to the pair production, in which required collision energy is twice larger than T mass.

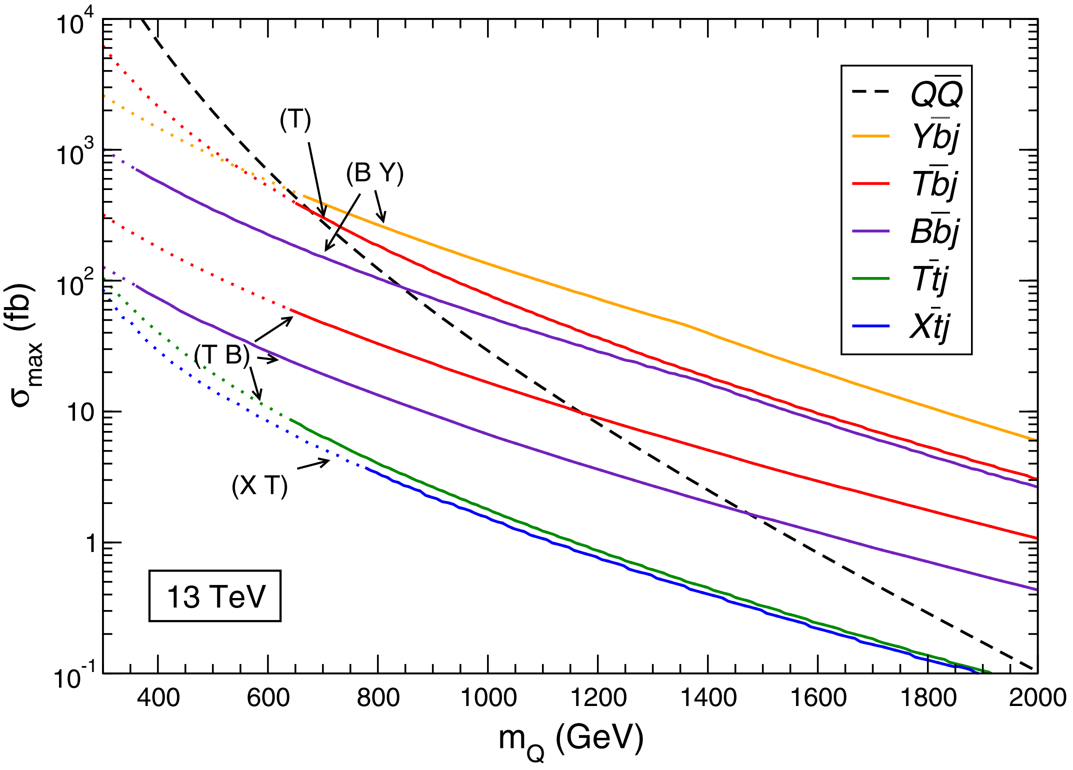

Figure 1.5: Production cross section of VLQs in each production mechanism and multiplets at the LHC with 13 TeV. The dashed line indicates the pair production and the red and green lines indicate the single T production associated with b and t, respectively, and the lines with (T), $(T\ B)$, and $(X\ T)$ indicate the singlet, doublet, and triplet multiplets, respectively. [7]

Chapter 2

LHC

The Large Hadron Collider(LHC) is a proton-proton collider operated at the highest center of mass energy $\sqrt{s} = 13$ TeV. Since the first collision in 2008, the LHC has been running as the most powerful probe of the particle physics. LHC Run1 was operated from 2010 to early 2013 with the center of mass energy $\sqrt{s} = 7$ or 8 TeV. After Run1, the LHC was shut down for about 2 years for maintenance and preparation for collisions with higher energy. After the shutdown, the LHC Run2 period started in June 2015, operated under the increased energy of $\sqrt{s} = 13$ TeV. The details of the design and performance of the LHC are described throughout this chapter.

2.1 LHC beam parameters

The LHC proton beams and collision are characterized by the parameters listed in this section.

Luminosity

Instantaneous machine luminosity L for a gaussian beam distribution is defined as

$$L = \frac{N_b^2 n_b f_{\mathrm{rev}} \gamma_r}{4\pi \epsilon_n \beta^*} F \ , \tag{2.1}$$

where N_b is the number of protons per bunch, n_b is the number of bunches per beam, f_{rev} is the revolution frequency, γ_r is the relativistic gamma factor, ϵ_n is the normalized transverse beam emittance, β^* is the beta function at the collision point and F is the geometric reduction factor with the beam crossing angle at the interaction point (IP) defined as following.

$$F = \left(\sqrt{1 + \left(\frac{\theta_c \sigma_z}{2\sigma^*} \right)^2} \right)^{-1} \ , \tag{2.2}$$

where θ_c is the full crossing angle at the IP, σ_z is the RMS bunch length and σ^* is the transverse RMS beam size at the IP.

Machine luminosity is an important parameter for collider physics because the number of events per a unit of time generated in the collision (N_{event}) is given by:

$$N_{\mathrm{event}} = L \sigma_{\mathrm{event}} \ , \tag{2.3}$$

where σ_{event} is the cross section of the considered event.

Emittance and β

Emittance is a parameter characterizing the size of a beam. The emittance with the dimension parallel to the beam axis is called "longitudinal emittance" (ϵ_s) and the other two dimensions are referred to as "transverse emittances" (ϵ).

The longitudinal emittance is defined as:

$$\epsilon_s = 4\pi\sigma_t\sigma_{\delta E/E_0}E_0 \ , \tag{2.4}$$

where σ_t is the bunch duration in time, $\sigma_{\delta E/E_0}$ is the relative energy spread, and E_0 is the nominal beam energy.

Concerning the position-angle phase space of the transverse dimension, the area enclosed by an ellipse of a single particle is invariant through the storage ring. The transverse emittance ϵ is defined so that $\pi\epsilon$ is equal to an area that contains the ellipses of certain ratio of particles. In a low emittance beam, particles are confined to a small distance and have nearly the same momentum. Since the beam transport system allows only particles whose momentum is close to the design value, keeping the emittance small leads small beam loss.

Another important parameter concerning the beam size is the amplitude function β. It is a parameter determined by the accelerator magnet configuration and powering as:

$$\beta = \frac{\pi\sigma^2}{\epsilon} \ , \tag{2.5}$$

where σ is the cross sectional size of the bunch. β is roughly the width of the beam squared divided by the emittance. A beam with low β is narrower and more squeezed.

Beams are squeezed at the IP to increase the number of collisions. A useful parameter to estimate this effect is β^*, defined as distance that the beam width gets twice as wide as at the IP.

Pileup

Since a bunch contains numerous number of protons and the cross section of the inelastic processes is as large as ~80 mb, multiple interactions can occur within one bunch crossing. Due to this effect, pileup, defined as the number of interactions per bunch crossing, can be up to 50 in the LHC setting during 2016. In principle, larger pileup leads to worse performance in measurements such as PID and energy measurement, thus it is important for detector operation to mitigate the effect of pileup.

The design parameters[10] of LHC are summarized in Table 2.1.

Table 2.1: Summary of the designed[10] and actual LHC parameters measured in 2016.

	Design	2016
proton energy [GeV]	7000	6500
Number of protons per bunch	1.15×10^{11}	1.1×10^{11}
Number of bunches	2808	2076
Bunch spacing [ns]	25	25
Transverse normalized emittance [μm$\cdot rad$]	3.75	3.4
β^* [m]	0.55	0.4
peak luminosity at the IP1 [$\mathrm{cm}^{-2}\mathrm{s}^{-1}$]	1.0×10^{34}	1.01×10^{34}

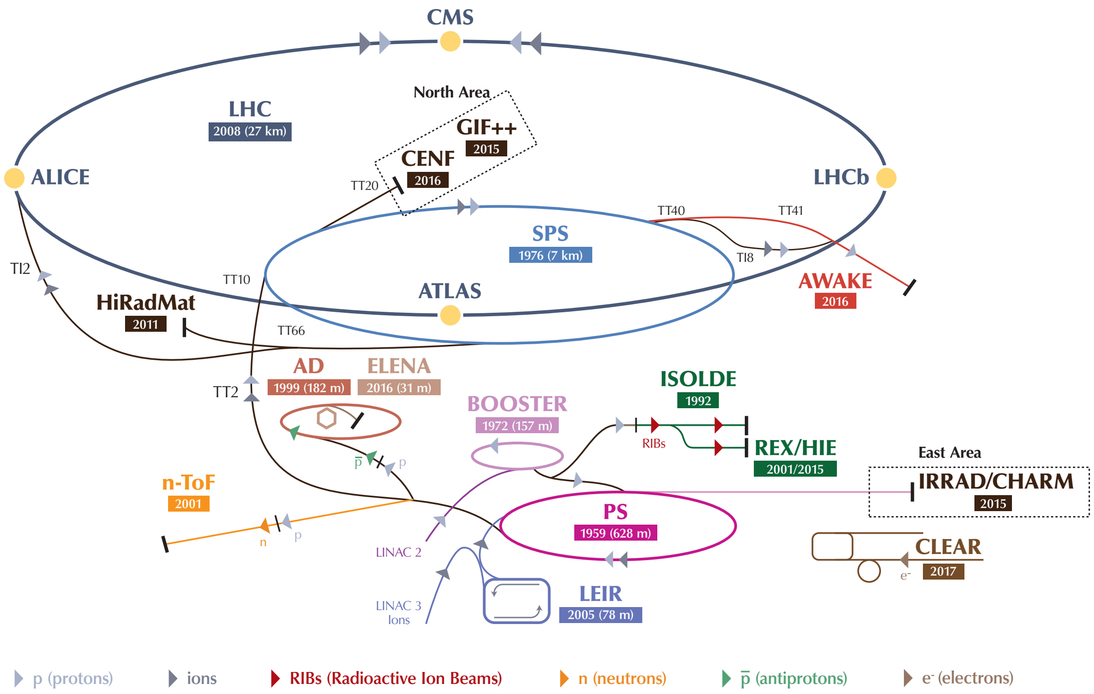

Figure 2.1: The LHC accelerator complex and the routes of protons and other particles[9].

2.2 LHC accelerator complex

The LHC system is composed of several accelerators. Throughout this section, I explain the structure and role of each component.

2.2.1 The proton injection system

Prior to the injection into the LHC main ring, protons are generated, gathered, and accelerated to 450 GeV by a series of accelerators(**LINAC2, PSB, PS, and SPS**). A diagram of the accelerator chain is shown in Fig. 2.1.

Proton source Protons are generated in the Duoplasmatron with hydrogen gas. In the Duoplasmatron, electrons emitted from a cathode filament interact with hydrogen gas to generate protons with the process below.

$$\begin{array}{cll} (1) & H_2 + e^- & \rightarrow \mathrm{H}_2^+ + 2\mathrm{e}^- \\ (2) & H_2^+ + e^- & \rightarrow \mathrm{H}^+ + \mathrm{H} + \mathrm{e}^- \\ (3) & H + e^- & \rightarrow \mathrm{H}^+ + 2\mathrm{e}^- \end{array}$$

The produced protons are accelerated by a static electric field with a voltage of 90 kV to approximately 1.4% speed of light, then they are sent to the **RFQ**(radio-frequency quadrupole), which speeds up and focuses the proton beam. After RFQ, the protons are sent to the linear accelerator (**LINAC2**).

LINAC2 Generated protons are further accelerated in LINAC2, which makes use of radiofrequency(RF) cavities to accelerate the protons. The RF cavities are metallic chambers containing an electromagnetic field which oscillates at 400 MHz. In the cavities, the field works to accelerate and sort protons into discrete packets called “bunches”. By the time protons reach the end of LINAC2, they gain up to energy of 50 MeV. The accelerated protons are then sent to the Proton Synchrotron Booster (**PSB**).

PSB PSB is a synchrotron working as the first circular accelerator in the LHC chain. It contains 4 superimposed rings, which receive 50 MeV protons from LINAC2 and accelerate them up to 1.4 GeV. The accelerated protons are sent to the Proton Synchrotron (**PS**).

PS PS is the oldest synchrotron at CERN with a circumference of 628.3 m. It accelerates protons up to 26 GeV. The accelerated protons are sent to the Super Proton Synchrotron (**SPS**). Prior to the ejection, the beam is debunched and rebunched by 40 MHz cavities to generate the bunch spacing of 25 ns.

SPS SPS, the second largest machine in the accelerator complex at CERN, is a synchrotron with a nearly 7 km circumference. It contains 1317 conventional magnets, including 744 dipoles to bend the protons around the ring. It accelerates protons up to 450 GeV. This is the final acceleration step before injection to the LHC main ring. After the acceleration, the protons are finally injected into the LHC main ring.

2.2.2 LHC main ring

The LHC main ring is a two-ring, superconducting collider installed in the LEP tunnel[11] with the circumference of approximately 27 km. After injection at 450 GeV, protons travel in opposite directions in separate beam pipes and boosted to the LHC design energy before collisions at the interaction points. The basic layout of the LHC main ring is shown in Fig. 2.2. As shown in the figure, the main ring is made of eight arcs and eight straight sections.

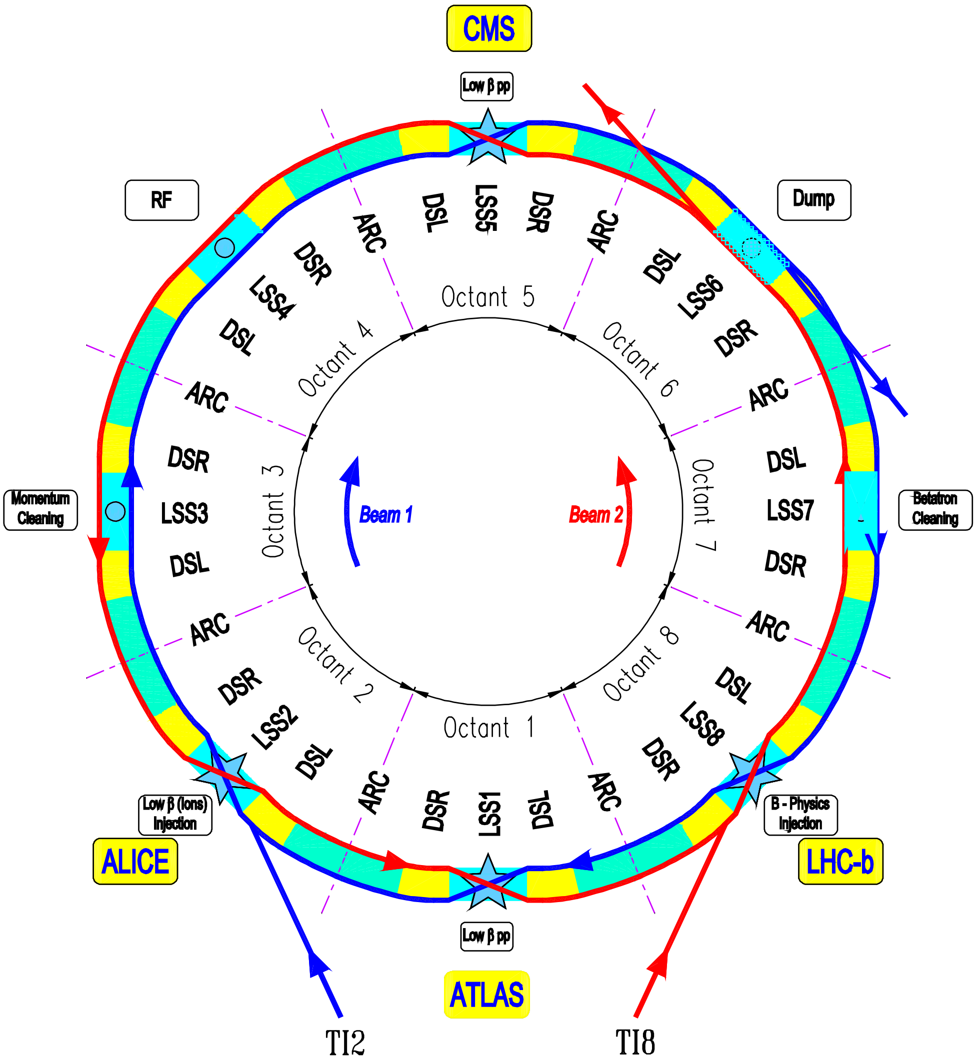

Figure 2.2: Schematic view of the LHC main ring. Beam 1 indicates the beam circulating clockwise and Beam 2 indicates the one circulating counter-clockwise.[10]

Beams are bent, focused, and de-focused using the magnet system in the arc sections, which are composed of 23 arc cells. One arc cell is 106.9 m long and composed of two 53.45 m half cells, each of which containing 5.355 m long cold mass in short straight section (SSS) and three 14.3 m long dipole magnets. The layout of the arc cell is shown in Fig. 2.3. The magnet system makes use of the technology based on superconducting Nb-Ti Rutherford cables. They are operated at the temperature of 1.9 K using a cooling system of superfluid helium. The main dipole magnets, used to bend the beam, supply the field of 8.33 T at the top energy of 7 TeV and 0.54 T at the injection energy of 450 GeV. The main quadrupole magnets, used to focus and de-focus the beam, supply the field gradient of 223 T/m at the top energy and 14.5 T/m at the injection energy. Multiple correction magnets, arranged between the main dipole and quadrupole magnets, are also used to correct the beam orbits.

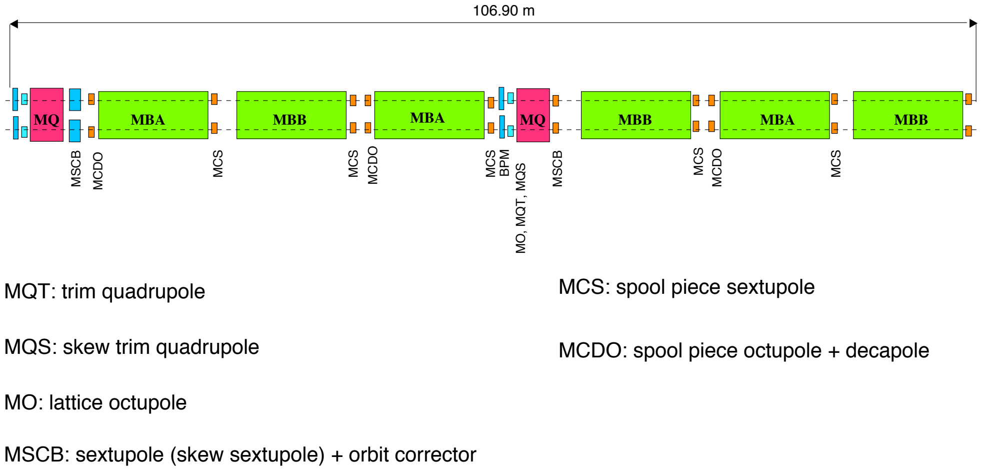

Figure 2.3: Schematic view of an LHC arc cell. MQ indicates the lattice quadrupole and MBA and MBB indicate main dipoles[10]. MBA and MBB are in principle same magnets but they use different structure of electronics

.

The LHC main ring contains four interaction points called Point 1, 5, 2, and 8 for ATLAS, CMS, ALICE, and LHC-b detectors, respectively.

The straight sections, approximately 528 m each, serve the experimental or utility insertion. The beam injection systems are located at Point 2 and Point 8 for Beam 1 and Beam 2, respectively. Two RF systems, one independent system for each beam, are located at Point 4. They capture, accelerate, and store the injected beams using the 400 MHz superconducting RF cavity. The amplitude of the RF field is 16 MV for each beam and the frequency is 400.790 MHz at top energy, and 8 MV/beam and 400.789 MHz at the injection energy of 450 GeV. In the RF region, the RF field accelerates beams with the energy gain of $\sim$485 keV/turn during the ramp time of approximately 20 minutes. After the acceleration, beams with the top energy cross at the interaction points.

2.3 LHC pp collision

When a proton-proton collision occurs, a parton in one proton interacts with a parton in another proton. Such interaction causes many kinds of physics processes such as production of Higgs, dijet, weak bosons, $t\bar{t}$, etc. Fig. 2.4 shows expected cross section of some of the benchmark processes at proton-(anti)proton colliders as a function of the center-of-mass energy. The physics process with the most significant cross section is the parton-parton scattering via QCD, which is more than 5 order of magnitude larger than the weak boson production. Thus, it is important to reduce QCD events efficiently in the data taking and event selection of the analysis.

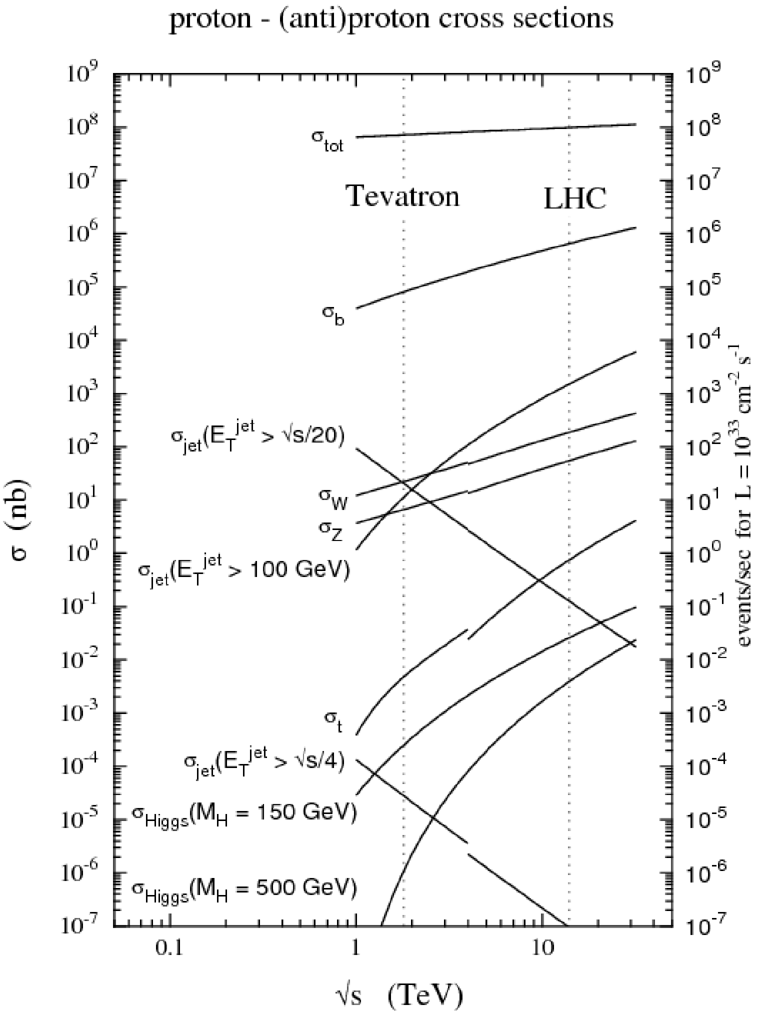

Figure 2.4: The cross section of the physics events via the $pp(\bar{p})$ collision as a function of the collision energy. [12]

Chapter 3

ATLAS detector

ATLAS(A Toroidal LHC ApparatuS) is one of the detectors located at LHC interaction points to detect and precisely measure kinematic properties of all the particles, except for neutrinos, produced by pp collisions of LHC. It consists of several subdetectors and magnet systems. The details of the ATLAS detector is discussed throughout this chapter. The construction and overview is described in Section 3.1, the magnet system is described in Section 3.2, details of each sub-detector are described in Section 3.3-3.5, and the trigger and DAQ system are explained in Section 3.6.

3.1 Detector overview

3.1.1 Coordinate system and nomenclature in ATLAS

The origin of the coordinate system is defined as the nominal interaction point. The z-axis is defined as the beam axis and the x-y plane as the plane transverse to the beam axis. The positive side in the x-axis is defined as to the center of the LHC ring, the positive y-axis as pointing upwards. Also, side-A of the detector is defined as that of positive z and side-C is in negative z, as illustrated in Fig. 3.1. ϕ is the azimuthal angle around the beam axis, θ is the polar angle from the beam axis, η the pseudo rapidity; $\eta = -\ln \tan\left(\frac{\theta}{2}\right)$, and the distance ΔR is defined as $\Delta R = \sqrt{\Delta\phi^2 + \Delta\eta^2}$, where $\Delta\phi$ and $\Delta\eta$ are ϕ and η difference between 2 points in the detector, respectively.

3.1.2 Goals and requirements for physics benchmarks

There are several physics benchmarks which ATLAS is expected to search for. The Higgs boson, which was successfully discovered in 2012[13], is an example of them. In the search for the Higgs boson, the most promising channel is $H \to \gamma\gamma$. Since the predominant $H \to b\bar{b}$ channel is largely affected by the QCD background, this channel is measured using the Higgs production in association with a vector boson (VH channel) where the vector boson decays into leptons. $H \to \tau\bar{\tau}$ channel is also important because Yukawa coupling of the lepton sector can be measured.

Supersymmetric particles[14] are also important topics. Assuming that R-parity is conserved, supersymmetric particles would involve cascades which always contain a lightest stable supersymmetric particle(LSP). As LSP is expected to interact very weakly with the detector, a significant missing transverse energy E_T^{miss} is expected in the final state. Low-energy processes such as $\tau \to 3\mu$, $\tau \to \mu\gamma$, $B_0 \to \mu\mu$ are considered as interesting as the search of new heavy particles because they can be helpful probe for new physics.

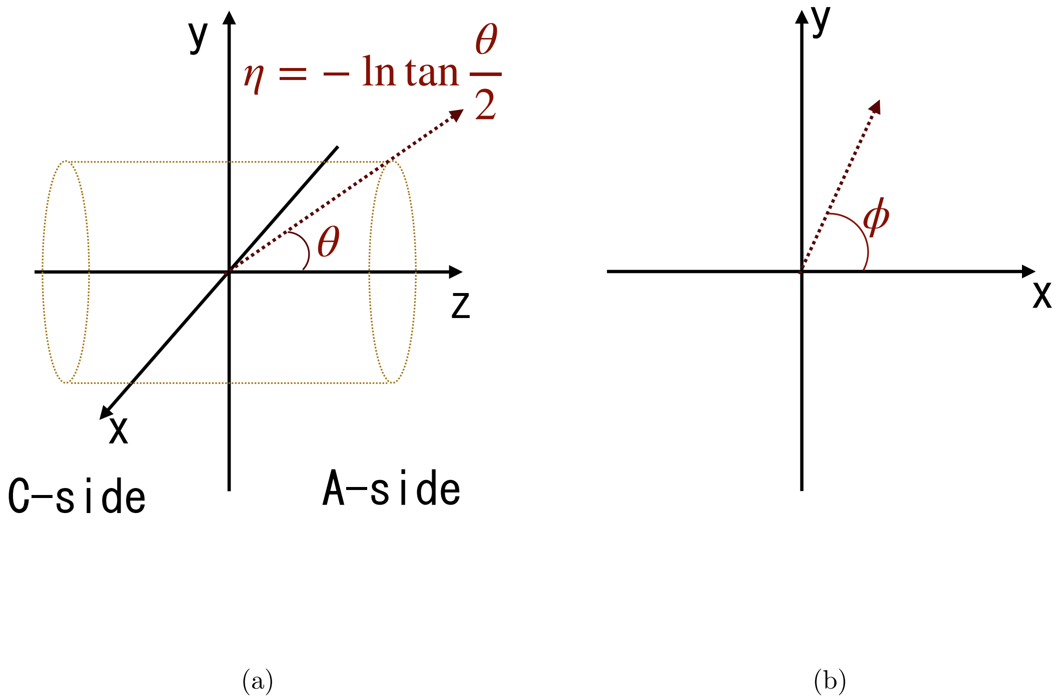

Figure 3.1: The schematic views showing the definition of the 3D axis, θ, and η(a) and x-y axis and ϕ(b).

To achieve high sensitivity to such processes, the ATLAS detector is designed to fulfill the requirements listed below.

- Fast, radiation-hard, and high-granularity electronics and sensors to enable efficient and stable data-taking under the high-radiation environment.
- Large acceptance in pseudorapidity with full azimuthal angle to reduce undetected particles and to achieve high resolution of E_T^{miss}.
- Good momentum resolution and reconstruction efficiency for charged particles to enable precise vertex reconstruction. These lead to good performance of τ-leptons and B-hadrons tagging.
- Electromagnetic calorimetry with high precision for electron and photon identification and measurement.
- Good identification and momentum resolution for muons in a wide range of momenta.
- Efficient triggering on low momentum objects with sufficient rejection to enable analysis over the large low-momentum background.

3.1.3 Structure of the ATLAS detector

The ATLAS detector is 25 m in height and 44 m in length, and its weight is about 7000 tons. It is nominally forward-backward symmetric with respect to the interaction point. Fig. 3.2 shows a schematic view of the detector.

As shown in the figure, the inner detectors (pixel detector, semiconductor tracker, and transition radiation tracker) are located in the most inner part. They are immersed in a

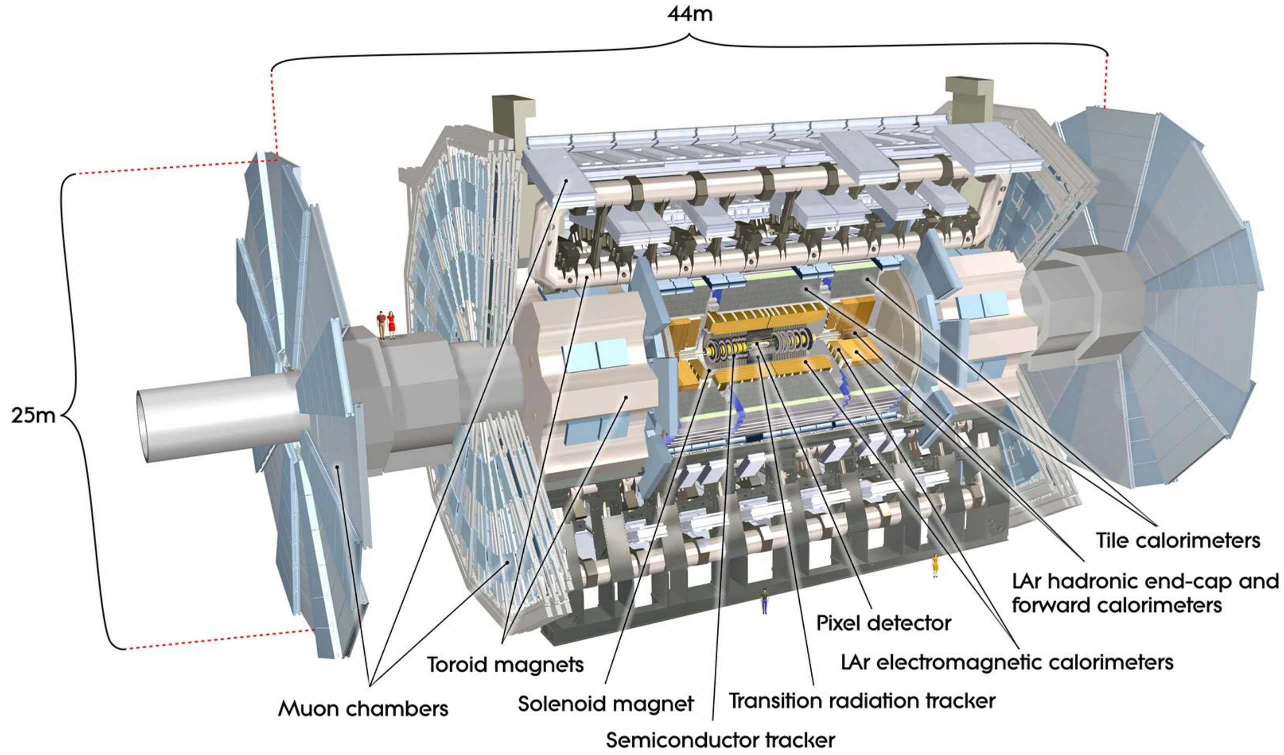

Figure 3.2: A schematic view of the ATLAS detector. [18]

2 T solenoidal field. The combination of the pixel and semiconductor tracker enables pattern recognition, momentum and vertex measurements, and electron identification. The transition radiation tracker is used to generate and detect transition radiation.

The electromagnetic sampling calorimeters with liquid-argon(LAr) and copper cover the range $|\eta| < 3.2$, and the scintillator-tile calorimeter provides the hadronic calorimetry region with $|\eta| < 1.7$. In the end-cap($|\eta| > 1.5$) regions, LAr calorimeter is also used as a hadronic calorimeter. The LAr forward calorimeters provide both electromagnetic and hadronic calorimetry and extend the coverage to $|\eta| \sim 4.9$.

The calorimeter is surrounded by the muon spectrometer, the outermost part of the ATLAS detector system. It measures muon momentum, charge, and position based on the magnetic deflection of muon tracks in the large superconducting air-core toroid magnets. The muon spectrometer system consists of 4 types of chambers; Monitored Drift Tubes(MDT's), Cathode Strip Chambers(CSC's), Resistive Plate Chambers(RPC's), and Thin Gap Chambers(TGC's). A precision measurement is held by MDTs in most of the η-range, while CSCs are used in the large η region where radiation is hard. TGCs and RPCs are used as trigger chambers, and they provide bunch-crossing identification, well-defined p_T thresholds, and the track measurements in the direction orthogonal to that determined by the precision-tracking chambers. RPCs cover the barrel region($|\eta| < 1.05$) and TGCs cover the endcap region($1.05 < |\eta| < 2.7$). TGCs provide trigger in the range of $1.05 < |\eta| < 2.4$.

3.2 Magnet system

The magnetic field, used to bend the tracks of charged particles, is provided by the ATLAS magnetic system, which consists of four superconducting magnets (one central solenoid, one barrel toroid, and two end-cap toroids). Details of the components and the magnetic fields are introduced in this section.

3.2.1 System components

The geometry of the magnet windings is shown in Fig. 3.3 and the main parameters are listed in Table 3.1. Overview of each magnet is described in the following.

Central solenoid

The central solenoid is designed to provide a 2 T axial magnetic field aligned on the beam axis for the inner tracker region. To suppress γ-conversions and achieve the desired performance, the layout was optimised to minimize the material thickness in front of the calorimeter, resulting in the assembly contribution of $\sim$0.66 radiation length in total. The magnet is based on a single-layer coil that is wound on a high-strength Al-stabilised NbTi conductor inside a 12 mm thick Al support cylinder. The inner and outer diameters of the solenoid are 2.45 m and 2.56 m, respectively, and its axial length is 5.8 m. The coil in the factory is shown in Fig. 3.4.

Barrel toroid

The barrel toroid is designed to provide a toroidal magnetic field of 0.5 T on average for the muon detectors in the central region. It fills the cylindrical volume surrounding the calorimeters. It consists of 8 coils encased in individual racetrack-shaped vacuum vessels made of stainless-steel. The coils are made of pure Al-stabilised Nb/Ti/Cu conductors wound into pancake-shaped. The inner and outer diameters are 9.4 m and 20.1 m, respectively, and its axial length is 25.3 m. The barrel toroids installed in the cavern are shown in Fig. 3.5.

End-cap toroids

The end-cap toroids are designed to provide a toroidal magnetic field of 1 T on average for the muon detectors in the end-cap regions. They are located just behind the forward calorimeters in both sides. Each of the magnet consists of a single cold mass built up from eight flat, square coil units and eight keystone wedges. The cold mass of the end-cap toroid is shown in Fig. 3.6.

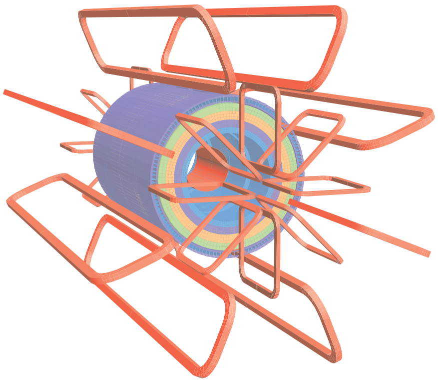

Figure 3.3: Geometry of magnet windings and tile calorimeter steel. The eight barrel toroid and end-cap toroid coils, and the solenoid windings inside the calorimeter are shown.[18]

Figure 3.4: Bare central solenoid after completion of the coil winding in the factory.[19]

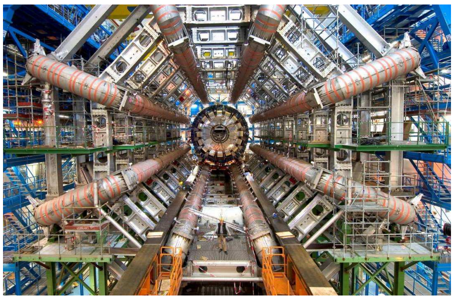

Figure 3.5: The barrel toroid and supporting structure in the cavern.[19]

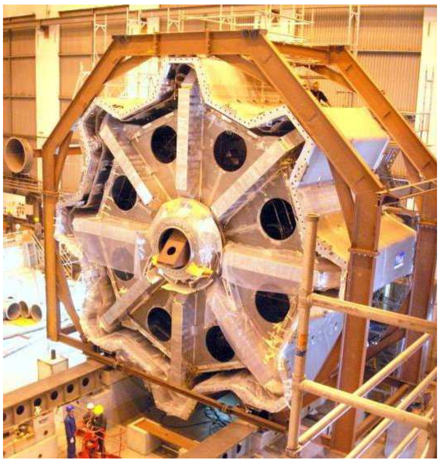

Figure 3.6: The end-cap toroid cold mass in the cryostat.[19]

Table 3.1: Main parameters of the ATLAS magnet system. [18]

Property	**Feature**	**Unit**	**Solenoid**	**Barrel toroid**	**End-cap toroids**
Size	Inner diameter	m	2.46	9.4	1.65
	Outer diameter	m	2.56	20.1	10.7
	Axial length	m	5.8	25.3	5.0
	Number of coils		1	8	2 × 8
Mass	Conductor	t	3.8	118	2 × 20.5
	Cold mass	t	5.4	370	2 × 140
	Total assembly	t	5.7	830	2 × 239
Coils	Turns per coil		1154	120	116
	Nominal current	kA	7.73	20.5	20.5
	Magnet stored energy	GJ	0.04	1.08	2 × 0.25
	Peak field in the windings	T	2.6	3.9	4.1
	Field range in the bore	T	0.9 - 2.0	0.2 - 2.5	0.2 - 3.5
Conductor	Overall size	mm^2	30 × 4.25	57 × 12	41 × 12
	Ratio Al:Cu:NbTi		15.6:0.9:1	28:1.3:3	19:1.3:1
	Number of strands(NbTi)		12	38 - 40	40
	Strand diameter(NbTi)	mm	1.22	1.3	1.3
	Critical current(at 5 T and 4.2 K)	kA	20.4	58	60
	Operating/critical-current ratio at 4.5 K	%	20	30	30
	Residual resitivity ratio for Al		> 500	> 800	> 800
	Temperature margin	K	2.7	1.9	1.9
	Number of units × length	m	4 × 2290	8 × 4 × 1730	2 × 8 × 2 × 800
Heat load	At 4.5 K	W	130	990	330
	At 60-80 K	kW	0.5	7.4	1.7
	Liquid helium mass flow	g/s	7	410	280

3.2.2 Magnetic field determination

It is important to determine the magnetic fields precisely for the momentum resolution of charged particles. In the ATLAS magnet system, the magnetic fields are reconstructed using calculation based on the Biot-Savart law and measurements by B-field sensors.

The magnetic field is computed with an assumption that all the magnets and detectors are located at the nominal position with the nominal shape. All the structures which can affect the B-fields, such as the ID cavity, the calorimeters, and the muon detectors are taken into account. As a result, the field strength at the interaction point is expected to be ∼1.998 T at nominal current, and to drop steeply from ∼1.8 T at $z = 1.7$ m to ∼0.9 T at the end of the ID cavity as shown in Fig. 3.7. In the muon detector region, the fields are expected to depend largely on η and ϕ. The expected bending power is calculated as integral of the magnetic field from the innermost MDT layer to the outermost MDT layer with respect to infinite momentum muons. The strength varies from 0.15 to 2.5 T, with an average value of 0.5 T in the barrel region, and from 0.2 to 3.5 T in the end-cap region as shown in Fig. 3.8.

Two types of sensors are used for B-field measurements. One is NMR prove, and the other is 3D Hall card[20] consisting of a rigid printed-circuit board carrying a small glass cube, with a Hall probe on each of three orthogonal faces. NMR proves measure the field strength $|\mathbf{B}|$ with an accuracy of ∼0.01 mT while 3D Hall cards measure both $|\mathbf{B}|$ and the direction of the field. The absolute 3D Hall cards accuracy on $|\mathbf{B}|$ is 0.2 mT up to $|\mathbf{B}|$=1.4 T and 1 mT up to 2.5 T, and the angular accuracy on the field direction is 2 mrad. 3D Hall cards can still work in the region under a gradient of a few tens of mT/cm, where NMR proves cease functioning. In the ID region, the magnetic fields measured by the sensors are fitted by the geometrical calculation, resulting in the residuals of ∼0.4 mT for all three field components. In the muon detectors region, all the readout of the sensors are used to

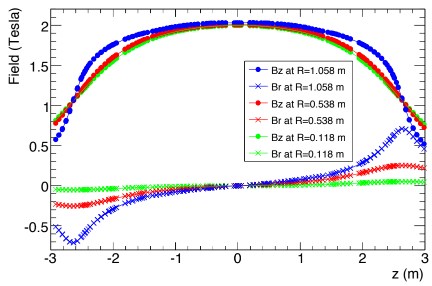

Figure 3.7: Predicted magnetic field in the ID cavity. The radial(B_r) and axial(B_z) field components depending on R and z are drawn.[18]

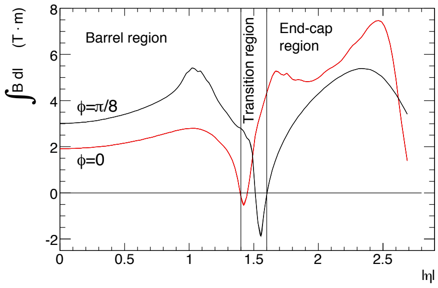

Figure 3.8: Predicted integrated magnetic field$\int B$dl in the muon region as a function of $|\eta|$ from the innermost to the outermost layer. The field is weak in the transition region, where barrel and end-cap fields overlap.[18]

reconstruct the position and shape of the coils and corresponding materials, and then the field in each point was calculated using the Biot-Savart law, resulting in relative accuracy of 0.2%.

3.3 Inner Detector

The ATLAS Inner Detector(ID) is designed to provide charged track measurements with excellent momentum resolution, and primary and secondary vertex identification. It covers the range in $|\eta| < 2.5$. It also provides electron identification over $|\eta| < 2.0$ in a wide range of energy between 0.5 GeV and 150 GeV.

ID is contained within a cylindrical envelope with the length of ±3512 mm and the radius of 1150 mm, within a solenoidal magnetic field of 2 T. The layout of ID is shown in Fig. 3.9. As shown in the figure, ID consists of three independent sub-detectors; Pixel, silicon microstrip(SCT), and transition radiation tracker(TRT). The discrete space-points from pixel layers and stereo pairs of SCT layers provide high-resolution pattern recognition at inner radii. At larger radii, tracking is provided by TRT comprising lots of layers of gaseous straw tube elements interleaved with transition radiation material to enhance the pattern recognition and improve the momentum resolution and electron identification over $|\eta| < 2.0$. Details of each sub-detector are described below.

3.3.1 Pixel

As shown in Fig. 3.9, the Pixel modules are arranged in four barrel layers and two end-caps each of which contains three disk layers. The innermost layer, corresponding to IBL[22] Pixel detectors, which did not exist in Run-1 period and was installed in May 2014. The basic parameters of each layer and disk are listed in Table 3.2. The data from Pixel are read out via Pixel modules consisting of electronics, sensors, and other related components. A module reads out 46080 channels corresponding to a sensor area of 63.4×24.4 mm^2 using 16 180 μm-thick front-end chips. A total of 1744 modules are used. The schematic view of a module is shown in Fig. 3.10.

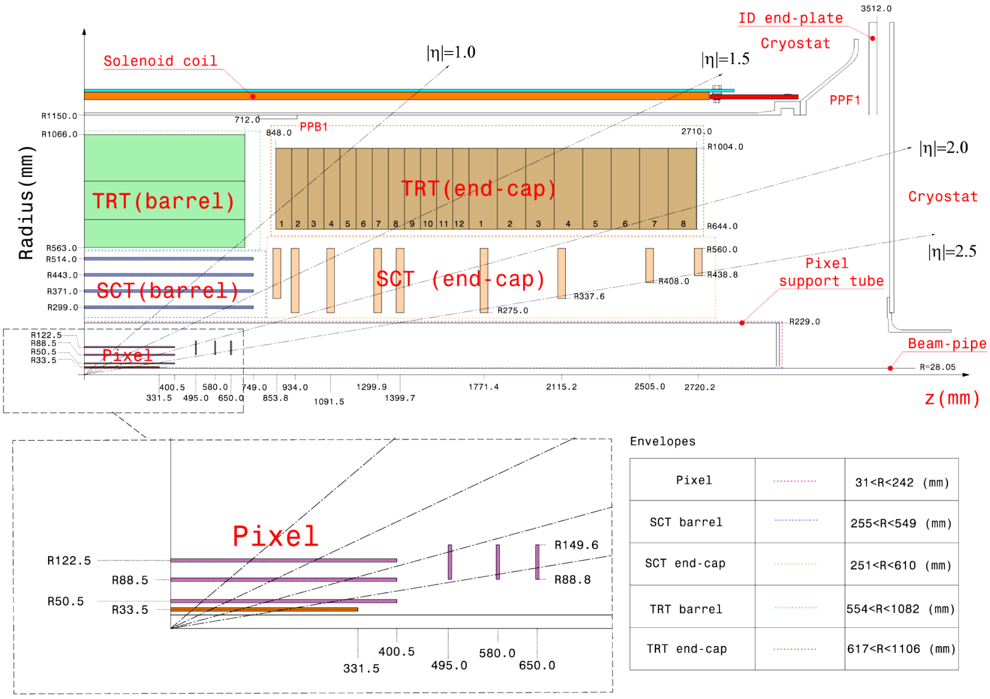

Figure 3.9: Schematic view of the ATLAS ID system showing each of the major detector elements. The labels PP1, PPB1, PPF1 indicate the patch-panels for the ID services.[21]

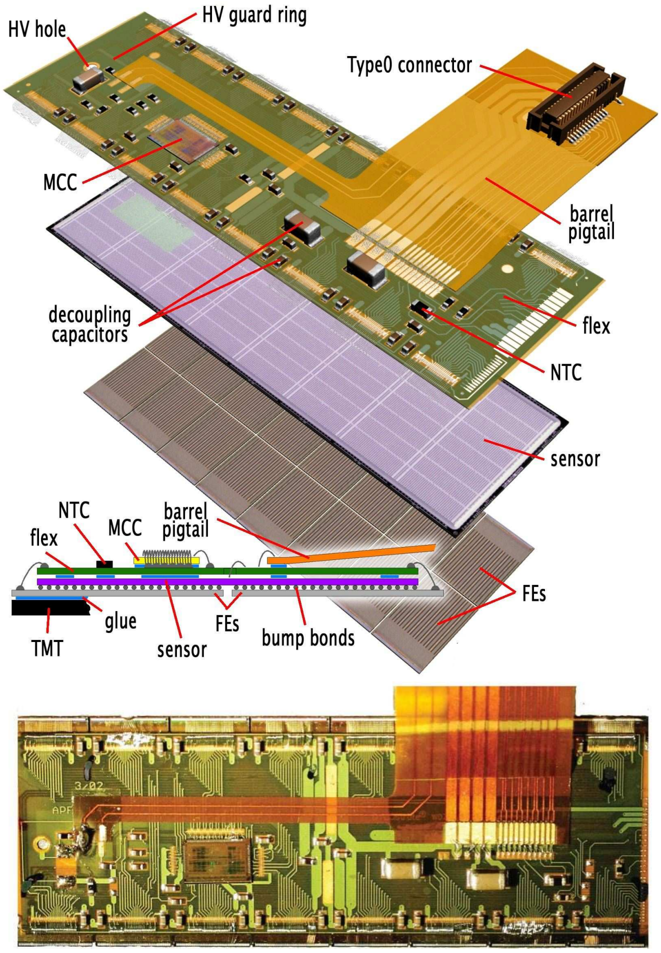

Figure 3.10: A schematic view of a Pixel module illustrating the major pixel and sensor elements. MCC is a chip dedicated to control the module and FE is front-end electronics. [23]

Table 3.2: Main parameters the Pixel detector.[18]

Barrel	**Radius(mm)**	**Staves**	**Modules**	**Pixels** ($\times 10^6$)
IBL	33.25	14	448	12.0
Layer-0	50.5	22	286	13.2
Layer-1	88.5	38	494	22.8
Layer-2	122.5	52	676	31.2
End-cap(one side)	**z(mm)**	**Sectors**	**Modules**	**Pixels** ($\times 10^6$)
Disk1	495	8	48	2.2
Disk2	580	8	48	2.2
Disk3	650	8	48	2.2
Total(Barrel and end-caps)			1968	92.4

The Pixel sensors are designed based on semiconductor detector technology that places an array of bipolar diodes on a high resistive n-type bulk. The diodes are made of implanting high positive(p^+) and negative(n^+) dose regions on each side of the wafer. A reverse bias voltage is applied to the diodes to extend the depletion region over whole of the bulk region so sensors can effectively collect and detect carriers generated by charged particles passing through the active volume of the sensor. The sensors are operated in the temperature range between -5 °C and -10 °C to reduce the leakage current and to avoid reverse annealing, which is an effect that the effective doping concentration N_{eff} increases on long time scale.

In the end-cap and outer 3 layers of barrel, about 90% of the pixels have the nominal size 50×400 μm^2 and the remaining pixels have the size 50×600 μm^2 in the regions at the read-out chips on a module. Each module consists of 47232 pixels arranged in 144 columns and 328 rows, but for reasons of space, 8 rows near the center line are ganged and resulting in 46080 readout channels. Smaller size of 50×250 μm^2 is employed in IBL to achieve stable operation under the high-radiation environment. Pixels of IBL are operated using a total of 448 modules, each of them consisting of 26880 pixels arranged in 80 columns and 336 rows.

The pixel modules are mounted on staves or sectors attached to support structure. In the barrel region, one stave of the outer three layers consists of 13 modules and the IBL stave consists of 32 modules while 6 end-cap modules are mounted on each sector. The performance of individual Pixel modules were measured in a test beam[23, 24]. At normal incident angle, the spatial resolution is about 12 μm, not significantly degraded after irradiation. The optimal resolution is 4.5 μm and 6.0 μm before and after irradiation, respectively in the incident angle of 10-15°. The Lorentz angle under the magnetic field of 2 T is 12° and 6° before and after irradiation, respectively.

3.3.2 SCT

The sensors of SCT make use of a single-sided p-in-n technology with AC-coupled readout strips. The sensor thickness of 285 ± 15 μm is chosen as a compromise between requirements of operation voltage, primary signal ionisation and simplicity of fabrication. The strip pitch is chosen to fulfill the requirements on digitising precision, granularity, particle occupancy and noise performance. The barrel sensors are in a rectangular shape with the pitch of 80 μm and the length of 6 cm while the end-cap sensors are in a trapezoidal shape with radial strips of constant azimuth with mean pitch of $\sim$80 μm. Each sensor consists of 768 active strips of 128 mm length, plus two strips at bias potential to define the sensor edge. The detector dimensions of the SCT sensors are summarised in Table 3.3 .

In the barrel region, the SCT sensors are mounted on the barrel SCT modules, which form four coaxial cylindrical layers(ID layers3-6). On each module, 770 SCT sensors (768 active and 2 dead) with 80 μm pitch are glued on the top and bottom side of a 380 μm-thick thermal pyrolitic graphite(TPG) base-board to form 128 mm long(126 mm active and 2 mm dead) unit. The sensors on the top and bottom side are rotated to make one axial and the other with a stereo angle of 40 mrad, resulting in sensitivity on both $\eta(z)$ and ϕ. The structure and sketch of a barrel SCT module are shown in Fig. 3.11.

The end-cap SCT modules, shown in Fig. 3.12, are mounted on nine end-cap disk layers in each detector side. Each of the modules has two sets of sensors glued back-to-back around the central TPG spine: one radial and the other with a stereo angle of 40 mrad to achieve a sensitivity on both η and ϕ as in the case of the barrel modules. Three types of modules, outer, middle, and inner, are used depending on the location. Parameters of the SCT layers in the barrel and end-caps are summarized in Table 3.4 and 3.5.

The performance of individual SCT modules was measured using a test beam[25]. The spacial resolution of $\sim$16 μm was measured in R-ϕ, which was not significantly degraded after irradiation while the measured Lorentz angle under a magnetic field of 2 T varied between 4.2° and 2.7° before and after irradiation, respectively.

Table 3.3: External cut dimensions of the SCT barrel and end-cap sensors. The inner-strip angle is the angle between adjacent strips of the sensors.[18]

Module type	**Sensor type**	**Cut length (mm)**	**Outer width (mm)**	**Inner width (mm)**	**Strip pitch (μm)**	**Inter-strip angle (μrad)**
Barrel	Barrel	63.960	63.560	63.560	80.0	0
End-cap inner	W12	61.060	55.488	45.735	56.9-69.2	207.0
End-cap middle	W21	65.0850	66.130	55.734	69.9-83.0	207.0
	W22	54.435	74.847	66.152	83.4-94.2	207.0
End-cap outer	W31	65.540	64.635	56.475	70.9-81.1	161.5
	W32	57.515	71.814	64.653	81.5-90.4	161.5

Table 3.4: SCT barrel layer parameters. The numbers in brackets indicate the average active sensor radii and overall length. The tilt angle is defined as the angle with respect to the tangent to the support cylinder surface in the plane perpendicular to the cylinder axis.[18]

Barrel cylinder layer	**Radius (mm)**	**Full length (mm)**	**Module tilt angle (degrees)**	**Number of modules**
3	284(299)	1540(1498)	11.00	384
4	355(371)	1540(1498)	11.00	480
5	427(443)	1540(1498)	11.25	576
6	498(514)	1540(1498)	11.25	672

Table 3.5: SCT endcap layer parameters.[18]

<table>
<tr><th>Disk</th><th>1</th><th>2</th><th>3</th><th>4</th><th>5</th><th>6</th><th>7</th><th>8</th><th>9</th></tr>
<tr><td>$|z|$ (mm)</td><td>853.8</td><td>934.0</td><td>1091.5</td><td>1299.9</td><td>1399.7</td><td>1771.4</td><td>2115.2</td><td>2505.0</td><td>2720.2</td></tr>
<tr><td>Outer modules</td><td colspan="9">52</td></tr>
<tr><td>Middle modules</td><td colspan="8">40</td><td>None</td></tr>
<tr><td>Inner modules</td><td>None</td><td colspan="5">40</td><td colspan="3">None</td></tr>
</table>

3.3.3 TRT

TRT covers the outermost part of the inner detector with multiple straw tubes with 4 mm diameter arranged in axial and radial directions in the barrel and end-cap regions, respectively as shown in Fig. 3.13 and 3.14. In the TRT tubes, the gas mixture of 70 % Xe, 27 % CO_2 and 3 % O_2 is packed with 5-10 mbar over-pressure. The anodes are 31 μm diameter tungsten (99.95 %) wires plated with gold of 0.5-0.7 μm. The wires are supported at the ends of the straw by an end-plug and directly connected to the front-end electronics, and kept at ground potential. The typical cathode voltage is -1530 V to get a gain of 2.5×10^4 . The anode resistance is approximately 60 Ω/m and the assembled straw capacitance is smaller than 10 pF. The signal attenuation length is $\sim$4 m, and the signal propagation time is $\sim$4 ns/m. The maximum electron collection time is $\sim$48 ns and the operational drift-time accuracy is $\sim$130 μm.

TRT is sensitive to both low energy photons emitted by transition radiation (TR) and minimum-ionising charged particles passing through the tubes. Since the signal amplitudes of

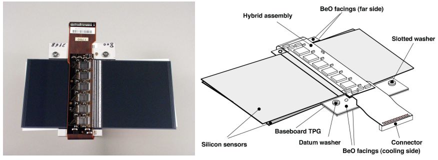

Figure 3.11: SCT module used in barrel region.[18]

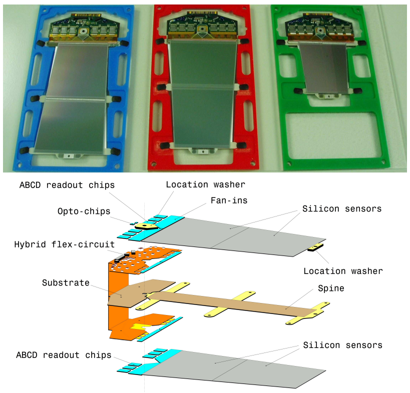

Figure 3.12: SCT endcap modules. The upper photograph shows the three types of modules(outer, middle, and inner from left to right.)[18]

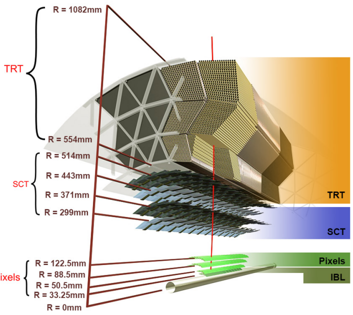

Figure 3.13: A layout of TRT and other elements of the inner detector in the barrel region.[26]

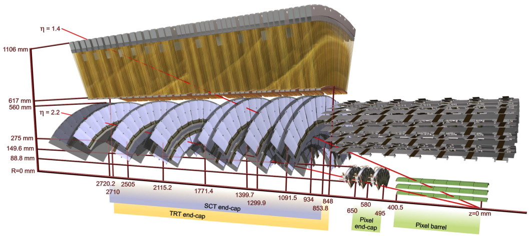

Figure 3.14: A layout of TRT and other elements of the inner detector in the end-cap region.[18]

the TR photons are much larger than charged particles, the distinction between TR photons and charged particles can be obtained in each straw using low($\sim$0.2 keV) and high($\sim$6 keV) thresholds in front-end electronics.

In the barrel region, TRT is divided into three rings from inside to outside, each composed of 32 modules, supported at both ends by frames. Each module consists of a carbon-fibre laminate shell and an internal array of straws embedded in a matrix of 19 μm-diameter polypropylene fibres as the transition radiation material. The straws form a uniform axial array with a mean spacing of $\sim$7 mm, and the modules are non-projective so that the dead region for high p_T tracks are reduced.

In the end-cap region, TRT in each side consists of two sets of independent wheels. The inner set contains 12 wheels, each of which consists of 8 successive layers spaced 8 mm apart. The outer set contains 8 wheels, 8 layers spaced 15 mm apart as shown in Fig. 3.9. Each layer consists of 768 radially oriented straws of 37 cm length with uniform azimuthal spacing, and the space between the layers is filled with layers of 15 μm thick polypropylene radiator foils. As a result, TRT contains 73 layers of straws in the barrel region and 160 straw planes interleaved with foils in the end-cap region. With this structure, all charged tracks with $p_T >$ 0.5 GeV and $|\eta| < 2.0$ will traverse at least 36 straws, except in $0.8 < |\eta| < 1.0$, barrel-end-cap transition region where the number of crossed straws decreases to a minimum of 22.

3.4 Calorimeters

The ATLAS calorimetry system consists of a number of sampling detectors with full ϕ-symmetric structure around the beam axis. The calorimeter components can be roughly divided into two types of detectors depending on the purpose. One is electromagnetic(EM) calorimeters constructed to measure the energy of electrons and photons, and the other is hadronic calorimeters to measure the energy of hadrons. They are further divided into several subsystems depending on the location.

The calorimeters near the beam axis are housed in three cryostats, one barrel and two end-caps. The barrel cryostat contains the EM barrel calorimeter while each of the two end-cap cryostats contains an EM end-cap calorimeter (EMEC), a hadronic end-cap calorimeter (HEC) located behind the EMEC, and a forward calorimeter (FCal) covering the forward region. All of the calorimeters described above use liquid argon(LAr) as the active medium because of good linearity in energy response, stability of response over time, and radiation-hardness. The hadronic calorimeter in the barrel region is the Tile calorimeter, in which scintillator tiles are used as sampling materials and steels as absorber. Each of the calorimeters consists of multiple layers. The number of layers, and granularity in each layer depends on $|\eta|$. The main parameters are listed in Table 3.6, and the geometry of the calorimeter system is shown in Fig. 3.15. Details of each component are described in the following sections.

3.4.1 Electromagnetic(EM) calorimetry

The purpose of EM calorimeters is to measure the energy and direction of electrons and photons. They are sampling calorimeters using LAr as the active material and lead plates glued to two stainless-steel sheets as absorbers. LAr and lead plates are arranged to form an accordion geometry shown in Fig. 3.16. This geometry provides full coverage in ϕ and a fast extraction of the signal at the electrodes located at the rear or the front.

Different geometry of the accordion waves are employed in end-cap(EMEC) and barrel calorimeters as indicated in Fig. 3.17. In the barrel calorimeter, waves are axial and run in ϕ, and the folding angles vary with radius, resulting in constant liquid-argon gap (Fig. 3.17(a)).

Table 3.6: Main parameters of each components of the calorimetry system.[18]

	Barrel		**End-cap**	
EM calorimeter				
	Number of layers and coverage			
Presampler	1	$\lvert\eta\rvert < 1.52$	1	$1.5 < \lvert\eta\rvert < 1.8$
Calorimeter	3	$\lvert\eta\rvert < 1.35$	2	$1.375 < \lvert\eta\rvert < 1.5$
	2	$1.35 < \lvert\eta\rvert < 1.475$	3	$1.5 < \lvert\eta\rvert < 2.5$
			2	$2.5 < \lvert\eta\rvert < 3.2$
	Granularity $\Delta\eta \times \Delta\phi$ versus $\lvert\eta\rvert$			
Presampler	0.025×0.1	$\lvert\eta\rvert < 1.52$	0.025×0.1	$1.5 < \lvert\eta\rvert < 1.8$
Calorimeter 1st layer	$0.025/8 \times 0.1$	$\lvert\eta\rvert < 1.40$	0.050×0.1	$1.5 < \lvert\eta\rvert < 1.8$
	0.025×0.025	$1.40 < \lvert\eta\rvert < 1.475$	0.025×0.1	$1.475 < \lvert\eta\rvert < 1.5$
			$0.025/8 \times 0.1$	$1.5 < \lvert\eta\rvert < 1.8$
			$0.025/6 \times 0.1$	$1.8 < \lvert\eta\rvert < 2.0$
			$0.025/4 \times 0.1$	$2.0 < \lvert\eta\rvert < 2.4$
			0.025×0.1	$2.4 < \lvert\eta\rvert < 2.5$
			0.1×0.1	$2.5 < \lvert\eta\rvert < 3.2$
Calorimeter 2nd layer	0.025×0.025	$\lvert\eta\rvert < 1.40$	0.050×0.025	$1.375 < \lvert\eta\rvert < 1.425$
	0.075×0.025	$1.40 < \lvert\eta\rvert < 1.475$	0.025×0.025	$1.425 < \lvert\eta\rvert < 2.5$
			0.1×0.1	$2.5 < \lvert\eta\rvert < 3.2$
Calorimeter 3rd layer	0.050×0.050	$\lvert\eta\rvert < 1.35$	0.050×0.025	$1.5 < \lvert\eta\rvert < 2.5$
	Number of readout channels			
Presampler	7808		1536(both sides)	
Calorimeter	101760		62208(both sides)	
LAr hadronic end-cap				
coverage			$1.5 < \lvert\eta\rvert < 3.2$	
Number of layers			4	
Granularity $\Delta\eta \times \Delta\phi$			0.1×0.1	$1.5 < \lvert\eta\rvert < 2.5$
			0.2×0.2	$2.5 < \lvert\eta\rvert < 3.2$
LAr forward				
coverage			$3.1 < \lvert\eta\rvert < 4.9$	
Number of layers			3	
Granularity $\Delta x \times \Delta y$ (cm)			Fcal 1: 3.0×2.6	$3.15 < \lvert\eta\rvert < 4.30$
			Fcal 1: ∼4 times finer	$3.10 < \lvert\eta\rvert < 3.15$, $4.30 < \lvert\eta\rvert < 4.83$
			Fcal 2: 3.3×4.2	$3.24 < \lvert\eta\rvert < 4.50$,
			Fcal 2: ∼4 times finer	$3.20 < \lvert\eta\rvert < 3.24$, $4.50 < \lvert\eta\rvert < 4.81$
			Fcal 3: 5.4×4.7	$3.32 < \lvert\eta\rvert < 4.60$,
			Fcal 3: ∼4 times finer	$3.29 < \lvert\eta\rvert < 3.32$, $4.60 < \lvert\eta\rvert < 4.75$
Readout channels			3524(both sides)	
Tile				
	Barrel		Extended barrel	
coverage	$\lvert\eta\rvert < 1.0$		$0.8 < \lvert\eta\rvert < 1.7$	
Number of layers	3		3	
Granularity $\Delta\eta \times \Delta\phi$	0.1×0.1		0.1×0.1	
Last layer	0.2×0.1		0.2×0.1	
Readout channels	5760	4092(both sides)		

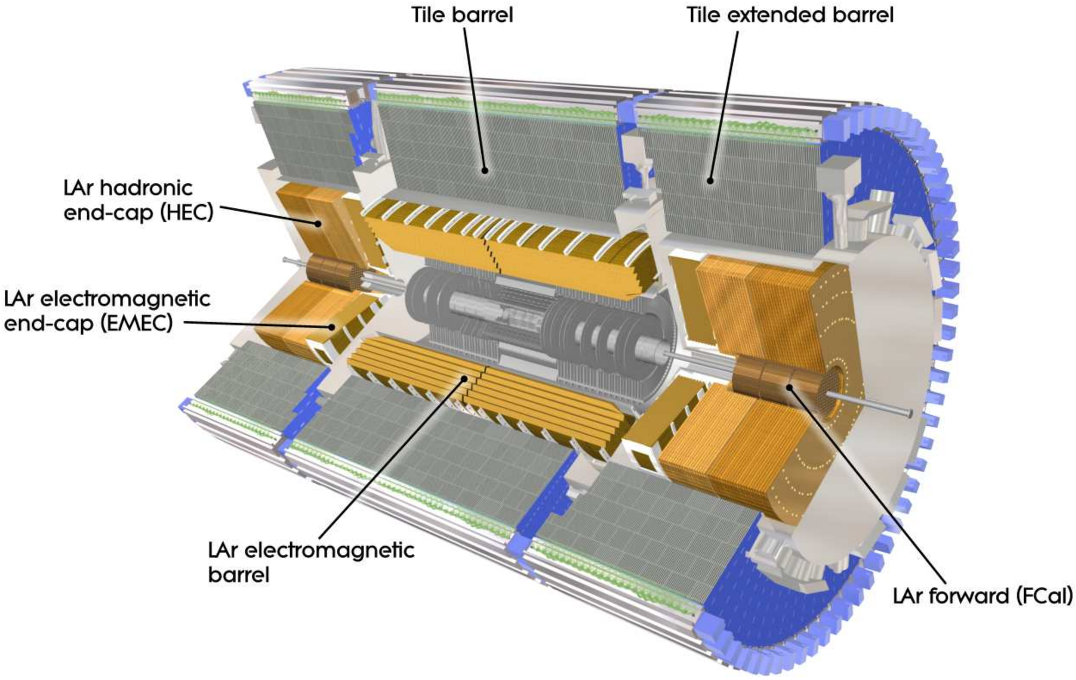

Figure 3.15: A schematic view of the ATLAS calorimeter system.[27]

On the other hand, waves of EMEC are parallel to the radial direction and run axially (Fig. 3.17(b)). Since the gap with liquid-argon of EMEC increases with radius, the wave amplitude and the folding angle of the absorbers vary with radius. These features of the geometry make the linearity and resolution very uniform over ϕ.

In the barrel region, the electrons and photons energy measurement is performed using barrel EM calorimeter plus a presampler, which is located in front of EM calorimeter to estimate the energy lost by the ID materials.

The barrel EM calorimeter is composed of two half barrels, one covering the $z > 0$ region($0 < \eta < 1.475$) and the other covering the $z < 0$ region($-1.475 < \eta < 0$). The length of each half barrel is 3.2 m and inner and outer diameters are 2.8 m and 4 m, respectively, and weight is 57 tons. Each half-barrel consists of 1024 accordion-shaped absorbers, interleaved with readout electrodes positioned in the middle of the gap by honeycomb spacers. The size of the drift gap in each side of the electrode is 2.1 mm, resulting in a total drift time of $\sim$459 ns for an operating voltage of 2000 V. Each half barrel is divided into 16 modules, each of them covering a region with $\Delta\phi = 22.5°$. The total thickness of a module is at minimum 22 radiation length(X_0), which increases from $22X_0$ to 33 X_0 between $|\eta| = 0$ and $|\eta| = 1.3$.

A module has three layers in depth(front, middle, and back as viewed from the interaction point). The signals in the front layer are read out at the low-radius side of the electrode while the signals in the middle and back layers are read out at the high-radius side of the electrode. There are in total 3424 readout cells per module. The granularity of each layer and region are listed in Table 3.6 and the radiation length of each layer is shown as a function of η in Fig. 3.18.

To correct the energy lost by the ID materials, the presampler is located in front of the EM calorimeter and the cryostat. It is a separate thin liquid-argon layer (11 mm in depth) employed to measure the shower caused by the interaction between the incident electrons or photons and the ID materials. The presampler layer is composed of 64 identical azimuthal

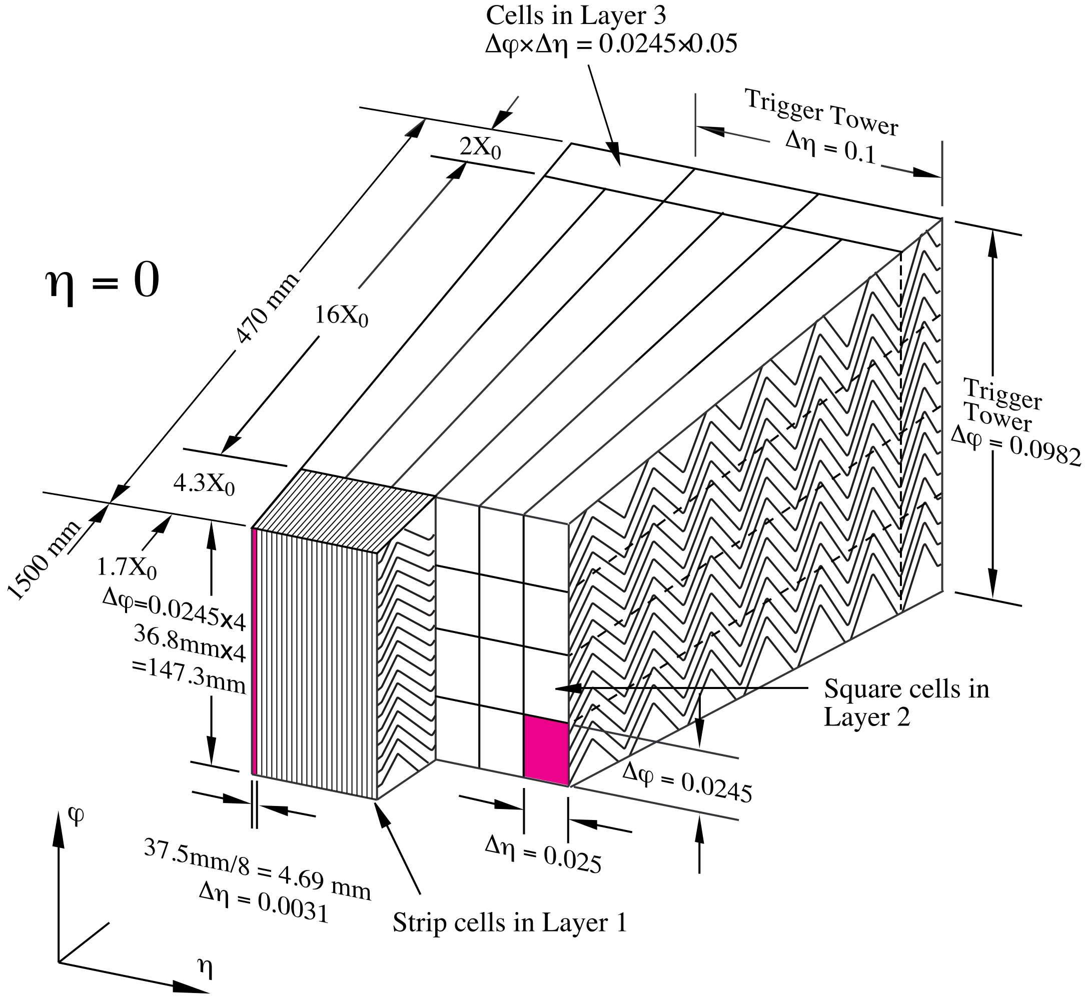

Figure 3.16: A sketch of a barrel calorimeter module with the accordion geometry. The granularity of η and ϕ of each layer is also shown. [28]

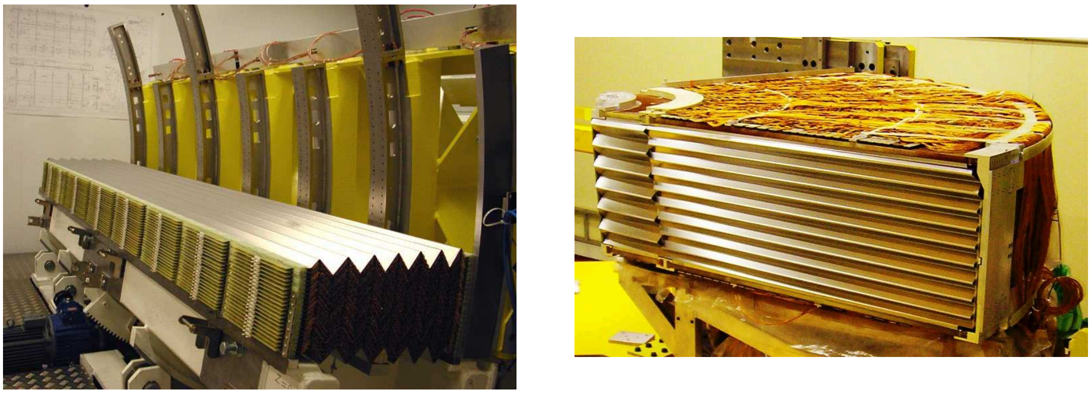

(a) (b)

Figure 3.17: Photographs of a barrel(a) and an EMEC LAr module(b). The geometry of the accordion waves are displayed.[18]

sectors (32 per half-barrel). Each sector is 3.1 m long and 0.28 m wide, resulting in the coverage in $\Delta\eta \times \Delta\phi$ of 1.52×0.2 . Each sector is composed of eight modules in different sizes, in lengths increasing with $|\eta|$ so a constant η-granularity of $\Delta\eta = 0.2$ is provided for each module, except for the module at the end of the barrel, whose η-coverage is 0.12 .

EMEC consist of two wheels, one of which is located on each side. Each wheel is 63 cm thick and 27 tons, and internal and external radii are 330 mm and 2098 mm, respectively. EMEC covers the region of $1.375 < |\eta| < 3.2$. The EMEC wheel in each region consists of two co-axial wheels with a 3 mm boundary at $|\eta| = 2.5$. Each inner wheel consists of 256 absorbers interleaved with readout electrodes while the outer wheel consists of 768 absorbers. The electrodes are located in the middle of the gaps by honeycomb spacers.

The active radiation length of EMEC is shown as a function of η in Fig. 3.19. The total thickness is larger than 24 X_0 except for $|\eta| < 1.475$. In the outer wheel, the thickness increases from 24 to 38 X_0 as $|\eta|$ increases from 1.475 to 2.5, and from 26 to 36 X_0 as $|\eta|$ from 2.5 to 3.2 in the inner wheel. The wheels are further divided into eight wedge-shaped modules without any discontinuity along the azimuthal angle. As for the barrel calorimeter, the precision region ($1.5 < |\eta| < 2.5$) is divided in depth into three longitudinal layers. The front layer, approximately with 4.4 X_0 of thickness, is segmented with strips along the η direction. The transverse size of the projective cell in the middle layer is $\Delta\eta \times \Delta\phi = 0.025 \times 0.025$ as the barrel. The back layer has a twice coarser granularity in η. The regions $|\eta| < 1.5$ and $2.5 < |\eta| < 3.2$ are segmented to two longitudinal layers and have a coarser transverse granularity.

The performance of the electromagnetic calorimeter is determined using test beams[29]. As shown in Fig. 3.20, the reconstructed energy response is linear within ±0.1%, and the energy resolution as a function of energy is shown in 3.21. The energy resolution has been fitted with the function[30]:

$$\frac{\sigma(E)}{E} = \frac{a}{\sqrt{E(GeV)}} \oplus b \; , \tag{3.1}$$

where a is the stochastic term and b is the constant term. As a result of the fitting, a stochastic term of 10% $\sqrt{\text{GeV}}$ and a constant term of 0.17 % have been obtained. Similar results have been obtained for EMEC as well. The measurement of response uniformity as

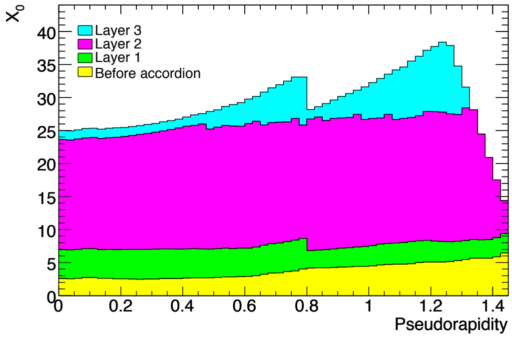

Figure 3.18: The radiation length X_0 of each barrel EM calorimeter layer shown as a function of η.[18]

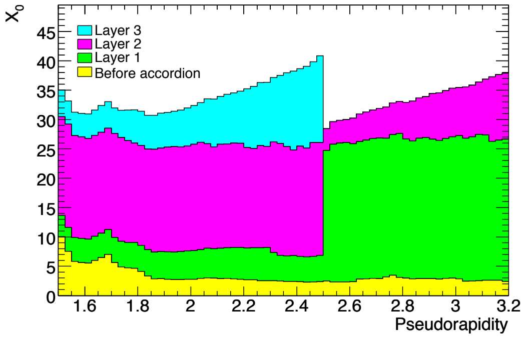

Figure 3.19: The radiation length X_0 of each EMEC layer shown as a function of η.[18]

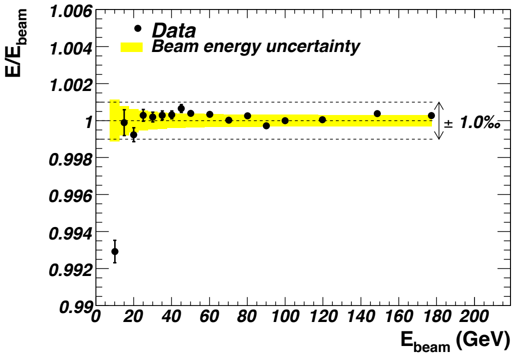

Figure 3.20: Linearity of response of a barrel LAr module at $|\eta| = 0.687$ as a function of the electron beam energy E_{beam}. [18]

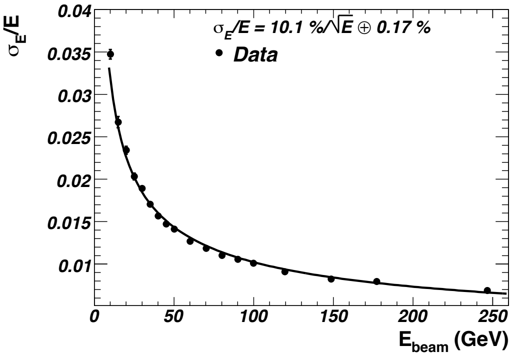

Figure 3.21: Fractional energy resolution of a barrel LAr module as a function of the electron beam energy E_{beam}.[18]

a function of η has revealed that the non-uniformity does not exceed 0.5 %, which is better than the design goal of 0.7 %. η resolution is about 1.5×10^{-4} and 3.3×10^{-4} for the front and middle layers, respectively. The π_0 rejection factor is 3.54 ± 0.12(statistical) for π_0 with p_T=50 GeV with a single photon efficiency of 90 %.

3.4.2 Tile calorimeter

The tile calorimeter is a sampling calorimeter using steel as the absorber and plastic scintillator tile as the active medium. It is located behind EM calorimeter and covers the region of $|\eta| < 1.7$. It is divided into three parts: a central barrel of 5.8 m length and two extended barrels of 2.6 m length each. All of them have an inner radius of 2.28 m and an outer radius of 4.25 m. The radial depth is approximately 7.4 λ (interaction length). Each barrel consists of 64 modules with a size of $\Delta\phi \sim 0.1$.

A sketch of a tile module geometry is shown in Fig. 3.22. Each module forms a periodic steel-scintillator structure with a ratio by volume of approximately 4.7:1. The scintillator tiles are oriented radially and perpendicular to the beam line to achieve almost seamless azimuthal coverage. Signals are read out using wavelength-shifting fibres and PMTs which are housed in the outer edge of the modules. The fibres have an attenuation length of 325

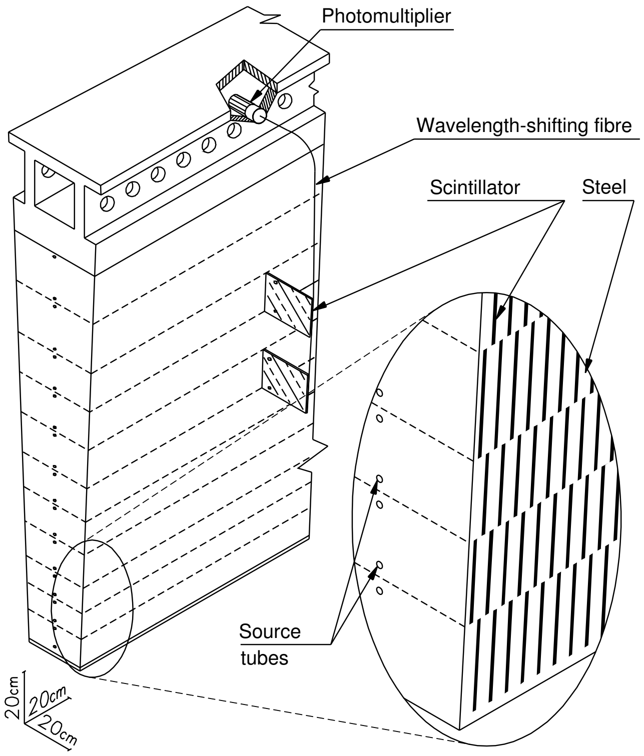

Figure 3.22: Schematic showing of Tile modules. [31]

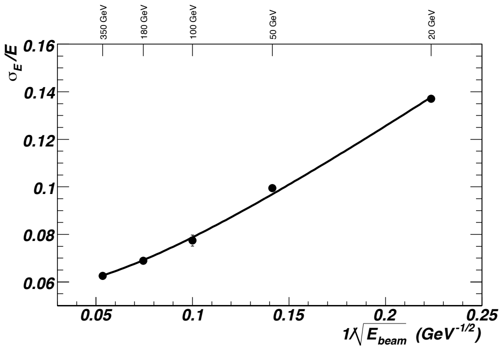

Figure 3.23: Fractional energy resolution of Tile calorimeter for isolated pion as a function of the beam energy at an incident angle $|\eta| = 0.35$. [18]

cm at a wavelength of 430 nm, with a spread in the distribution of the attenuation length of ∼3 % and in light output of ∼3 %. The three-dimensional cell structure is defined by the fibre grouping: Fibres are grouped in three radial sampling depth, approximately with 1.5, 4.1, and 1.8 λ thick at $\eta = 0$. These cells have dimensions of $\Delta\eta \times \Delta\phi = 0.1 \times 0.1$ in the first two layers and 0.2×0.1 in the last layer.

The performance of Tile calorimeter is measured using hadron test beams. The fractional energy resolution σ_E/E for isolated pions was measured as a function of the beam energy and impact angle. The result of the resolution measurement at $\eta = 0.35$ is shown as an example in Fig. 3.23. The result is fitted with the parametrization in Eq. 3.1 with the best fit of $a = (56.4 \pm 0.4)\%$ and $b = (5.5 \pm 0.1)$ %. The module-to-module uniformity in the mean response is found to be independent of η and to show an average spread of 1.4 %.

3.4.3 Hadron Endcap calorimeter (HEC)

HEC is a copper/liquid-argon sampling calorimeter contained in the same cryostats with EMEC and FCal to cover the region of $1.5 < |\eta| < 3.2$.

HEC in each side consists of two wheels; one is a front wheel (HEC1) and the other is a rear wheel (HEC2). They are cylindrical with an outer radius of 2030 mm. Each of the wheels consists of 32 identical wedge-shaped modules (Fig. 3.24). The modules are connected by the stainless-steel connecting-bar system at the outer wheel perimeter and the small copper connecting bars at the inner radius.

Among all the modules, flat copper plates are arranged with fixed gap. Each module of HEC1 is composed of 24 copper plates, each of which is 25 mm thick, plus a 12.5 mm thick front plate, and each of HEC2 is composed of 16 copper plates, each of which is 50 mm thick, plus a 25 mm thick front plate. The gaps between the plates are all 8.5 mm in the width. The resulting sampling fraction for HEC1 and HEC2 are 4.4 % and 2.2 %, respectively. The wheels have an inner radius of 372 mm for the first nine plates of HEC1 and of 475 mm for the remaining plates and all the plates of HEC2.

As shown in Fig. 3.25, three electrodes are located in the 8.5 mm gap between the grouped plates, resulting in dividing the gaps into four separate LAr drift zones with 1.8 mm width. The space between the electrodes is maintained using a honeycomb sheet. Each drift zone is individually supplied high voltage. The middle electrode carries a pad structure covered by a high-resistive layer as the readout electrode. This pad also defines the lateral segmentation of the calorimetry to provide a semi-pointing geometry with the granularity of $\Delta\eta \times \Delta\phi =$

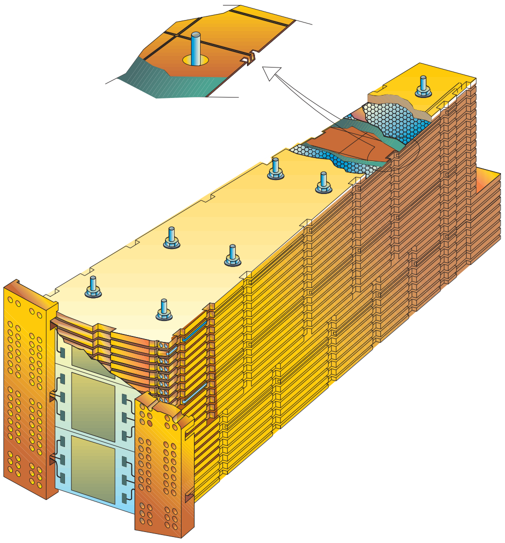

Figure 3.24: Schematic view of a HEC module, with a cut-away showing the readout structure.[18]

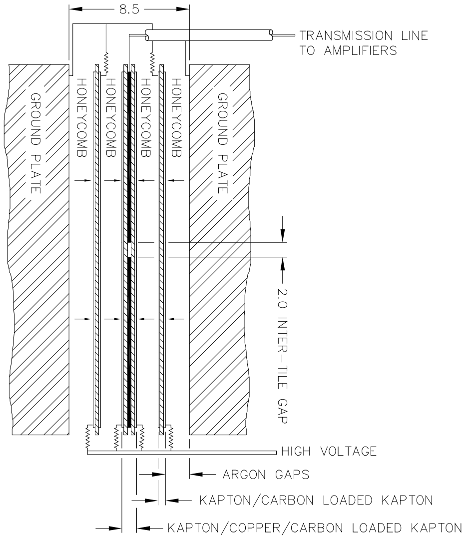

Figure 3.25: Schematic of the arrangement of the HEC readout structure in the gap region. All dimensions are in mm.[28]

0.1×0.1 in the region of $|\eta| < 2.5$ and 0.2×0.2 in the region with larger $|\eta|$. The other electrodes carry surfaces of high resistivity to which the high voltage is applied at. With the nominal high voltage of 1800 V, the typical drift time of electrons in the drift zone is 430 ns. The readout cells are defined by pads etched on the central foil in each gap.

As a result of exposure to test-beams, the fractional energy resolution to electrons is obtained with fitting in Eq. 3.1 with a stochastic term $a = (21.4 \pm 0.1)\%\ \sqrt{\text{GeV}}$ and a constant term b compatible with zero within errors. The fractional energy resolutions of π^+ and π^- are also measured as shown in Fig. 3.26. Fits to these results again using Eq. 3.1 yielded the stochastic terms of $(84.6 \pm 0.3)\ \%\ \sqrt{\text{GeV}}$ and of $(81.7 \pm 0.4)\ \%\ \sqrt{\text{GeV}}$ for π^- and π^+, respectively, and constant term of zero within errors.

3.4.4 Forward calorimeter (FCal)

FCal is housed in the same cryostats as EMEC and HEC to cover over $3.1 < |\eta| < 4.9$. As they are located at high η, with a distance of approximately 4.7 m from the interaction point, they are exposed to intense particle flux. Thus, they are designed to have very small liquid-argon gaps (< 2 mm) in order to avoid ion build-up problems and to provide material density as high as possible. Such small gaps are obtained using an electrode structure with small-diameter rods, centered in tubes parallel to the beam direction. As an example of the FCal structure, a schematic view of the first layer of FCal is displayed in Fig. 3.27.

As seen in Fig. 3.28, FCal is split into three modules, whose longitudinal width is 45 cm, one electromagnetic module (FCal1) and two hadronic modules (FCal2 and FCal3). For FCal1, copper is chosen as the absorber to optimise the resolution and the heat removal, while tungsten is chosen for FCal2 and FCal3 to provide containment of hadronic showers and to minimise the lateral spread of the showers. Main parameters of each module are listed in Table 3.7. Signals are read out from the side of FCal1 closer to the interaction point and

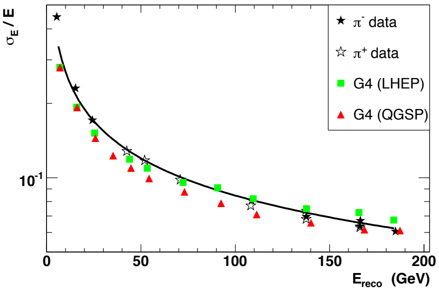

Figure 3.26: Fractional energy resolution of HEC as a function of reconstructed energy of π^- and π^+. The line indicates the fit result of π^+, the red and green points indicate the GEANT4 simulation results with different physics packages.[18]

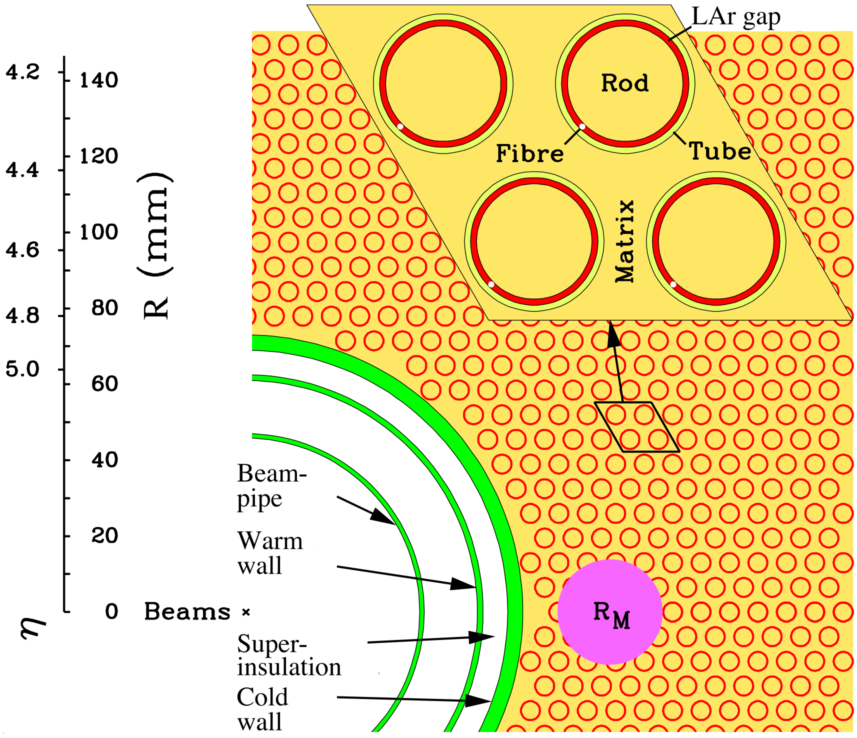

Figure 3.27: A schematic view of the electrode structure of FCal1. R_M indicates the Moliere radius.[18]

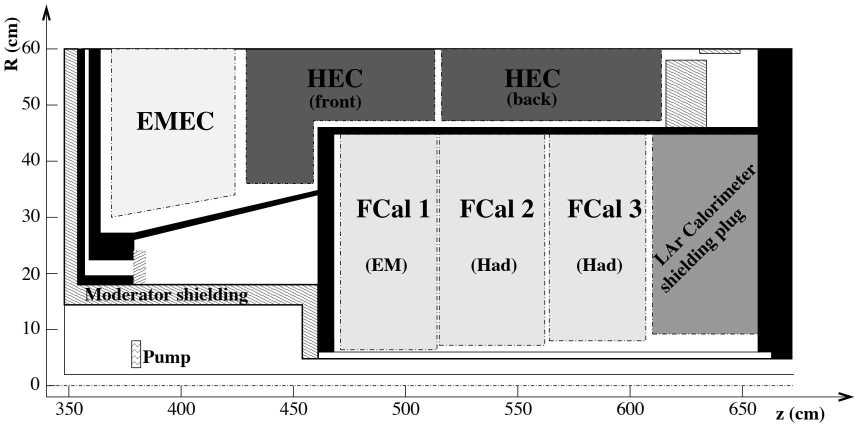

Figure 3.28: Schematic diagram showing three FCal modules. The other calorimeter components housed at the same cryostat is also shown.[18]

from the side of FCal2 and FCal3 farther from the interaction point. With this arrangement, the cables and connectors can be located away from the back of FCal1, where the maximum radiation damage is expected.

The performance is measured using test-beams of electrons and pions. The fit to the the measurement in the electron beam with Eq. 3.1 yielded a stochastic term of (28.5 ± 1.0) % $\sqrt{\text{GeV}}$ and a constant term of (3.5 ± 0.1) % $\sqrt{\text{GeV}}$. The fractional resolution to pion energy is measured using two techniques: (1) using a single weight per module, yielded a stochastic term of (94.2 ± 1.6) % $\sqrt{\text{GeV}}$ and a constant term of (7.5 ± 0.4) % $\sqrt{\text{GeV}}$. (2) using radial weights, yielded better resolution with stochastic and constant terms of 70 % and 3.0 %, respectively. These results are shown in Fig. 3.29.

Table 3.7: Main parameters of three FCal modules.[18]

	FCal1	**FCal2**	**FCal3**
Function	Electromagnetic	Hadronic	Hadronic
Mass of module(kg)	2119	3826	3695
Main absorber material	Copper	Tungsten	Tungsten
LAr gap width (mm)	0.269	0.376	0.508
Radiation length(X_0)	27.6	91.3	89.2
Absorption length(λ)	2.66	3.68	3.60
Number of electrodes	12260	10200	8224
Number of readout channels	1008	500	254

3.5 Muon spectrometer

The muon spectrometer is located at the outermost part of the ATLAS detector. It is designed to detect muons generated at the interaction point and to measure their momentum in the region of $|\eta| < 2.7$. The muon spectrometer system consists of four subdetectors: MDT, CSC, TGC, and RPC. TGC and RPC are used as trigger detectors covering the end-cap and barrel regions, respectively. MDT and CSC are used as precision-tracking detectors. MDT

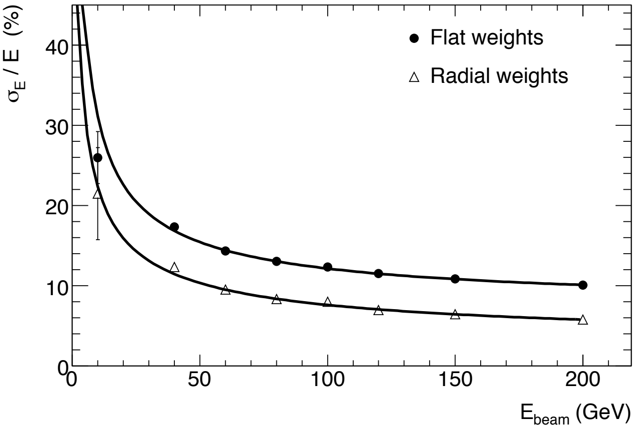

Figure 3.29: Fractional energy resolution of FCal for pion measurements.[18]

covers both barrel and end-cap region over $|\eta| < 2.7$ except for the radiation-hard region; the innermost layer of the end-cap $2 < |\eta| < 2.7$, where CSC is employed instead. The arrangement of the detectors is shown in Fig. 3.30 and 3.31. Details of each detectors are described in the following sections.

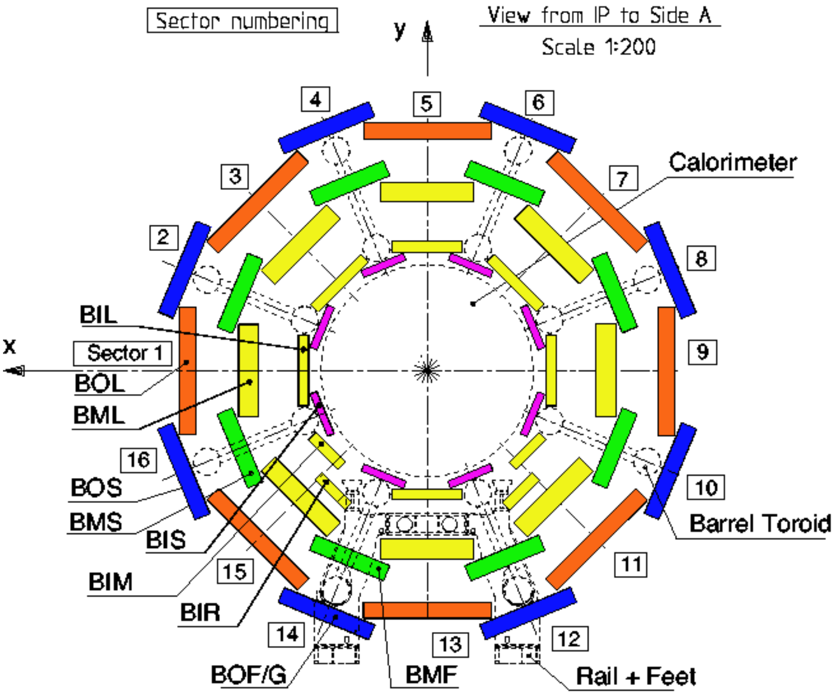

Figure 3.30: Cross section of the barrel muon system in a plane perpendicular to the beam axis.[18]

3.5.1 MDT

As described above, MDT is designed to measure muon tracks precisely in both barrel and end-cap regions. MDT chambers in the barrel region are arranged in three concentric cylindrical shells around the beam axis with the radii of approximately 5 m, 7.5 m, and 10 m. In the end-cap region, chambers form four large wheels in each side. The wheels are perpendicular to the beam axis and located at $|z| \sim$7.4 m, 10.8 m, 14 m, and 21.5 m . The chamber system has octant symmetry along the ϕ direction as the toroid magnetic fields. Each octant is divided into two sectors with slightly different lateral extensions: a large and a small sector.

The MDT chambers are represented using three characters like "BML", as indicated in Fig. 3.30 and 3.31. The first character, always "B" or "E', indicate barrel or endcap. The second one can be "I", "M", "O", and "E", indicating the layer of inner, middle, outer, and extended. The last character indicates the size, which can be "L" or "S", indicating large and small, respectively.

The basic element of MDT chambers is a pressurised drift tube(Fig. 3.32) with a diameter of 29.970 mm, operating with Ar/CO_2 gas(93:7) at 3 bar. When a charged particle passing through a tube ionizes the gas, electrons resulting from the ionization are collected at the central anode wire made of tungsten-rhenium with diameter of 50 μm. A high voltage of 3080 V is applied to the anode wires, resulting in a gas gain of 2×10^4. Each wire is connected to the HV supply system and the readout electronics at the opposite ends. The concentricity of the wire with respect to the tube is kept by the end-plugs with an accuracy of $\sigma < 10$ μm.

The drift tubes are arranged to run along ϕ to measure the muon tracks in the bending plane. They are gathered to form the layers, which are further gathered to form MDT chambers with trapezoidal and rectangular shape in end-cap and barrel region, respectively. All the MDT chambers consist of two groups of tube layers, called multi-layers. In the innermost layers, each multi-layer consists of four tube layers while the middle and outer layers consist of three. Each chamber is mounted on a support frame of solid aluminium beams providing mechanical rigidity to the structure. The frames also carry most of the

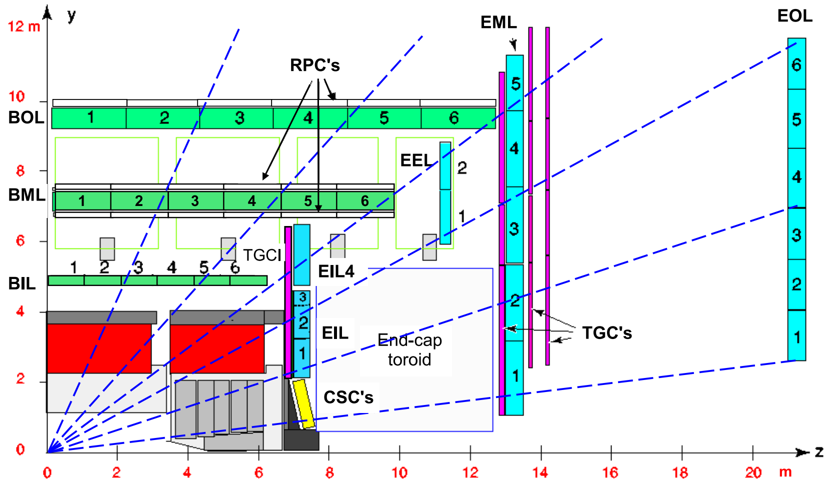

Figure 3.31: Side view of the muon system in a plane containing the beam axis.[18]

interfaces to gas supplies, the electronics, monitoring, and alignment service. Fig. 3.33 shows a mechanical structure of a MDT chamber.

The deformation of a chamber is monitored using an internal chamber alignment system with four sets of optical rays(red lines in Fig. 3.33), two are parallel and two are diagonal to the tube direction. It makes use of LED's and CCD sensors attached to the outer spacers and lenses attached to the middle plane to measure deformations of a few μm.

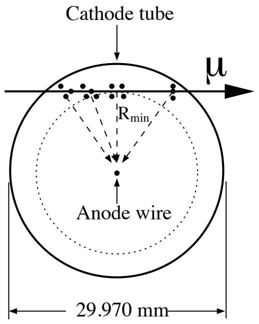

Figure 3.32: A sketch of MDT tube and its response to a muon passing through it.[18]

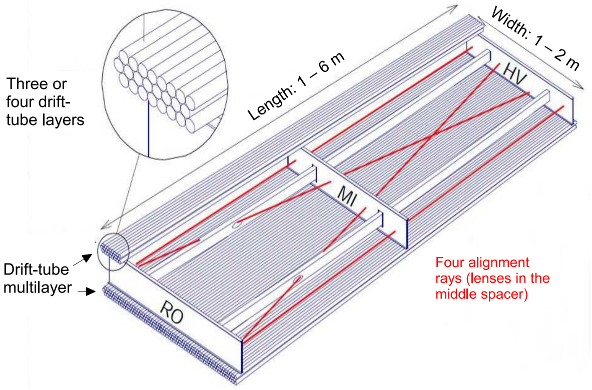

Figure 3.33: A mechanical structure of a MDT chamber. Readout electronics is located on the RO side and high voltage supplies are on the HV side. The red lines indicate the optical rays used in the internal alignment system.[32]

There are multiple types of chambers depending on the location. Their names, location, and main parameters are summarized in Table 3.8 and 3.9.

Table 3.8: Main parameters of MDT barrel chambers. [18]

Name	**Layer**	**Chambers**	**Tube layers**	**Location in R (mm)**	**Tubes/ layer**	**Length along z (mm)**	**Width along ϕ (mm)**
BIS	inner	96	2×4	4550	30	916	1820
BIS7	inner	16	2×4	4550	30	916	1820
BIS8	inner	16	1×3	4620	16	496	1000
BIL	inner	72	2×4	4949	36	1096	2820
BIM	inner	20	2×4	5353	36	1096	1685
BIR	inner	24	2×4	6056	36	916	1685
BMS	middle	72	2×3	8095	48	1497	3220
BMF	middle	12	2×3	8095	64	1937	3220
BML	middle	94	2×3	7139	56	1697	3700
BEE	middle	32	1×4	4415	48	1457	1060
BOS	outer	72	2×3	10569	72	2177	3920
BOF	outer	16	2×3	10675	64	2177	3920
BOG	outer	18	2×3	10675	40	1216	3920
BOL	outer	96	2×3	9500	72	2177	5110

Table 3.9: Main parameters of MDT end-cap chambers.[18]

Name	Layer	Chambers	Tube layers	Location in $\|z\|$(mm)	Tubes/ layer	Radial length(mm)	Width along ϕ(mm)
EIS	inner	32	2×4	7261	36	1096	1745
EIL	inner	48	2×4	7675	54	1637	3295
EES	extra	32	2×3	10276	40	1216	2951
EEL	extra	30	2×3	11322	40	1216	4703
EMS	middle	80	2×3	13878	64	1937	3860
EML	middle	80	2×3	14294	64	1937	6008
EOS	outer	96	2×3	21424	48	1457	4202
EOL	outer	96	2×3	21840	48	1457	6503

The raw signals from MDT tubes are first amplified, shaped, and discriminated by dedicated chips, and then routed to TDC, which measures the arrival time of leading and trailing edges to reconstruct the position of the charged particle. The RMS of timing is 0.23 ns, corresponding to an average uncertainty of position measurement of approximately 5 μm. Then a track segment is reconstructed in each chamber. The resolution on the central point of a track segment in a 3(4)-tube multi-layer is 50(40) μm, and the resulting resolution in a chamber is 35(30) μm. As a result, when a track crosses three MDT chambers, a sagitta is measured with a resolution of ΔS=45 μm, corresponding to a momentum resolution of $\delta p/p = \Delta S \times p/500$ μm, where p is given in the unit of TeV.

3.5.2 Cathode Strip Chamber

In the region of $|\eta| > 2$, in the first end-cap layer, the counting rate exceeds the limit of MDT, which is about 150 Hz/cm^2, whereas the limit of Cathode Strip Chamber(CSC), about 1000 Hz/cm^2, is sufficient up to the forward boundary of the muon system at $|\eta| = 2.7$. Thus, CSC is used as a precision-tracking chamber in this region.

The basic element of CSC is a multiwire proportional chamber. Ar/CO$_2$ gas(80:20) is packed under the operating voltage of 1900 V to achieve the gas gain of $\sim 6 \times 10^4$. The anode wires are oriented in the radial direction while cathodes are segmented with strips with two directions, one perpendicular to and the other parallel to the wires. Signals are read out from the strip, and the position of a track is measured by interpolation between the charges induced on neighbouring strips. Strips are arranged with a readout pitch of 5.31 mm and 5.56 mm for the large and small chambers, respectively, in the bending direction, resulting in a resolution better than 100 μm per CSC plane. In the non-bending direction, strip segmentation is coarser and the resolution is 5 mm. The structure of the chambers is shown in Fig. 3.34.

The whole CSC system, shown in Fig. 3.35, consists of two disks with eight chambers for each (eight small and eight large chambers), and each single chamber consists of four planes of multiwire proportional chambers. The disks are located at $|z| = 7$ m, mounted together with the MDT and TGC, and occupy the radial space between 881 mm and 2081 mm, corresponding to $2 < |\eta| < 2.7$.

3.5.3 TGC

The basic element of TGC is a multiwire proportional chamber. As shown in Fig. 3.36, TGC chambers have the cell geometry with the wire-to-cathode distance of 1.4 mm and wire-to-wire distance of 1.8 mm. With a highly quenching gas mixture of CO$_2$ and n-C$_5$H$_{12}$ (n-pentane)

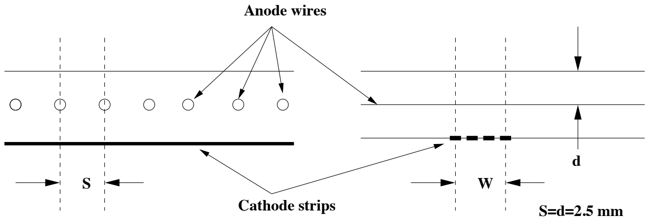

Figure 3.34: Structure of the CSC cells looking down the wires (left), and in perpendicular direction(right).[18]

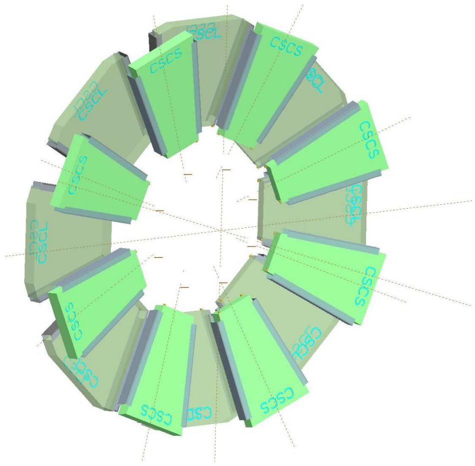

Figure 3.35: Layout of a CSC disk with eight small and large chambers.[18]

with the ratio 55:45, TGC is operated under the potential of approximately 2800 V, resulting in a gas gain of $\sim 3 \times 10^5$.

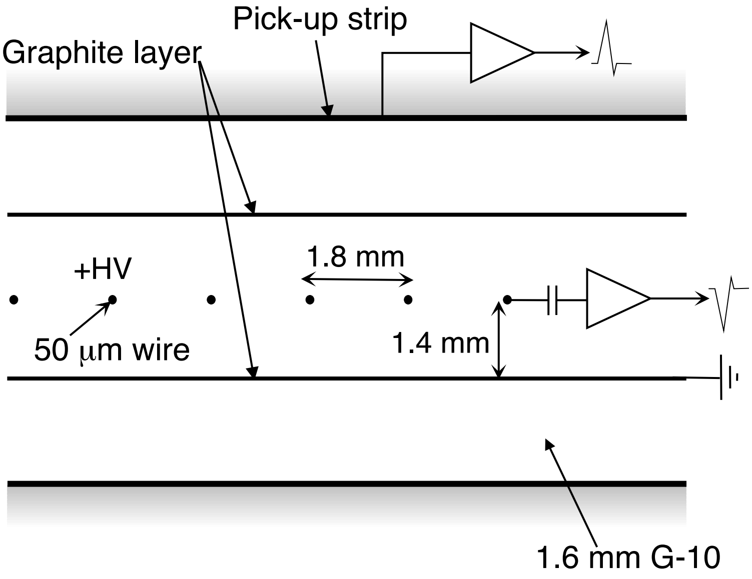

Figure 3.36: TGC structure including anode wires, cathodes layers(graphite) G-10 layers as insulator, and a pick-up strip orthogonal to the wires.[18]

TGC provides two functions in the end-cap region($|\eta| > 1.05$). One is muon trigger and the other is muon track measurement in the azimuthal coordinate to complement the measurement in MDT. There are nine layers of TGC chambers in each side: seven middle layers around $|z| \sim 15$ m to complement the middle MDT, and two inner layers around $|z| \sim 7$ m to complement the inner MDT. The middle seven layers are arranged in one triplet

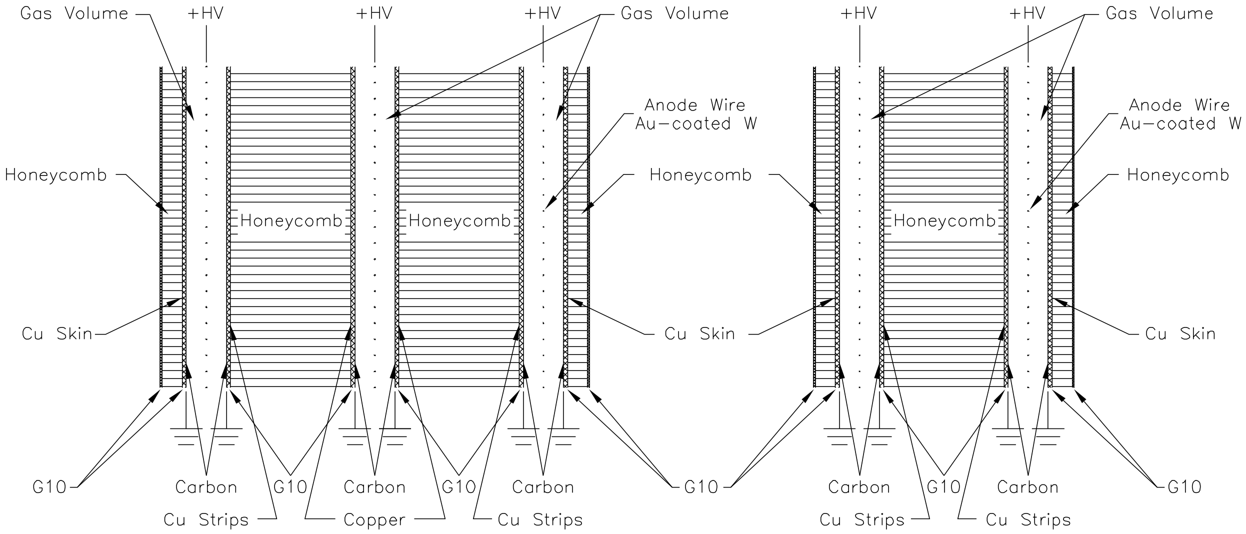

Figure 3.37: Cross section of TGC triplet and doublet modules.[18]

and two doublets, and the inner two layers are arranged in one doublet. The triplet and doublet structures consist of wire planes (anode), cathode planes, strip planes, shields and honeycomb support structure as shown in Fig. 3.37. The wire and strip plates are connected to the electronics to readout the signal. The radial, bending coordinate is measured by the wires and the azimuthal coordinate is measured by the strips. The chambers in the middle layers are mounted in two concentric rings, an outer (end-cap) covering the range $1.05 < |\eta| < 1.92$, and an inner (forward) covering the range $1.92 < |\eta| < 2.4$, to form circular disks.

3.5.4 RPC

RPC provides muon trigger and azimuthal measurement in the barrel region. RPC is a gaseous parallel electrode-plate detector operated with the electric field of 4.9 kV/mm applied between two resistive plates parallel to each other at a distance of 2 mm. The plates are made of phenolic-melaminic plastic laminate, and the gas is a mixture of $C_2H_2F_4$/Iso-C_4H_{10}/SF_6 (94.7/5/0.3). When a charged particle passes through the gas, the drift motion of the avalanche electrons induces a signal, read out via capacitive coupling to metallic strips mounted on the outer faces of the plates.

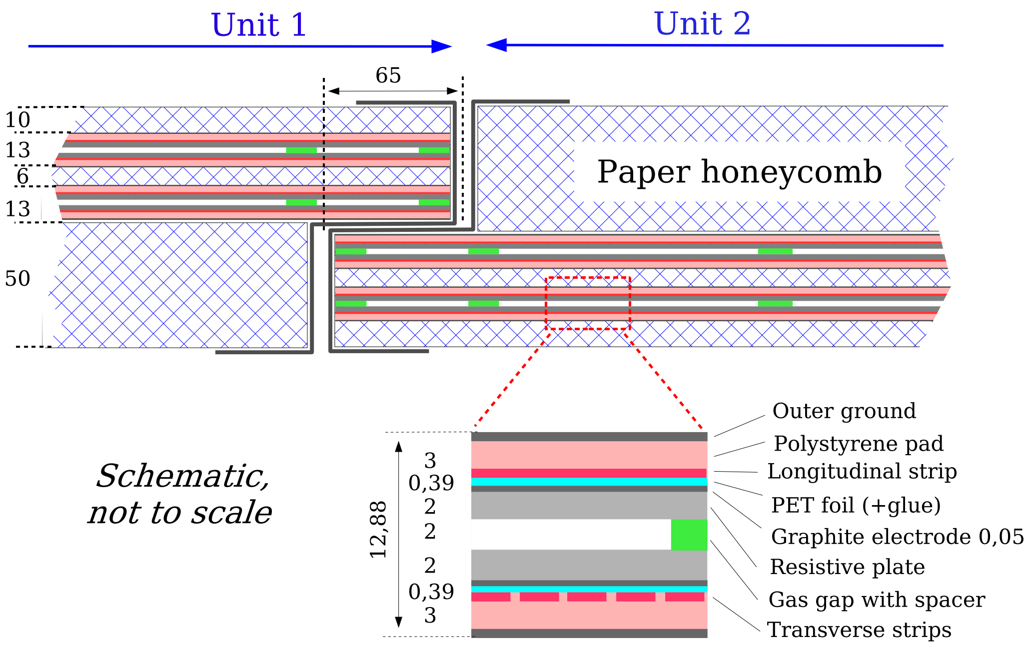

Figure 3.38: Cross section of two units of RPC joined to form a chamber. Dimensions are given in mm.[18]

Two rectangular layers of the gas volume are connected contiguously to each other to form a unit as shown in Fig. 3.38. In a unit, the readout strips of the two gas volumes are orthogonal so the position can be measured in both η and ϕ direction. The RPC units are further connected to form the whole RPC system with three concentric cylindrical layers around the beam axis, referred to as the three stations. The three stations are called RPC1, RPC2, and RPC3 from the inner to outer layer. The hit position is measured in both η and ϕ direction in each station. The barrel cylindrical structure is divided in ϕ direction into 16 as MDT. The arrangement of the RPC stations is shown in Fig. 3.39, and the parameters of the stations are listed in Table 3.10.

Table 3.10: Segmentation of the RPC system, the unit for R and $|z|$ is mm.[18]

	Small sector				**Large sector**			
Station	**Units**	**Chambers**	**R**	**Maximum $\lvert z\rvert$**	**Units**	**Chambers**	**R**	**Maximum $\lvert z\rvert$**
RPC1	148	84	7820	9362	149	94	6800	9147
RPC2	148	84	8365	9362	149	94	7478	9660
RPC2	176	92	10229	12847	192	96	9832	12267

3.6 Trigger and data acquisition system

While the LHC bunch crossing occurs with the rate of approximately 40 MHz, the readout rate is reduced to ∼1 kHz by the trigger system because of the limitations of the communication speed and computing resources[33]. The trigger system in Run2 consists of two levels of event selection. The first selection is a hardware-based trigger (Level-1 trigger, L1), and the second is a software-based trigger (High Level Trigger, HLT). The Level-1 trigger searches for signatures from high-p_T muons, electrons/photons, jets, and τ-leptons and de-

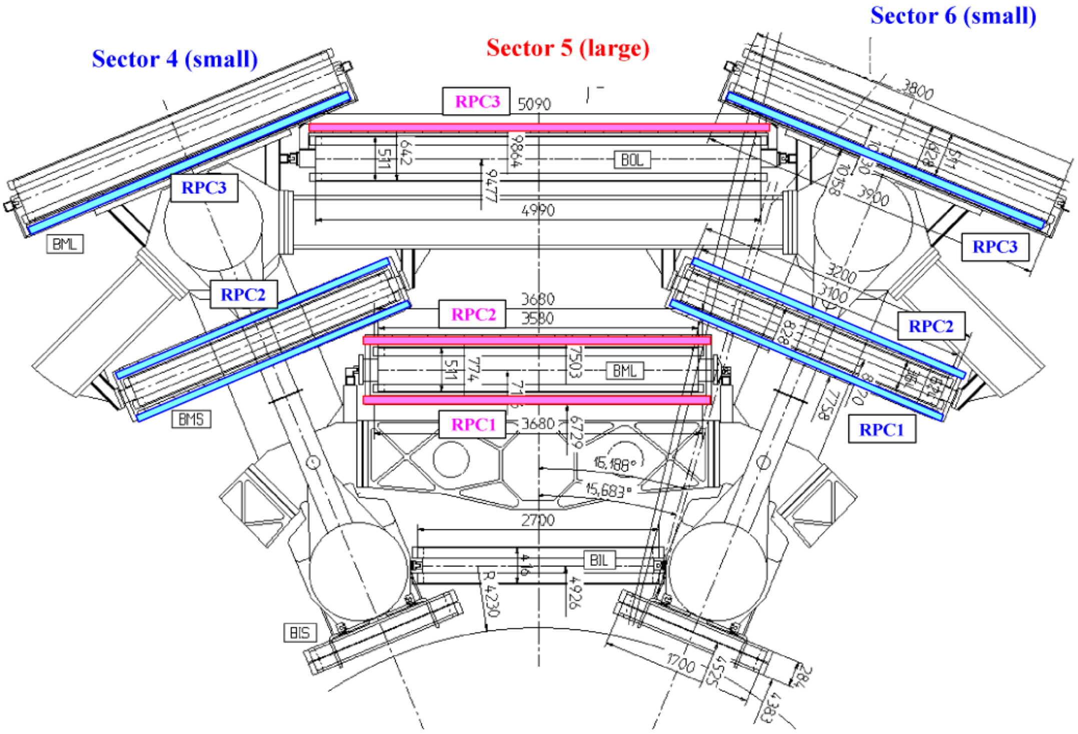

Figure 3.39: Cross section of the upper part of the muon barrel system. RPC chambers are marked in colour. Dimensions are given in the unit of mm.[18]

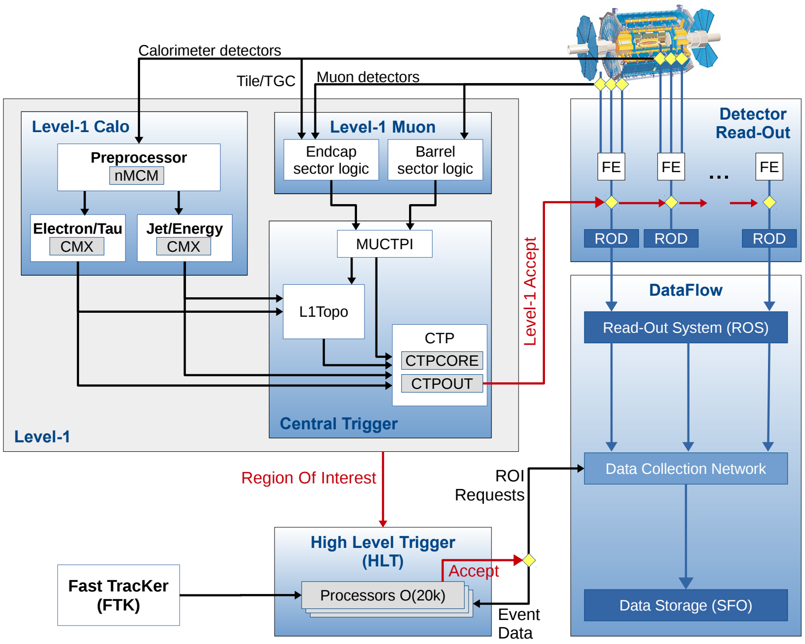

Figure 3.40: A schematic view of the ATLAS trigger and DAQ system. FTK is the system to provide track information to HLT at L1 rate, but it was not in use in 2015 and 2016 data taking.[33]

termines Region-of-Interest (RoI) in the detector using coarse granularity calorimeter and muon detector information.

The Level-1 trigger thresholds are configured to make the trigger rate approximately 100 kHz. When an event is accepted by the Level-1 trigger, the decision is sent to all the detector readout electronics within the latency of 2.5 μs to readout full data, and then RoIs are sent to HLT in which more sophisticated algorithms run using full granularity detector information. The HLT trigger rate is about 1 kHz and a processing time is about 200 ms. A schematic view of the trigger system is shown in 3.40.

3.6.1 Level-1 trigger

The Level-1 trigger performs the event selection based on information from the calorimeters and muon detectors (RPC for barrel and TGC for end-cap). The aim of the trigger using calorimeters (L1Calo) is to identify high-E_T objects detected by calorimeters such as electrons, photons, jets, and τ-leptons decaying into hadrons.

Events with large E_T^{miss} and total transverse energy are also tagged by the L1Calo. The trigger using muon detectors (muon trigger) aims to identify muons. It searches for patterns of hits consistent with muons originating from the interaction point. The overall accept decision of L1 is made by the Central Trigger Processor (CTP), which combines the information from different types of detectors.

L1Calo

Then, the data are transmitted to the other two systems: Cluster Processor (CP) and Jet/Energy-sum Processor (JEP). CP identifies electron/photon and τ-lepton candidates

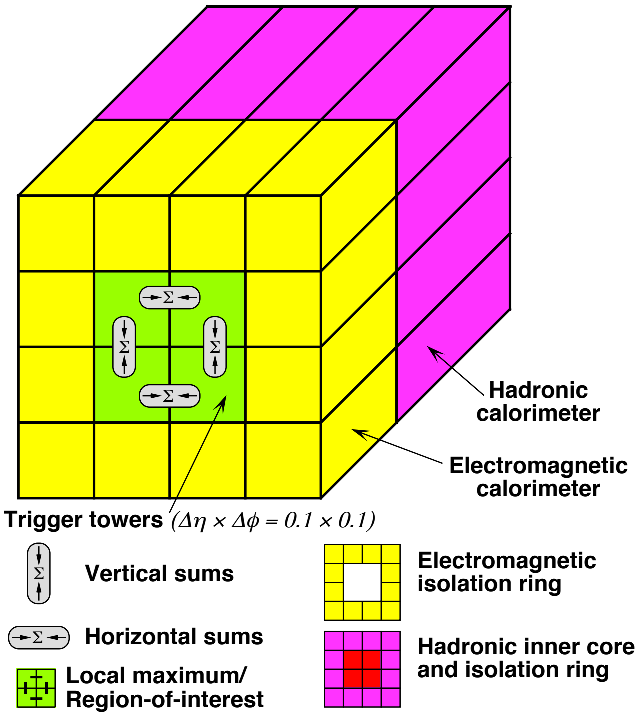

Figure 3.41: A schematic view of the trigger cluster used in the electron/photon trigger.[18]

above the corresponding programmable thresholds, and JEP identifies jet candidates and produces scalar sum of E_T and E_T^{miss}. The electron/photon and τ triggers cover the region of $|\eta| < 2.5$, where the inner detector measures the tracks precisely, and the jet trigger covers $|\eta| < 3.2$. In the E_T^{miss} and scalar sum triggers, E_T in the region up to $|\eta| = 4.9$ is taken into account. The granularity unit of L1Calo is called "trigger tower", corresponding to 0.1×0.1 in $\Delta\eta \times \Delta\phi$ in most parts and larger at high $|\eta|$.

The algorithms of electrons/photons and τ triggers run in CP as described below. The electron/photon trigger identifies clusters with size of $\Delta\eta \times \Delta\phi = 0.2 \times 0.2$. As displayed in Fig. 3.41, clusters are composed of 2×2 trigger towers in which at least one of the four possible two-tower sums of nearest neighbouring electromagnetic towers exceeds a pre-defined threshold. The clusters are also required to be isolated: 12 towers surrounding ring in the electromagnetic calorimeter, as well as 2×2 hadronic towers core sum behind the cluster are required not to exceed the programmable thresholds. The τ trigger, searching for narrow hadronic jets, use the similar algorithm as electron/photon trigger. Each of the four possible two-tower sums of nearest-neighbour electromagnetic towers is added to the 2×2 hadronic-tower core sum just behind, and then compared to the pre-defined threshold. The isolation veto requires that the surrounding 12-towers ring around the RoI in either the electromagnetic or hadronic towers do not exceed the thresholds. L1Calo consists of three sub-systems. The first system is the pre-processor, which digitises the analogue input signals, associates them with specific bunch-crossing, and calculates the transverse-energy values.

The jet, sum of E_T, and E_T^{miss} algorithms run in JEP. The jet algorithm calculates E_T sums in the windows consisting of 2×2, 3×3, and 4×4 trigger towers and then compare them with the pre-defined thresholds. The energy-summation algorithm produces sums of E_T and E_T^{miss}, and then compare them with the thresholds.

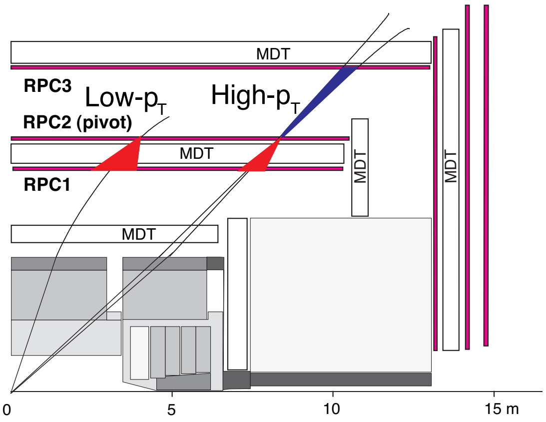

Figure 3.42: A schema of the L1 muon barrel trigger. The arrangement of the three stations (RPC1, RPC2, and RPC3) and examples for roads of low- and high-p_T triggers are shown.[18]

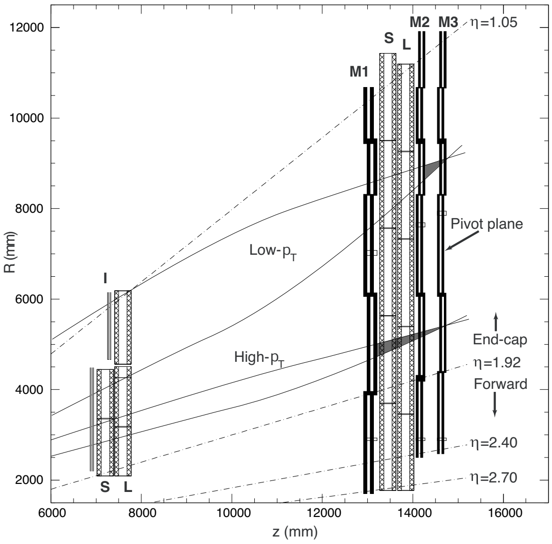

Figure 3.43: A schema of the L1 muon end-cap trigger. The arrangement of the three stations(M1,M2, and M3), and the inner layer(I) is shown.[18]

Muon trigger

In both the barrel and end-cap regions, the L1 muon trigger is based on three trigger stations. The trigger algorithm is to require a coincidence of hits between trigger stations within a road, which is consistent with a track of a muon from the interaction point. Since the width of the road is correlated to the p_T of the incoming muon, thresholds are applied on the width.

The muon trigger in the barrel region ($|\eta| < 1.05$) makes use of the RPC detectors. As shown in Fig. 3.42, the three stations consisting of one RPC doublet each are arranged in three concentric barrel layers (RPC1, RPC2, RPC3 from inner to outer). The trigger algorithm runs as following: when a hit is detected in the doublet of RPC2 (the pivot plane), a corresponding hit in RPC1 is searched for within a road whose center is defined by the line of conjunction of the hit in the pivot plane with the interaction point. When a hit is found and the 3-out-of-4 coincidence in the four layers is satisfied, the low-p_T trigger is accepted. Then, the algorithm searches for corresponding hit in RPC3. It requires 1-out-of-2 possible hits of the RPC3 doublet (high-p_T trigger). Three thresholds are prepared for low- and high-p_T triggers each. In both cases, the trigger information in η and ϕ is combined to form RoIs.

In the end-cap region ($1.05 < |\eta| < 2.4$), TGC is used for the L1 muon trigger. As shown in Fig. 3.43, the three stations are arranged in three end-cap wheel layers in each side (M1, M2, M3 from inner to outer). M1 is triplet and M2 and M3 are doublet. The trigger algorithm runs as following. The pivot plane of TGC is M3. When a hit is detected in M3, the low-p_T trigger searches for corresponding hits in M2 and requires a 3-out-of-4 coincidence. If the low-p_T requirement is satisfied, the high-p_T coincidence runs to search for corresponding hits in M1 triplet requiring 2-out-of-3 coincidence. The trigger algorithm further requires 1-out-of-2 coincidence on corresponding region of the Inner layer in order to suppress background. This requirement is applied only on high-p_T thresholds(≥ 15 GeV) and the region covered by the Inner layer ($1.3 < |\eta| < 1.9$, and partially $1.05 < |\eta| < 1.3$). As RPC, the trigger information is combined to form RoIs.

3.6.2 High Level Trigger

High Level Trigger(HLT) is implemented as software applications for much more sophisticated algorithms than the L1 trigger. The HLT system makes use of the RoI information as well as the readout data. The dedicated hardware modules are used to handle and transport the RoI and readout information, then the HLT application runs in ∼1500 machines at ∼115 kHz to make a trigger decision, resulting in the HLT trigger rate of approximately 1 kHz. Thousands of trigger configuration, summarized as "Trigger menu", are prepared to optimise the sensitivity of the physics analyses. Pre-scale factors are defined in each of the configuration so that the overall trigger rate does not exceed the limit.

Chapter 4

Data and Monte Carlo samples

Details of LHC *pp* collision data and Monte Carlo(MC) simulation samples used in the analysis are explained in this chapter.

4.1 LHC *pp* collision data

This analysis is based on the LHC *pp* collision data at $\sqrt{s} = 13$ TeV collected by ATLAS during 2015 and 2016. The LHC configuration was adjusted during this period to achieve larger luminosity, hence larger instantaneous luminosity was realized at the latter period as shown in Fig. 4.1, while the pileup, which was 13.7 in average in 2015, increased to 24.9 in average in 2016 as displayed in Fig. 4.2. In terms of the total luminosity, LHC delivered *pp* collision of 4.2 and 38.5 fb^{-1}, in which 3.9 and 35.6 fb^{-1} were recorded by ATLAS in 2015 and 2016, respectively. Fig. 4.3 shows the integrated luminosity as a function of date in 2015 and 2016.

Prior to the analysis, recorded data is required to be flagged as “good” by the ATLAS common selection criteria called “Good Runs List (GRL)” selection, which selects periods of data that satisfy all the requirements as following:

- LHC is running in the stable-beam mode

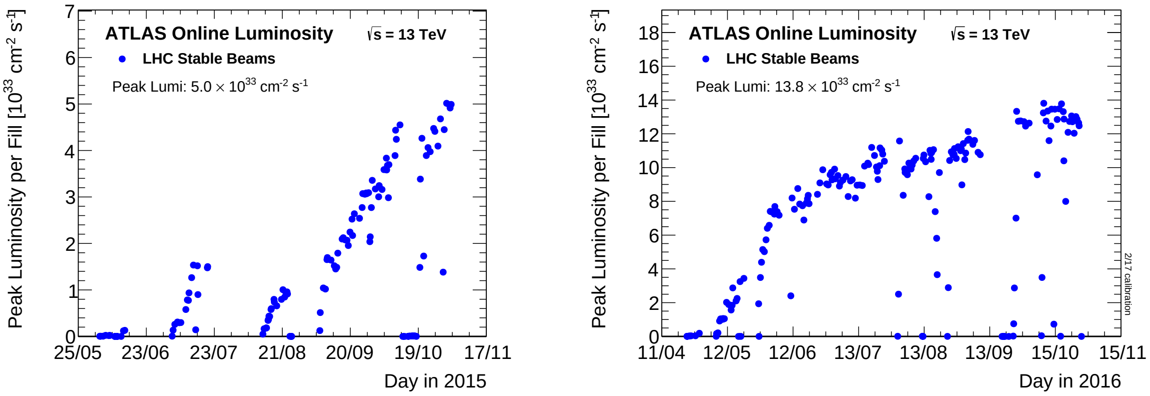

(a)

(b)

Figure 4.1: The LHC peak luminosity per fill as a function of date in 2015(a) and 2016(b). Larger peak luminosity is achieved in the latter period.

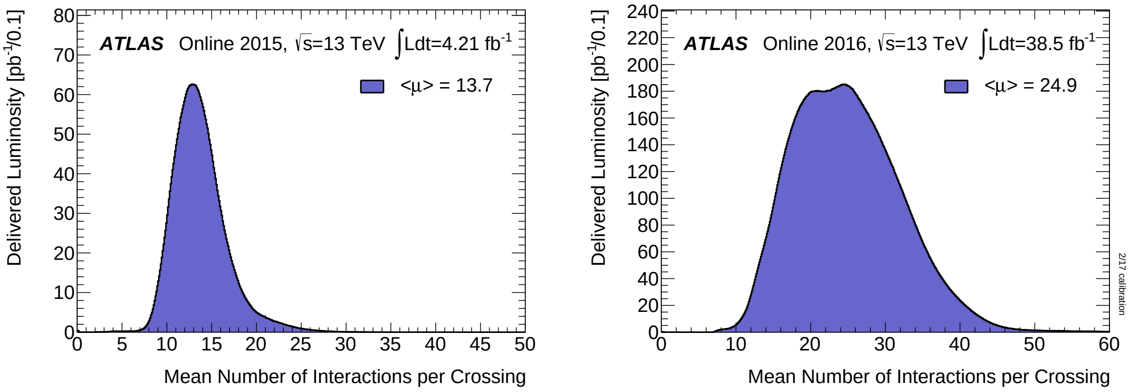

(a) (b)

Figure 4.2: Distribution of the pile-up μ in 2015(a) and 2016(b). Larger pile-up is recorded in 2016 than 2015 due to the LHC configuration.

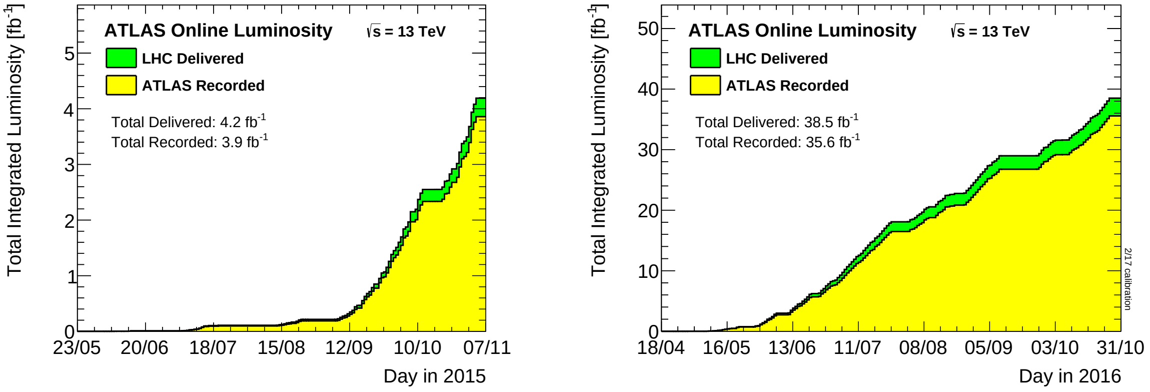

(a) (b)

Figure 4.3: The integrated delivered and recorded luminosity as functions of date in 2015(a) and 2016(b).

- The toroid and solenoid magnets are on with the nominal field.
- All the sub-detectors and DAQ components are working.
- Not too many noisy channels exist.

After the GRL selection, the remaining data of 3.2 and 33.0 fb^{-1} have been used in the analysis.

4.2 Monte Carlo samples

The contribution of VLQ signal and SM background events are estimated using the Monte Carlo(MC) simulation technique. Details of the general MC production procedure and the settings of each sample are described in the following. This chapter is focused on the simulation settings and the impact of each BG sample on the analysis is discussed in Chapter 7.

4.2.1 General MC production procedure in ATLAS

In the ATLAS MC simulation, physics events are first generated in parton-level by event generators. After the parton-level event generation, the parton shower, the radiation emissions by partons in accordance with the QCD perturbation, and jet fragmentation are computed. There are two types of generators in terms of the treatment of parton shower and jet fragmentation. One is the full generators, which calculate the parton shower and fragmentation, and the other is the parton level generators, which generate only parton-level events and require a full generator to perform the parton shower and fragmentation.

After fragmentation, interactions between the generated particles and ATLAS detector are computed based on GEANT4[34] simulation, which includes shower generation in electromagnetic and hadron calorimeters as well as hits of inner and muon detectors. The signals of the ATLAS detector are treated in the same way as the real data to reconstruct objects with the procedures introduced in Chapter 5. In the final step, the reconstructed objects and recorded events are corrected to fix the discrepancy between data and MC.

4.2.2 VLQ signal samples

Pair production

Vector-like T pair production ($T\bar{T}$) samples are generated with PROTOS[40] interfaced with PYTHIA8[37] for the showering using the NNPDF2.3 LO PDF set[38] and the A14 tune[39]. The VLQ mass of each sample ranges from 0.5 TeV up to 1.4 TeV, each containing 250000 generated events.

Single production

Vector-like T single production samples were generated based on the VLQ UFO model[35] using MADGRAPH5[36] interfaced with PYTHIA8 for the showering using the NNPDF2.3 LO PDF set and the A14 tune. Samples ranging from 0.7 TeV up to 2.0 TeV VLQ mass are produced with a nominal coupling of 0.5, and several mass points are produced with a coupling of 0.1 and 1.0 to study the kinematic property dependency on the coupling. Each mass and coupling dataset contains 250000 events.

Single production with different couplings

Due to the limitation of CPU resources and storage, the official samples described above are produced with only the nominal coupling of $\kappa_T = 0.5$ in most of the mass points. Since the decay width of T depends on the coupling, it is important to investigate the impact of the coupling on the kinematic property. Thus, the reweighting procedure is applied to the nominal $\kappa_T = 0.5$ samples to generate samples with κ_T ranging from 0.1 to 1.6 in step of 0.1 in each of the mass point. In the reweighting procedure, $O(10^7)$ events with a given coupling is generated by MadGraph and the T mass distribution is compared to the distribution of the official $\kappa_T = 0.5$ samples to compute the reweighting factor depending on the T mass. Examples of reweighting are shown in Fig. 4.4.

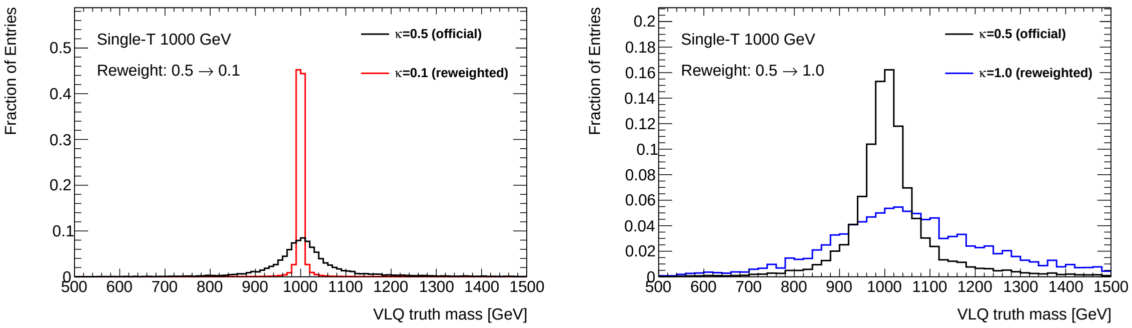

(a) (b)

Figure 4.4: Examples of the T mass reweighting procedure. Reweighting from $\kappa_T = 0.5$ to $\kappa_T = 0.1$(a) and from $\kappa_T = 0.5$ to $\kappa_T = 1.0$(b). The larger coupling leads to larger decay width because the lifetime gets shorter.

4.2.3 SM background samples

The background processes, which are further discussed in Chapter 7, are also simulated as following.

Z+jets

Samples of Z boson production plus associated jets are generated using Sherpa2.2.1[41] with the NNPDF30NNLO PDF tune for the parton shower and NNPDF PDF set for the matrix element. The samples are produced in slices of max(H_T, $p_T(Z)$) and filtering the heavy flavour composition, where H_T is the scalar sum of jets p_T. To assign a generator uncertainty, additional samples are produced using MadGraph and Pythia8 with the A14 NNPDF2.3 LO tune for showering and NNPDF30_nlo_as_0118 PDF set for the matrix element. In order to ensure enough statistics in the high p_T region, the Sherpa and MadGraph samples are generated in slices of max(H_T, $p_T(Z)$) and H_T, respectively, where H_T is the scalar sum of p_T of jets.

Diboson (VV)

The diboson (WW, WZ, and ZZ) samples are produced using Sherpa2.2.1 using the NNPDF3.0 NNLO PDF set.

Triboson (VVV)

The triboson (WWW, WWZ, WZZ, and ZZZ) samples are produced using SHERPA2.1 using the CT10 PDF set.

$\mathbf{t\bar{t}}$

The $t\bar{t}$ samples of $\sim 6 \times 10^7$ events are generated with POWHEG[42] and PYTHIA8 with the A14 tune for the showering and CT10 PDF set for the matrix element. In the samples, a filter is applied to require that at least one of the top quarks decay leptonically.

$\mathbf{t\bar{t} + X}$

The samples for the production of a $t\bar{t}$ pair in association with vector bosons are generated by MADGRAPH5 (for $t\bar{t} + WW$ process) and MADGRAPH5_aMC@NLO[43] (for $t\bar{t} + W/Z$ process) interfaced with PYTHIA8 for hadronization and using the NNPDF2.3 LO PDF set and the A14 tune.

Single top

The top quark single production samples are produced using POWHEG+PYTHIA8 with Perugia2012 tune for the showering and the CT10 PDF set.

Chapter 5

Object reconstruction and tagging

The detector signals are combined to reconstruct physics objects (charged tracks, vertices, charged leptons, and jets). The details of the objects reconstruction algorithm are described throughout this chapter.

5.1 Charged track and vertex reconstruction

Charged particles passing through the Inner Detector(ID) leave signals with a curvature corresponding to its momentum and the local magnetic field, hence their trajectories can be reconstructed with the following procedure[44].

The reconstruction procedure begins by clustering: gathering consecutive pixel and strip channels where the charge is above threshold. A three-dimensional space-point, defined as the point where a charged particle traverses the active material of ID, is measured in each cluster.

After the clustering, track candidates are reconstructed using seeds formed from sets of three space-points. Candidates are first required to associate at least one additional space-point compatible with the trajectory to improve the purity, then tracks are rebuilt using the additional space-points from the remaining layers of pixel and SCT. Then, a stringent ambiguity-solver applies further requirements on the track candidates. It first calculates the "track score" of each candidate, corresponding to track quality. The calculation makes use of number of clusters assigned to the candidate, number of holes: intersections of the reconstructed track trajectory with a sensitive detector element that does not contain a matching signal, the χ^2 of the track fitting, and logarithm of the track momentum. Candidates with bad score are rejected at this level. After the track score requirement, the candidates are reconstructed and recorded if they satisfy all the final requirements below.

- $p_T > 400$ MeV,
- $|\eta| < 2.5$,
- Minimum of 7 pixel and SCT clusters (12 are expected),
- Maximum of either one pixel cluster or two SCT clusters on the same layer are shared among more than one track,
- Not more than two holes in the combined pixel and SCT detectors,
- Not more than one hole in the pixel detector,
- IBL hits + B-layer hits ≥ 1,
- $|d_0^{BL}| < 2.0$ mm,
- $|z_0^{BL} \sin\theta| < 3.0$ mm,

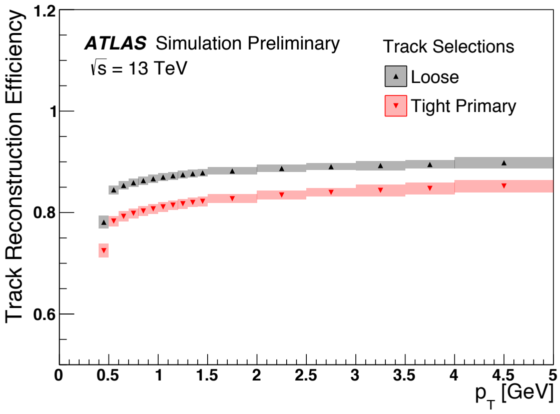

Figure 5.1: The efficiency of track reconstruction measured based on simulation. “Tight primary” indicates a tighter selection algorithm that is not in use in this analysis. [45]

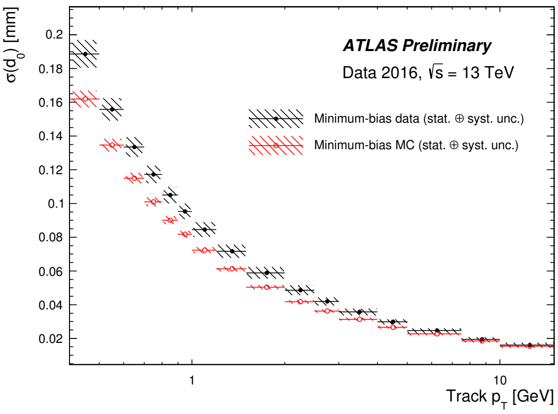

Figure 5.2: The resolution of d_0 as a function of track p_T measured using MC and 2016 data. [45]

where d_0^{BL} is the transverse impact parameter with respect to the beam line and z_0^{BL} is the longitudinal distance between the point at which d_0^{BL} is measured and the primary vertex.

The efficiency of track reconstruction is up to 90 % as shown in Fig. 5.1. The resolution of the transverse impact parameter d_0, largely depending on the track p_T, is below 200 μm for low p_T tracks and below 20 μm for high p_T ($>$ 10 GeV) tracks as shown in Fig. 5.2.

The vertices, the positions at which pp interactions occur, are identified using the reconstructed tracks. The vertex finding algorithm[46] begins with the vertex seeds obtained from the $z-$position at the beamline of a reconstructed track, then an iterative χ^2 fit is made using the seed and nearby tracks. In the iterative fit, weight ω is calculated for each track: larger ω is assigned to tracks with smaller χ^2. The iteration stops when the vertex candidate position does not change by more than 1 μm. Tracks displaced by more than 7σ from the vertex are used to seed a new vertex reconstruction, resulting in up to $\sim$45 vertices reconstruction per bunch crossing in the 2016 LHC settings, where σ is the RMS size of the vertex.

The vertices reconstruction efficiency and position resolution depend largely on the number of associated tracks: larger number of associated tracks lead to better efficiency and resolution. The efficiency varies from $\sim$85 % (2 tracks) to $>$99 % ($\geq$ 5 tracks) as shown in Fig. 5.3, and the position resolution along $x-$ and $y-$ axes varies from $\sim$0.15 mm ($\leq$ 5 tracks) to $\sim$0.02 mm ($\sim$30 tracks), and the position resolution along $z-$ axis varies from $\sim$0.3 mm ($\leq$ 5 tracks) to $\sim$0.04 mm ($\sim$ 30 tracks) as shown in Fig. 5.4.

5.2 Muon reconstruction

Muons are reconstructed[48] using combination of tracks independently reconstructed in the muon spectrometer (MS tracks) and ID (ID tracks).

MS track reconstruction begins with a search for hit patterns inside each MDT chamber to form MDT segments, which are reconstructed by a straight-line fit to the hits found in each layer. The RPC and TGC hits are also used to measure the coordinate orthogonal to the bending plane. Then, muon track candidates are built by combination of segments

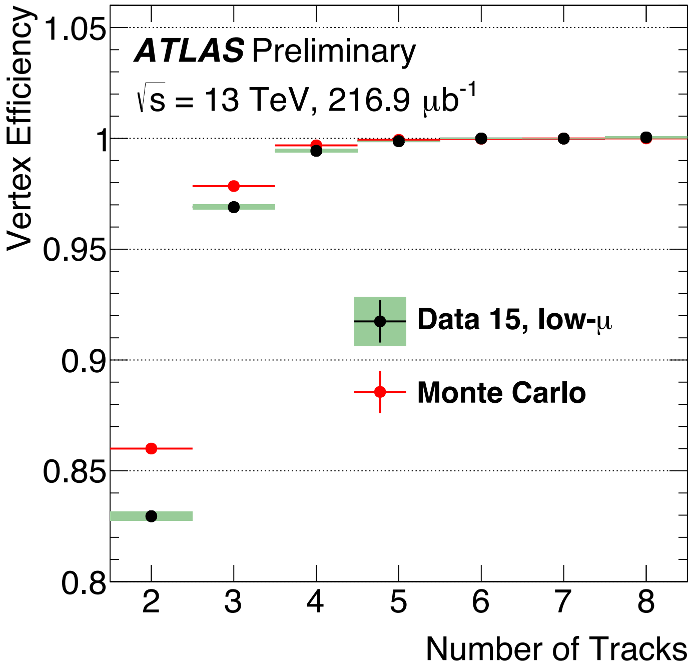

Figure 5.3: The vertex reconstruction efficiency in MC expectation and measurement in Run2.[47]

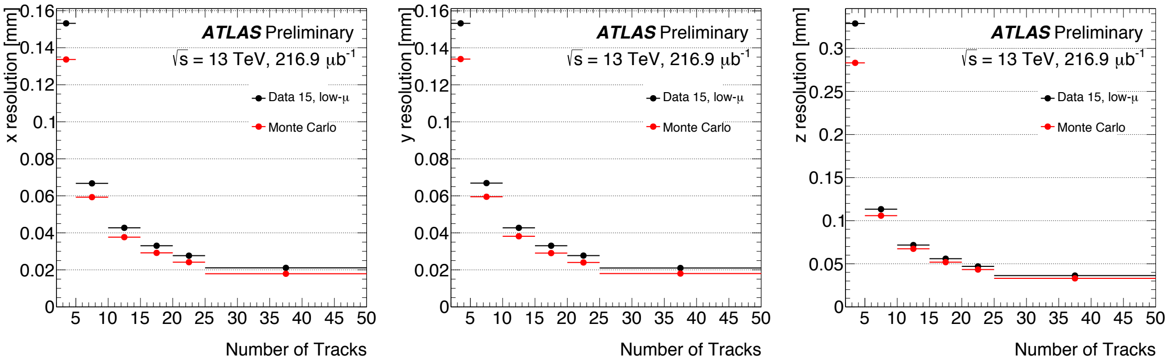

(a) (b) (c)

Figure 5.4: Position resolutions of vertex reconstruction along x-axis(a), y-axis(b), and z-axis(c), as a function of the number of associated tracks.[47]

in different layers. The track building algorithm first uses segments generated in the middle layers as seeds, and searches for segments in the outer and inner layers. Segments are required to pass the criteria based on hit multiplicity, fit quality, relative positions and angles. A track candidate is accepted if at least two segments are matched and the χ^2 of the fit satisfies the criteria.

ID tracks are reconstructed with the procedure described in Section.5.1. Additional requirements listed below are applied on the ID tracks in order to guarantee a robust momentum measurement.

- At least one Pixel hit,
- at least five SCT hits,
- less than three Pixel or SCT holes,
- at least 10 % of the TRT hits originally assigned to the track. This requirement is applied to the region $0.1 < |\eta| < 1.9$ only.

In the overall muon reconstruction, a combined track is formed with a global refit using the hits from both MS and ID. In the fit procedure, MS hits are added to or removed from MS tracks to improve the fit quality. When an ID track matches to an extrapolation of an MS track or an MS track matches to an extrapolation of an ID track, p_T is calculated using a weighted average of ID and MS tracks:

$$p_T^{CB} = f \cdot p_T^{MS} + (1 - f) \cdot p_T^{ID} \; , \tag{5.1}$$

where f is a weight parameter determined from simulation, and p_T^{CB}, p_T^{MS}, p_T^{ID} are p_T of a combined track, MS track, and ID track, respectively.

Further requirements listed below are applied to improve the purity and resolution of muons.

- ≥ 3 hits in at least two MDT layers, except for tracks in $|\eta| < 0.1$, where at least one MDT layer is required but no more than one MDT hole layer are allowed,
- q/p significance, defined as the absolute value of the difference between the ratio of the charge and momentum of the muons measured in the ID and MS divided by the sum in quadrature of the corresponding uncertainties, is smaller than 7,
- isolation: $p_T^{\text{varcone30}}/p_T < 0.06$ where $p_T^{\text{varcone30}}$ is defined as the scalar sum of the transverse momenta of the tracks with $p_T > 1$ GeV in a cone size ΔR, which is 0.3 for muons with $p_T < 30$ GeV and $\frac{10\text{ GeV}}{p_T^{\mu}}$ for muons with larger p_T,
- $p_T > 28$ GeV and $|\eta| < 2.5$,
- originating from the primary vertex: d_0 significance is smaller than 3 and $|z_0 \sin\theta| < 0.5$ mm.

The first two requirements are the ATLAS *Medium* muon identification criteria, and the third is the *FixedCutTightTrackOnly* isolation criteria.

The reconstruction efficiency is measured as Fig. 5.5 using $Z \to \mu\mu$ and $J/\psi \to \mu\mu$ tag-and-probe method. This method makes use of events containing a pair of opposite charge muons with the invariant mass consistent with Z or J/ψ. One of the muon(probe muon) is used for efficiency calculation and the other(tag muon) is not included in the calculation. The efficiency is stable at > 99 % in $p_T > 6$ GeV. In terms of η dependency, the efficiency is almost flat above 99 % in most of the region, except for $|\eta| < 0.1$, where a gap in MS exists. The efficiency slightly drops at $1.0 < |\eta| < 1.4$, corresponding to the transition region between barrel and end-cap.

The momentum resolution was measured by fitting the invariant mass of dimuon matching to $Z \to \mu\mu$ or $J/\psi \to \mu\mu$. As shown in Fig. 5.6, the invariant mass resolution $\sigma_{\mu\mu}$ was

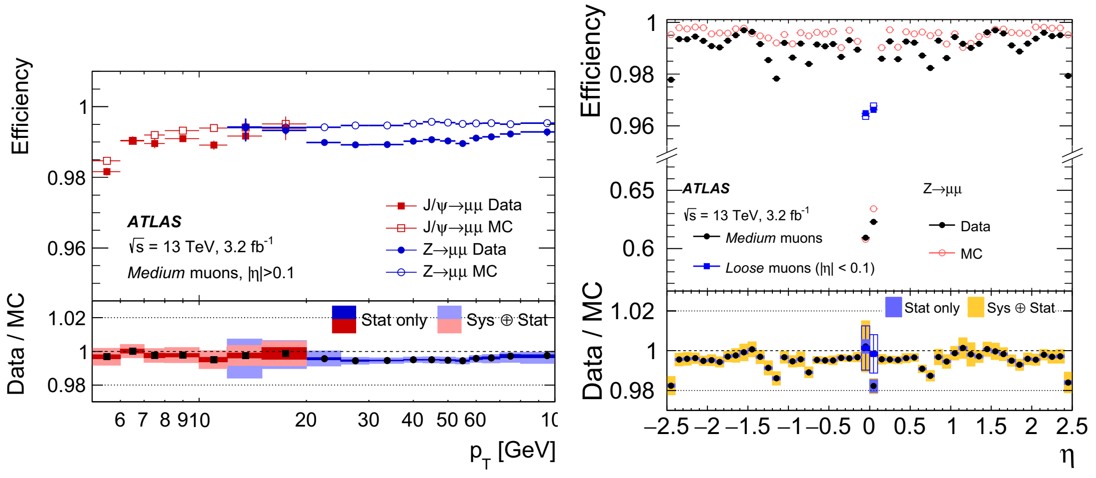

(a) (b)

Figure 5.5: Muon reconstruction efficiency with *Medium* selection computed based on tag-and-probe method as a function of p_T(a) and η(b)[48].

estimated to be approximately 1.6 % in small $|\eta|$ and 1.9 % in the region of $|\eta| > 1.5$. Assuming that two muons are reconstructed with same resolution, the correlation between $\sigma_{\mu\mu}$ and the mean of the mass distribution $m_{\mu\mu}$ can be written as:

$$\frac{\sigma_{\mu\mu}}{m_{\mu\mu}} = \frac{1}{\sqrt{2}} \frac{\sigma_{p_\mu}}{p_\mu}, \tag{5.2}$$

where p_μ and σ_{p_μ} are the momentum and its resolution, respectively. As a result, the relative momentum resolution $\frac{\sigma_{p_\mu}}{p_\mu}$ is 2.3 % and 2.9 % in small and large $|\eta|$, respectively. The resolution is slightly better in the low p_T region measured by the $J/\psi \rightarrow \mu\mu$ as shown in Fig. 5.7.

In terms of the MC muons, the momentum is corrected to fix the discrepancy between data and MC. In the correction procedure, p_T of both MS and ID tracks are corrected as:

$$p_T^{\text{Cor, Det}} = \frac{p_T^{\text{MC, Det}} + \sum_{n=0}^{1} s_n^{Det}(\eta,\phi) \left(p_T^{\text{MC,Det}}\right)^n}{1 + \sum_{m=0}^{2} \Delta r_m^{\text{Det}}(\eta,\phi) \left(p_T^{\text{MC, Det}}\right)^{m-1} g_m}, \tag{5.3}$$

where Det is ID or MS, p_T^{Det} is the transverse momentum measured by ID or MS, g_m is normally distributed random variable, and the terms $\Delta r_m^{\text{Det}}(\eta,\phi)$ and $s_n^{\text{Det}}(\eta,\phi)$ are the momentum resolution smearing and the scale correction parameters, respectively, which are measured based on the $Z \rightarrow \mu\mu$ and $J/\psi \rightarrow \mu\mu$ tag-and-probe method.

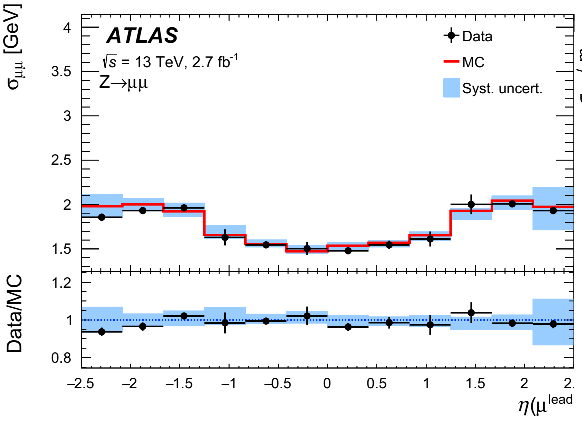

Figure 5.6: Resolution of the dimuon invariant mass as a function of η. [48]

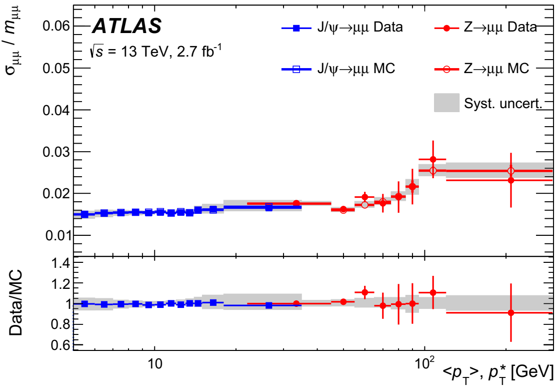

Figure 5.7: Relative resolution of muon momentum. High-p_T region is measured based on $Z \to \mu\mu$ and low-p_T is based on $J/\psi \to \mu\mu$ tag-and-probe. [48]

5.3 Electron reconstruction

Electron reconstruction[49, 50] makes use of the ID and the electromagnetic (EM) calorimeter. At the beginning of the reconstruction algorithm, the energy deposit in the EM calorimeter is reconstructed as an EM cluster, which is used as a seed of the algorithm. Then, a search for charged tracks loosely matched to the EM clusters is performed. The EM cluster is rejected if no associated tracks exist. Otherwise it is reformed with larger calorimeter regions and treated as an electron if the cluster and the matched tracks fulfill kinematic requirements, and then the energy of the original electron is computed by calibration for the EM cluster. Details of each step are described in the following.

EM cluster reconstruction

The unit of the EM calorimeter is a cell with a dimension of $\Delta\eta \times \Delta\phi = 0.025 \times 0.025$. A sliding window algorithm searches for local maximum deposited energy in a window with a size of 3×5 cells. If the total transverse energy in the window exceeds 2.5 GeV, a longitudinal tower is reconstructed as an EM cluster seed. The efficiency of the cluster reconstruction is measured based on MC, ranging from 95% at $E_T = 7$ GeV to more than 99% above $E_T = 15$ GeV.

Track-cluster matching

The track-cluster matching is performed using the barycenter of the EM cluster and the track extrapolated to the middle layer of the EM calorimeter. A track is regarded as matched if it passes either of two requirements below:

(i). With at least four silicon hits, the track direction is consistent with the EM cluster within 0.05 in η and 0.2 in ϕ on the side the track is bending towards or 0.05 in ϕ on the opposite side. If the track has less than four silicon hits (TRT-only track), only ϕ requirement above is applied.

(ii). The track after rescaling the momentum to the measured cluster energy is consistent with the EM cluster within 0.1 in ϕ on the side the track is bending towards or 0.05 in ϕ on the opposite side. If the track is not TRT-only, its η is further required to be consistent within 0.05.

The matched tracks are again fitted with Gaussian Sum Filter (GSF)[51] algorithm using the track and cluster parameters to take into account the bremsstrahlung effects.

Kinematic requirements

The cluster matched to a track is regarded as an electron cluster and re-formed using 3×5(5×5) towers of cells in the barrel(endcap) EM calorimeter. The energy of the original electron is estimated by calibration of the EM cluster using a multivariate technique[52]. To improve the purity, the analysis in this thesis makes use of kinematic properties of electrons fulfilling all the requirements below.

- $E_T > 28$ GeV,
- $|\eta| < 2.47$ excluding the barrel-endcap transition regions ($1.37 < |\eta| < 1.52$),
- d_0 significance is smaller than 5 and $|z_0 \sin\theta| < 0.5$ mm,
- fulfilling the *FixedCutTightTrackOnly* isolation criteria, the same as the definition described in Section5.2.
- fulfilling the *tight likelihood* identification criteria, with 80 % efficiency for electrons with $E_T \approx 40$ GeV.

The energy resolution varies depending on $|\eta|$ due to the detector structure and is largely degraded at large $|\eta|$, especially in $1.2 < |\eta| < 1.8$ due to the interaction with the upstream materials. The electron energy resolution was measured based on both MC and data using $Z \to e^+e^-$ events and a parameter c_i is estimated to set corrections as

$$\left(\frac{\sigma_E}{E}\right)_{data} = \left(\frac{\sigma_E}{E}\right)_{MC} \oplus c_i, \tag{5.4}$$

where i is the bin number of η. The simulated resolution varies from ~1% to ~15% from the high E_T electrons detected in the central region to the low E_T electrons in $|\eta|$ ~1.6 region as shown in Fig. 5.8 and c_i, corresponding to the difference in resolution between data and MC, is found to be at most 0.03, as shown in Fig. 5.9.

In MC simulation, the energy scale correction α_i is assigned to each reconstructed electrons to correct the difference of energy scale between data and MC written as:

$$E^{data} = E^{MC}(1 + \alpha_i), \tag{5.5}$$

where i is the bin number of η. The correction parameter α_i is estimated using $Z \to e^+e^-$ again. If e^+ and e^- are reconstructed in regions i and j, the relation between invariant mass of data and MC can be written as

$$m_{ij}^{data} = m_{ij}^{MC}(1 + \frac{\alpha_i + \alpha_j}{2}), \tag{5.6}$$

thus α_i can be estimated by comparing the m_{ij} distribution of data and MC. As a result of this estimation, the absolute value of α_i is at most ~0.03 as displayed in Fig. 5.10.

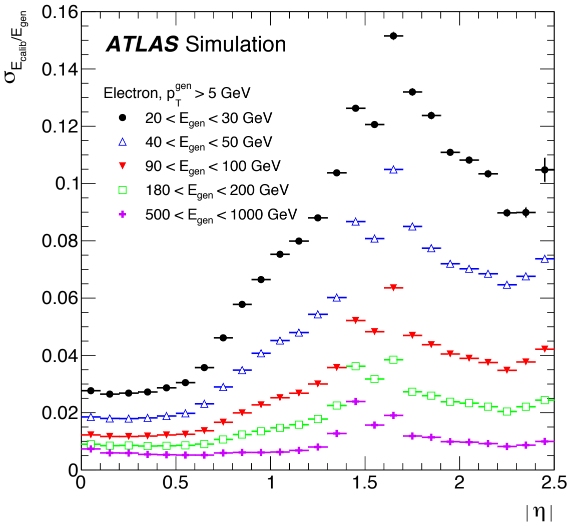

Figure 5.8: Energy resolution of electrons as a function of $|\eta|$, computed based on MC simulation.[53]

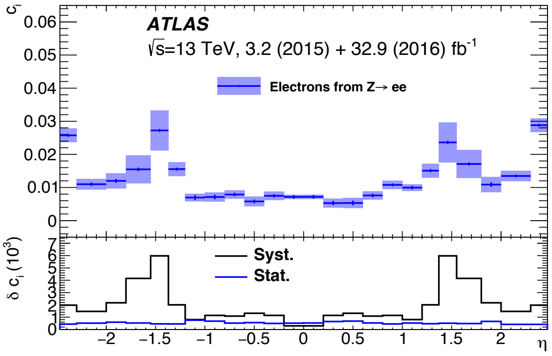

Figure 5.9: The correction parameter c_i as a function of η.[53]

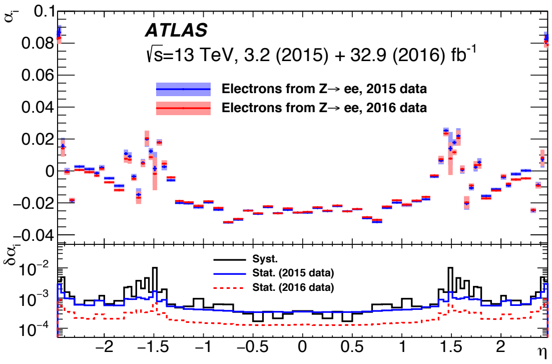

Figure 5.10: Electron energy scale difference between data and MC simulation.[53]

5.4 Jet reconstruction

When a parton is emitted by an inelastic pp collision, it is not directly detected because it generates hadrons before it reaches detectors. Hence, it is detected as collimated shower of hadrons, often referred to as "jet". Jets are reconstructed based on energy deposits in calorimeters with the following procedure.

5.4.1 General jets reconstruction

In the first step of jets reconstruction, calorimeter cells are grouped into topological clusters (topoclusters) as inputs of jets reconstruction. The topocluster algorithm first searches for seed cells, which are calorimeter cells whose energy deposit exceed 4σ where σ is width of pedestal. And then the neighbor cells exceeding 2σ are added to the cluster, and further all the neighbor cells of $\geq 2\sigma$ cells are added if positive energy is deposited.

If more than one cells with the energy deposit exceeds 500 MeV within a topocluster and none of the neighbor cells have larger signal, the original topocluster is split between the corresponding cells. If a cell has more than one neighbor cells exceeding 500 MeV, its energy deposit is shared among the two highest-energy topoclusters (cluster 1 and 2) with the weights of ω_1 and ω_2 defined as:

$$\omega_1 = \frac{E_1}{E_1 + rE_2} \tag{5.7}$$

$$\omega_2 = 1 - \omega_1 \tag{5.8}$$

$$r = \exp(d_1 - d_2), \tag{5.9}$$

where d_i is the distance between the cell and the barycenter of topocluster i and E_i is the energy of the topocluster i.

Topoclusters are merged to reconstruct jets by the anti-k_t algorithm[54]. It first calculates d_{ij} and d_{iB} defined as:

$$d_{ij} = \min(k_{Ti}^{-2}, k_{Tj}^{-2})\frac{\Delta_{ij}^2}{R^2} \tag{5.10}$$

$$d_{iB} = k_{Ti}^{-2}, \tag{5.11}$$

where k_{Ti} is the transverse momentum of the cluster i, $\Delta_{ij}^2 = (y_i - y_j)^2 + (\phi_i - \phi_j)^2$ where y_i is the rapidity of the cluster i, and R is predefined radius parameter.

Next, the algorithm identifies the smallest value among d_{ij} and d_{iB}. If d_{ij} is the smallest, the clusters i and j are merged and again d_{ij} and d_{iB} are computed based on redefined clusters. If d_{iB} is smallest, the cluster i is identified as a jet and removed from the list of clusters used as inputs to compute d_{ij} and d_{iB}. This procedure is repeated until no cluster is left in the list.

In ATLAS, two types of jets are defined in the analysis. One is “small-R jets”, computed based on the anti-k_t algorithm with the radius parameter $R = 0.4$, and the other is “large-R jets”, computed with $R = 1.0$. The latter is usually used to identify highly boosted massive objects decaying into quarks.

5.4.2 Small-R jet reconstruction

After anti-k_t reconstruction with the radius parameter $R = 0.4$, several steps of jet-energy-scale(JES) calibration is applied to small-R jets to improve the precision of energy measurement.

The first step of calibration is the origin correction, which changes the four-momentum of jets to point to the hard scatter vertex instead of the center of the detector. While the jet energy is not affected in this correction, it improves η resolution from 0.06 to 0.045 at a jet p_T of 20 GeV and from 0.03 to below 0.006 at a jet p_T above 200 GeV[73].

The origin correction is followed by pile-up corrections to subtract the contribution of pile-up. This correction is performed using several correction parameters: the medium p_T density ρ, the number of primary vertex N_{PV}, and the average pile-up $< \mu >$ are assigned to each single event and the area of a jet A, N_{PV}-dependent correction α, and $< \mu >$-dependent correction β are assigned to each single jet. The medium p_T density parameter ρ is computed as the density of p_T of jets reconstructed with k_t algorithm[54] with $R = 0.4$, which is sensitive to soft radiation. The area A is computed using ghost association. In this procedure, simulated particles of infinitesimal momentum, referred to as "ghosts", are added uniformly in solid angle to the event before jet reconstruction. Then, A is measured from the number of associated ghosts in a jet. The residual parameters α and β are estimated based on the difference of p_T between the reconstructed jet and MC truth jet as functions of p_T and η of reconstructed jets. After estimating all the parameters above, p_T of a jet is corrected as:

$$p_T^{corr} = p_T^{reco} - \rho \times A - \alpha \times (N_{PV} - 1) - \beta \times \mu, \tag{5.12}$$

where p_T^{reco} and p_T^{corr} are p_T of jet before and after the pile-up correction, respectively. η and ϕ are not corrected by this correction.

Since calorimeters are calibrated based on electromagnetic(EM) interactions with electrons, the energy measured by the procedures above corresponds to EM scale, which is different from interactions with hadrons. Thus, further correction is required to measure the energy of incoming hadrons. In this correction, the energy of reconstructed jets(E_{reco}) is compared to the energy of truth jets using the MC-truth information of hadrons(E_{truth}). The average energy response, defined as the mean of a Gaussian fit to E_{reco}/E_{truth}, is computed as a function of binned E_{truth} and η_{det}, where η_{det} is the pseudorapidity with respect to the center of the detector. The inverse of average energy response is taken as the jet calibration factor.

The last step of calibration is $in-situ$ calibration, which takes into account the difference of jet response between data and MC. It is quantified by balancing p_T of a jet and other well-measured objects. In the central region($|\eta| < 0.8$), $in - situ$ calibration is performed based on leptonically decaying Z boson, photon, and multiple low p_T jets as the well-measured objects. In the outer region($0.8 < |\eta| < 4.5$), jets are calibrated using well-measured central jets (η-intercalibration). $In - situ$ calibration is performed in each p_T bin as displayed in Fig. 5.11.

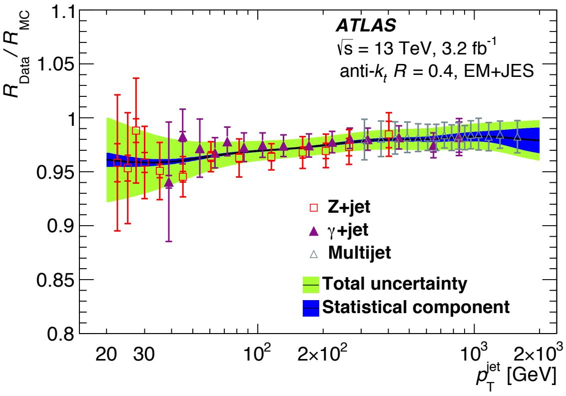

Figure 5.11: Ratio of jet response of MC and data as a function of jet p_T[73]

.

The analysis utilizes jets with $p_T > 25$ GeV and $|\eta| < 4.5$. Jets with $|\eta| < 2.4$ and $p_T < 60$ GeV are required to fulfill a cut in the jet vertex tagger (JVT)[56], the value corresponding to the probability of the jet originating from the primary vertex, of at least 0.59. Jets with

$|\eta| < 2.5$ are referred to as central jets and with $2.5 < |\eta| < 4.5$ as forward jets.

b-tagging

Small-R jets originating from b-quarks, referred to as "b-jets", are identified by the b-tagging algorithm. In b-tagging, a discriminant variable is computed based on MV2c10[60, 61], a multivariate algorithm. MV2c10 makes use of 24 input variables. Two are p_T and η of the jet, and the others are outputs of IP2D, IP3D[62], SV[62], and Jet Fitter[63], which are basic tagging algorithms.

The taggers IP2D and IP3D are based on the impact parameter significance. While IP2D makes use of only the transverse impact parameter significance d_0/σ_{d_0}, IP3D makes use of the transverse impact parameter significance $z_0 \sin\theta/\sigma_{z_0 \sin\theta}$ as well, where d_0 and $z_0 \sin\theta$ are the distance in the closest approach in $r - \phi$ plane and in the longitudinal plane, respectively. A positive (negative) sign is assigned if the vertex is in front (behind) the primary vertex with respect to the direction of jet. Next, they categorize the associated tracks into 14 categories using the presence of hits in each layer of inner detector and calculate the likelihood of $b-$, $c-$, and light-jets hypothesis as the outputs of the algorithms.

The SV algorithm aims to reconstruct inclusive displaced secondary vertices within the jet. It first reconstructs two-track vertices using the tracks associated to jets, and tracks are rejected if they form a vertex likely originating from the decay of K_s or Λ, photon conversions or hadronic interactions with the detector material. Then, a single vertex is reconstructed using the remaining tracks. The outputs of this algorithm are the properties of the reconstructed tracks.

JetFitter reconstructs the full decay chain of $PV \rightarrow b \rightarrow c$-hadron. It makes use of Kalman filter to find a common line to be drawn between PV, the b-hadron vertex, and the c-hadron vertex. The outputs are the property of the reconstructed vertices.

In the final step of MV2c10, the BDT score is calculated using 24 variables listed in Table 5.1 as inputs. The output score distribution for $b-$jets, $c-$jets, and light-jets are displayed in Fig. 5.12. In this analysis, small-R jets with the score larger than the lower threshold of 0.65 are treated as $b-$jets. This threshold corresponds to the efficiency of $\sim$77 % and a rejection of $\sim$6 and $\sim$30 with respect to $c-$ and light-jets.

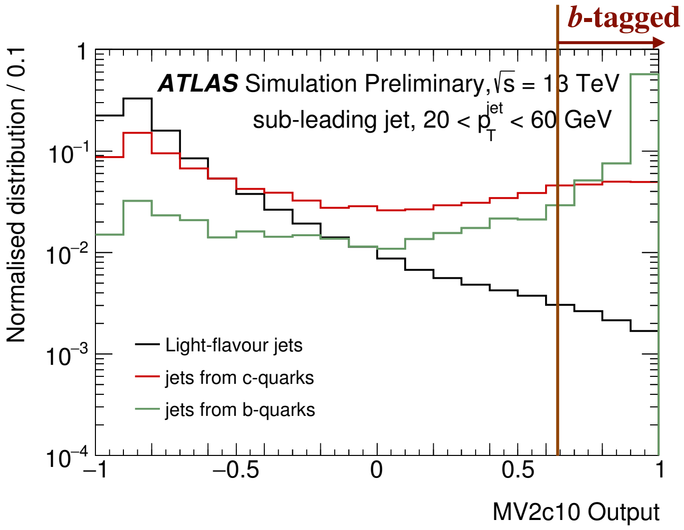

Figure 5.12: Normalized MV2c10 output distribution for b-, c-, and light-flavour jets in multi-jet events.[61]

Table 5.1: The input variables used in the MC2c10 algorithm.

Input	Variable	Description
Kinematics	p_T(jet)	Transverse momentum of the jet.
	η(jet)	Pseudo-rapidity of the jet.
IP2D, IP3D	$\log(P_b/P_{light})$	likelihood ratio between the $b-$ and light-jet hypotheses.
	$\log(P_b/P_c)$	likelihood ratio between the $b-$ and $c-$jet hypotheses.
	$\log(P_c/P_light)$	likelihood ratio between the $c-$ and light-jet hypotheses.
SV	m(SV)	Invariant mass of tracks at the secondary vertex assuming pion masses.
	f_E(SV)	Fraction of the charged jet energy in the secondary vertex.
	$N_{TrkAtVtx}$(SV)	Number of tracks used in the secondary vertex.
	$N_{2TrkVtx}$(SV)	Number of two-tracks vertex candidates.
	L_{xy}(SV)	Transverse distance between the primary and secondary vertices.
	L_{xyz}(SV)	Distance between the primary and secondary vertices.
	S_{xyz}(SV)	Distance between the primary and secondary vertices divided by its uncertainty.
	ΔR(jet,SV)	ΔR between the jet axis and the direction of the secondary vertex relative to the primary vertex.
Jet Fitter	$N_{2TrkVtx}$(JF)	Number of 2-track vertex candidates (before decay chain fit).
	m(JF)	Invariant mass of tracks from displaced vertices assuming pion masses.
	S_{xyz}(JF)	Significance of the average distance between the primary and displaced vertices.
	f_E(JF)	Fraction of the charged jet energy in the secondary vertices.
	$N_{1-trkvertices}$(JF)	Number of displaced vertices with one track.
	$N_{\geq 2-trkvertices}$(JF)	Number of displaced vertices with more than one track.
	$N_{TrkAtVtx}$(JF)	Number of tracks from displaced vertices with at least two tracks.
	$\Delta R(\vec{p}_{jet}, \vec{p}_{vtx})$	ΔR between the jet axis and the vectorial sum of the momenta of all tracks attached to displaced vertices.

5.4.3 Large-R jet reconstruction

Large-R jets are reconstructed by the anti-k_t algorithm with the radius parameter $R = 1.0$ and then trimming[57] is applied to reduce the impact of soft contribution from pile-up and underlying events. In the trimming procedure, subjets are reconstructed using the radius parameter of 0.2, and then all clusters belonging to subjets whose p_T is less than 5 % of p_T of the original large-R jet are removed from the large-R jet reconstruction. After the trimming, the energy of large-R jets is calibrated by the JES calibration with the same procedure as small-R jets.

The mass of a large-R jet is also calculated with the following procedure. First, the calorimeter-based mass (m^{calo}) and the track-assisted mass (m^{TA}) are defined as:

$$m^{calo} = \sqrt{\left(\sum_j E_j\right)^2 - \left(\sum_j p_j\right)^2}, \tag{5.13}$$

$$m^{\mathrm{TA}} = \frac{p_T^{\mathrm{calo}}}{p_T^{\mathrm{track}}} \times m^{\mathrm{track}}, \tag{5.14}$$

where E_j and p_j are the energy and momentum of the j-th calorimeter-cell cluster constituent, p_T^{calo} is the transverse momentum of the large-R jet, p_T^{track} is the transverse momentum of the four-vector sum of tracks associated to the large-R jet, and m^{track} is the mass of this four-vector sum. The mass of large-R jet is calculated as the combination of m^{calo} and m^{track}:

$$m = \frac{\sigma_{\mathrm{calo}}^{-2}}{\sigma_{\mathrm{calo}}^{-2} + \sigma_{\mathrm{TA}}^{-2}} m^{\mathrm{calo}} + \frac{\sigma_{\mathrm{TA}}^{-2}}{\sigma_{\mathrm{calo}}^{-2} + \sigma_{\mathrm{TA}}^{-2}} m^{\mathrm{TA}}, \tag{5.15}$$

where σ_{calo} and σ_{TA} are the resolution of m^{calo} and m^{TA}, respectively. In-situ calibration is performed to large-R jets p_T as well as mass, as displayed in Fig. 5.13.

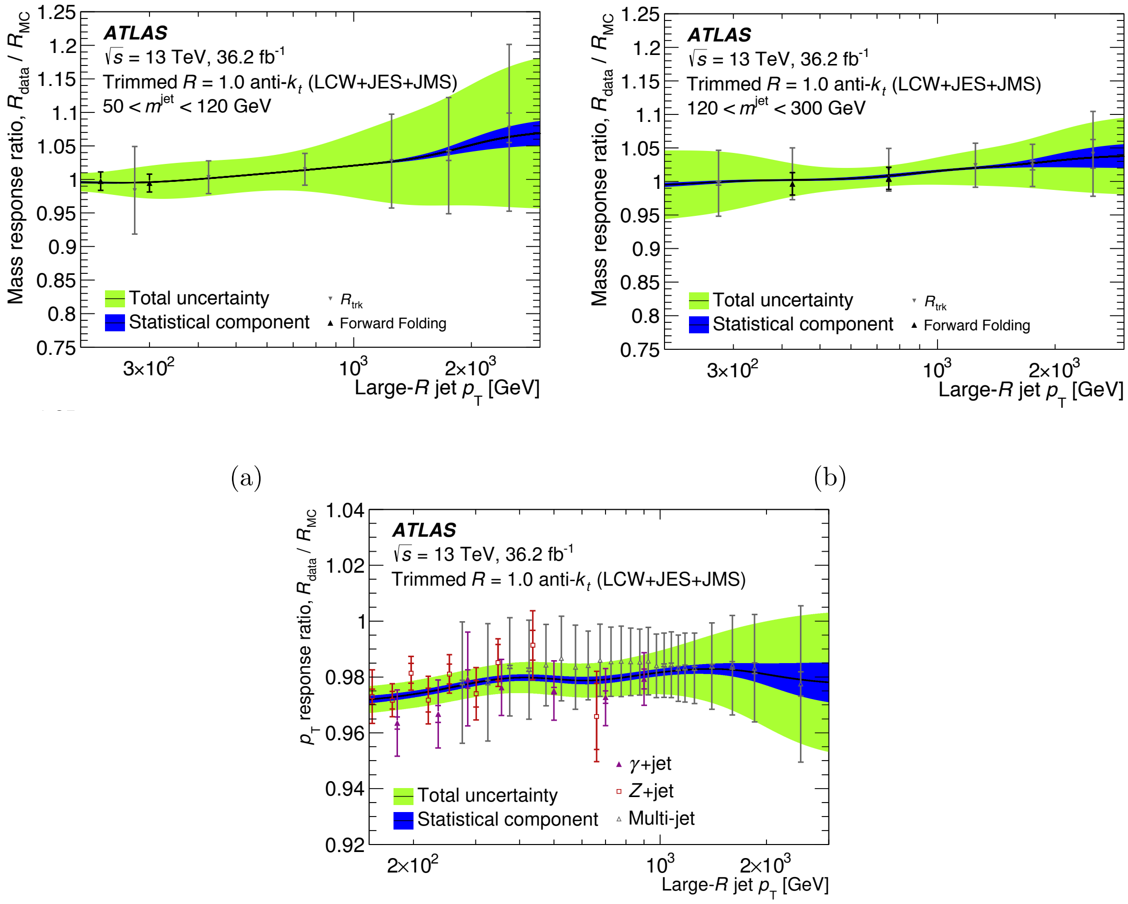

(a)

(b)

(c)

Figure 5.13: The in-situ calibration factors applied to large-R jets. Calibration factors of mass in low mass region(a), high mass region(b) and factors of p_T(c).[64]

Another important parameters of large-R jets are the N-subjettiness τ_N, which quantifies how likely a jet is composed of N subjets. To compute τ_N, N candidate subjets are identified using the exclusive-k_T algorithm[59], and then calculate

$$\tau_N = \frac{1}{d_0} \sum_k p_{T,k} \min\{\Delta R_{1,k}, \Delta R_{2,k}, ..., \Delta R_{N,k}\}, \tag{5.16}$$

where k runs over the jet constituents, $\Delta R_{j,k}$ is the distance in η-ϕ plane between the constituent k and the jet candidate j, and d_0 is the normalization factor.

top-tagging

In the case a top quark is generated as a decay product of a heavy(∼1 TeV) particle such as T, it can be identified as a large-R jet using a top-tagging algorithm explained here.

When a top quark decays hadronically, three quarks are generated as decay products. One is a down-type quark, which is b-quark in most of the cases, and two quarks are the decay products of W boson. Typically such quarks are detected as separate small-R jets (resolved jets), however, they can also be detected as one large-R jet fully containing all these quarks

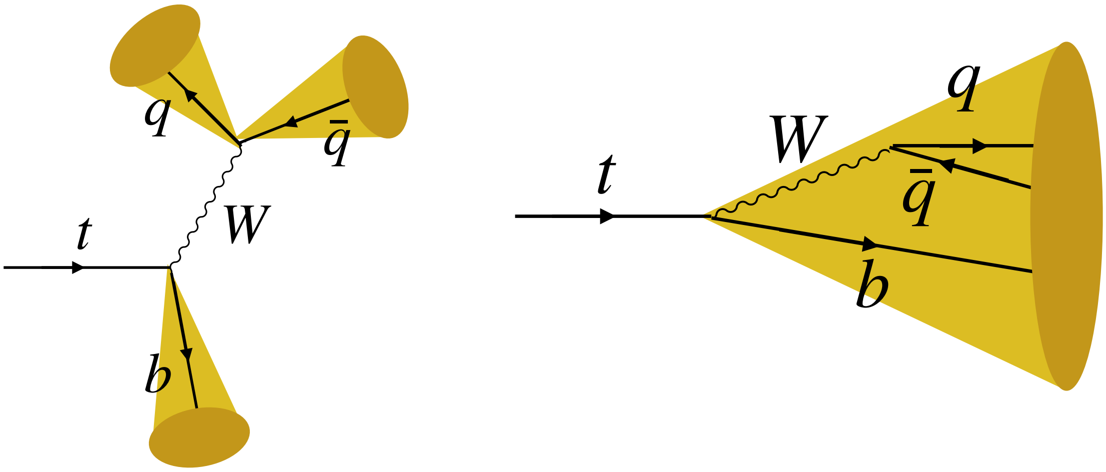

(a) (b)

Figure 5.14: Schematic views of top detection by resolved(a) and boosted jet(b).

(boosted jet). Its probability significantly increases if the transverse momentum of a top is as high as a few hundred GeV because of the Lorentz boost of the original top in that case. The schematic view of the resolved and boosted jets are illustrated in Fig. 5.14.

Large-R jets originated from top quarks have characteristic properties compared to ones originated from other processes such as QCD. In ATLAS, an algorithm called "boosted top tagger" is employed to identify the large-R jets from top quark using p_T, mass, and $\tau_{32} \equiv \frac{\tau_3}{\tau_2}$, the ratio of 2- and 3-subjettiness. Since jets originating from the hadronic top more likely have mass compatible with top quark and small τ_{32} compared to other processes, and their distribution significantly changes with p_T as shown in Fig. 5.15, upper thresholds on τ_{32} and lower thresholds on the jet mass are applied for each jet p_T bin. Threshold of each p_T bin is selected to keep the tagging efficiency to be ∼50 % while maximizing the rejection of non-top jets, resulting in the rejection factor of ∼15 for p_T ∼500 GeV jets and ∼8 for p_T ∼1500 GeV jets.

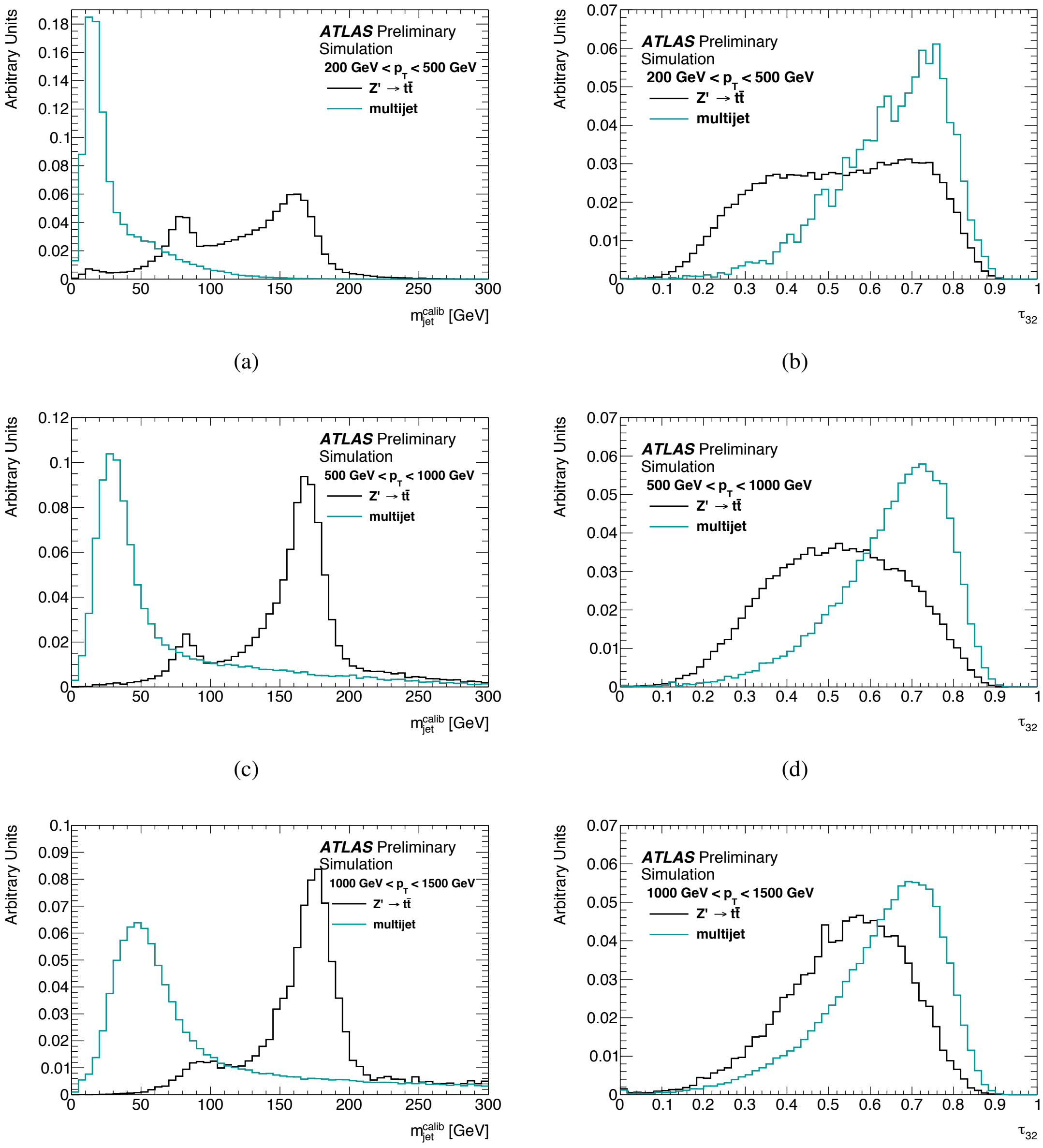

(a) (b)

(c) (d)

(e) (f)

Figure 5.15: Distributions of mass $m_{\mathrm{jet}}^{\mathrm{calib}}$((a),(c),(e)) and τ_{32}((b),(d),(f)) and mass in three jet p_T bins: $200 < p_T < 500$ GeV ((a),(b)), $500 < p_T < 1000$ GeV ((c),(d)), and $1000 < p_T < 1500$ GeV ((e),(f))[65]

Chapter 6

Analysis strategy

The target of this analysis is to the charge +2/3 VLQ (referred to as “T”) produced via the single production process. The single production is chosen because larger cross section is possible in the mass region of > 700 GeV in the singlet model. Since the single production of T in the other multiplets, doublet and triplet, are suppressed as discussed in Section 1.2.3, the analysis is performed with respect to only the singlet model.

The decay channel used in this analysis is $T \to Zt$, whose diagram in displayed in Fig. 6.1. Z is reconstructed using a pair of same-flavor and opposite sign leptons (e^+e^- or $\mu^+\mu^-$) and t is reconstructed as a large-R jet accepted by the top-tagger algorithm, and then T is reconstructed with Z and t.

6.1 Overview of analysis strategy

In this analysis, a signal region(SR), control regions(CRs), and a validation region(VR) are considered. The SR is defined to have large signal-to-background ratio so that data/MC

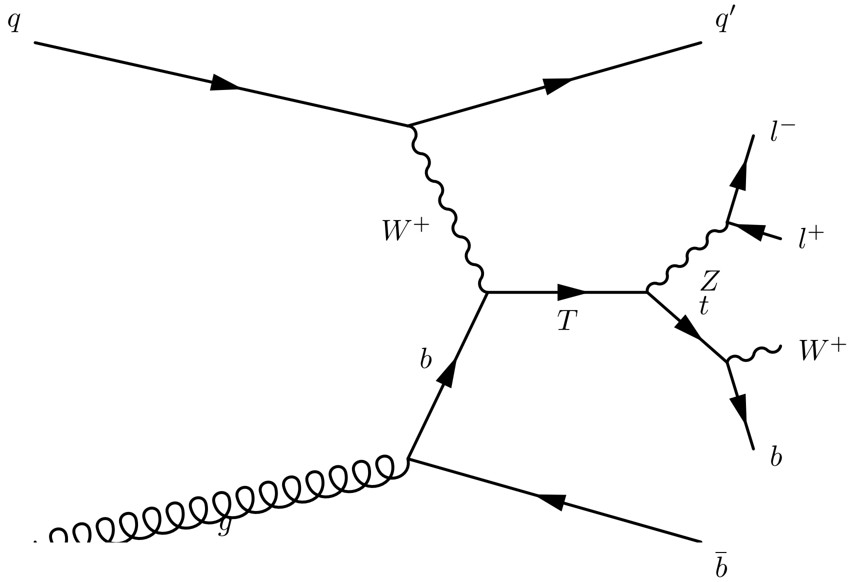

Figure 6.1: A Feynman diagram of single production of T decaying into Zt, where Z decays to l^+l^- and t decays hadronically.

comparison in this region is sensitive to contribution of T. The CRs and the VR are defined to have the kinematic property close to the SR while the contribution of T is suppressed compared to the background processes. The observed data in the CRs and the SR are used mainly to estimate the nuisance parameters corresponding to the systematic uncertainties discussed in Chapter 8. This estimation is validated using the events in VR, whose data and MC are not used in the estimation. The detailed procedure of the estimation of the signal contribution and the nuisance parameters is discussed in Section 6.3.

Among the SR, CRs, and VR, a leptonically decaying Z boson is required to be reconstructed. This requirement effectively suppresses backgrounds not containing real Z such as QCD events. The selection for the SR further requires at least one top-tagged large-R jet. Since the cross section of SM processes that actually contain both Z and t in the final state is quite small, the major component of SM events in the SR is expected to be events containing misidentified Z or t. Details of the definition of the SR, CRs, and VR are discussed in the following sections.

6.2 Event selection

6.2.1 Preselection

The preselection is defined to pick out events containing $Z \to l^+l^-$ efficiently. In this selection, events are required to fulfill all the criteria listed below.

(1) Single lepton trigger fires.
(2) Exactly two leptons (electrons or muons) with $p_T > 30$ GeV are reconstructed.
(3) Two leptons have same flavor and opposite sign (e^+e^- or $\mu^+\mu^-$).
(4) The invariant mass of the dilepton system is consistent with Z boson mass(91.2 GeV) within 10 GeV.
(5) At least one small-R jet is reconstructed.
(6) At least one large-R jet is reconstructed.
(7) p_T of the dilepton system is greater than 200 GeV.

The requirement (1) accepts only events that at least one of the unprescaled single lepton triggers listed in Table 6.1 and 6.2. Events are rejected if no single-muon(electron) trigger is fired while the reconstructed leptons are muons(electrons). Different sets of trigger requirements are applied to 2015 and 2016 runs because of the different pileup and detector environment. The inclusive muon(electron) trigger efficiency with respect to $T \to Zt, Z \to \mu^+\mu^-(e^+e^-), t$ decaying hadronically events is ∼95(99)%. The efficiency dependence on the T mass is shown in Fig. 6.2. The requirements (2), (3), and (4) are applied to select only events consistent with Z, the aim of (5) and (6) is to select events compatible with the following event selections, and (7) is applied to reject low energy events.

Table 6.1: List of the single muon triggers used in this analysis.

period	name	threshold	isolation	Other information
2015	HLT_mu20_iloose_L1MU15	20 GeV	loose (fixed cone size)	Requiring 15 GeV L1 muon trigger
2015+2016	HLT_mu50	50 GeV	none	
2016	HLT_mu26_ivarmedium	26 GeV	medium (variable cone size)	

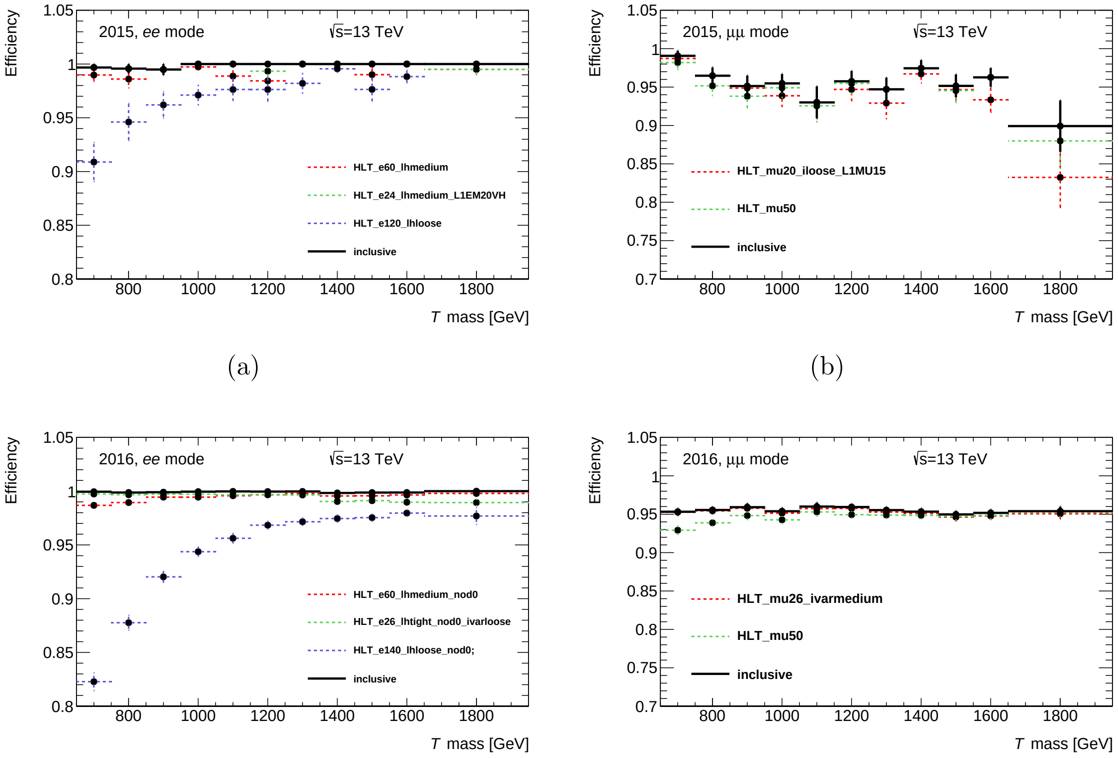

(a) (b)

(c) (d)

Figure 6.2: Single lepton trigger efficiency with respect to the T signal events. (a) Electron trigger in 2015, (b) Muon trigger in 2015, (c) Electron trigger in 2016, (d) Muon trigger in 2016.

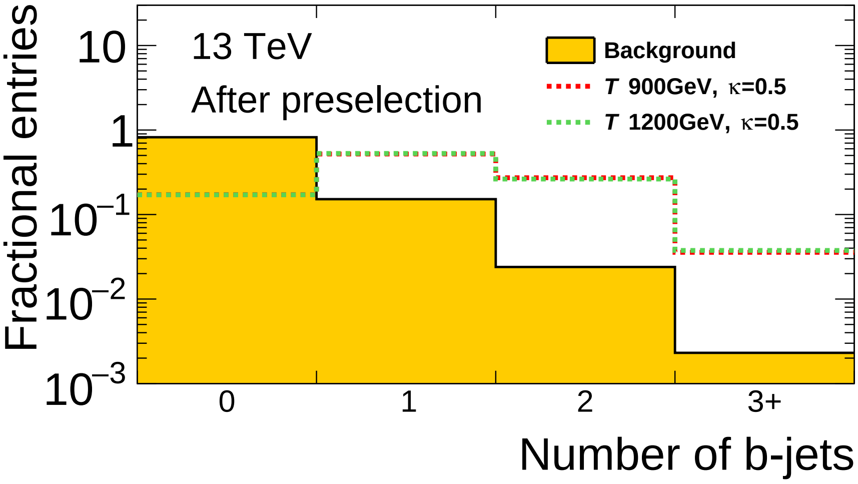

Figure 6.3: Comparison of the performance of b-jets requirement with respect to signal and background events after preselection.

Table 6.2: List of single electron triggers used in this analysis.

period	name	threshold	likelihood	Other information
2015	HLT_e60_lhmedium	60 GeV	medium	
	HLT_e24_lhmedium_L1EM20VH	24GeV	medium	Requiring 20 GeV L1 EM trigger
	HLT_e120_lhloose	120 GeV	loose	
2016	HLT_e60_lhmedium_nod0	60 GeV	medium	d_0 information is not used
	HLT_e26_lhtight_nod0_ivarloose	26 GeV	tight	variable cone isolation, d_0 is not used
	HLT_e140_lhloose_nod0	140 GeV	loose	d_0 is not used

After the preselection, events are divided into the SR, CRs, and a VR in accordance with the variables described in the following.

6.2.2 Discriminant variables

Presence of b-jets

Likelihood of b-jet is a useful tool used in many analyses in ATLAS because a requirement of at least one b-jet can suppress light-flavor events quite effectively. As indicated in Fig. 6.3, the number of b-jets can be a good discriminant variable to separate signal and background in this analysis as well.

Each of T single production events should contain two b-quarks in the final state. One is the decay product of t and the other is from the association with the gluon splitting ($\bar{b}$ in Fig. 6.1). However, the associated b is not efficiently tagged because it has wide distribution over $|\eta|$ up to $|\eta| < 4$ and relatively small p_T as shown in Fig. 6.4. Thus the efficiency for $\geq$2 b-jets requirement is as low as $\sim$30 % while it can reduce background significantly. The expected distribution of b-jets multiplicity and performance of the b-jets requirements with respect to the signal and background events are shown in Fig. 6.5.

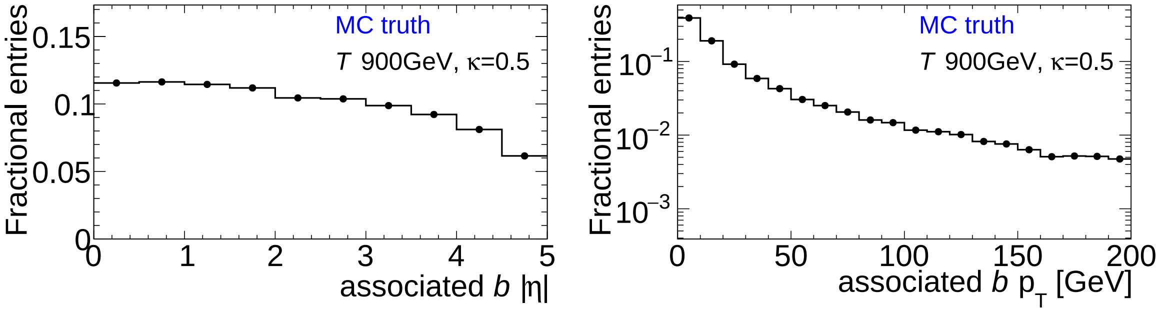

(a)

(b)

Figure 6.4: Distribution of $|\eta|$(a) and p_T(b) of the associated b quark. These histograms are generated based on the signal sample with the mass of 900 GeV coupling of 0.5 .

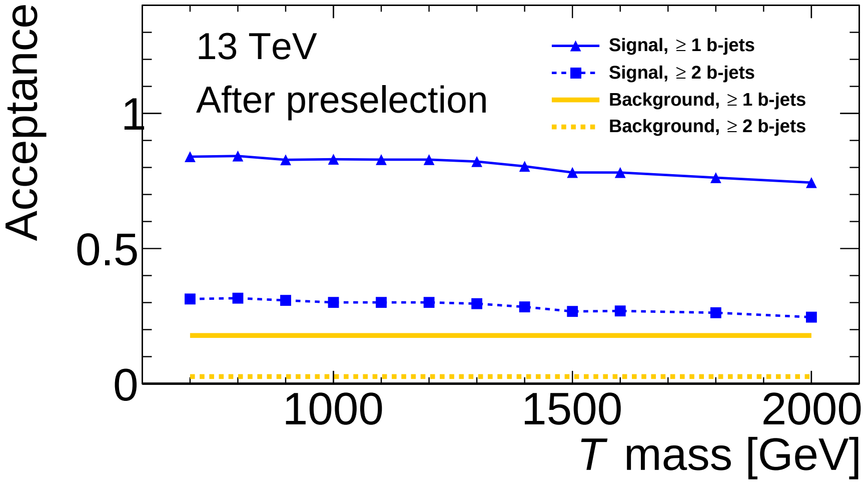

Figure 6.5: Comparison of the efficiency of b-jets requirement with respect to signal and background events after preselection.

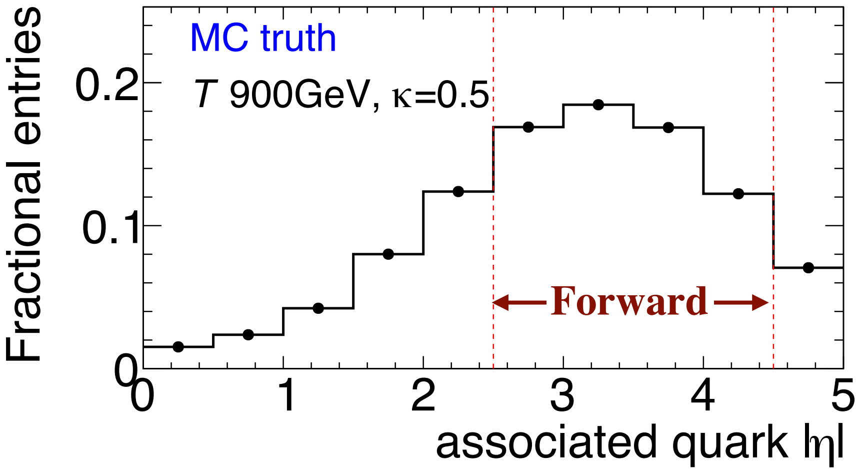

Figure 6.6: $|\eta|$ distribution of the associated quark.

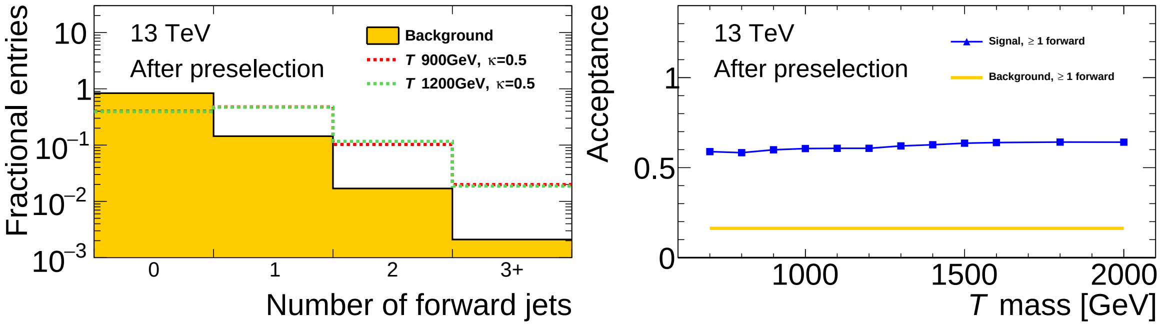

(a)

(b)

Figure 6.7: Distribution of the forward jets multiplicity in signal and background(a) and the efficiency of forward jets requirements as a function of mass of T(b).

Presence of forward jets

An additional quark corresponding to q' in Fig. 6.1 is also produced in association with T. It typically has small momentum transfer and relatively large $|\eta|$ as shown in Fig. 6.6, resulting in jets reconstructed in the forward region ($2.5 < |\eta| < 4.5$) with the probability of $\sim$60 %. Since forward jets are not reconstructed in most of the background processes, the requirements for the forward jet can reduce background by $\sim$80 %. This requirement is also useful for distinction between the single production and pair production of T because the associated quark does not appear in the pair production process. The expected distribution of forward jets multiplicity and performance of forward jets requirements with respect to signal and background events are shown in Fig. 6.7 .

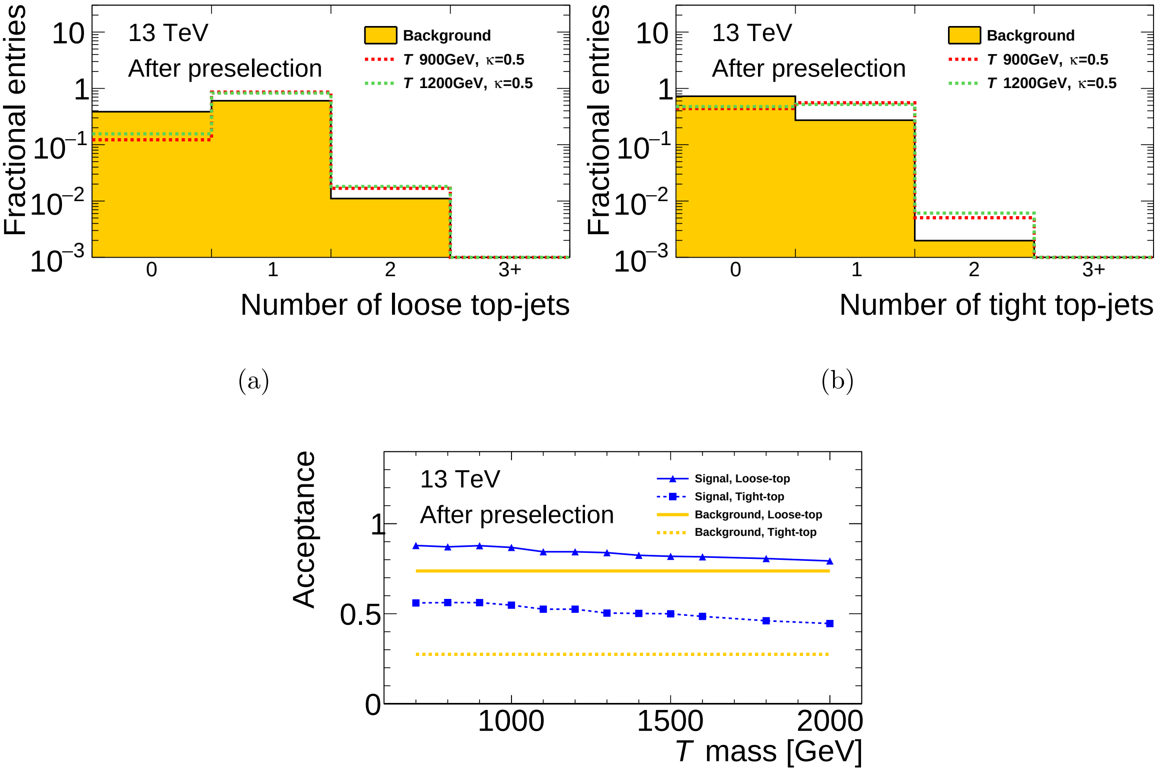

(a)

(b)

(c)

Figure 6.8: The top-jets multiplicity tagged by the loose top-tagger(a) and the tight top-tagger(b), and the efficiency of top-jets requirements with respect to background and T signal with all the considered mass(c).

Presence of top-jets

The existence of the boosted top quark is one of the most significant feature of the T signal. Hence, requirement of "top-jets", the large-R jets tagged as hadronically decaying top quark by the boosted top tagger algorithm described in Section 5.4, works efficiently to separate signal from background. Two working points of the top tagger are available. One is the loose working point corresponding to the efficiency of ∼80 % and the other is the tight corresponding to the efficiency of ∼50 %. The expected distribution of top-jets multiplicity and performance of top-jets requirements with respect to the signal and background events are shown in Fig. 6.8. This analysis makes use of the tight working point as discussed later.

6.2.3 Signal region

In the SR definition, the requirements are chosen to enhance the signal contribution over the background. Two possible requirements on the top-jets and the b-jets are indicated in the previous section, i.e. requiring a loose top-jet or tight top-jet, and requiring ≥1 b-jet or ≥2 b-jets. The performance of all the combinations of the requirements above is compared as shown in Fig. 6.9 to conclude that the requirements of the tight top-jet and ≥1 b-jet has the best performance in the low mass region (< 1200 GeV) in terms of $S/\sqrt{B}$ ratio, where S and

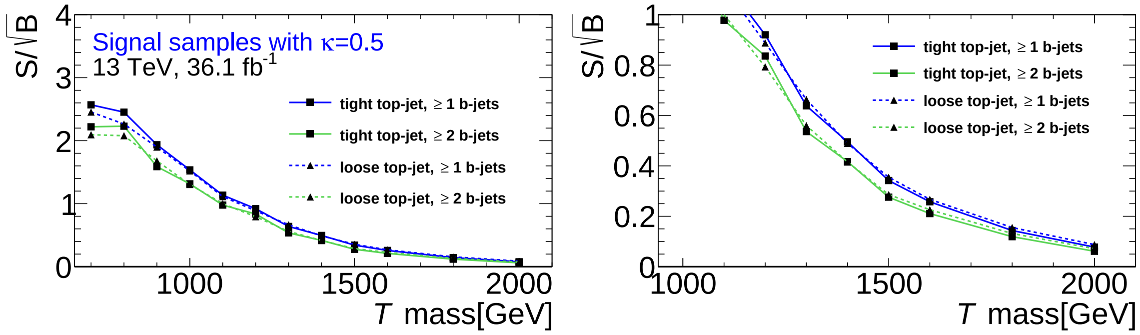

(a) (b)

Figure 6.9: Expected $S/\sqrt{B}$ ratio with respect to $\kappa = 0.5$ samples as a function of mass of T. The distribution in the range of $700 < m_T < 2000$ GeV is displayed in (a) and the large mass region($1100 < m_T < 2000$ GeV) is displayed in (b). Signal and background are normalized to the integrated luminosity of 36.1 fb^{-1} .

B are the expected number of signal and background entries in the SR under the integrated luminosity of 36.1 fb^{-1}. The loose top-jet requirement can be slightly better in the high mass region ($>$ 1200 GeV), but the tight top-jet requirement is chosen in this analysis to optimize the analysis to the mass region of ∼1000 GeV. From here, “top-jet” indicates the tight top-jet for simplicity.

Summarizing the discussion above, the final selection of SR are listed below:

(1) At least one b-jet is reconstructed.
(2) At least one top-jet is reconstructed.
(3) At least one forward jet is reconstructed.

In the SR, T candidate is reconstructed with the top-jet and a Z boson. The top-jet with the largest p_T is chosen in the reconstruction if more than one top-jet exists. The expected invariant mass distribution of T candidates, shown in Fig. 6.10, is used in the fitting procedure to estimate the contribution of the T signal.

6.2.4 Control regions and validation region

The CRs are used to set constraints on background modelling and nuisance parameters by fitting MC to data. The forward jet requirement is not applied in the CRs in order to keep large statistics. In this analysis, two CRs are defined. One is referred to as “0 b-tagged jet CR” or “CR0” and the other is referred to as “≥1 b-tagged jet CR” or “CR1”. In both of the CRs, the requirements include:

(1) No top-jets exists.
(2) At least one large-R jet satisfies the p_T and mass top-tagging criteria while it does not satisfy the τ_{32} criteria.

The second requirement is applied to accept events with kinematics close to the SR. If an event satisfying the requirements above contains b-jets, it is categorized into the CR1, otherwise into the CR0. The CRs are dominated by Z+jets background. The entries in the CRs are sensitive to Z+jets normalization and estimation of nuisance parameters, and the comparison

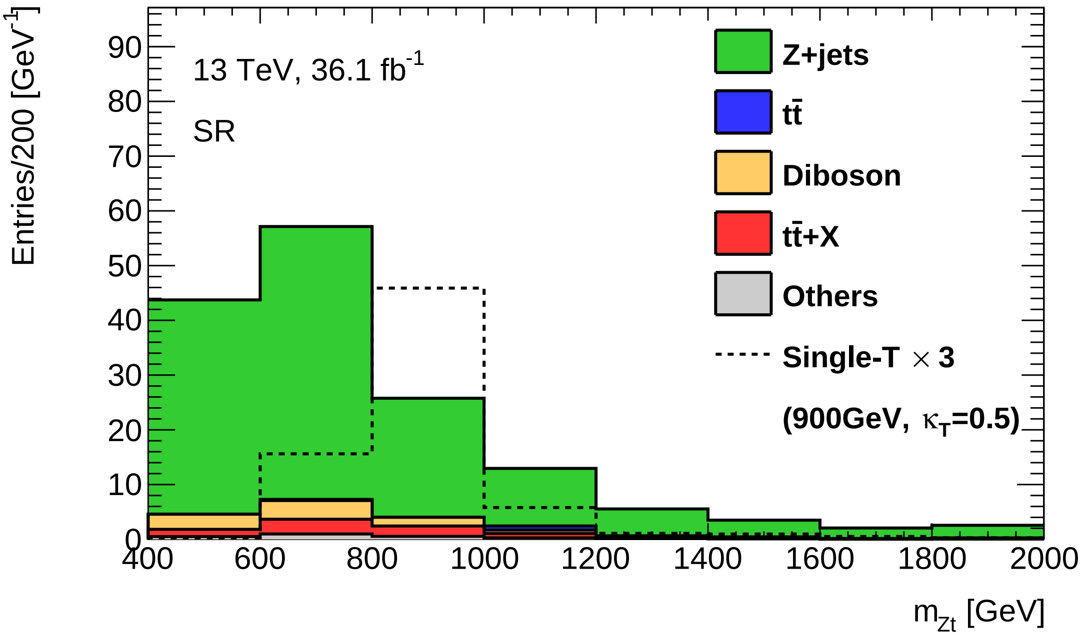

Figure 6.10: MC expectation of T mass distribution of signal and background processes.

between the CR0 and CR1 enables estimation of heavy flavour components in Z+jets events. In the CRs, T is reconstructed with Z and the large-R jet whose p_T is the largest among the ones satisfying the requirement (2).

The entries in the VR are not used in the fitting procedure. They are compared with MC after fitting events in the CRs to validate that the fitting is correct. The VR is defined to set the events close to the SR while it is orthogonal to other regions. The requirements for the VR are:

(1) No b-jets is reconstructed.
(2) At least one top-jet is reconstructed.
(3) At least one forward jet is reconstructed.

T is reconstructed using the same procedure as the SR. The expected distributions of the T mass in the CRs and the VR are shown in Fig. 6.11 .

Ignoring the forward jet requirement, the selection for the SR and the CR1 is quite similar. The difference between them is whether the top-tagger τ_{32} requirement is passed or not. It is also the case of the VR and the CR0. Thus, the fitting using the events in the CRs is almost the same as fitting using the side bands of τ_{32}, as shown in Fig. 6.12 .

In all regions, further selection is applied to reject events with $H_T(\text{jets}) + E_T^{miss} > T$ mass, where H_T(jets) is the scalar sum of small-R jets p_T. This requirement is applied in order to reduce the VLQ pair production contamination as discussed in AppendixA,

Fig. 6.13 shows the expected $S/\sqrt{B}$ distribution and efficiency in each region with respect to the single $T \to Zt$ events.

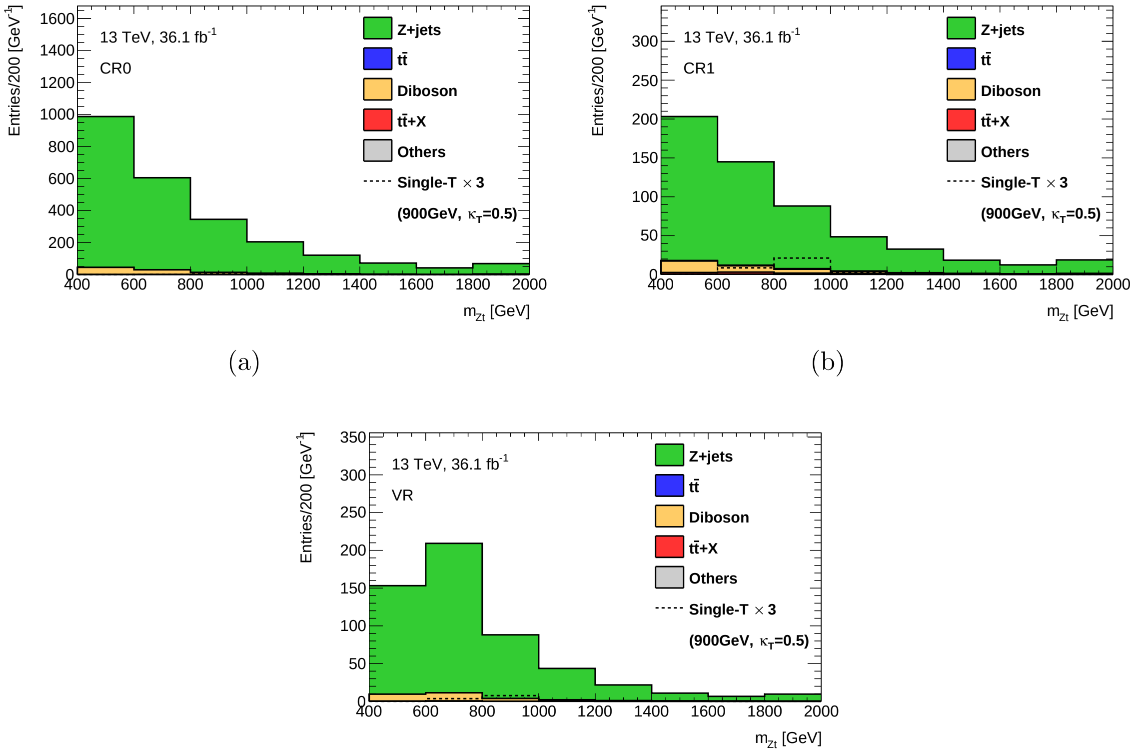

(a)

(b)

(c)

Figure 6.11: MC expectation of T mass distribution in the CR0(a), CR1(b), and the VR(c).

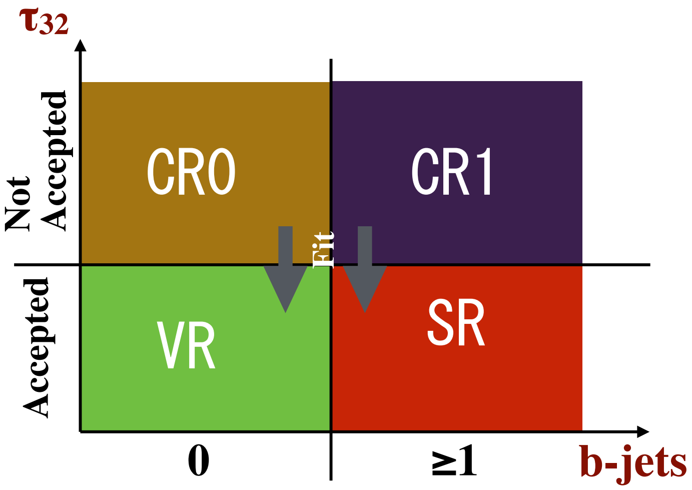

Figure 6.12: Definition of the CRs, VR, and SR with the number of b-jets and τ_{32} of large-R jets.

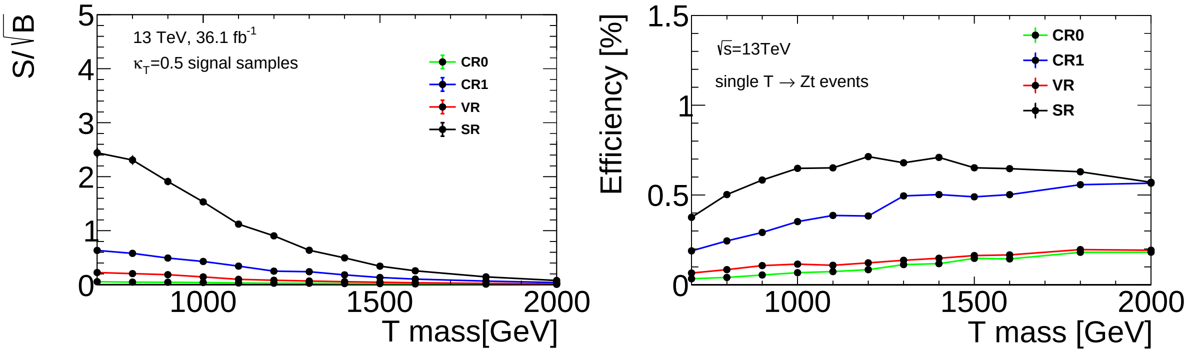

(a)

(b)

Figure 6.13: The expected $S/\sqrt{B}$(a) and efficiency(b) of all the regions as a function of mass of T.

6.3 Statistical analysis

6.3.1 General description

The statistical analysis is based on a binned likelihood function $L(\mu, \vec{\theta})$, constructed as a product of Poisson probability functions over all bins of the T mass distribution histograms, where μ is the signal strength of T and $\vec{\theta}$ is a set of nuisance parameters corresponding to systematic uncertainties which affect the signal and background expectation in each bin. $L(\mu, \vec{\theta})$ is explicitly written as:

$$L(\mu, \vec{\theta}) = \prod_{b}^{\text{bins}} P(N_b|\mu \cdot S_b(\vec{\theta}) + B_b(\vec{\theta})) \times \prod_{j}^{\text{Syst}} G(\vec{\theta}_j|\vec{\theta}_j^0, 1), \tag{6.1}$$

where $P(n|\lambda) = \frac{\lambda^n}{n!}\exp(-\lambda)$ is the poisson distribution, $G(x|x_0, \sigma) = \frac{1}{\sqrt{2\pi\sigma}}\exp\left(-\frac{(x-x_0)^2}{2\sigma^2}\right)$ is the Gaussian distribution, N_b is the observed entry in the bin b, $S_b(\vec{\theta})$ and $B_b(\vec{\theta})$ are the expected number of signal and background entries in b, respectively, and $\vec{\theta}_j^0$ is the central value of the nuisance parameter j.

In the fitting procedure, the combination of μ and $\vec{\theta}$ that maximizes the likelihood, denoted by $\hat{\mu}$ and $\hat{\hat{\vec{\theta}}}$, is searched for. At this stage, constraints on the nuisance parameters are set as $\hat{\sigma}_i = \sqrt{|V_{ii}|}$, where $\hat{\sigma}_i$ is the constraint of the $\vec{\theta}_i$ around $\hat{\hat{\vec{\theta}}}_i$ and V is the covariant matrix defined below:

$$\left(V^{-1}\right)_{ij} = -\frac{\partial^2 \ln L\left(\mu, \vec{\theta}\right)}{\partial\vec{\theta}_i \partial\vec{\theta}_j}\Big|_{\mu=\hat{\mu}, \vec{\theta}=\hat{\hat{\vec{\theta}}}} \ . \tag{6.2}$$

Likelihood is a useful tool to estimate the compatibility of the observed data and hypotheses. One of the parameters to judge the compatibility is the p-value, p_μ, corresponding to the probability that the experimental result equal to or more extreme than the observed result is realized under an assumption that the signal strength is μ. Calculation of p_μ makes use of the profile likelihood ratio $\lambda(\mu)$ (or $\tilde{\lambda}(\mu)$) and the test statistics q_μ (or $\tilde{q}_\mu$) defined based on the likelihood as:

$$\lambda(\mu) = \frac{L\left(\mu, \hat{\hat{\vec{\theta}}}_\mu\right)}{L\left(\hat{\mu}, \hat{\vec{\theta}}\right)} , \tag{6.3}$$

$$q_\mu = \begin{cases} -2\ln\lambda(\mu) & (\hat{\mu} \leq \mu) \\ 0 & (\hat{\mu} > \mu) \end{cases} , \tag{6.4}$$

where $\hat{\hat{\vec{\theta}}}_\mu$ is the value of the nuisance parameters maximising the likelihood for a given μ. The region with $\mu < 0$ is not allowed in the analysis searching for signals of new particles. Thus, $\tilde{\lambda}(\mu)$ and $\tilde{q}_\mu$ defined below are used instead in this analysis.

$$\tilde{\lambda}(\mu) = \begin{cases} \frac{L\left(\mu, \hat{\hat{\vec{\theta}}}_\mu\right)}{L\left(\hat{\mu}, \hat{\vec{\theta}}\right)} & (\hat{\mu} \geq 0) \\ \frac{L\left(\mu, \hat{\hat{\vec{\theta}}}_\mu\right)}{L\left(0, \hat{\hat{\vec{\theta}}}_0\right)} & (\hat{\mu} < 0) \end{cases} , \tag{6.5}$$

$$\tilde{q}_\mu = \begin{cases} -2\ln\tilde{\lambda}(\mu) & (\hat{\mu} \leq \mu) \\ 0 & (\hat{\mu} > \mu) \end{cases} . \tag{6.6}$$

Defining $f(\tilde{q}_\mu|\mu, \vec{\theta})$ as the probability that $\tilde{q}_\mu$ is observed under the condition of $(\mu, \vec{\theta})$, p-value of the hypothesis $(\mu, \vec{\theta})$ can be written as:

$$p_{\mu,\vec{\theta}} = \int_{\tilde{q}_\mu,\mathrm{obs}}^{\infty} f(\tilde{q}_\mu|\mu, \vec{\theta}) d\tilde{q}_\mu , \tag{6.7}$$

where $\tilde{q}_\mu$, obs is observed $\tilde{q}_\mu$. Finally, the p-value is defined as the largest $p_{\mu,\vec{\theta}}$ that can be realized by choosing proper $\vec{\theta}$ as

$$p_\mu = \max_{\vec{\theta}} p_{\mu,\vec{\theta}} . \tag{6.8}$$

In general, the observation of smaller p_μ means that the result is less compatible with the hypothesis.

Two series of statistical analysis are performed in the search for T. One is the discovery test, which computes $p-$value of the hypothesis in absence of T, referred to as "null-hypothesis". The other is limit setting, which computes the upper limit on the production cross section times branching ratio, $\sigma(pp \to \mathrm{single}T) \times BR(T \to Zt)$.

6.3.2 Discovery test

The null-hypothesis is equal to the hypothesis with $\mu = 0$, hence the discovery test makes use of p_0, the p-value with $\mu = 0$. The parameters defined in the previous section can be written in the specific case of $\mu = 0$ as,

$$\tilde{\lambda}(0) = \begin{cases} \frac{L(0,\hat{\hat{\vec{\theta}}}_0)}{L(\hat{\mu},\hat{\vec{\theta}})} & (\hat{\mu} \geq 0) \\ 1 & (\hat{\mu} < 0) \end{cases} , \tag{6.9}$$

$$\tilde{q}_0 = \begin{cases} -2\ln\tilde{\lambda}(0) & \hat{\mu} \geq 0 \\ 0 & \hat{\mu} < 0 \end{cases} , \tag{6.10}$$

$$p_0 = \max_{\vec{\theta}} p_{0,\vec{\theta}} = \max_{\vec{\theta}} \int_{\tilde{q}_0,obs}^{\infty} f(\tilde{q}_\mu|0, \vec{\theta}) d\tilde{q}_0 . \tag{6.11}$$

Evidence of new particle will be claimed if the observed p_0 is smaller than 0.0027, corresponding to significance of 3σ, and discovery will be claimed if p_0 smaller than 6×10^{-7}, corresponding to 5σ. There are two ways to compute p_0. One is based on all the bins of SR and the other is based on each single bin of SR independently. The former is referred to as "Global p_0" and the latter as "local p_0".

6.3.3 Limits setting

The limit on the cross section times branching ratio is computed with the CLs method[66, 67] . In the CLs method, $CL_{\mathrm{s+b}} = p_\mu$ and $CL_{\mathrm{b}} = p_0$ are computed with a given μ. These variables correspond to the confidence level of the hypothesis of signal presence with the strength μ and null-hypothesis, respectively. CL_s is defined as the ratio of $CL_{\mathrm{s+b}}$ and CL_{b} as:

$$CL_{\mathrm{s}} = \frac{CL_{\mathrm{s+b}}}{CL_{\mathrm{b}}}, \tag{6.12}$$

and the signal strength μ is rejected if CL_{s} is smaller than a given threshold, which is 0.05 in this analysis, corresponding to 95% C.L.

Chapter 7

SM background processes

The event selection discussed in the previous chapter indicates that this analysis is affected mainly by the SM processes containing real Z bosons. Events containing top or other heavy particles are also expected to have impacts. The expected property and impact of such processes are discussed throughout this chapter.

7.1 Z+jets

The Z+jets process is the largest background in this analysis due to large production cross section($\sim$60 nb), whose major production diagram is shown in Fig. 7.1, The associated jets are dominated by the light(u,d, and s) quarks, but c and b quarks can be associated as well. The process associated with t quarks are possible as well, but they are considered as another category of backgrounds ($t\bar{t}+X$) because the cross section is as small as 1 pb and the kinematics is quite different.

7.1.1 Misidentification of the top-tagger

Since Z+jets events do not contain real t quarks, they contaminate the SR only if large-R jets are misidentified by the top-tagger. The expected probability of misidentification is computed using the Sherpa MC samples. While the misidentification probability with respect to the

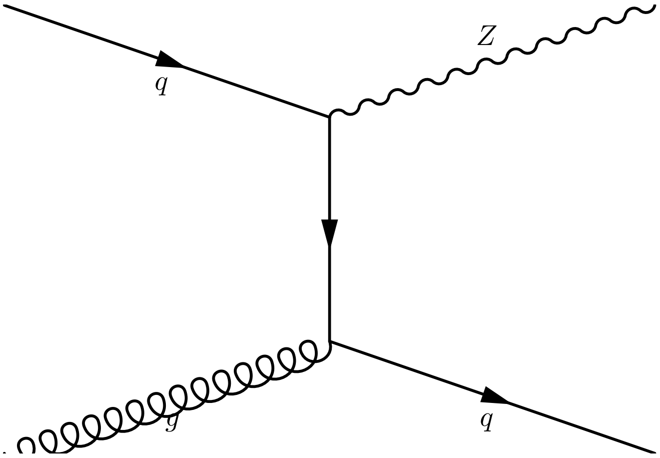

Figure 7.1: The major Z+jets production mechanism at LHC.

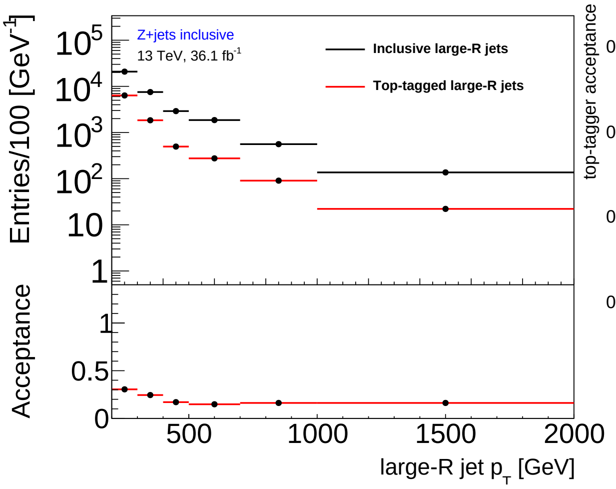

Figure 7.2: Misidentification probability of the top-tagger as a function of the large-R jets p_T.

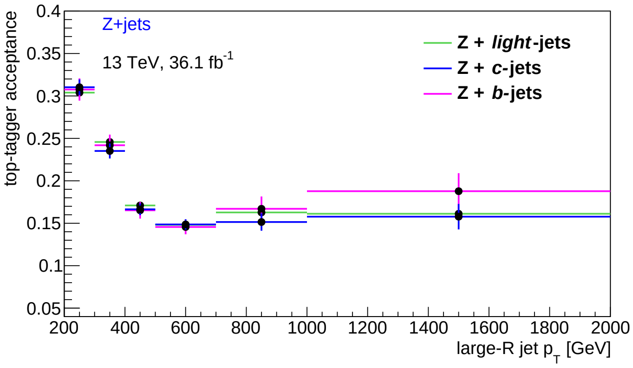

Figure 7.3: Misidentification probability of the top-tagger among b-, c-, light-quark jets as functions of large-R jets p_T.

inclusive large-R jets is 26.8±0.2 %, the probability explicitly depends on p_T of the large-R jets as shown in Fig. 7.2. Large-R jets with higher p_T are less likely to be tagged because the tagger thresholds are tighter.

Slight difference of the dependency between the jet flavor is expected as Fig. 7.3: misidentification probabilities with respect to Z + light, c, and b quarks are 30.4±0.3 %, 31.0±0.9 %, and 30.8±1.3 % in $p_T < 300$ GeV region and 16.1±0.5 %, 15.8±1.5 %, and 18.8±2.1 % in $p_T > 1000$ GeV region, respectively. Hence, the accuracy of the expectation of the composition ratio is important for the expectation of the kinematic distribution in the SR as well as of the event yields.

7.1.2 MC modelling

While the contribution of the Z + jets processes is basically computed with Monte Carlo samples of SHERPA2.2.1 generator, the samples based on MADGRAPH are compared to the SHERPA samples to assign an uncertainty of the Monte Carlo modelling. The discrepancy between two generators on the main variables used in this analysis are shown in Fig. 7.4. This difference shows that MADGRAPH events more likely contain b-tagged jets and top-tagged jets while they less likely contain forward jets and high p_T Z. These lead to the difference of the acceptance in the SR as shown in Table 7.1, and comprehensively the event yields in the SR as well as kinematic distribution. As a result, 133.5(SHERPA) and 95.2(MADGRAPH) events are expected to be observed in the SR, as summarized with other numbers in Table 7.2. The distributions of the reconstructed VLQ mass are compared in Fig. 7.5. Since this corresponds to the uncertainty on the SR event yields of as large as ∼30 %, it has a large impact on the analysis. However, it should be suppressed by comparing the data and MC expectation in the CRs.

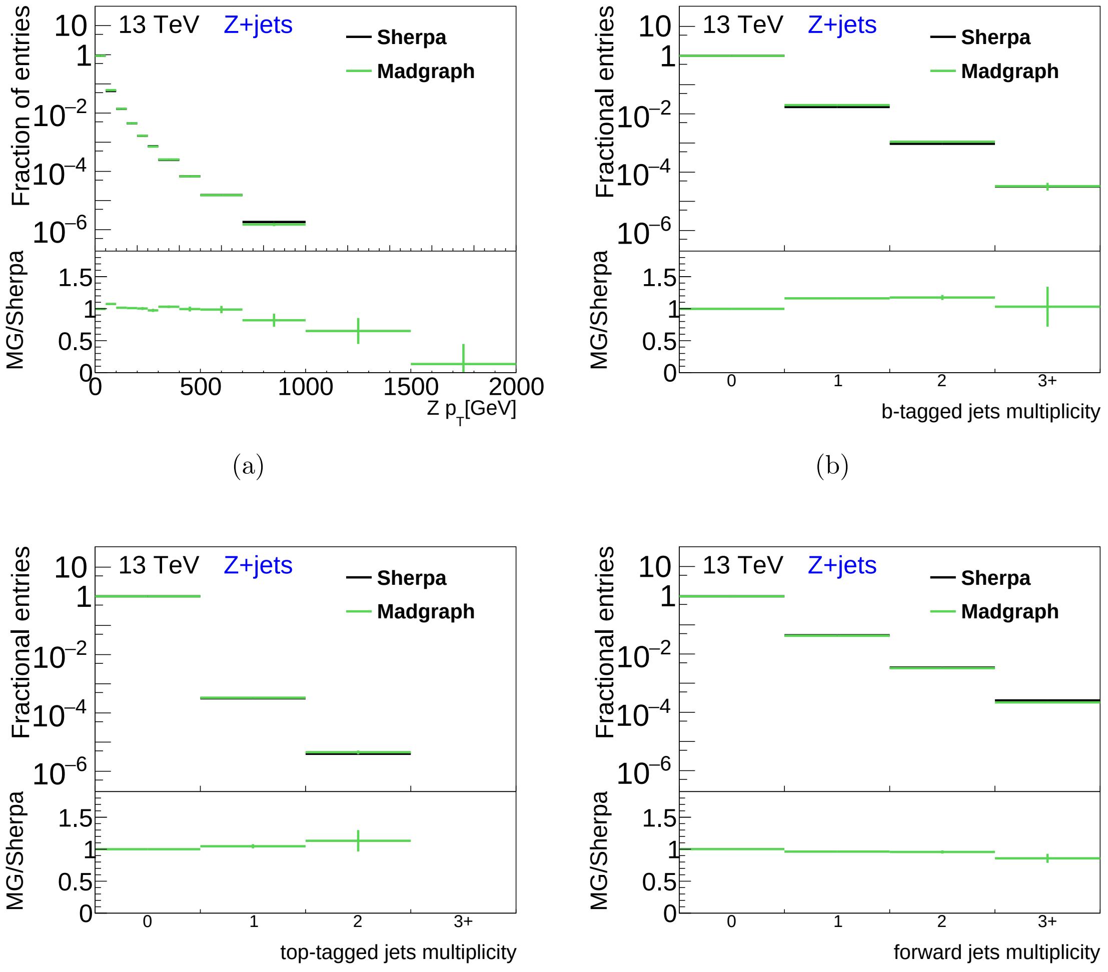

(a)

(b)

(c)

(d)

Figure 7.4: Comparison between SHERPA and MADGRAPH samples in terms of Z p_T(a), b-jets multiplicity(b), top-jets multiplicity(c), and forward jets multiplicity(d).

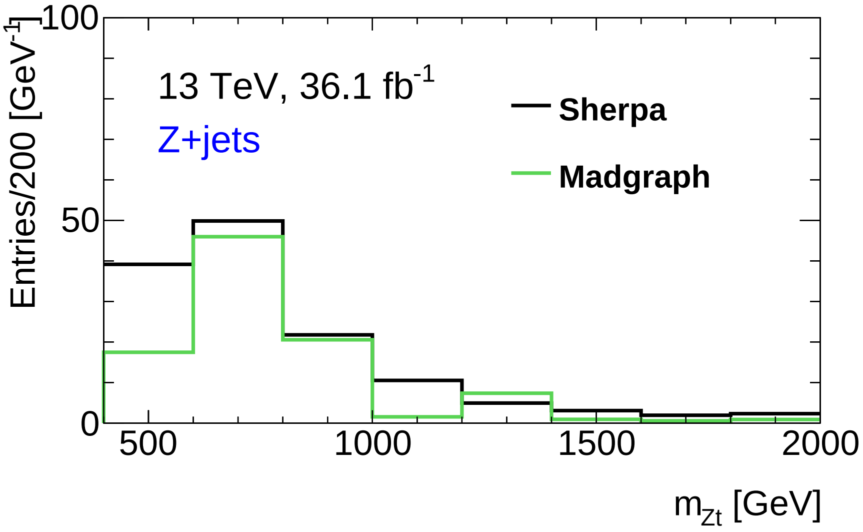

Figure 7.5: The expected Sherpa and MadGraph distribution of the reconstructed T mass in SR

Table 7.1: The acceptance of the SR requirements with respect to Sherpa and MadGraph samples. The statistical uncertainty is small enough($\sim 10^{-3}$ %) compared to the results.

SR Requirements	Acceptance(Sherpa)	Acceptance(MadGraph)
$Zp_T > 200$ GeV	0.31 %	0.31 %
>0 b-jets	1.8 %	2.1 %
>0 top-jets	0.032 %	0.034 %
>0 forward jets	4.8 %	4.6 %

Table 7.2: Expected event yields of Z+jets computed based on Sherpa and MadGraph in each region. Discrepancy of ~28.8% is observed in the SR. Only the statistical uncertainty is taken into account in this table.

	Z+jets(Sherpa)	Z+jets(MadGraph)
CR0	2335.2 ± 26.4	2905.5 ± 115.0
CR1	518.8 ± 12.0	468.1 ± 50.4
VR	513.9 ± 9.3	517.7 ± 41.2
SR	133.6 ± 4.7	95.2 ± 17.7

7.1.3 MC modelling uncertainty suppression by fits

The large modelling uncertainty is suppressed by the fitting procedure described in Section 6.3. The expected performance of the fitting is estimated using Asimov dataset, an artificial dataset whose property is set to be equal to the MC expectation. Assuming that only the modelling uncertainty is considered in the analysis, the uncertainty on the event yields in the SR is suppressed from 28.8 % to 2.6 %. Since all of the systematic uncertainty are simultaneously treated in the fitting in the real analysis, the actual suppression is not as

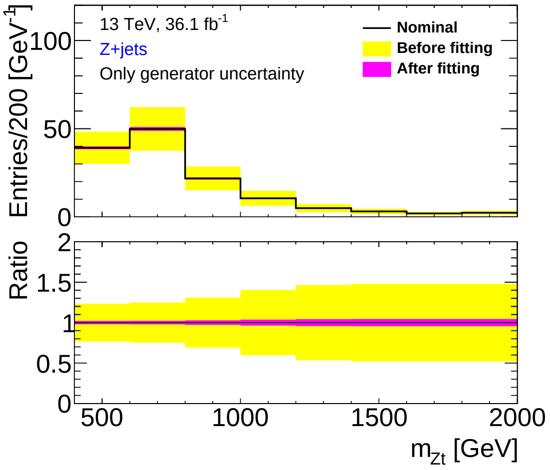

Figure 7.6: The generator uncertainty on the event yields as a function of the reconstructed mass before and after fitting considering only the modelling uncertainty.

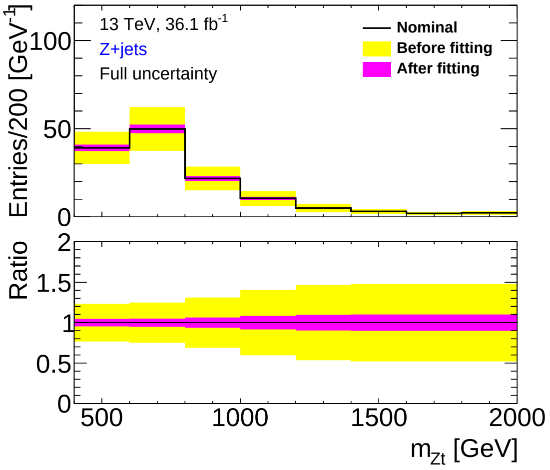

Figure 7.7: The generator uncertainty on the event yields as a function of the reconstructed mass before and after fitting considering all the uncertainties.

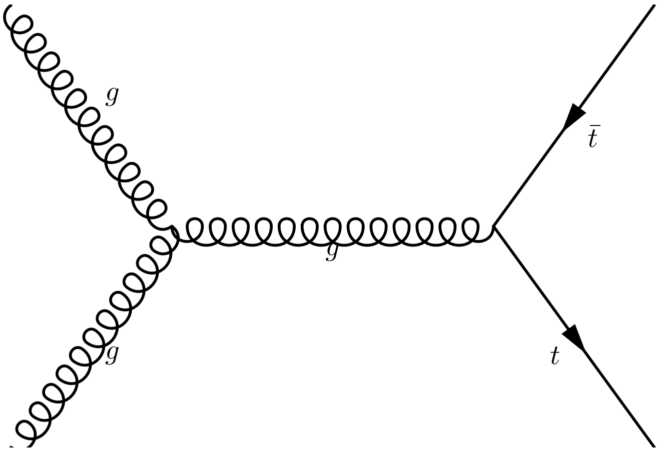

Figure 7.8: The major $t\bar{t}$ production mechanism at LHC.

large as the case above. In this case, the generator uncertainty after fitting is expected to be 5.8 %. The uncertainty on the kinematic distribution in the both cases are shown in Fig. 7.6 and 7.7.

7.2 $t\bar{t}$

In LHC, pairs of top quarks are mostly generated via the gluon fusion processes shown in Fig. 7.8. The $t\bar{t}$ events can be categorized into the SR only if a Z boson is misidentified in the event. The distribution of the invariant mass of pairs of leptons is shown in Fig. 7.9. They

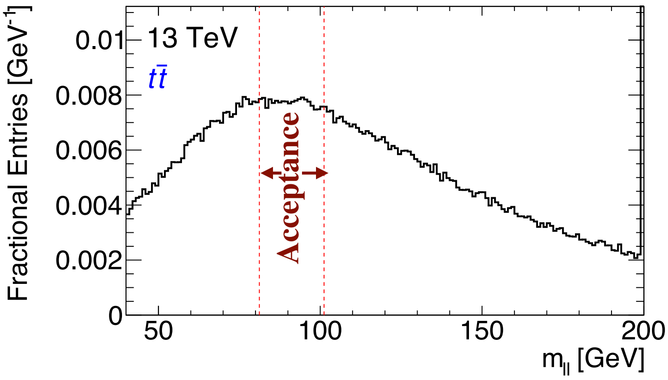

Figure 7.9: The distribution of two leptons invariant mass. Only the events with same flavor opposite sigh pairs. The lower and higher threshold of Z reconstruction acceptance is shown as well.

are identified as the decay products of Z if they have same flavor and opposite charge, and the invariant mass consistent with Z within 10 GeV. The acceptance of this selection with respect to two leptons events is $\sim$7.8 %.

The selection for SR requires a top-jet as well as a Z boson. There are two processes of $t\bar{t}$ considered to contain both reconstructed Z and top. One is the semileptonic events(Fig. 7.10(a)), where one of the t quark decays hadronically and tagged as top-jet, and the other decays leptonically. Z is reconstructed using the lepton from t and an additional lepton which is accidentally reconstructed. The other process is leptonic(Fig. 7.10(b)), where both of t decay leptonically and Z is reconstructed using the leptons from t, and the large-R jet of non-t quark is misidentified as top.

About 1.0 % of the $t\bar{t}$ events containing Z and about 2.0 % of $t\bar{t}$ SR events are semileptonic. The ratio of the decay modes expected to be observed after Z boson requirement and the SR selection are shown in Fig. 7.11.

In both semileptonic and leptonic processes, the probability that both Z and top-jet are reconstructed is quite small because an additional lepton is required in the semileptonic process and a misidentified top-jet is required in the leptonic process. Hence, the $t\bar{t}$ events are largely suppressed in the SR, resulting in the expected contamination less than 1 event before fitting, as shown in Table 7.3. This is almost negligible compared to the Z+jets background.

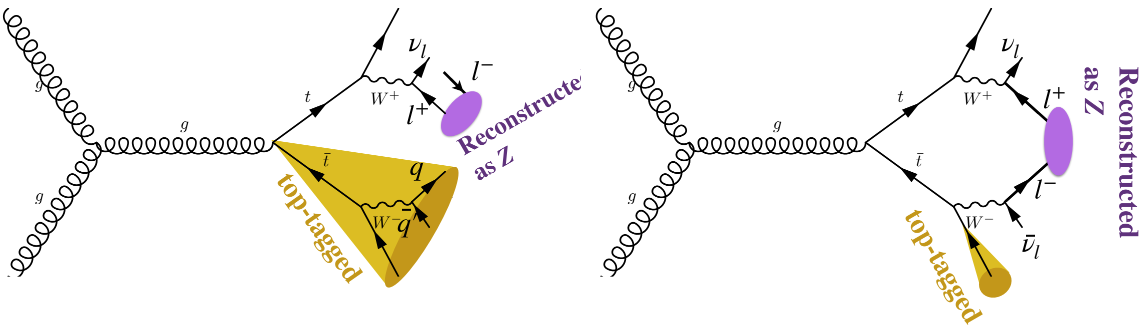

(a) $t\bar{t}$ semileptonic process (b) $t\bar{t}$ leptonic process

Figure 7.10: $t\bar{t}$ processes that can be recognised to contain both reconstructed Z and top-jets.

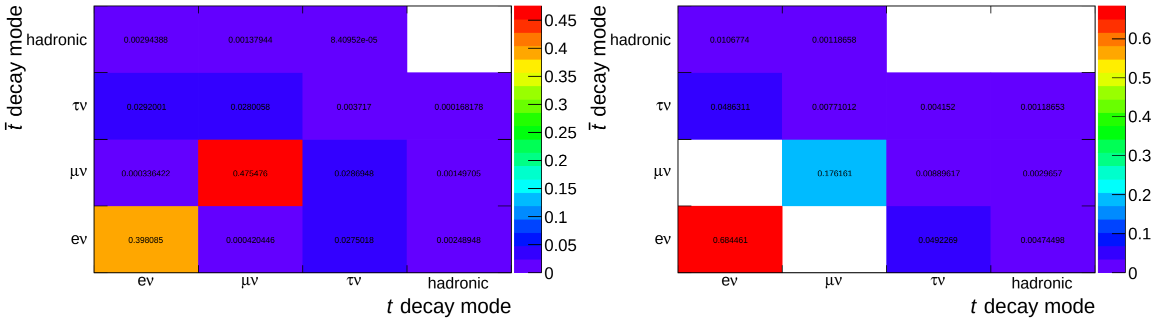

(a) (b)

Figure 7.11: The ratio of event yields in each decay processes after Z boson requirement(a) and the SR requirement(b).

Table 7.3: Expected event yields of $t\bar{t}$ background. Only the statistical uncertainty is taken into account.

	ttbar
CR0	0.85 ± 0.42
CR1	3.4 ± 1.0
VR	$< 10^{-2}$
SR	0.95 ± 0.48

7.3 Diboson

A pair of vector bosons (diboson) can be produced by the proton-proton collision according to the diagram in Fig. 7.12. The combinations of bosons considered in this analysis are WW,

WZ, and ZZ, corresponding to the total production cross section of ~40 pb. The dominant process contaminating the SR is VZ, where Z decays leptonically and V decays hadronically, which is shown in Fig. 7.13, because the misidentification probability of the top-tagger is higher for jets originating from vector bosons compared to QCD jets.

Approximately 9 diboson events are expected to be observed in the SR. The expected event yields of each process in each region are listed in Table 7.4.

Table 7.4: Expected event yields of diboson background. The contribution is dominated by the WZ and ZZ processes as expected. Only the statistical uncertainty is taken into account.

	WW	WZ	ZZ	total
CR0	2.6 ± 0.2	76.8 ± 2.2	25.1 ± 1.1	104.5 ± 2.5
CR1	0.56 ± 0.22	19.8 ± 1.4	14.3 ± 1.0	34.6 ± 1.6
VR	0.52 ± 0.08	20.1 ± 1.1	6.9 ± 0.5	27.6 ± 1.2
SR	0.08 ± 0.04	6.5 ± 0.9	2.4 ± 0.4	9.0 ± 1.0

7.4 $t\bar{t} + X$

Pair production of top quarks in association with heavy particles is categorized into $t\bar{t} + X$ background. The $t\bar{t}+X$ processes considered in this analysis include $t\bar{t}$ production associated

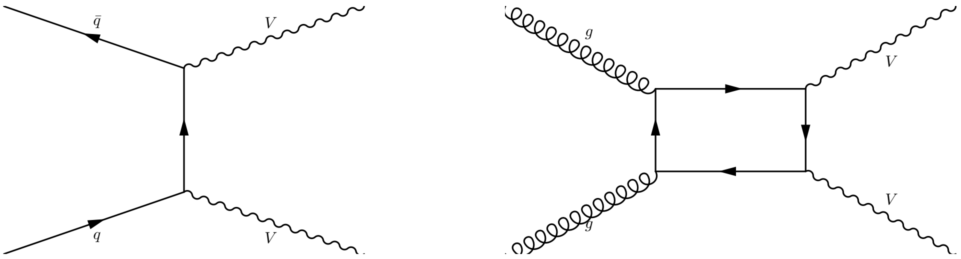

Figure 7.12: Diagram of diboson production processes in LHC.

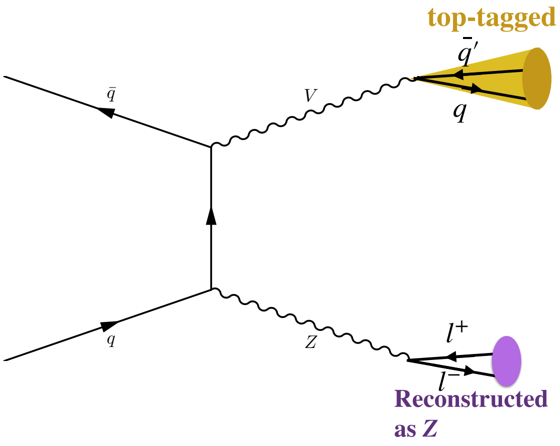

Figure 7.13: Diagram of diboson production processes in LHC.

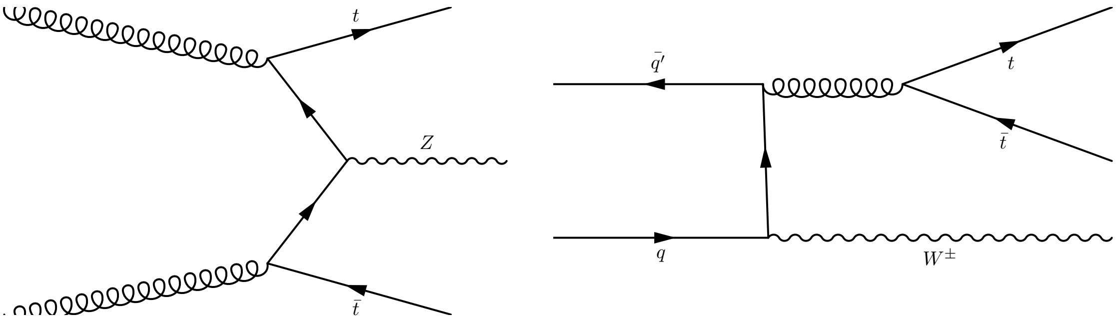

(a) Diagram of a pair of top quarks generated in association with Z.

(b) Diagram of a pair of top quarks generated in association with W.

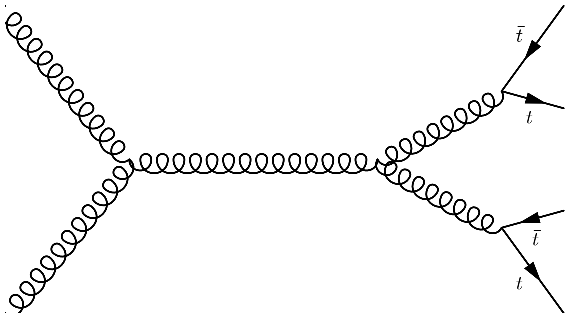

(c) Diagram of four top quarks generation.

Figure 7.14: Diagrams of $t\bar{t} + X$ processes considered in this analysis.

with Z, W, and the production of 4 top quarks. The diagrams of these background processes are displayed in Fig. 7.14. Relatively high SR acceptance is expected in these processes because they always contain real top quarks and potentially real Z. However, they have quite small impact on this analysis because of their low production cross section of < 1 pb. The expected event yields of $t\bar{t} + W$ and 4 top quarks processes are smaller than 0.01 in all of the regions, while $O(1)$ events of the $t\bar{t} + Z$ process are expected to be observed, as summarized in Table 7.5.

Table 7.5: Expected event yields of $t\bar{t} + X$ backgrounds. The contribution is dominated by $t\bar{t} + Z$ processes and $t\bar{t} + W$ and 4 top processes are almost negligible. Only the statistical uncertainty is taken into account.

	$t\bar{t} + Z$	$t\bar{t} + W$	4 top	total
CR0	1.2 ± 0.1	$< 10^{-2}$	$< 10^{-2}$	1.21 ± 0.1
CR1	8.5 ± 0.2	$< 10^{-2}$	$< 10^{-2}$	8.5 ± 0.2
VR	1.0 ± 0.1	$< 10^{-2}$	$< 10^{-2}$	1.0 ± 0.1
SR	7.3 ± 0.2	$< 10^{-2}$	$< 10^{-2}$	7.3 ± 0.2

7.5 Other backgrounds

"Others" category of the background processes includes triboson production (WWW, WWZ, WZZ, and ZZZ) and single top quark production. The diagrams are shown in Fig. 7.15. The single top production process is similar to the single production of T, however, the acceptance of SR is not expected to be large because top quarks never decay into Z boson. The event yields of the triboson are expected to be small for the same reason of $t\bar{t} + X$

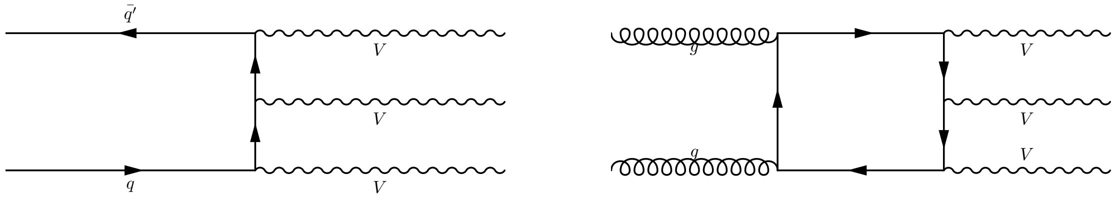

(a) Diagrams of a triboson production process.

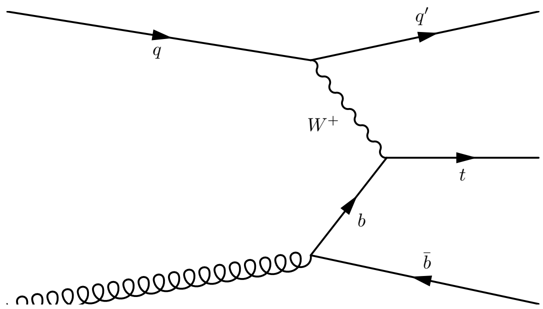

(b) Diagram of the single production of a top quark.

Figure 7.15: Diagrams of the "Others" background processes considered in this analysis.

processes. The production cross sections of the triboson and the single top are ∼0.01 pb and ∼81 pb, respectively. The expected event yields are listed in Table 7.6.

Table 7.6: Expected event yields of "Others" background. The contribution is dominated by single top processes and triboson are almost negligible. Only the statistical uncertainty is taken into account.

	triboson	single top	total
CR0	0.04 ± 0.01	0.64 ± 0.16	0.68 ± 0.16
CR1	$< 10^{-2}$	1.8 ± 0.2	1.8 ± 0.2
VR	$< 10^{-2}$	0.55 ± 0.13	0.55 ± 0.13
SR	$< 10^{-2}$	2.5 ± 0.2	2.5 ± 0.2

Chapter 8

Systematic uncertainty

Details of the systematic uncertainty considered in this analysis are described throughout this chapter. All the sources of uncertainty are listed in Section 8.1 and the impact of the major uncertainty on the event yields and shape of the reconstructed T mass is described in Section 8.2 and Section 8.3, respectively.

8.1 List of considered systematic uncertainty

8.1.1 Detector-related uncertainty

Luminosity: The integrated luminosity is determined using the dedicated calibration runs[68]. The uncertainty of the luminosity measurement in 2015 and 2016, which is 2.1% in total, is considered as the uncertainty on the integrated luminosity.

Electron: Electron uncertainties include the uncertainty of energy scale, energy resolution, efficiency of trigger, reconstruction, and isolation requirements.

The electron energy scale uncertainty arises from the uncertainty of the energy calibration procedure including energy shift induced by pile-up, calibration of EM calorimeter layers and presampler, the materials in front of the calorimeter, non-linearity of the cell energy measurement, and modelling of the shower shape. In the barrel region, the uncertainty is dominated by the layers calibration uncertainty, while the impact of the upstream materials, non-linearity, and shower shape uncertainty increase. The total scale uncertainty is up to a few percent in wide range of η as displayed in Fig. 8.1.

The resolution uncertainty is contributed by the shower and sampling fluctuations in the calorimeter, the fluctuations in energy loss by the upstream materials, noise of electronics, pile-up noise. The shower and sampling fluctuations are estimated by the resolution measurement using $Z \rightarrow ee$ events as described in Section 5.3 . The impact of upstream materials are estimated using MC simulation with additional materials, and the electronics and pile-up noise are derived from events recorded by random trigger. As a result, the resolution is measured in the energy range 30-60 GeV with a precision of 5-10% while the uncertainty increases to 20-50% in high energy range. Compared to low η region, the resolution in large η is slightly worse while smaller uncertainty is achieved as displayed in Fig. 8.2 .

The electron reconstruction, identification, and isolation efficiencies are related to the electrons selection introduced in Section 5.3 . In this analysis, electrons are required to satisfy $tight$ identification and $FixedCutTightTrackOnly$ isolation criteria after the reconstruction. Hence, the efficiency of electrons used in the analysis can be written as:

$$\epsilon_{el} = \epsilon_{reco} \times \epsilon_{ID} \times \epsilon_{Iso}, \tag{8.1}$$

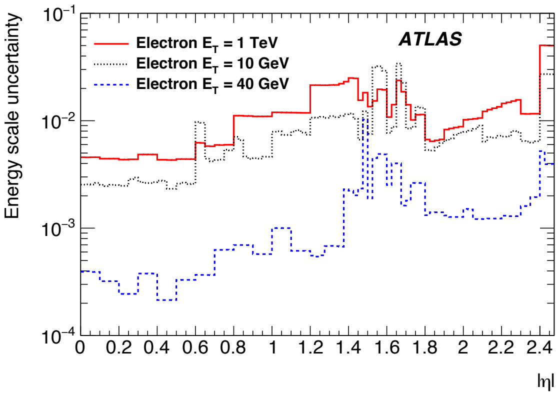

Figure 8.1: The total uncertainty of energy scale for an electron as a function of η. [53]

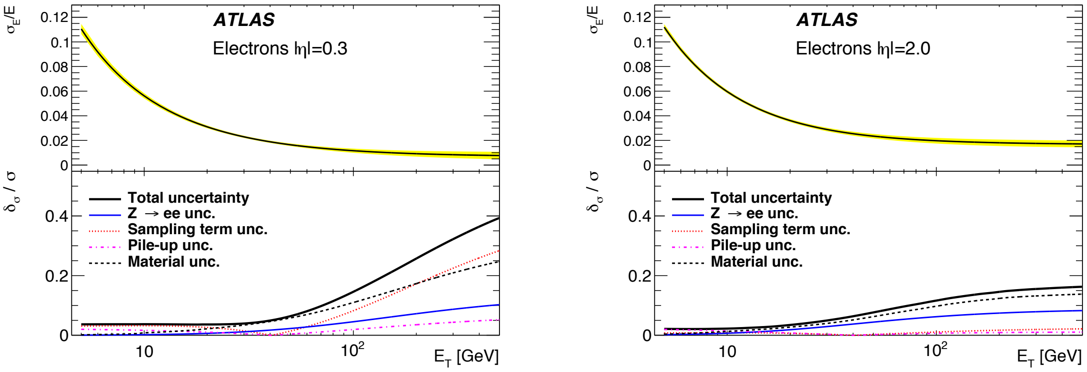

(a)

(b)

Figure 8.2: Relative energy resolution and uncertainty of an electron as a function of E_T in $|\eta|$ =0.3 (a) and 2.0 (b).[53]

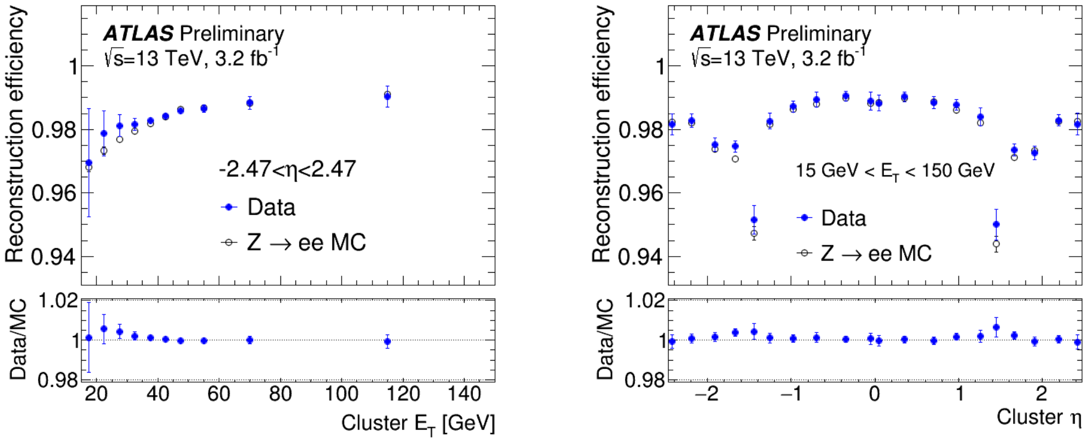

(a) (b)

Figure 8.3: The electron reconstruction efficiency of data and MC and the ratio as a function of cluster E_T(a) and η(b). The absolute value and error bars of the lower plot is assigned as the scale factors and uncertainty[69].

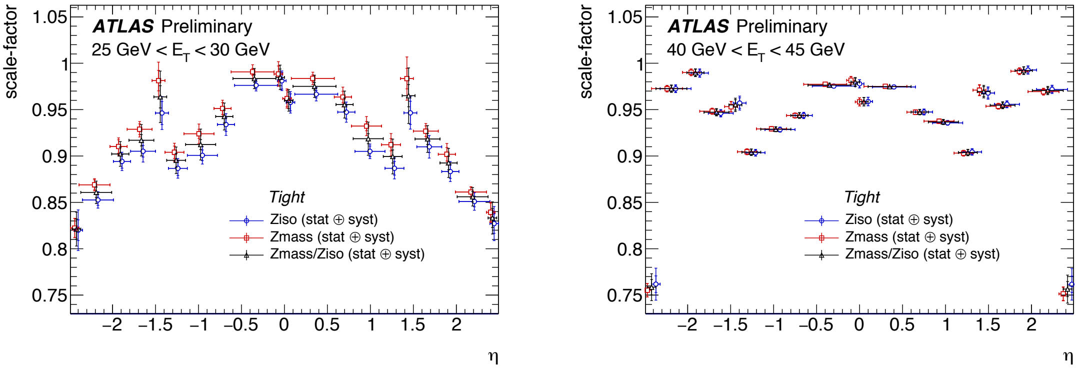

(a) (b)

Figure 8.4: Scale factors of ϵ_{ID} in the energy range 25 GeV< E_T <30 GeV(a) and 40 GeV< E_T <45 GeV(b) as a function of η[69].

where $\epsilon_{reco}, \epsilon_{ID}, \epsilon_{Iso}$ are the efficiencies of reconstruction, identification, and isolation requirements, respectively. They are estimated using the tag-and-probe method of $Z \to ee$ and $J/\psi \to ee$ in both data and MC, and the MC efficiency is compared to data to compute the scale factors which correct MC. The results of the $\epsilon_{reco}, \epsilon_{ID}$ estimation and their uncertainty are displayed in Fig. 8.3 and 8.4, respectively. The isolation uncertainty, which is not shown in this thesis, is estimated to be smaller than 0.5% in wide range of η and E_T.

The electron trigger efficiency is related to the number of total recorded events. It is also measured based on $Z \to \mu\mu$ and $J/\psi \to \mu\mu$ tag-and-probe method and the data/MC ratio is computed as scale factors. The statistical fluctuation is assigned as the uncertainty of the trigger scale factors.

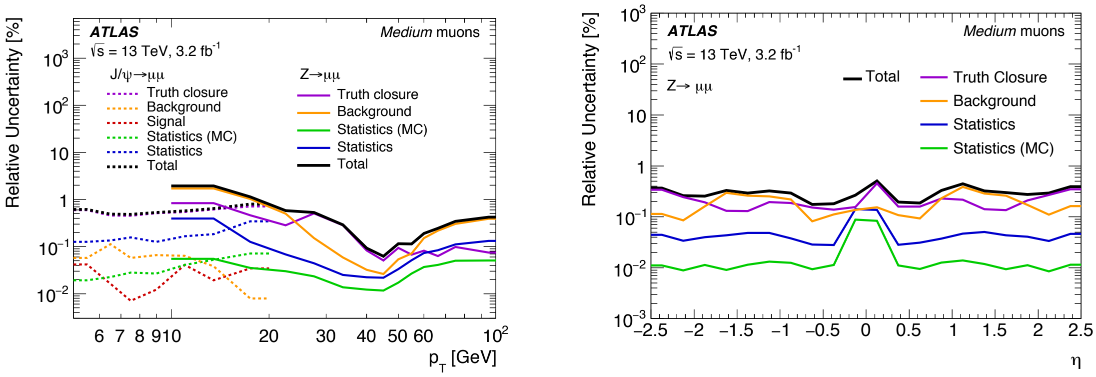

(a) (b)

Figure 8.5: The uncertainty of the muon *medium* selection efficiency as a function of p_T(a) and η(b), derived from $Z \to \mu\mu$ and $J/\psi \to \mu\mu$ tag-and-probe.

Muon: Muon uncertainties include the scale factors of the trigger, reconstruction, and isolation as in the case of electrons, and the additional scale factor of track-to-vertex-association (TTVA). They are measured based on the tag-and-probe method of $Z \to \mu\mu$ and $J/\psi \to \mu\mu$[48]. The statistical uncertainty of data and MC samples and contribution of non-Z events are considered to be source of systematic uncertainty of the scale factors. Remaining possible uncertainties are measured as the difference between the results of tag-and-probe and measurements based on truth information of MC, which is referred to as "Truth closure". As results of the measurements, the relative uncertainty of the *medium* muon selection efficiency is found to vary from ~2% to ~0.1% as a function of p_T and not to depend on η significantly, as indicated in Fig. 8.5. The isolation efficiency of the *LooseTrackOnly* criteria, shown in Fig. 8.6, is almost flat over wide range of p_T and the relative uncertainty is smaller than 0.5%. The uncertainty of TTVA and trigger efficiency are also measured using the tag-and-probe method and found to be both smaller than 1% in wide range of p_T.

The muon scale uncertainty is related to the momentum correction of Eq. 5.3. The correction parameters are also measured based on the tag-and-probe method and the uncertainty is found to be approximately 0.05%.

Small-R jet: One of the uncertainty related to small-R jet is the jet energy scale (JES) uncertainty. JES is measured using three processes, Z+jets, γ+jets, and multi jets, as explained in Section 5.4, each of which is affected by several sources of uncertainty listed in Table 8.1. They are combined and treated as eight independent nuisance parameters, which are referred to as "Effective NPs", in accordance with the correlation between the sources. The total uncertainty on the reconstructed energy is up to 4%, as shown in Fig. 8.7.

Other uncertainties are related to η-intercalibration explained in Section 5.4, flavour composition of jets, effect of pile-up, and punch-through of jets. Their combined impact on the jet energy is below 1.5%.

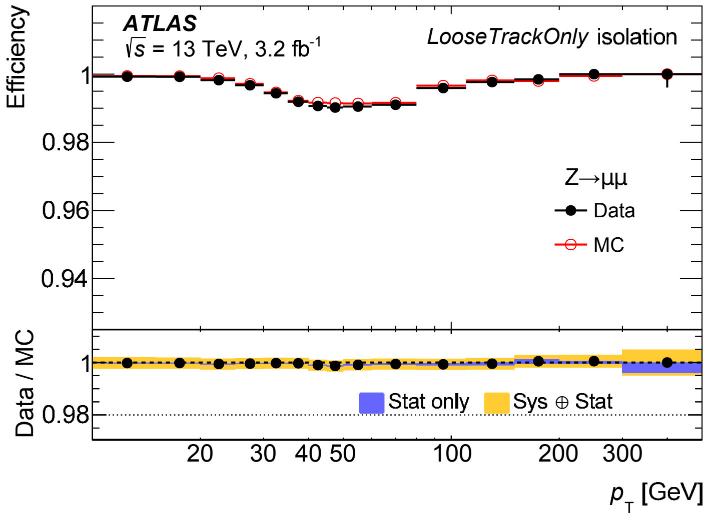

Figure 8.6: The efficiency and uncertainty of *LooseTrackOnly* isolation selection[48].

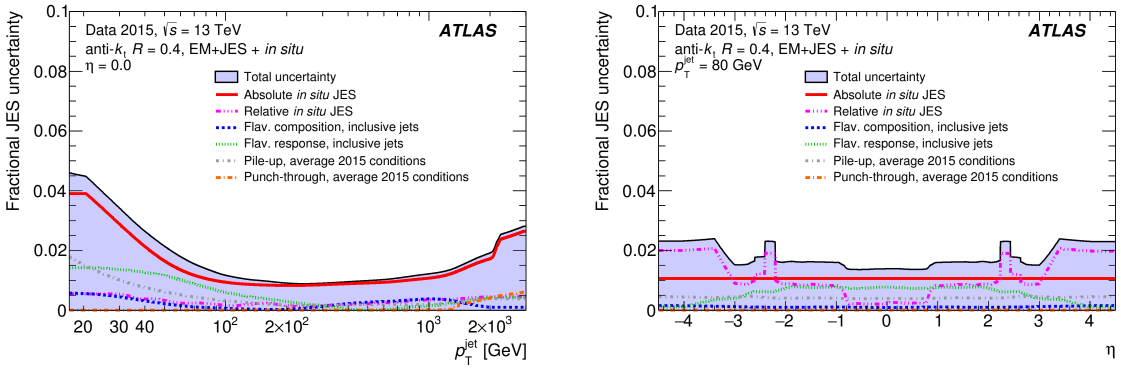

(a)

(b)

Figure 8.7: Fractional JES uncertainty as a function of p_T(a) and η(b)[73].

Table 8.1: The sources of JES uncertainty.

Measurement	Source	Description
Z/γ + jets	LAr energy scale	The electron energy scale of LAr calorimeter
	LAr smearing	LAr smearing of MC
	LAr material	Materials of LAr calorimeter
Z+jets	k-term	Out-of-cone radiation
	MC generator	Difference of Z+jets MC generators
	muon scale	Momentum scale of muons
	muon smearing in ID	Momentum smearing of muons in ID
	muon smearing in MS	Momentum smearing of muons in MS
	veto	Z+jets radiation
	statistics	Statistics
	dϕ	The cut of dϕ between Z and jet
γ + jets	MC generator	Difference betweenγ+jets MC generators
	Out-of-cone	Out-of-cone radiation
	Purity	Photon purity
	veto	γ + jets radiation
	statistics	Statistics
	dϕ	The cut of dϕ between γ and jet
Multi jet balance	jet topology	Jet topology
	Fragmentation	Jet fragmentation
	Threshold	Jet threshold
	statistics	Statistics

Large-R jet: Uncertainties in the mass, p_T, and τ_{32} of large-R jets are measured using the comparison between the data and MC[75, 76]. The uncertainty in the mass is taken to be correlated with the uncertainty in p_T. The fractional uncertainty in p_T ranges from ∼2% to ∼6% from the large-R jet p_T of 300 GeV to 3000 GeV, while the uncertainties in mass and τ_{32} are below 4% in wide range of p_T. The uncertainty in resolution of p_T, mass, and τ_{32} are taken to be 2%, 20%, and 15%, respectively.

***b*-tagging:** The uncertainty of b-tagging efficiency is measured based on the tag-and-probe method of $t\bar{t}$[78], a leptonically decaying top quark is used as a tag and the b-quark generated by the other top quark is used as a probe to measure the efficiency. As shown in Fig. 8.8, the uncertainty ranges from ∼15% in the low p_T region to ∼5% in the region of ∼300 GeV.

Pile-up: A correction factor is applied in each MC event to correct the pile-up distribution. The statistical uncertainty of the correction factor is treated as the pileup correction uncertainty.

8.1.2 Theory-related uncertainty

Cross section: Cross section uncertainty is assigned on each background samples based on the MC simulation: ±5.0% for Z+jets[79], +5.6/-6.1% for $t\bar{t}$[80], ±6.0% for diboson[81], +13.3/-11.9% for $t\bar{t}+W$, +10.4/-11.9% for $t\bar{t}+Z$ and $t\bar{t}+ll$[82].

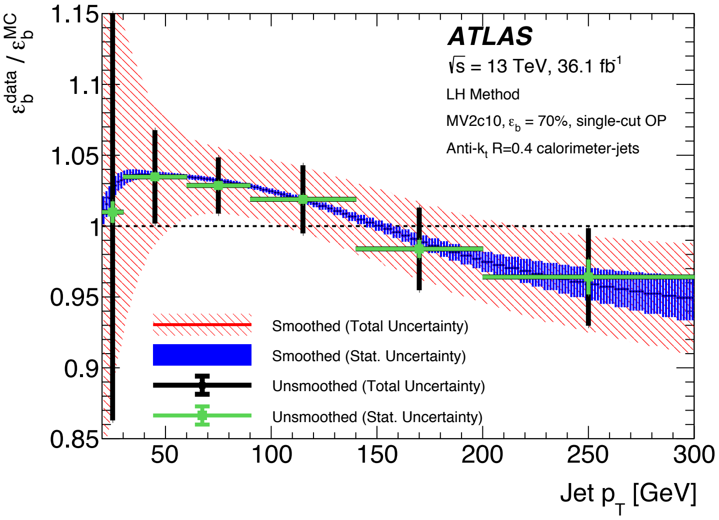

Figure 8.8: The b-tagging efficiency ratio of data and MC and uncertainty[78].

Choice of PDF set: The uncertainty related to the choice of PDF set is computed based on the comparison between the samples of NNPDF NLO PDF set with the other PDF sets: MMHT2014 NNLO[83] and CT14 NNLO PDF[84].

Parton distribution function scaling: The effect of variations of the factorization scale μ_f and the renormalization scale μ_r on PDF is taken into account. The nominal setting is $\mu_f = \mu_r = 1.0$, whereas the alternative settings are $(\mu_r, \mu_f) = (0.5, 0.5), (0.5, 1.0), (1.0, 0.5), (2.0, 1.0), (1, 0, 2.0)$, and $(2.0, 2.0)$.

MC generator: As described in Chapter 4 and 7, the dominant Z+jets background is estimated using SHERPA2.2.1 and MADGRAPH. The difference between the two generators is assigned as the generator uncertainty.

Forward jet acceptance: The uncertainty of 11% is set in the forward jet acceptance to fix the data/MC discrepancy.

8.2 The uncertainty impact on event yields in the signal region

The impact on signal and background event yields of each uncertainty is shown in Table 8.2 and 8.3, respectively. The uncertainty with the largest impact on the SR is Z+jets generator uncertainty of 25.0% and the second-largest is Forward jet uncertainty of 11.0%. The total uncertainty of SR event yields is 12.4% (signal) and 33.3% (background).

Table 8.2: List of the considered nuisance parameters and their impacts on the signal events. Only the parameters which affect the SR event yields by more than 1 % are shown.

Nuisance parameter	SR	CR1	CR0
Forward jet	+0.110/-0.110	+0.000/+0.000	+0.000/+0.000
Large-R jet kinematics	+0.009/-0.027	+0.035/-0.027	+0.013/-0.016
Jet flavor composition	+0.017/-0.015	-0.002/-0.001	+0.008/+0.009
JET_EtaIntercalibration_Modelling	+0.016/-0.012	-0.003/-0.004	-0.001/+0.020
Large-R jet modelling	+0.009/-0.016	+0.020/-0.031	+0.020/-0.015
JET_Pileup_RhoTopology	+0.008/-0.006	+0.000/-0.003	-0.000/+0.017
JET_EffectiveNP_1	+0.003/-0.005	-0.004/-0.002	-0.001/+0.017
JET_EtaIntercalibration_NonClosure	+0.011/-0.008	-0.000/-0.002	+0.000/+0.008
Luminosity	+0.021/-0.021	+0.021/-0.021	+0.021/-0.021
LARGERJET_Tracking_Kin	-0.001/-0.006	+0.019/-0.026	-0.002/-0.013
MUON_EFF_SYS	+0.015/-0.015	+0.014/-0.013	+0.012/-0.011
EL_EFF_ID_TOTAL_1NPCOR_PLUS_UNCOR	+0.012/-0.012	+0.014/-0.014	+0.015/-0.015

Table 8.3: List of the considered nuisance parameters and their impacts on the background events. Only the parameters which affect the SR event yields by more than 1 % are shown.

Nuisance parameter	SR	CR1	CR0
Z+jets generator	-0.250	-0.090	+0.233
Forward jet	+0.110/-0.110	+0.000/+0.000	+0.000/+0.000
Large-R jet kinematics	+0.068/-0.080	+0.052/-0.051	+0.053/-0.051
Jet flavor composition	+0.067/-0.066	+0.001/+0.001	-0.006/+0.005
Scale of μ	+0.035/-0.061	+0.078/-0.092	+0.086/-0.102
Large-R jet p_T resolution	-0.053	-0.046	-0.039
JET_EtaIntercalibration_Modelling	+0.037/-0.047	-0.003/+0.003	-0.002/+0.002
Large-R jet mass resolution	-0.046	+0.128	+0.167
FT_EFF_Eigen_Light_0	-0.045/+0.044	-0.057/+0.057	+0.010/-0.010
PDF	+0.020/-0.044	+0.009/-0.084	+0.004/-0.099
Z+jets cross section	+0.044/-0.044	+0.046/-0.046	+0.048/-0.048
Large-R jet modelling	+0.043/-0.031	+0.034/-0.036	+0.033/-0.039
JET_Pileup_RhoTopology	+0.026/-0.036	+0.002/-0.002	-0.003/+0.003
JET_EffectiveNP_1	+0.018/-0.027	+0.000/-0.001	-0.003/+0.003
JET flavor response	-0.025/+0.015	+0.002/-0.001	+0.002/-0.002
JET_EtaIntercalibration_NonClosure	+0.017/-0.022	+0.002/-0.001	+0.001/-0.000
Luminosity	+0.021/-0.021	+0.021/-0.021	+0.021/-0.021
LARGERJET_Tracking_Kin	+0.018/-0.017	+0.020/-0.024	+0.022/-0.023
FT_EFF_Eigen_C_0	-0.016/+0.016	-0.015/+0.015	+0.003/-0.003
MUON_EFF_SYS	+0.014/-0.013	+0.014/-0.014	+0.013/-0.013
FT_EFF_Eigen_Light_1	+0.014/-0.014	+0.016/-0.016	-0.003/+0.002
DiBoson cross section	+0.012/-0.012	+0.012/-0.012	+0.009/-0.009
EL_EFF_ID_TOTAL_1NPCOR_PLUS_UNCOR	+0.012/-0.012	+0.011/-0.011	+0.012/-0.011

8.3 The uncertainty impact on shape of the discriminant variables

As well as the event yields, the uncertainty also affects the reconstructed T mass distribution, the discriminant variable of this analysis. Fig. 8.9 shows the impact of uncertainty on the reconstructed T distribution in each region, indicating that the uncertainty of each bin is ∼30 % and the most bin with the largest uncertainty in SR is the bin of $1600 < m_{Zt} < 1800$ GeV, whose uncertainty is up to $\sim 50\%$.

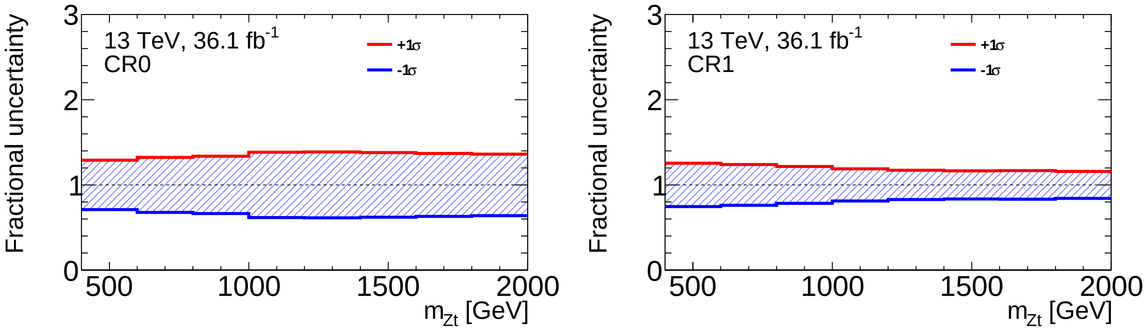

(a) CR0

(b) CR1

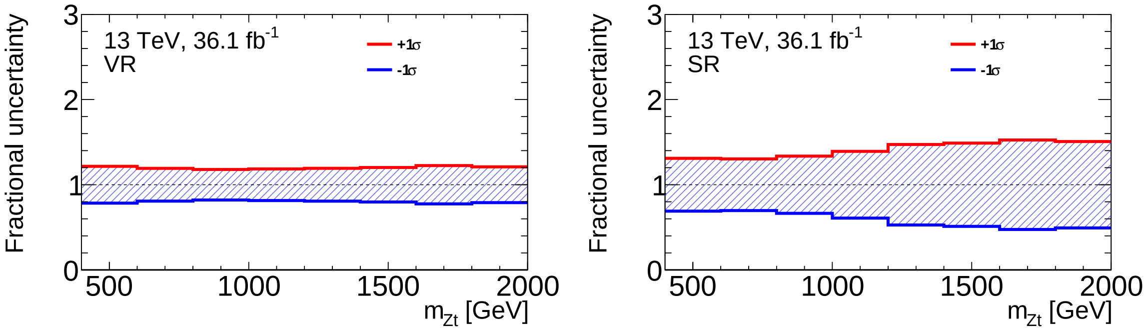

(c) VR

(d) SR

Figure 8.9: The impact of the systematic uncertainty in each bin of CR0(a), CR1(b), VR(c), and SR(d).

Chapter 9

Fitting before unblinding the signal region

The observed data in the SR had been masked until a validation was done using data. The expected performance of the fitting was measured with artificial datasets as described in Section 9.1, and then the fitting was performed with the observed data in the CRs as discussed in Section 9.2. The normal fitting procedure and additional procedures were performed and compared to each other at this stage to confirm the stability of the fitting.

9.1 Asimov fit

In prior to the fitting with the observed data, another fitting was performed with Asimov datasets, artificial datasets whose properties are exactly the same as the MC expectation. The aim of the Asimov data is to measure expected performance of the fitting. Two series of Asimov datasets were prepared. One is "Asimov B" and the other is "Asimov $S+B$", the data in absence and presence of the T signal, respectively.

Asimov B

In the background-only Asimov dataset, the event yields and shape are equal to the background estimation, hence the MC expectation is supposed not to be changed by the the fitting. The only difference between before and after the fitting is constraint on the nuisance parameters, resulting in smaller uncertainty in the event yields. The expected event yields in each region is summarized in Table 9.1. The event yields was unchanged as expected and the uncertainty was suppressed especially in Z+jets because the generator uncertainty, which is the largest uncertainty before the fitting, was strongly constrained by up to 77 %.

Table 9.1: Expected number of background events. The uncertainties out and in of the bracket indicate the uncertainty before and after the fitting, respectively.

	CR0	CR1	VR	SR
Z+jets	2335.2 ± 816.4(137.6)	518.8 ± 133.6(51.9)	513.9 ± 89.6(53.6)	133.5 ± 46.8(16.2)
Diboson	104.5 ± 136.6(119.5)	34.6 ± 47.4(41.5)	27.6 ± 36.9	9.0 ± 11.6(9.8)
$t\bar{t}$	0.85 ± 0.73(0.71)	3.4 ± 1.7(1.6)	$< 10^{-3}$	0.95 ± 0.85(0.84)
$t\bar{t}+X$	1.2 ± 0.2(0.2)	8.5 ± 1.2(1.1)	0.99 ± 0.21(0.19)	7.3 ± 1.3(1.1)
Others	0.68 ± 0.18(0.18)	1.8 ± 0.2(0.2)	0.56 ± 0.18(0.17)	2.5 ± 0.4(0.3)

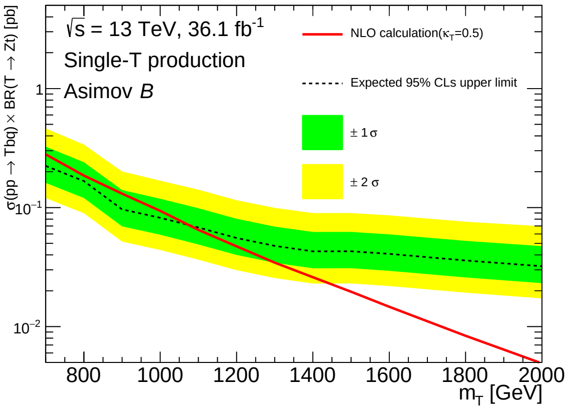

Figure 9.1: Expected limit based on $\kappa_T = 0.5$ signal samples and background-only Asimov dataset.

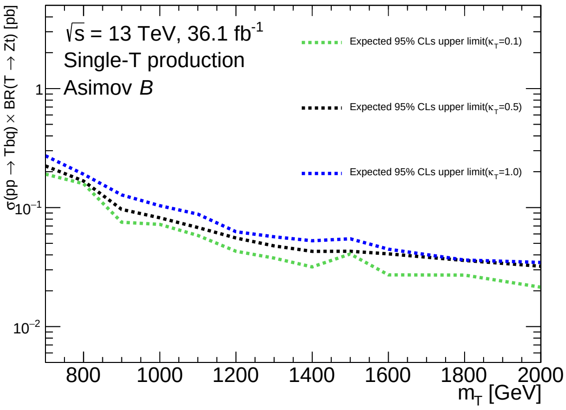

Figure 9.2: Expected limit based on $\kappa_T = 0.1$(green), $\kappa_T = 0.5$(black), and $\kappa_T = 1.0$(blue) signal samples and background-only Asimov dataset. Tighter limits are achieved with smaller κ_T because of the narrower decay width.

The background-only Asimov is useful in settings limits on the cross section of T under an assumption that no significant excess is observed. The expected limits on $\sigma(\text{single } T)$ $\times BR(T \to Zt)$ computed using the $\kappa_T = 0.5$ samples are shown in Fig. 9.1. The comparison between different sets of κ_T is also performed as shown in Fig. 9.2.

Asimov $S + B$

The Asimov $S + B$ configuration is useful in the estimation of the expected significance with presence of signal. In the estimation, fitting was performed under a constraint with the signal strength $\mu = 0$, corresponding to the null-hypothesis. The distribution of the SR events after the fitting was compared to the observed data, which is Asimov $S + B$ dataset in this case, to calculate p_0, the p-value with respect to the null-hypothesis.

Both global and local p_0 were computed in this study. The former is the p-value calculated based on the whole SR distribution, and the latter is the p-value calculated with respect to each bin of the SR. The expected global p_0 dependent on the mass of T is estimated using signal samples at several mass points with $\kappa_T = 0.5$ as shown in Fig. 9.3. Fig. 9.4 indicates an example of the expected local p_0 distribution computed based on the Asimov $S + B$ sample with the T signal sample with the T mass of 900 GeV and κ_T=0.5 . The histogram for "Background" in the upper plot indicates the result of fitting with null-hypothesis. Larger significance (or small p_0) was observed in the bin with large discrepancy between the null-hypothesis expectation and Asimov $S + B$.

The global p_0 value was computed with the Asimov $S + B$ datasets of all the mass and couplings considered in this analysis as shown in Fig. 9.5. In terms of the significance, the evidence is expected to be observed with 3 σ if the coupling κ_T is up to 0.7 in the T mass<1000 GeV region and 1.0 in the region with the T mass around 1500 GeV, and discovery with 5 σ

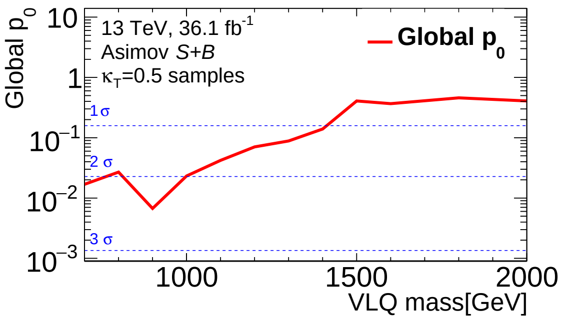

Figure 9.3: Global p_0 computed using Asimov $S + B$ datasets with $\kappa_T = 0.5$ signal samples. Larger significance is expected on the low mass samples because of larger production cross section.

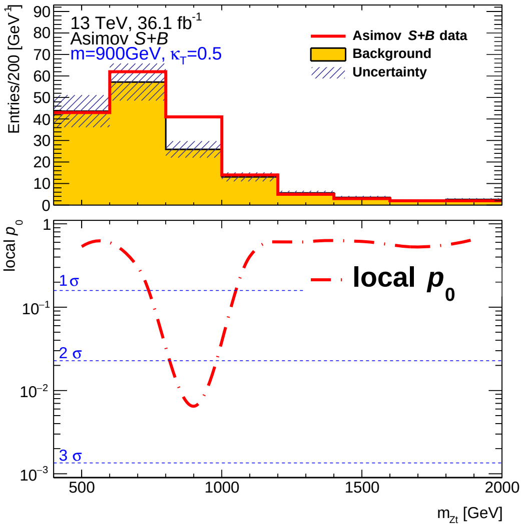

Figure 9.4: Local p-value estimation with the Asimov dataset generated with signal sample of 900 GeV for T mass and $\kappa_T = 0.5$ coupling.

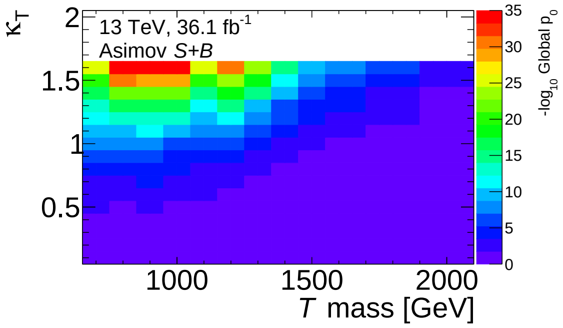

Figure 9.5: Expected global p_0 computed with the Asimov $S + B$ datasets as a two-dimensional function of T mass and coupling κ_T.

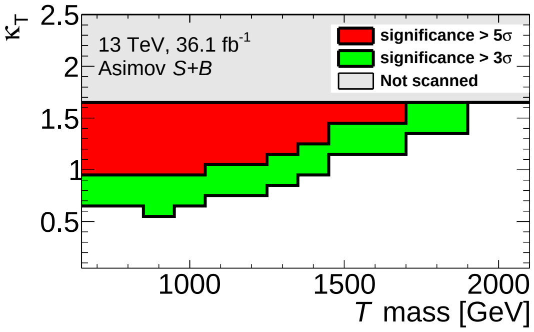

Figure 9.6: Significance of the signal in regions defined with T mass and coupling κ_T. The evidence or discovery is expected to be claimed with the significance of 3 σ and 5 σ, respectively.

is expected if κ_T is up to 1.0 in mass$<$ 1000 GeV or $\sim$1.5 around 1500 GeV, as indicated in Fig. 9.6.

In the fitting on Asimov $S + B$ with null-hypothesis, the expected event yields can be varied from the expectation before the fitting because of the discrepancy between the Asimov data and null-hypothesis. As an example, the expected event yields after fitting with the benchmark Asimov dataset(900 GeV, $\kappa_T = 0.5$) is listed in Table 9.2.

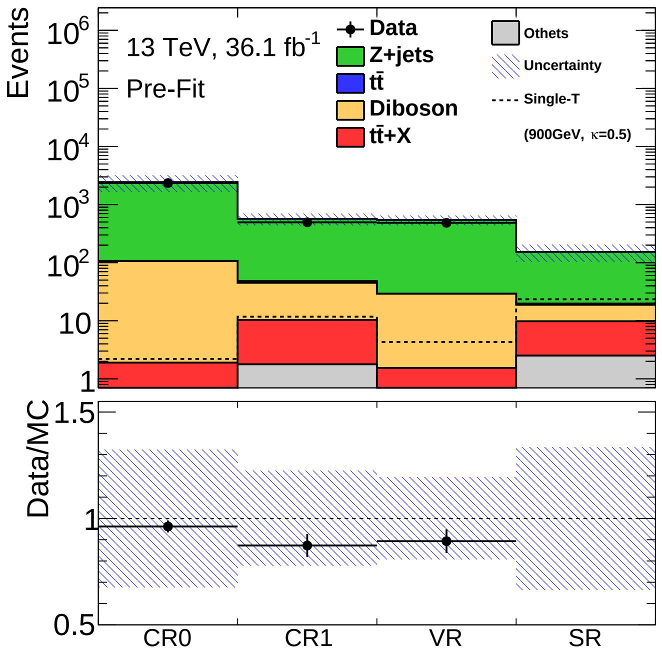

Figure 9.7: Comparison of observed data and MC expectation in CRs and VR. The ratio is consistent with 1 among all the three regions.

Table 9.2: Expected number of background events after fitting under null-hypothesis and Asimov $S + B$.

	CR0	CR1	VR	SR
Z+jets	2353.2 ± 142.2	532.7 ± 50.43	513.7 ± 61.6	135.5 ± 19.3
Diboson	85.6 ± 124.7	28.0 ± 43.2	22.5 ± 33.7	7.4 ± 10.5
$t\bar{t}$	0.83 ± 0.71	3.5 ± 1.7	$< 10^{-3}$	0.95 ± 0.84
$t\bar{t} + X$	1.2 ± 0.2	8.6 ± 1.1	0.99 ± 0.18	7.3 ± 0.98
Other	0.68 ± 0.18	1.8 ± 0.22	0.56 ± 0.17	2.5 ± 0.28

9.2 Fitting in the control regions before unblinding

9.2.1 Observed data in the control and validation regions

Prior to fitting, the observed data was compared to the MC expectation to verify the consistency. The comparison was performed only in the CRs and the VR while the SR was masked. In terms of the event yields, the data was found to be consistent with MC within the uncertainty. The number of observed events in CR0, CR1, and VR are 2350, 495, and 485, respectively, while 2442.5±786.703, 567.1±124.4, and 543.0±101.9 events were expected by MC. This result is summarized in Table 9.3 and Fig. 9.7.

The distributions of the invariant mass m_{Zt} are also compared between data and MC as shown in Fig. 9.8. While good agreement is observed in most of the bins, slight discrepancy was observed in some of the bins. The largest discrepancy was found in the bin for 1600 $< m_{Zt} <$ 1800 GeV of the VR, where 3 events were observed while 6.6±1.5 events were expected. The data/MC comparison was also performed with other properties as discussed

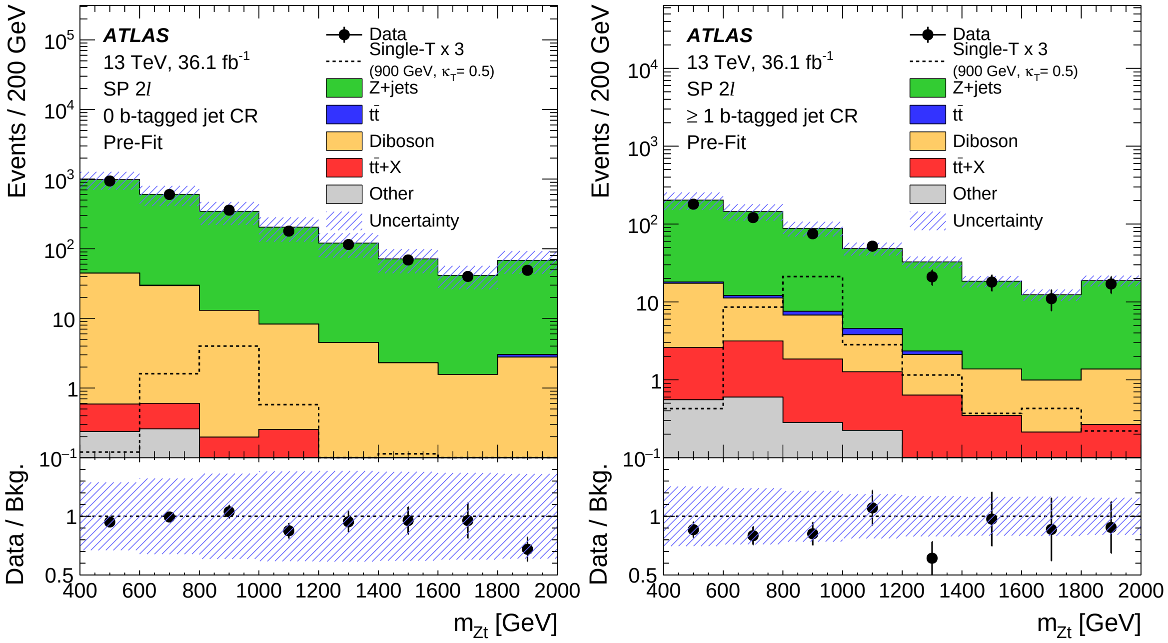

(a) CR0 (b) CR1

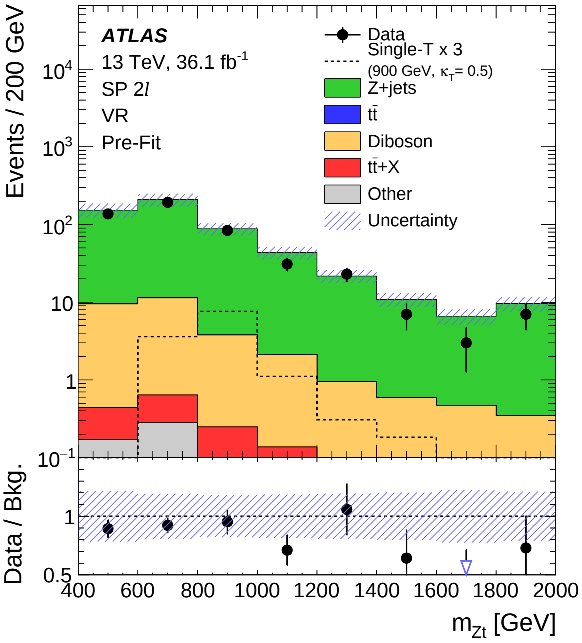

(c) VR

Figure 9.8: Data/MC comparison of the reconstructed T mass distribution in CR0(a), CR1(b), and VR(c).

in Appendix B.1.

Table 9.3: Event yields at the pre-fit level in the CRs, VR, and SR.

	CR0	CR1	VR	SR
T (900 GeV, κ_T= 0.5)	2.2 ± 0.4	11.7 ± 0.9	4.3 ± 0.8	23.5 ± 2.9
Z+jets	2335.2 ± 816.4	518.82 ± 133.62	513.87 ± 89.6	133.5 ± 46.8
$t\bar{t}$	0.85 ± 0.73	3.4 ± 1.7	$< 10^{-3}$	0.95 ± 0.85
Diboson	104.5 ± 136.6	34.6 ± 47.4	27.6 ± 36.9	9.0 ± 11.6
$t\bar{t}$+X	1.2 ± 0.2	8.5 ± 1.2	0.99 ± 0.21	7.3 ± 1.3
Others	0.68 ± 0.18	1.8 ± 0.2	0.56 ± 0.18	2.5 ± 0.4
Total Bkg.	2442.5 ± 786.7	567.1 ± 124.4	543.0 ± 101.9	153.3 ± 50.0
Data	2350	495	485	-
Data/Bkg.	0.96 ± 0.31	0.87 ± 0.20	0.89 ± 0.17	-

9.2.2 Fitting with normal and alternate settings

Multiple settings of fitting were performed based on the observed data in CRs to verify the stability of fitting.

- **Nominal setting:** The systematic uncertainties listed in Chapter 8, including all the theory and detector uncertainty, are taken into account as the nuisance parameters.
- **Alternative setting A:** An additional nuisance parameter corresponding to the ratio of b-quark presence in the Z+jet events is considered.
- **Alternative setting B:** Additional nuisance parameters corresponding to the ratio of high p_T Z is considered.

There is difference among these procedures in the treatment of Z+jets normalization. The nominal fitting is performed under an assumption that the Z+jets events can be normalized by one parameter, α_Z. The alternatives A and B introduce two independent normalization parameters, $\alpha_{Z_{\rm LF}}$ and $\alpha_{Z_{\rm HF}}$ in A and $\alpha_{Z_{\rm soft}}$ and $\alpha_{Z_{\rm hard}}$ in B. The parameters $\alpha_{Z_{\rm HF}}$ and $\alpha_{Z_{\rm LF}}$ are the factors applied to the Z+jets samples containing and not containing b-quark, and the parameters $\alpha_{Z_{\rm soft}}$ and $\alpha_{Z_{\rm hard}}$ are applied to the Z+jets samples with the truth p_T of Z boson less and greater than 500 GeV, respectively. The samples were separated based on MC truth information. $\mathcal{N}_{ri}$, the expected number of Z+jets events observed in the bin i of the region r, can be generally written as:

$$\mathcal{N}_{ri} = \mathcal{L}\alpha_Z\sigma_Z\epsilon_Z(r,i) \qquad \cdots \text{Nominal}\ , \tag{9.1}$$

$$\mathcal{N}_{ri} = \mathcal{L}\left[\alpha_{Z_{\rm LF}}\sigma_{Z_{\rm LF}}\epsilon_{Z_{\rm LF}}(r,i) + \alpha_{Z_{\rm HF}}\sigma_{Z_{\rm HF}}\epsilon_{Z_{\rm HF}}(r,i)\right] \qquad \cdots \text{Alternative}\ A\ , \tag{9.2}$$

$$\mathcal{N}_{ri} = \mathcal{L}\left[\alpha_{Z_{\rm soft}}\sigma_{Z_{\rm soft}}\epsilon_{Z_{\rm soft}}(r,i) + \alpha_{Z_{\rm hard}}\sigma_{Z_{\rm hard}}\epsilon_{Z_{\rm hard}}(r,i)\right] \qquad \cdots \text{Alternative}\ B\ , \tag{9.3}$$

where $\mathcal{L}$ is the integrated luminosity, which is 36.1 fb^{-1} in this analysis, σ_X is the official cross section of physics process X, and $\epsilon_X(r,i)$ is the acceptance of the bin i of the region r with respect to X. By definition, the equation $\sigma_Z = \sigma_{Z_{\rm LF}} + \sigma_{Z_{\rm HF}} = \sigma_{Z_{\rm soft}} + \sigma_{Z_{\rm hard}}$ is always practical. Assuming that ϵ, σ, and $\mathcal{L}$ are well measured based on MC and other measurements, the fitting of Alternative A and B is expected to be sensitive to the additional normalization factors.

Nominal

The comparison of best-fit results between data and MC in the CRs and the VR, and the expectation in the SR are shown in Fig. 9.9 and expected and observed number of events are summarized in Table 9.4. The normalization factor for the Z+jets events was estimated to be 0.98 ± 0.04. While good agreement was observed in the event yields in most of the bins, the discrepancy remained in the VR in the bin for $1600 < m_{Zt} < 1800$ GeV.

Table 9.4: Event yields in data and MC after normal fitting.

	CR0	CR1	VR	SR
Z+jets	2289.2 ± 130.3	472.6 ± 44.0	486.4 ± 61.4	118.4 ± 20.0
$t\bar{t}$	0.79 ± 0.71	3.3 ± 1.7	$< 10^{-3}$	0.95 ± 0.84
Diboson	65.7 ± 104.7	19.8 ± 36.6	17.0 ± 28.2	5.6 ± 8.8
$t\bar{t}$+X	1.2 ± 0.2	8.3 ± 1.1	0.99 ± 0.18	7.1 ± 1.0
Others	0.66 ± 0.18	1.7 ± 0.2	0.55 ± 0.17	2.5 ± 0.3
Total Bkg.	2357.6 ± 166.9	505.8 ± 57.3	504.8 ± 67.6	134.8 ± 20.1
Data	2350	495	485	-
Data/Bkg.	1.00 ± 0.07	1.02 ± 0.12	1.04 ± 0.15	-

Alternatives

After the fitting using data in the CRs, the data/MC comparison was performed in both alternative A and B with the same way as the nominal, and the results are summarized in Table 9.5 and 9.6. In terms of event yields, no large discrepancy was observed in either of A or B. The event shapes were also compared as shown in Fig. 9.10(Alternative A) and Fig. 9.11(Alternative B). The shape is reasonably close to the nominal result as discussed later and the discrepancy in the VR remained in both A and B. The normalization factors were estimated: $\alpha_{Z_{HF}} = 0.98 \pm 0.05$, $\alpha_{Z_{LF}} = 1.00 \pm 0.05$ in A, and $\alpha_{Z_{hard}} = 0.98 \pm 0.04$, $\alpha_{Z_{soft}} = 1.0 \pm 0.05$ in B.

Table 9.5: Event yields between data and MC after fitting of alternative A.

	CR0	CR1	VR	SR
Z+b	430.5 ± 31.5	382.9 ± 30.0	118.9 ± 16.0	102.5 ± 15.0
Z+$light$	1890.8 ± 109.9	93.1 ± 22.2	372.5 ± 46.4	18.0 ± 6.9
$t\bar{t}$	0.74 ± 0.71	3.42 ±1.67	$< 10^{-3}$	0.91 ± 0.84
Diboson	59.9 ± 99.9	17.7 ± 34.6	15.3 ± 27.1	5.0 ± 8.4
$t\bar{t} + X$	1.2 ± 0.2	8.3 ± 1.1	0.98 ± 0.18	7.1 ± 1.0
Other	0.67 ± 0.18	1.7 ± 0.2	0.54 ± 0,17	2.5 ± 0.28
Total Bkg.	2356.9 ± 103.1	507.2 ± 34.1	508.2 ± 71.4	136.0 ± 22.1
Data	2350	495	485	-
Data/Bkg.	1.00 ± 0.05	0.98 ± 0.08	0.95 ± 0.14	-

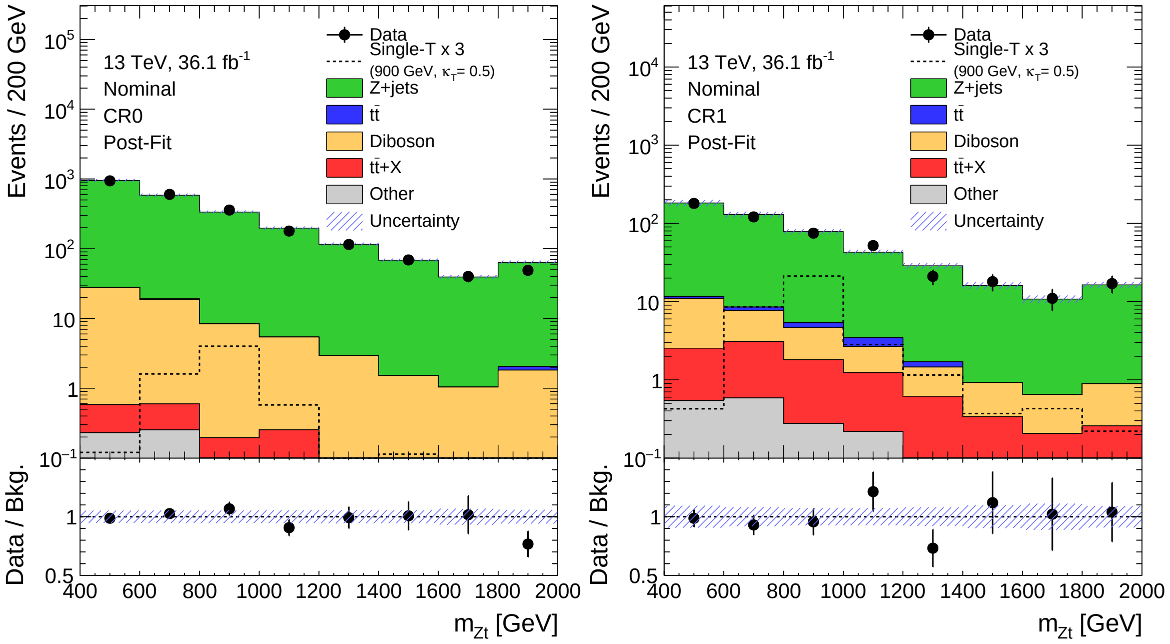

(a) CR0 (b) CR1

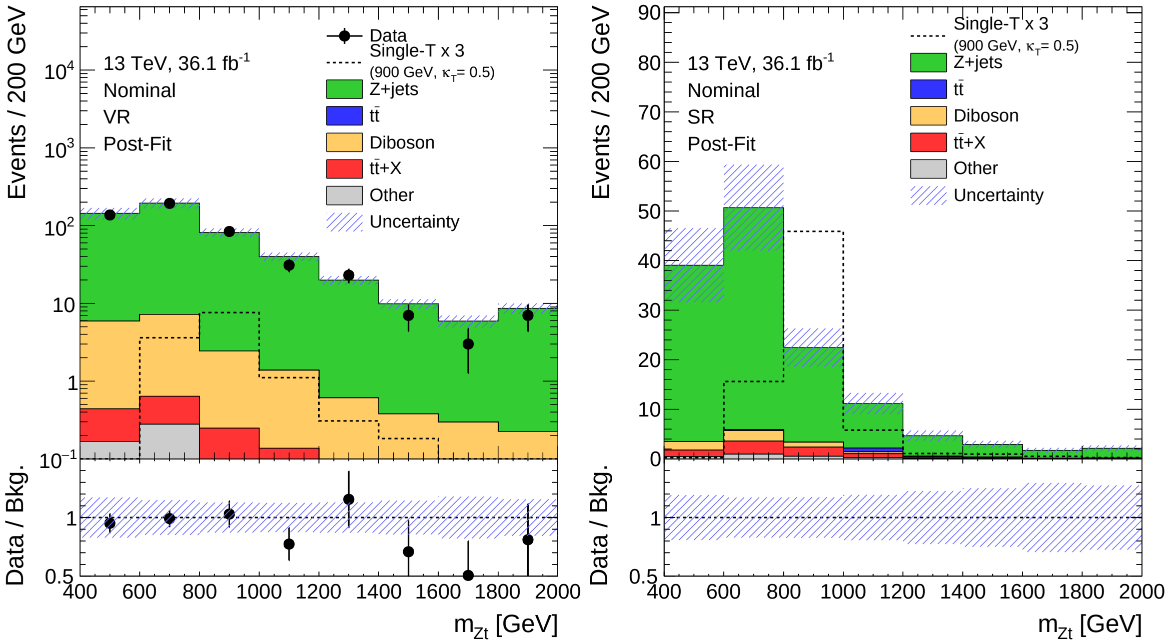

(c) VR (d) SR

Figure 9.9: Data/MC comparison in the CR0(a), CR1(b), VR(c), and MC expectation in the SR(d) after the normal fitting.

Table 9.6: Event yields between data and MC after fitting of alternative B.

	CR0	CR1	VR	SR
hard Z+jets	615.4 ± 36.0	165.3 ± 12.9	165.5 ± 12.4	47.4 ± 4.9
soft Z+jets	1695.3 ± 80.9	317.3 ± 23.1	324.4 ± 51.0	74.2 ± 14.7
$t\bar{t}$	0.80 ± 0.71	3.56 ± 1.67	$< 10^{-3}$	0.90 ± 0.84
Diboson	49.0 ± 96.5	14.6 ± 33.5	12.7 ± 26.4	4.3± 8.2
$t\bar{t} + X$	1.2 ± 0.2	8.2 ± 1.1	0.98 ± 0.18	7.0 ± 0.98
Other	0.65 ± 0.18	1.72 ± 0.22	0.54 ± 0.17	2.42 ± 0.27
Total Bkg.	2362.4 ± 100.4	510.7 ± 34.2	504.2 ± 72	136.2 ± 22.6
Data	2350	495	485	-
Data/Bkg.	0.99 ± 0.05	0.97 ± 0.08	0.96 ± 0.14	-

Comparison between nominal and alternatives settings

Comparisons of the Z+jets normalization factors α_Z, $\alpha_{Z_{HF}}$, $\alpha_{Z_{LF}}$, $\alpha_{Z_{hard}}$, $\alpha_{Z_{soft}}$ measured by the normal and alternate fittings are shown in Fig. 9.12. The best-fit values are all consistent with α_Z within 2 %, which is smaller than the original uncertainty of 5 %.

In terms of the shape expectation in the SR, the background estimation in each bin was compared as shown in Fig. 9.13. Among all of the bins, the entries of the alternative settings are consistent with the nominal setting within 6% in both A and B. This is small enough compared to the nominal uncertainty of ∼20 %. Throughout these investigations, stability of the fitting procedure was successfully confirmed and the nominal fitting was chosen to be used in the following procedure after the SR unblinding because of its simplicity.

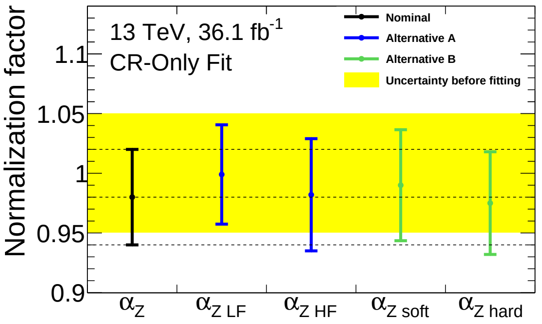

Figure 9.12: Comparison with the normalization factors measured in between the normal and alternate settings.

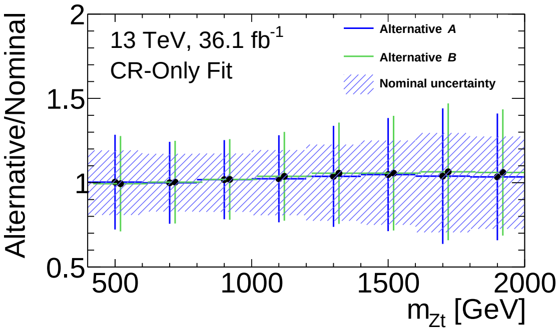

Figure 9.13: Comparison of the expectations in each SR bin between the nominal and alternative settings.

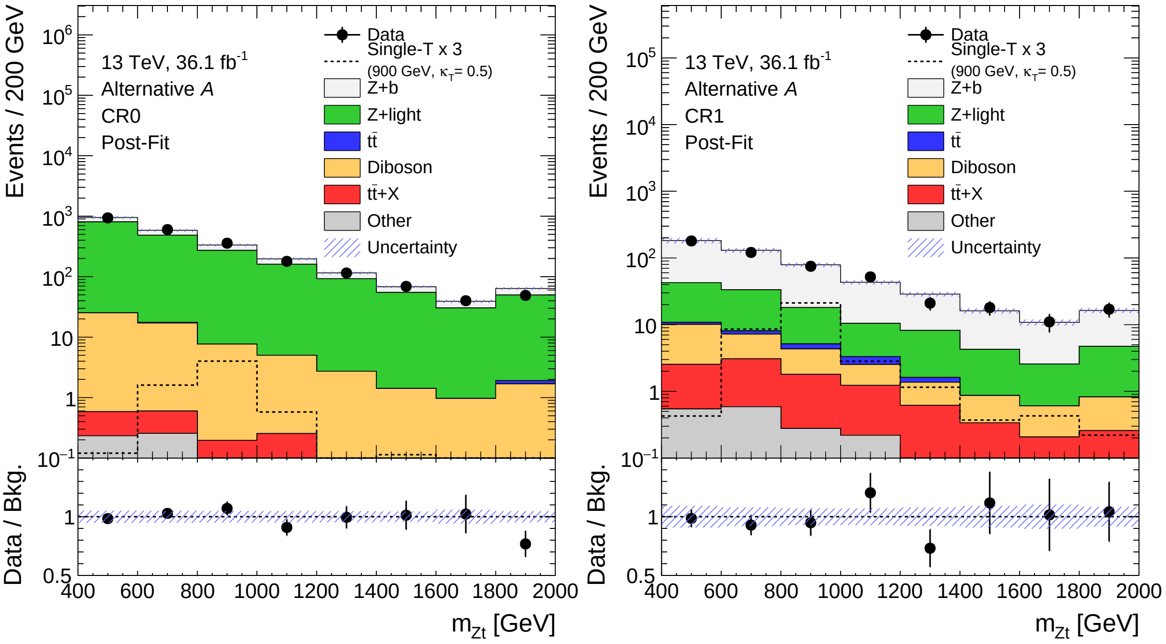

(a) CR0 (b) CR1

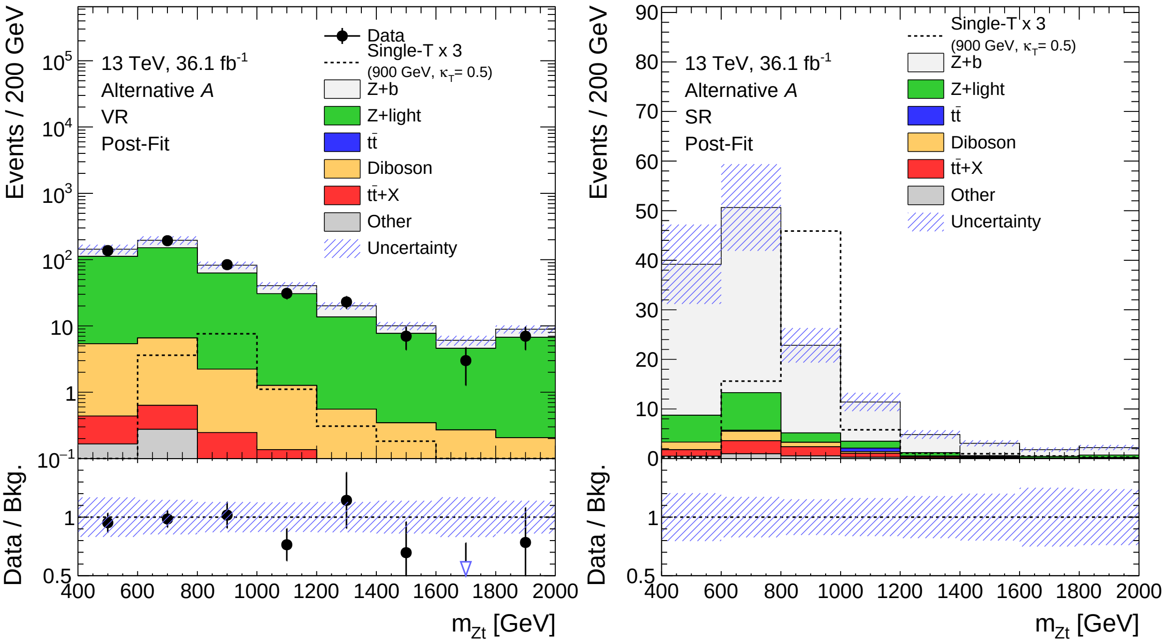

(c) VR (d) SR

Figure 9.10: Data/MC comparison in the CR0(a), CR1(b), VR(c), and MC expectation in the SR(d) after the fitting of alternative A.

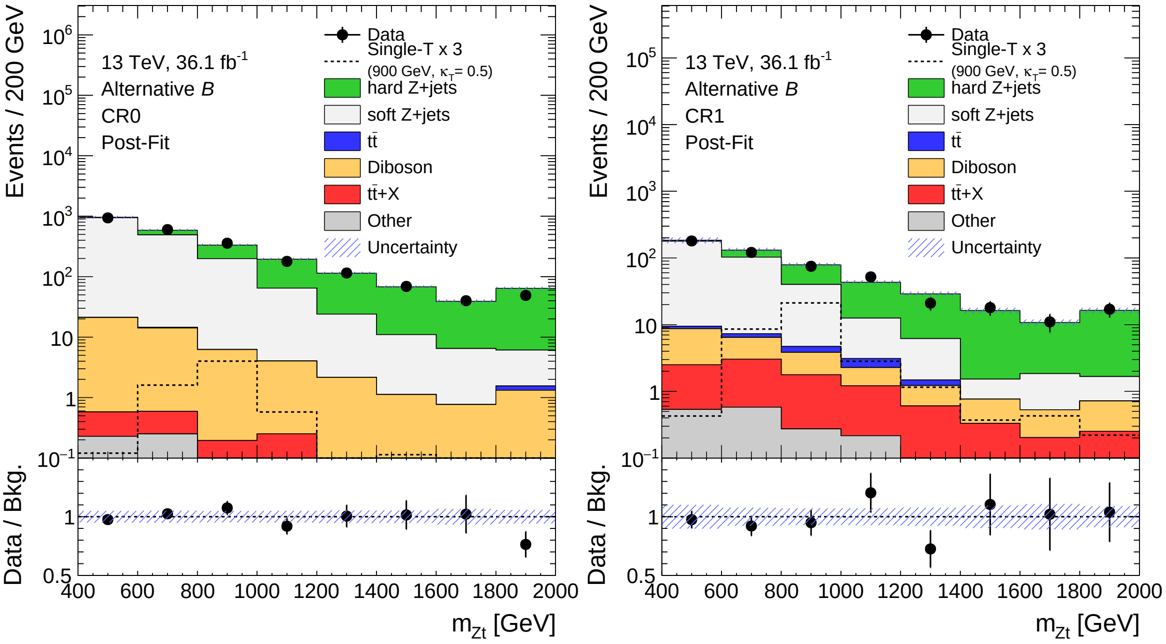

(a) CR0 (b) CR1

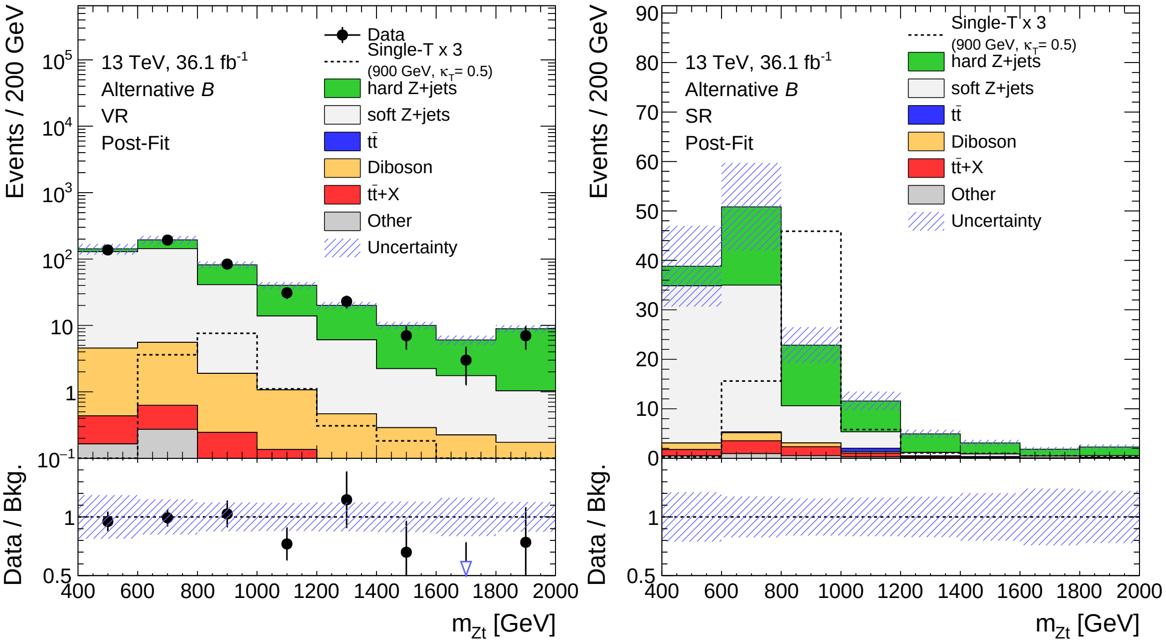

(c) VR (d) SR

Figure 9.11: Data/MC comparison in the CR0(a), CR1(b), VR(c), and MC expectation in the SR(d) after the fitting of alternative *B*.

Chapter 10

Results

After the confirmation of validity and stability in the fitting based on the CRs as discussed in the previous chapter, the SR was fully unblinded to set conclusions using the observed data. First the result of fitting based only on the CRs with null-hypothesis is discussed in Section 10.1, and then the fitting using both the CRs and SR assuming the existence of T is discussed in Section 10.2.

10.1 Null-hypothesis test

In the null-hypothesis test, the nuisance parameters were estimated using only the CRs, hence the background estimation is exactly the same as the results of the nominal fitting described in Section 9.2, which expects 134.8 ± 20.1 background entries in the SR. The observed number of events in the SR is 124, consistent with the background-only estimation.

In terms of the event shape, some discrepancy was observed as summarized in Table 10.1 and visualized in Fig. 10.1. The largest discrepancy between the data and MC was observed in the bin for $1600 < m_{Zt} < 1800$ GeV, where 1.72 ± 0.51 events are expected and 5 events are observed. Details of the observed 5 events are further discussed in Chapter 11. p-value of the null hypothesis, p_0, was computed based on these results according to the procedure discussed in Section 6.3. Global p_0, corresponding to the consistency of the null-hypothesis and the distribution in Fig. 10.1, was found to be 0.79. Local p_0, the p-value computed in each bin, is also considered. The smallest local p_0 of 0.023 corresponding to the significance of 2.0 σ was observed in the bin for $1600 < m_{Zt} < 1800$ GeV. The local p_0 in each SR bin are shown in Fig. 10.2. These results are summarized in Table 10.1. As a result of the null-hypothesis test, no significant excess over 2 σ was observed and concluded that the observed data is consistent with the SM prediction.

10.2 Limit settings

Since no significant excess over the background prediction was observed as discussed in the previous section, the observed data in the SR was compared to the hypothesis of T presence to set upper limits on the production cross section times the branching ratio. In this step, entries in the SR and the CRs are fully used in the fitting. The fitting was performed with all the combinations of the mass and the couplings considered in this analysis. The fitting results with the benchmark sample with the T mass of 900GeV and $\kappa_T = 0.5$ is shown in Fig. 10.3 as an example. The signal strength μ was estimated to be -0.30 ± 0.34 if negative μ was allowed, and $< 10^{-3}$ with the uncertainty of 0.23 if negative μ was forbidden. The cross section times branching ratio was calculated with respect to the combination of all the considered mass

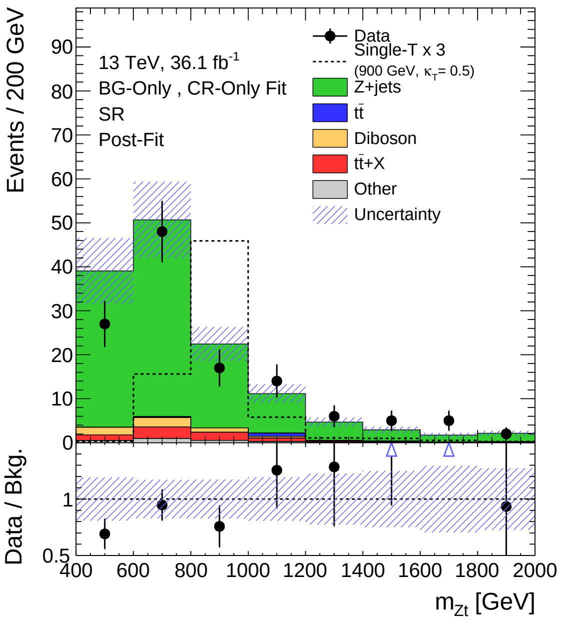

Figure 10.1: Comparison of the distribution of the reconstructed mass between MC expectation based on null-hypothesis and observed data in SR.

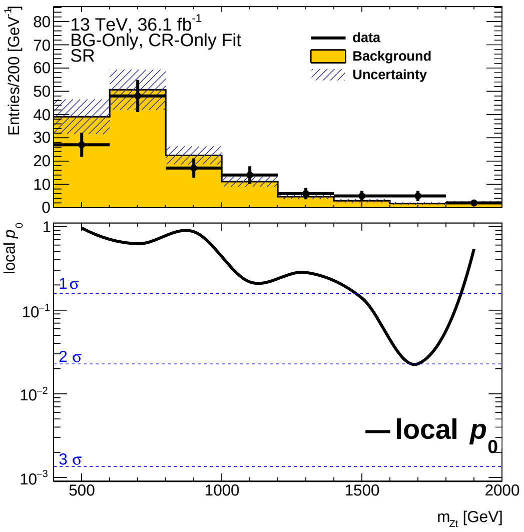

Figure 10.2: Local p_0 computed in each bin of SR.

Table 10.1: Bin-by-bin comparison between MC expectation based on null-hypothesis and observed data in the SR.

Bin in SR	BG estimation	Data	Data/BG	local p_0
$[400, 600]$	39.1 ± 7.5	27	0.69 ± 0.19	0.9
$[600, 800]$	50.7 ± 8.7	48	0.95 ± 0.21	0.62
$[800, 1000]$	22.4 ± 3.9	17	0.76 ± 0.23	0.87
$[1000, 1200]$	11.1 ± 2.2	14	1.26 ± 0.41	0.22
$[1200, 1400]$	4.67 ± 1.06	6	1.29 ± 0.60	0.28
$[1400, 1600]$	2.92 ± 0.73	5	1.70 ± 0.87	0.14
$[1600, 1800]$	1.72 ± 0.51	5	2.90 ± 1.55	0.023
$[1800, 2000]$	2.14 ± 0.59	2	0.93 ± 0.71	0.53
Total	134.8 ± 22.4	124	0.92 ± 0.17	

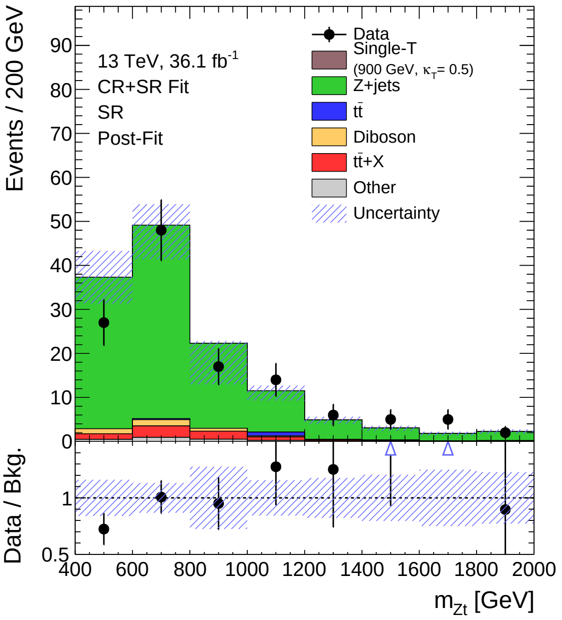

Figure 10.3: Comparison of the distribution of the reconstructed mass between MC expectation after S+B fitting and observed data in the SR. The contribution of T is too small to be seen because the signal strength of best-fit result is as small as $< 10^{-3}$.

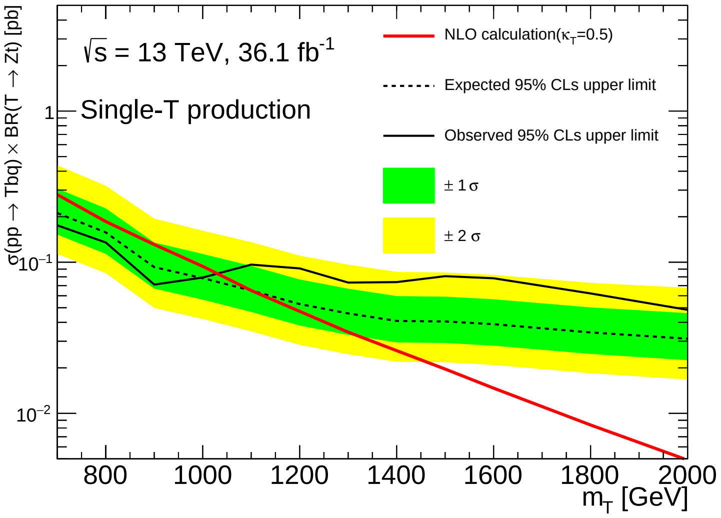

Figure 10.4: One-dimensional limits on the cross section times branching ratio computed based on the benchmark coupling $\kappa_T = 0.5$.

and coupling. The 1-D limit on the benchmark coupling is shown in Fig. 10.4. The observed limit is looser than the expectation in the high mass region of > 1100 GeV because a small excess is observed in data over the MC in the high mass region.

This result leads to limits on the combination of mass and coupling. The expression of c_W, introduced in Eq. 1.62, was chosen to represent the limits on the coupling. Under an assumption that the branching ratio is constant over c_W, the limit can be calculated as shown in Fig. 10.5. However, in the singlet model, the branching ratio indirectly depends on c_W because both c_W and c_Z are functions of the mixing parameter θ^u_L introduced in Eq. 1.54, which is referred to as θ_L for simplicity here because the down-type VLQs do not appear in this analysis. According to the discussion in Section 1.2.2, c_W and c_Z can be written as $c_W = \sqrt{2}|\sin\theta_L|$ and $c_Z = \frac{m_Z}{m_W}|\sin\theta_L\cos\theta_L|$ in the singlet model and the small production cross section is realized in the region of small $|\sin\theta_L|$ while small branching ratio of $T \to Zt$ is realized in the region of large $|\sin\theta_L|$. Thus the upper and lower limit can be set as Fig. 10.6. As results of the 2-dimensional limit, the upper limit on coupling c_W is $\sim$0.4 in low mass ($<$ 900 GeV) and increases to $\sim$3 on $\sim$ 2000GeV T and the limit of $\sin\theta_L$ is observed in $<$ 1200 GeV.

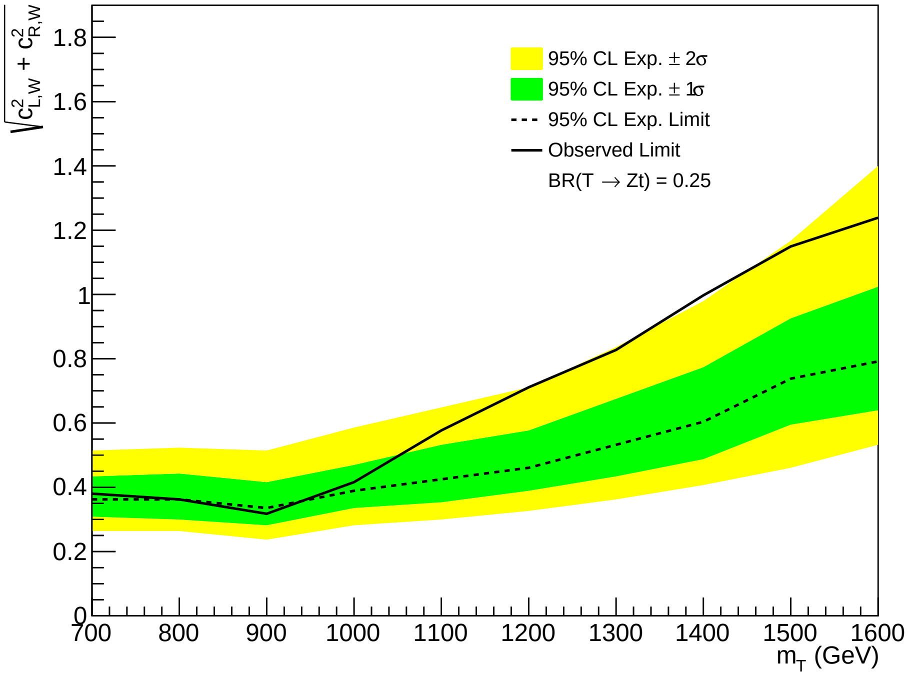

Figure 10.5: Observed and expected upper limit of c_W as a function of T mass.

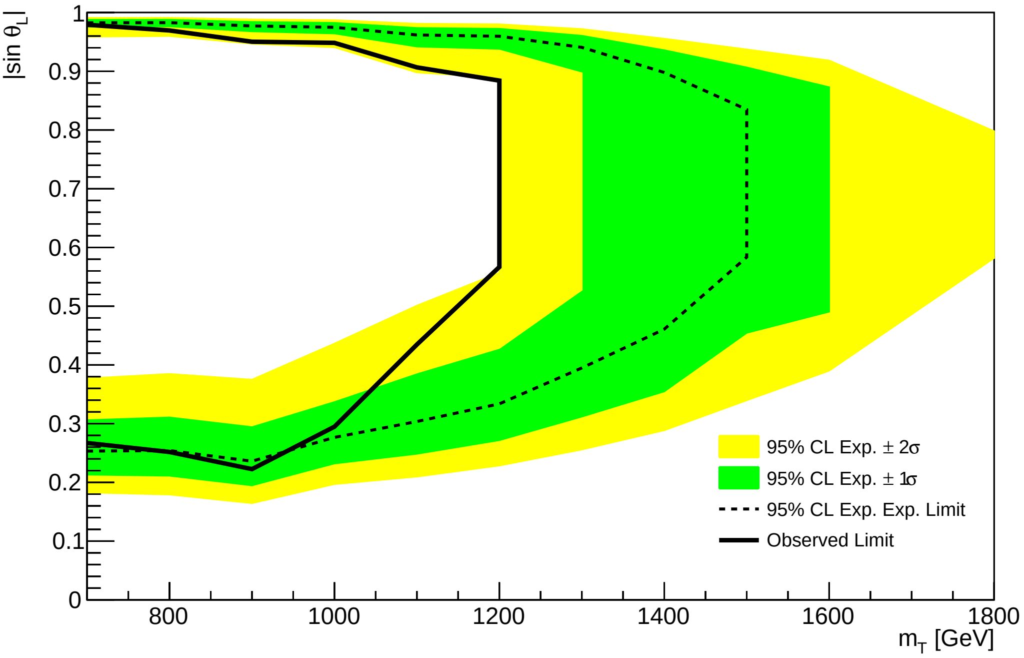

Figure 10.6: Limit of the mixing angle θ_L as a function of T mass, set on the mass region of lighter than 1200 GeV.

Chapter 11

Discussions

11.1 Observed events in the large m_{Zt} bin

As discussed in the previous chapter, 5 events were observed in the SR in the bin for $1600 < m_{Zt} < 1800$ GeV while only 1.72 ± 0.51 background events were expected. The local significance of this excess is 2.0 σ, which is too small to claim discovery nor evidence. Since 1800 GeV is too heavy to solve the hierarchy problem, this excess is not expected to be the signal of T. However, it is still possible that it reflects something beyond SM.

The general property of the 5 events are summarized in Table 11.1, which includes the run number, date, average pileup $< \mu >$, the instantaneous luminosity, reconstructed mass of Zt system, and the decay mode of Z.

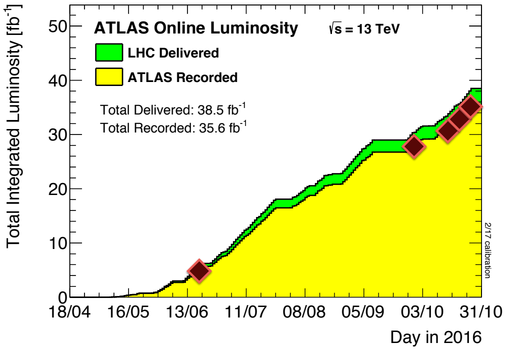

Figure 11.1: The total luminosity as a function of date. The brown diamonds indicate the date of 5 events.

All the 5 events were observed in 2016 and 4 of them were in October, the period when LHC was operated with the largest luminosity in 2015 and 2016. Hence, one can presume that the environment of the large instantaneous luminosity affected something to enhance the probability for the events to be observed in the large m_{Zt} bin in the SR. However, the instantaneous luminosity and $< \mu >$ were not extremely large compared to the usual settings of LHC in 2016 as can be seen in Fig. 11.2, thus the excess cannot be explained by unknown effects from the large instantaneous luminosity so far.

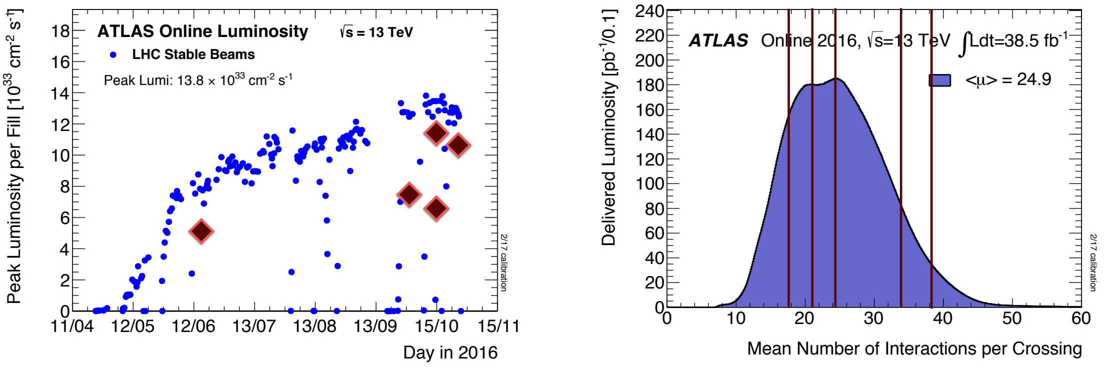

(a) Peak luminosity delivered to ATLAS by LHC as a function of date during 2016. The brown diamonds indicate the instantaneous luminosity of the timing when the 5 observed events were recorded.

(b) Distribution of the average pileup $< \mu >$ recorded in 2016. The brown lines indicate $< \mu >$ of the 5 observed events.

Figure 11.2: LHC parameters for the observed 5 events in the distribution of whole the 2016 events.

Table 11.1: The general information of the observed 5 events. Inst. Lumi indicates the instantaneous luminosity $[10^{33}\ \mathrm{cm}^{-2}\mathrm{s}^{-1}]$ and mode indicates the decay mode of Z boson.

Run num.	Date	$< \mu >$	Inst. Lumi	m_{Zt} [GeV]	Mode
302053	15th June 2016	17.6	5.2	1665	$\mu^+\mu^-$
309674	1st October 2016	24.3	7.7	1742	e^+e^-
310691	16th October 2016	38.6	11.4	1660	$\mu^+\mu^-$
310691	16th October 2016	20.7	6.3	1698	e^+e^-
311402	25th October 2016	34.0	10.6	1609	$\mu^+\mu^-$

All the reconstructed objects in the events were scanned to take a closer look. Fig. 11.3 is an event display showing the reconstructed leptons and large-R jets in the Event 860188556 in Run 310691 as an example of the observed events. The upper part of the event display is the cross section of the x-y plane and the lower is of the z-y plane. The property of reconstructed objects considered in this analysis are listed in Table 11.2. The opposite sign muons were identified as the decay products of a Z with the kinematic property of m_Z =95.8 GeV, p_T =891.8 GeV, $\eta = -0.94$, and ϕ =2.51 . In terms of the kinematics in the x-y plane, $\Delta\phi$ between the direction of the Z boson and the top-jet is 3.07, quite close to back-to-back. The Z boson and the top-jet were used to reconstruct T with m_T = 1659.6 GeV, p_T =194.1 GeV, η =-2.71, and ϕ =2.78. Remaining 4 events are discussed in Appendix D.

Table 11.2: Properties of the reconstructed objects in Run 310691, Event 860188556. The mass is not assigned to the small-R jets.

Object	p_T or E_T [GeV]	η	ϕ	mass [GeV]	other information
μ^+	156.4	-1.11	2.36	0.11	-
μ^-	737.6	-0.90	2.54	0.11	-
large-R jet	707.4	-0.64	-0.70	252.6	top-tagged
small-R jet	82.6	-0.36	-0.04	-	b-tagged
small-R jet	62.5	-2.5	3.07	-	forward jet
small-R jet	637.9	-0.69	-0.80	-	-
small-R jet	74.4	0.15	-0.38	-	-
small-R jet	63.6	0.17	0.53	-	-
small-R jet	31.3	1.25	0.16	-	-
T	194.1	-2.71	2.78	1659.6	-

11.2 Comparison with pair production analyses in ATLAS

T, vector-like quark with the electric charge of $+2/3$, was searched for with other channels as well in ATLAS. One of the channels is a search for pair production, referred to as "$T\bar{T}$", using the dilepton pair as the decay products of Z. The object reconstruction and the acceptance in the requirement for the Z boson mass are the same among the single production and $T\bar{T}$ analyses.

To achieve large acceptance with respect to various event topology of $T\bar{T}$, the analysis was performed with 3 channels fully orthogonal to one another. The first channel is "2ℓ+0-1J", which requires exactly 2 leptons and 0 or 1 large-R jets reconstructed in an event. This channel is sensitive to the low mass T, whose decay products are not boosted enough to be reconstructed as a single large-R jet. The second is "$2\ell+\geq 2$J", which requires exactly 2 leptons and more than 1 large-R jets, sensitive to the high mass T, whose decay products are boosted enough to be reconstructed as large-R jets. The last one is "$\geq 3\ell$", which requires more than 2 leptons to be sensitive to events containing leptonically decaying particles such as $W \to l\nu$. The target topology of each channel is sketched in Fig. 11.4.

Among all the channels, background-enriched CRs were constructed to estimate and constrain the uncertainty, and signal-enriched SRs to estimate the contribution of the $T\bar{T}$ events. The statistical analysis was performed according to the discussion in Section 6.3. No significant excess was observed in any of the SRs in the 3 channels after fitting.

The upper limit on the cross section of $T\bar{T}$ was computed with 95% CL based on these results, excluding singlet T with mass below 1030 GeV, as displayed in Fig. 11.5. The coupling c_W or the mixing angle $\theta_{L,R}$ were not taken into account in the $T\bar{T}$ analysis because they do not affect the tree-level production cross section of $T\bar{T}$. Comparing with this result, the single production analysis(Fig. 10.6) successfully set limits on larger m_T while the limit is valid only in restricted range of the mixing angle.

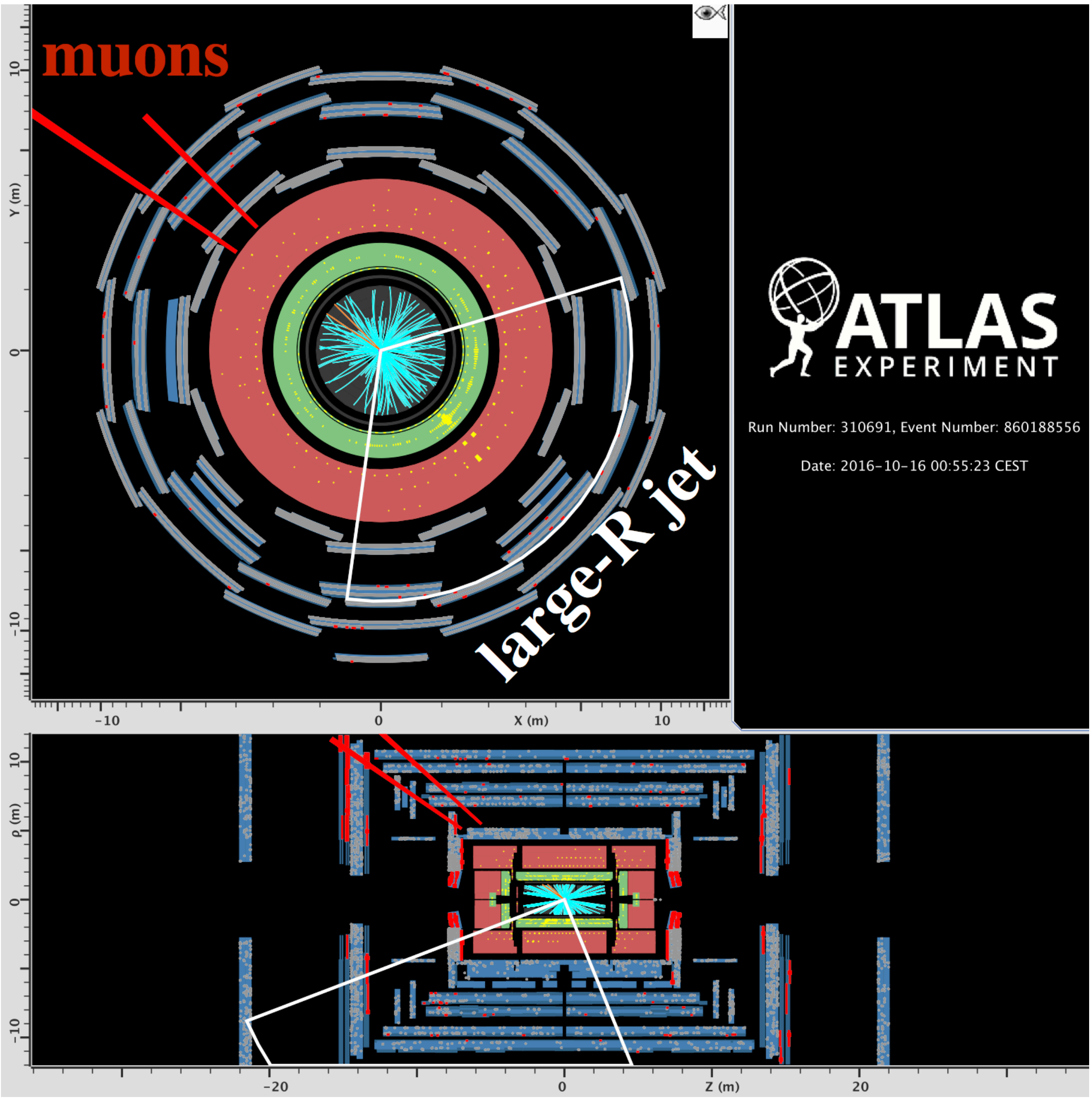

Figure 11.3: An event display of Run number 310691, Event Number 860188556, one of the events observed in the large m_{Zt} bin in the SR. The upper plot is the cross section in the x-y plane and the lower is in the z-y plane.

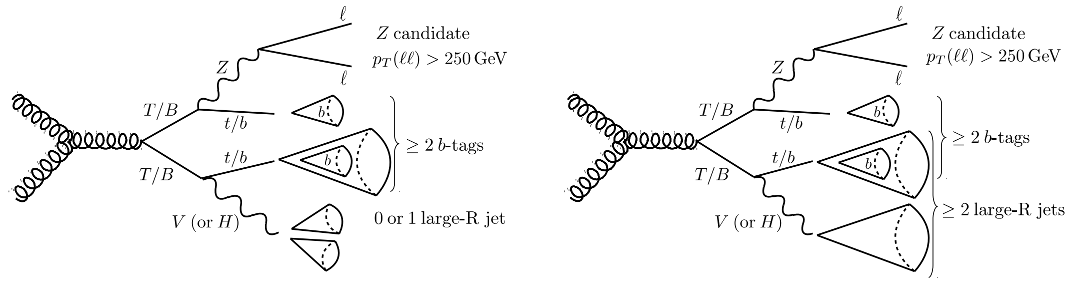

(a) 2ℓ+0-1J channel

(b) $2\ell+\geq$2J channel

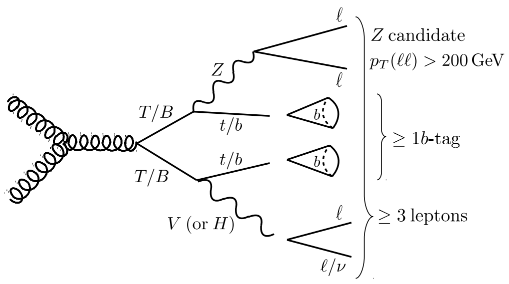

(c) $\geq 3\ell$ channel.

Figure 11.4: Diagrams of events each analysis channel is sensitive to.

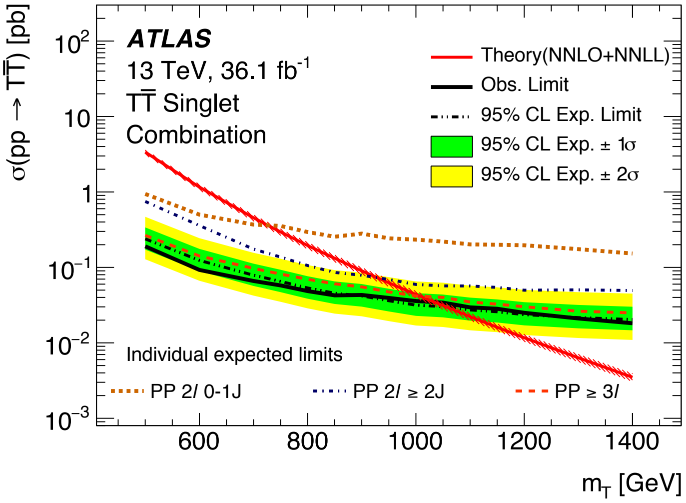

Figure 11.5: A limit on cross section set by the $T\bar{T}$ analysis.

Chapter 12

Conclusions

The search for the vector-like quark with the charge +2/3, referred to as T, was reported through this thesis. The analysis was performed based on the LHC pp collision data of $\sqrt{s} = 13$ TeV recorded during 2015 and 2016, corresponding to the integrated luminosity of 36.1 fb^{-1}.

The search was focused on the single production of T because larger production cross section is possible in searchable mass region compared to the pair production. The analysis strategy was optimized to search for $T \rightarrow Zt$ decay channel in which Z decays into $e^{+}e^{-}$ or $\mu^{+}\mu^{-}$ and t decays hadronically because requirements on leptons and top-quark are promising in terms of background suppression. One of the feature of this analysis is the usage of boosted top tagger algorithm to identify top quarks with high momenta. This algorithm had not been used in the previous analysis in Run1 because it had not been sensitive to low mass T, but it was effective in the mass region searched for in this thesis.

In the analysis, two control regions (CRs), one validation region (VR), and one signal region (SR) were defined based on the presence of top-jets, b-jets, and forward jets. The CRs were defined to contain large amounts of background events whose kinematic properties were close to the SR so that the systematic uncertainty on the SR was able to be estimated and constrained. The observed data in the SR was masked until the validation and optimization of fitting procedure based on the CRs were complete.

After unblinding, the observed events in the SR was compared to background estimation. In the SR, 124 events were observed in total while the background estimation was 134.8 ± 22.4. The observed data is consistent with the MC estimation in terms of both event yields and event shapes. The p-value of null hypothesis, p_0, was estimated to be 0.79 and the most significant local p_0 was 0.023, equal to the significance of approximately 2 σ.

Fitting was performed with signal presence hypothesis as well to set limits on $\sigma(\mathrm{single}T) \times BR(T \rightarrow Zt)$ at 95 % confidence level. As results, the upper limit on the coupling c_W was set in all the considered mass region and upper and lower limit on the mixing angle θ_L was set in the region with $m_T < 1200$ GeV. This extended the excluded region of T mass and mixing where the Higgs hierarchy problem can be naturally solved.

APPENDIX A

Contamination of VLQ pair production events

T can be produced via the pair production($T\bar{T}$) channel as well as the single production channel. Since the target of this analysis is the single production, the SR selection described in Section 6.2 contains two requirements in order to minimize the contamination of $T\bar{T}$.

One is the forward jet selection, which requires at least one forward jet. As shown in Fig.A.1, it reduces the $T\bar{T}$ events which pass the SR selections except for the forward jet selection by ∼75 % while the efficiency of the single production events is ∼60 %. This selection is applied to the SR and VR.

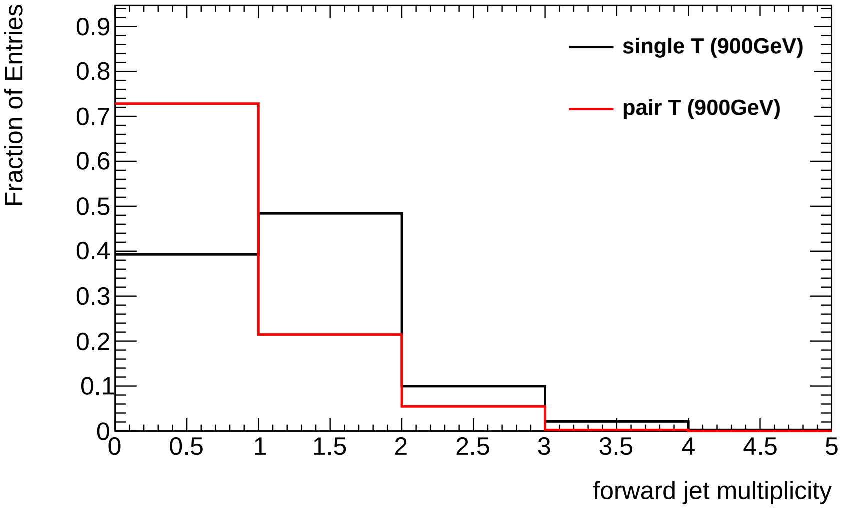

Figure A.1: The forward jet multiplicity of the VLQ pair and single production events.

Another selection is the $H_T + E_T^{miss}$ selection, which requires that $H_T + H_T^{miss}$ is smaller than the reconstructed T mass, where H_T is the scalar sum of the jets p_T. Since the $T\bar{T}$ events contain two massive particles, the total energy of their decay products tend to be larger than the single T mass. The 2D (T mass, $H_T + E_T^{miss}$) distribution of VLQ single and pair production events are shown in Fig.A.2. The acceptance of the selection w.r.t. the other SR selection is nearly constant over the VLQ mass in both the pair and single production cases: ∼20% for pair production and ∼90% for the single production events as shown in Fig.A.3.

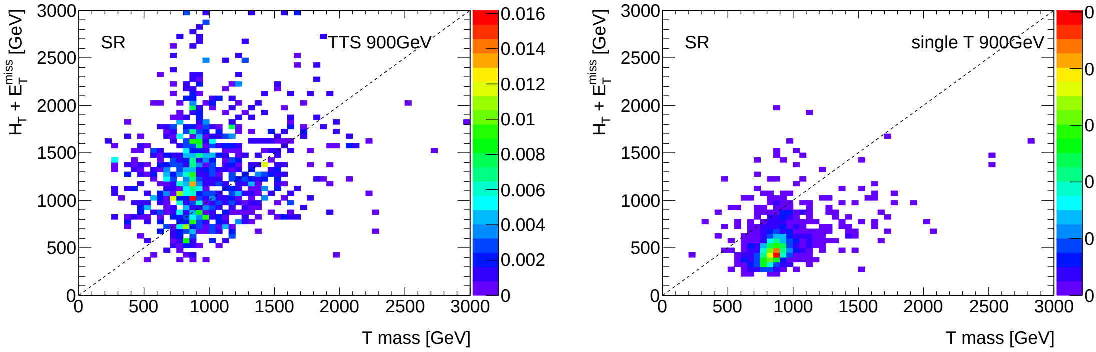

(a) (T mass, $H_T + E_T^{miss}$) 2D distribution of $T\bar{T}$ events.

(b) (T mass, $H_T + E_T^{miss}$) 2D distribution of T single production events.

Figure A.2: (T mass, $H_T + E_T^{miss}$) 2D probability distribution of VLQ pair(a) and single(b) production events in the SR. MC samples of 900GeV T are used to generate these plots.

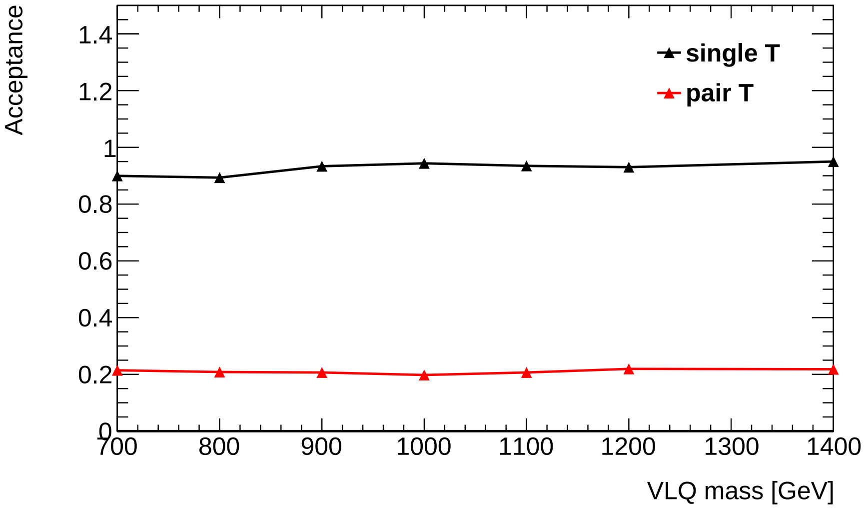

Figure A.3: The acceptance of the $H_T + E_T^{miss}$ selection w.r.t. the SR selection of the VLQ pair and single production events. The acceptance of $\sim$ 90% and $\sim$20% are expected for the single and pair production events, respectively.

APPENDIX B

Data/MC plots

The Data/MC comparison plots of various kinematic distribution are listed here. These distributions are not used in the fitting.

B.1 Pre-fit

Data/MC comparison plots in the pre-fit level are shown in this chapter. The distribution of Z p_T(Fig.B.1), large-R jets p_T(Fig.B.2), large-R jets mass(Fig.B.3), electrons p_T(Fig.B.4), muons p_T(Fig.B.5), and $\Delta\phi$ between the reconstructed Z and top candidate(Fig.B.6) are considered.

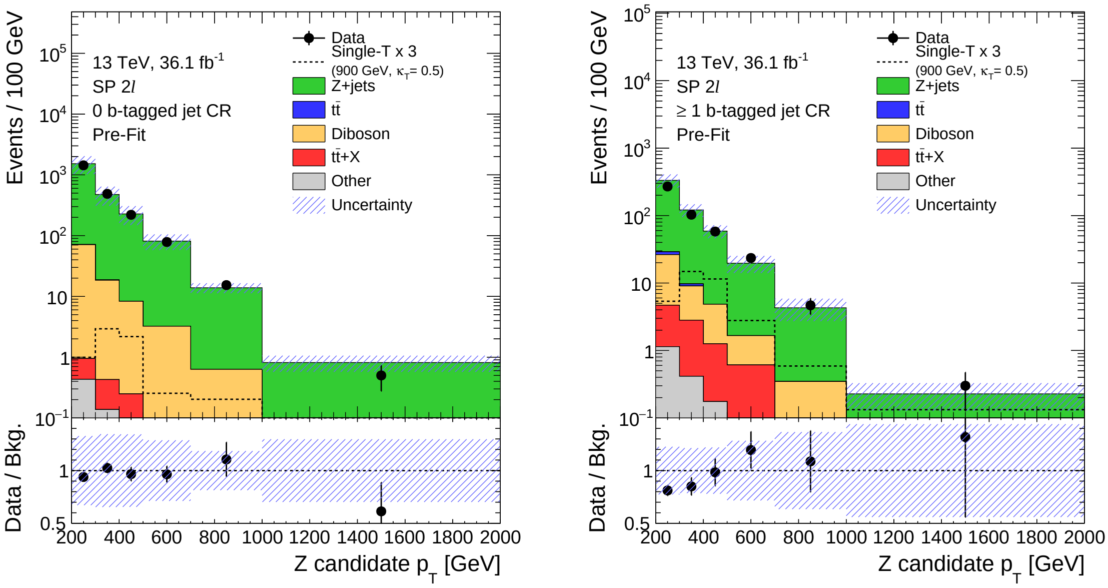

(a) Data/MC comparison in the 0b0t CR (b) Data/MC comparison in the b0t CR

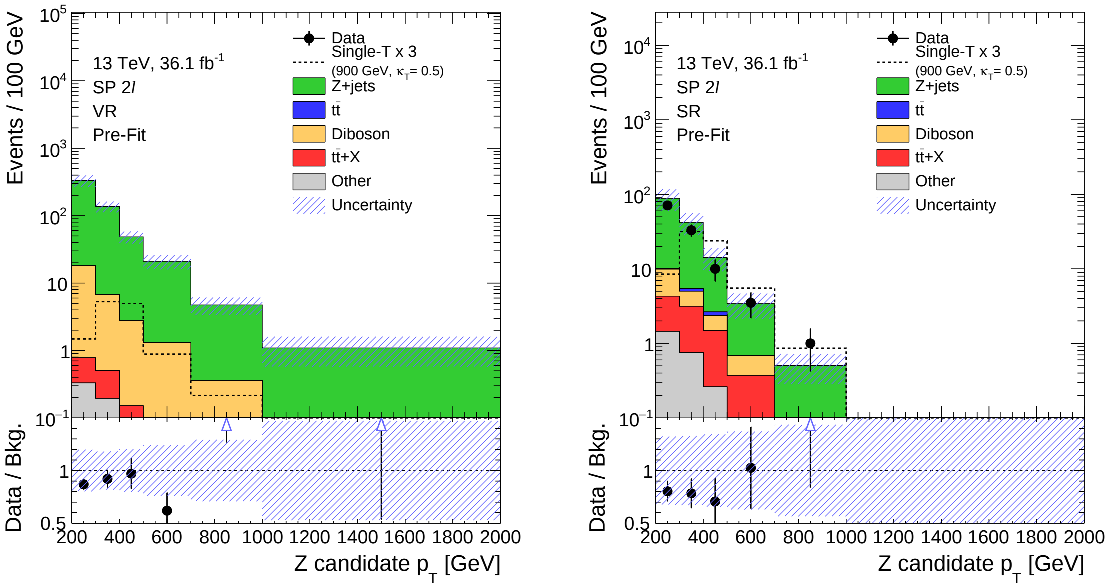

(c) Data/MC comparison in the VR (d) Data/MC comparison in the SR

Figure B.1: Data/MC comparison(before fitting) of the reconstructed Z p_T distribution in the 0b0t CR(a), b0t CR(b), VR(c), and SR(d).

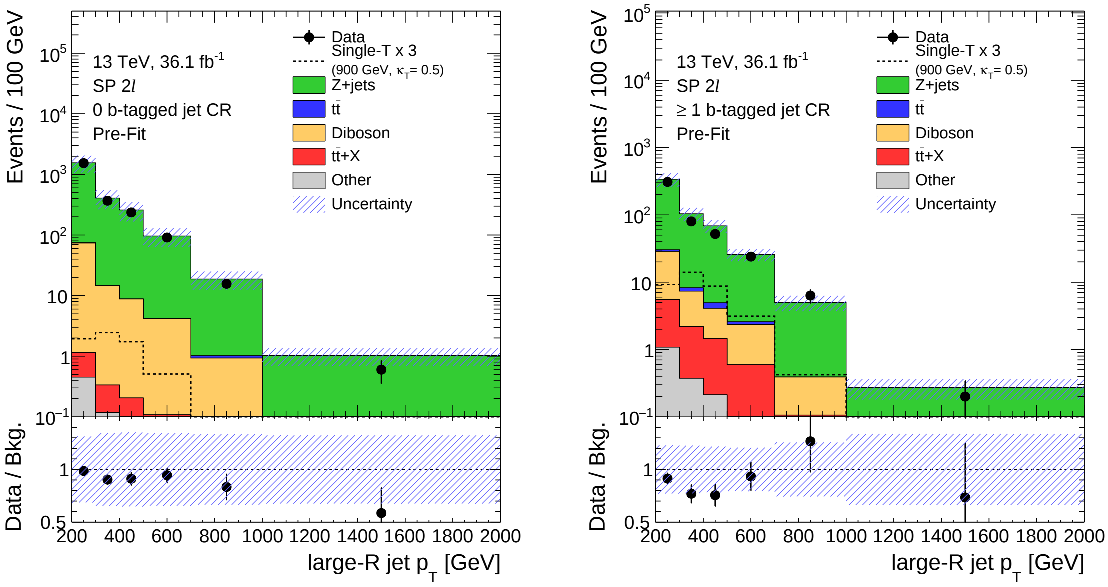

(a) Data/MC comparison in the 0b0t CR (b) Data/MC comparison in the b0t CR

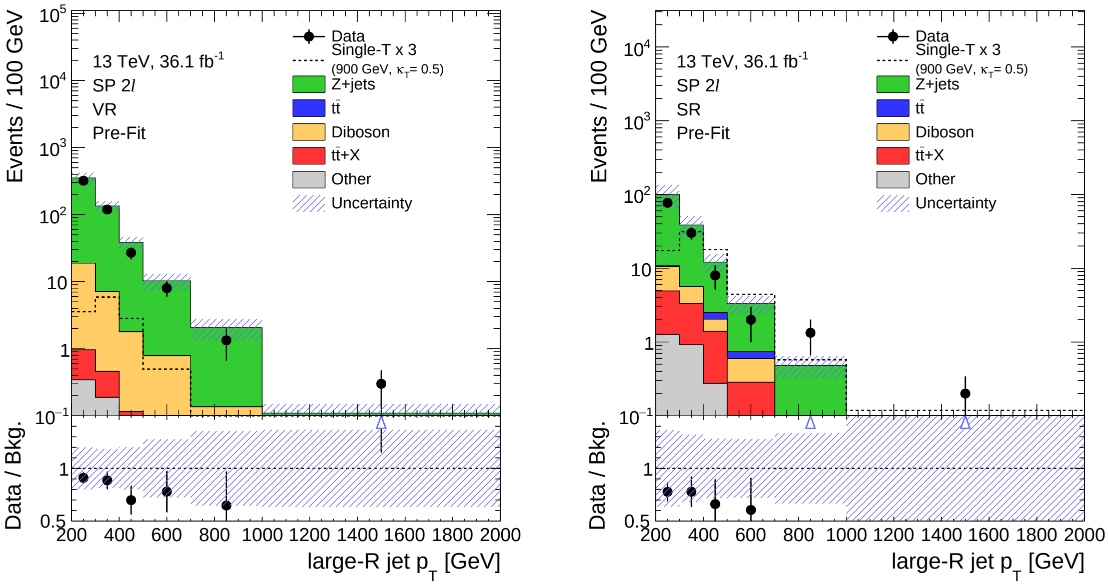

(c) Data/MC comparison in the VR (d) Data/MC comparison in the SR

Figure B.2: Data/MC comparison(before fitting) of the reconstructed large-R jet p_T distribution in the 0b0t CR(a), b0t CR(b), VR(c), and SR(d).

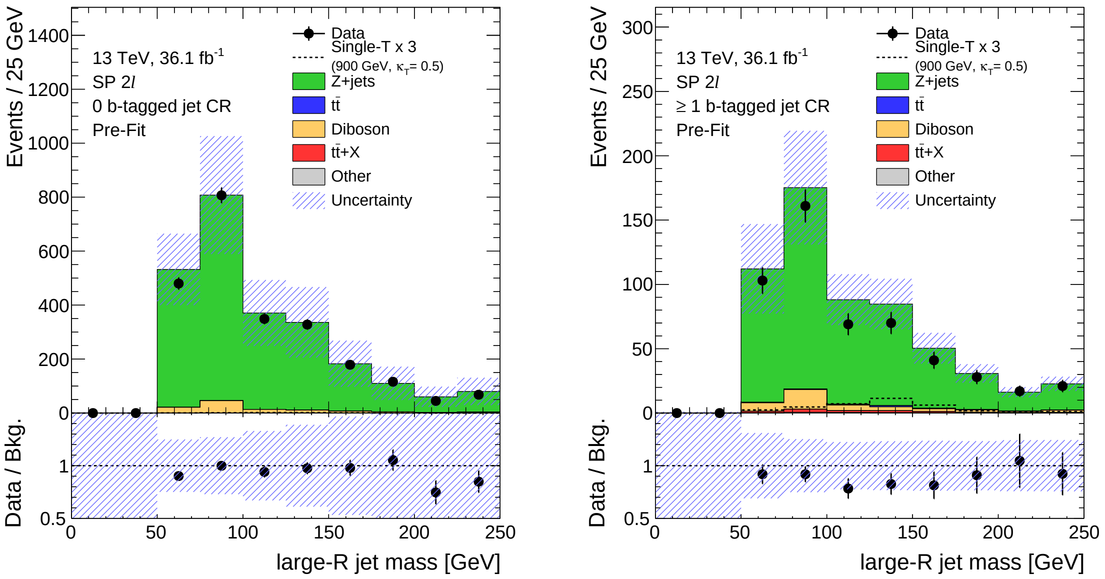

(a) Data/MC comparison in the 0b0t CR (b) Data/MC comparison in the b0t CR

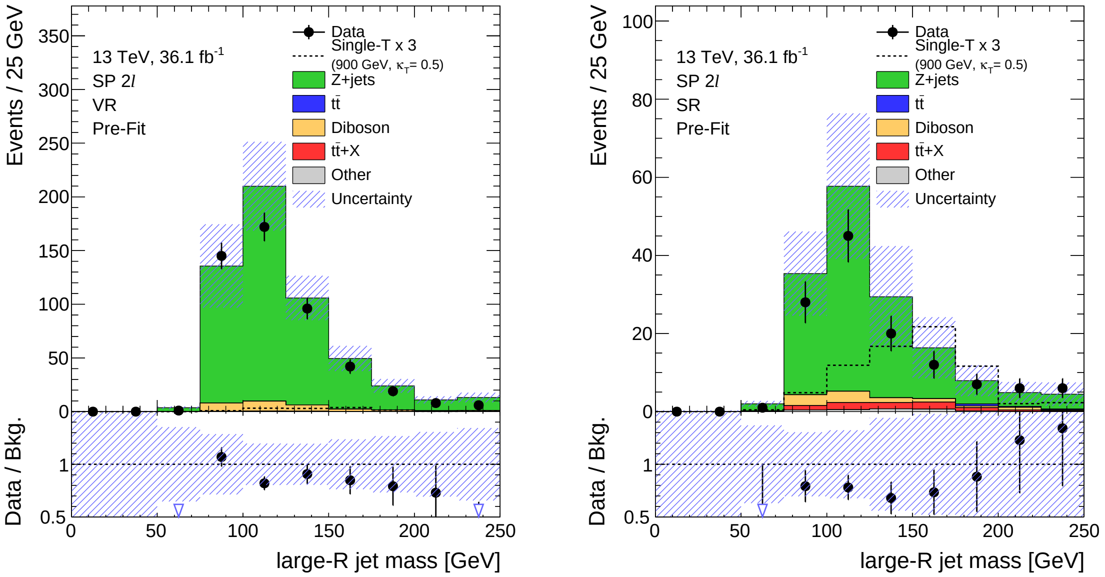

(c) Data/MC comparison in the VR (d) Data/MC comparison in the SR

Figure B.3: Data/MC comparison(before fitting) of the reconstructed large-R jet mass distribution in the 0b0t CR(a), b0t CR(b), VR(c), and SR(d).

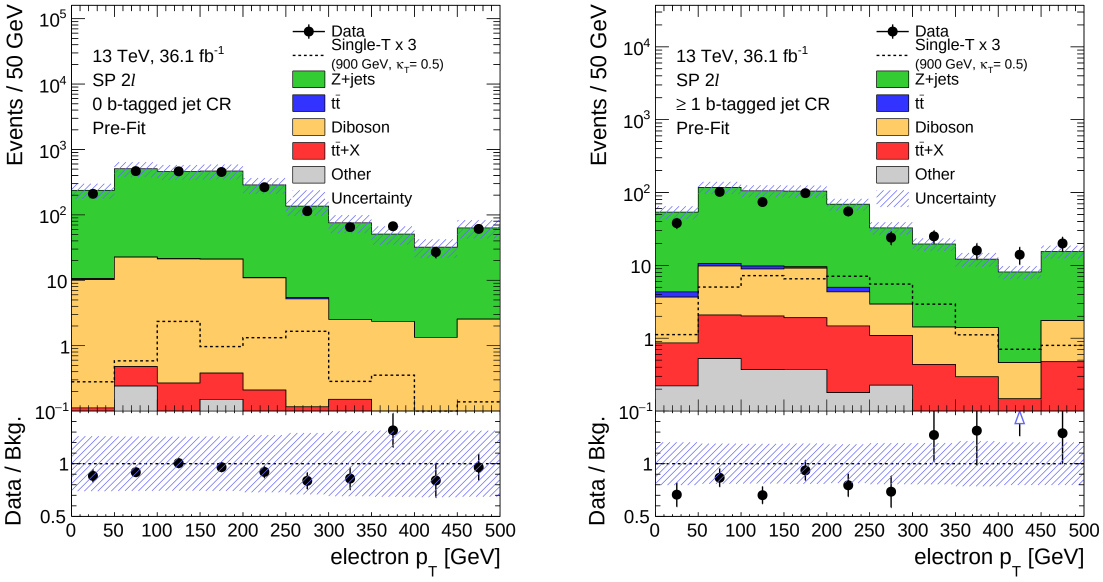

(a) Data/MC comparison in the 0b0t CR (b) Data/MC comparison in the b0t CR

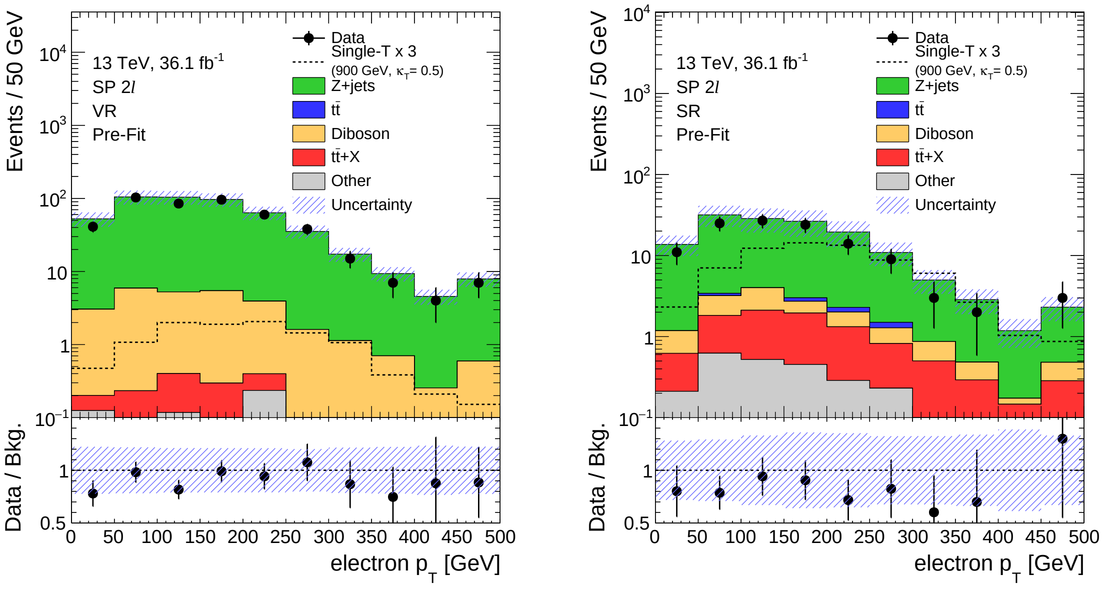

(c) Data/MC comparison in the VR (d) Data/MC comparison in the SR

Figure B.4: Data/MC comparison(before fitting) of the reconstructed electron p_T distribution in the 0b0t CR(a), b0t CR(b), VR(c), and SR(d).

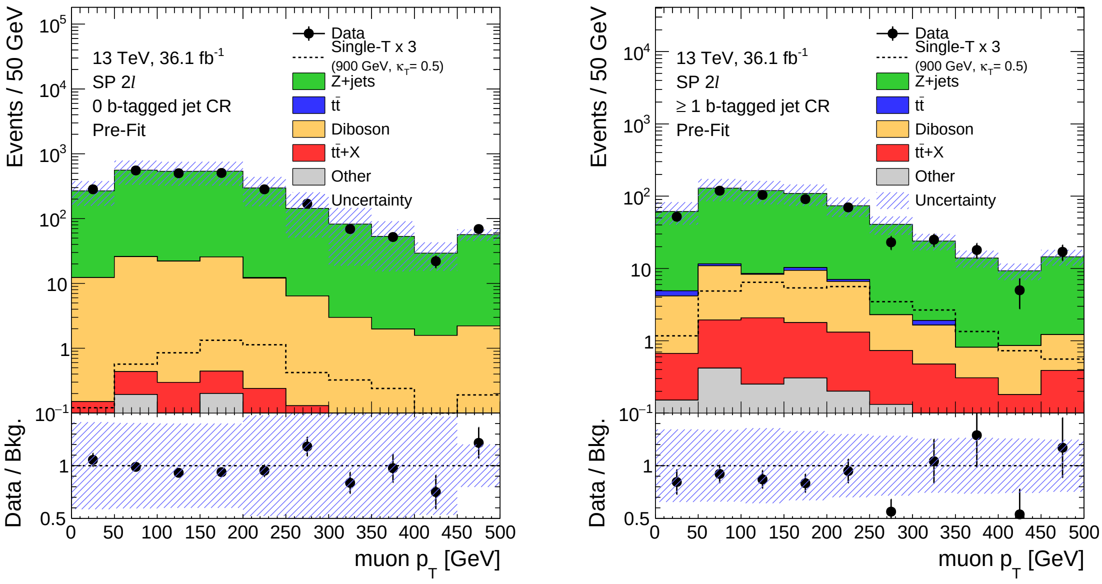

(a) Data/MC comparison in the 0b0t CR

(b) Data/MC comparison in the b0t CR

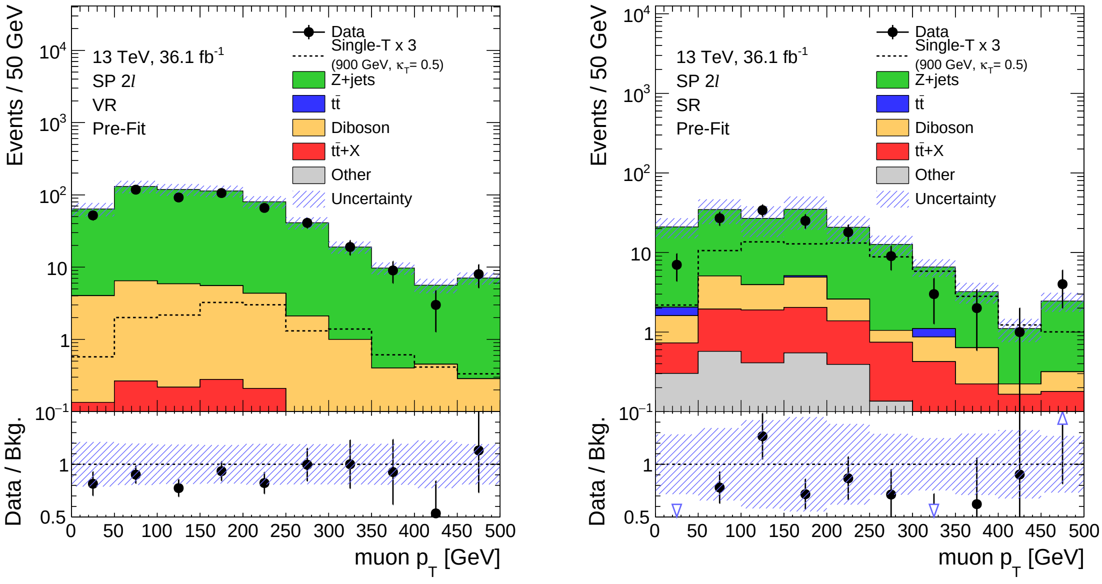

(c) Data/MC comparison in the VR

(d) Data/MC comparison in the SR

Figure B.5: Data/MC comparison(before fitting) of the reconstructed muon p_T distribution in the 0b0t CR(a), b0t CR(b), VR(c), and SR(d).

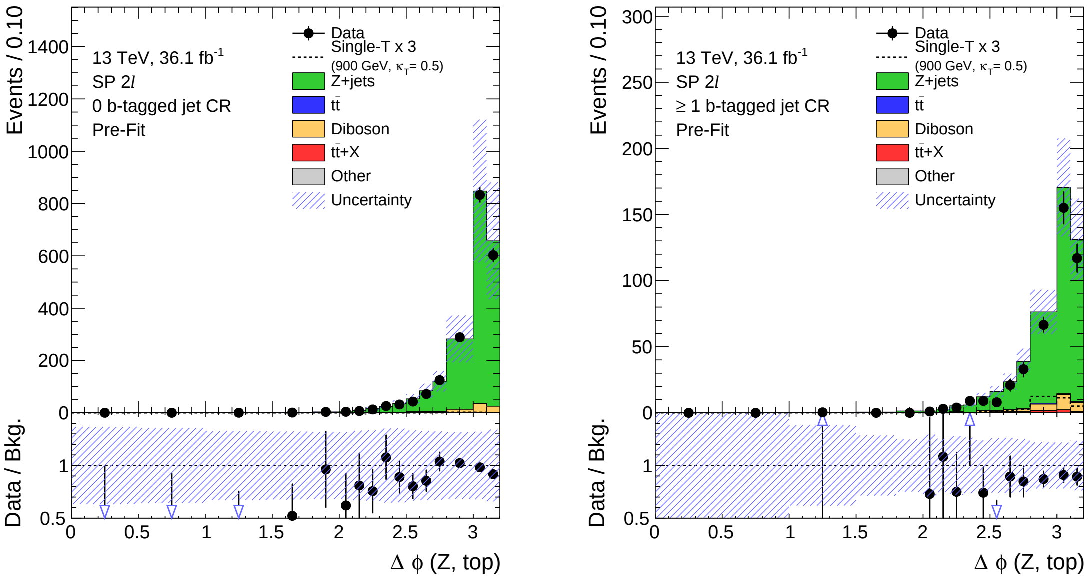

(a) Data/MC comparison in the 0b0t CR (b) Data/MC comparison in the b0t CR

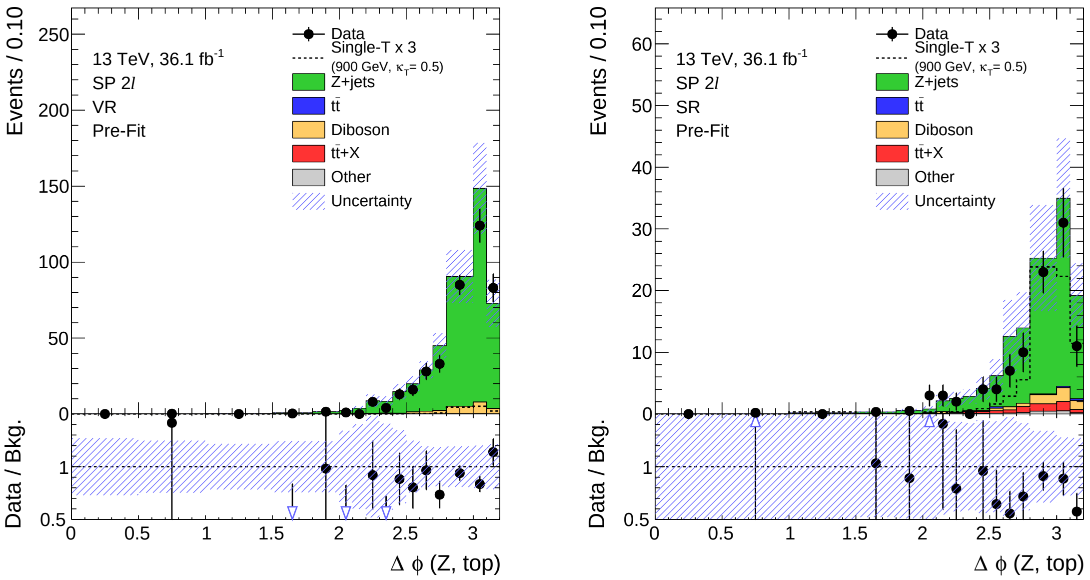

(c) Data/MC comparison in the VR (d) Data/MC comparison in the SR

Figure B.6: Data/MC comparison(before fitting) of $\Delta\phi$ between the reconstructed Z and top candidate distribution in the 0b0t CR(a), b0t CR(b), VR(c), and SR(d).

B.2 Post-fit

Data/MC comparison plots in the post-fit level are shown in this chapter. The distribution of Z p_T(Fig.B.7), large-R jets p_T(Fig.B.8), large-R jets mass(Fig.B.9), electrons p_T(Fig.B.10), muons p_T(Fig.B.11), and $\Delta\phi$ between the reconstructed Z and top candidate(Fig.B.12) are considered.

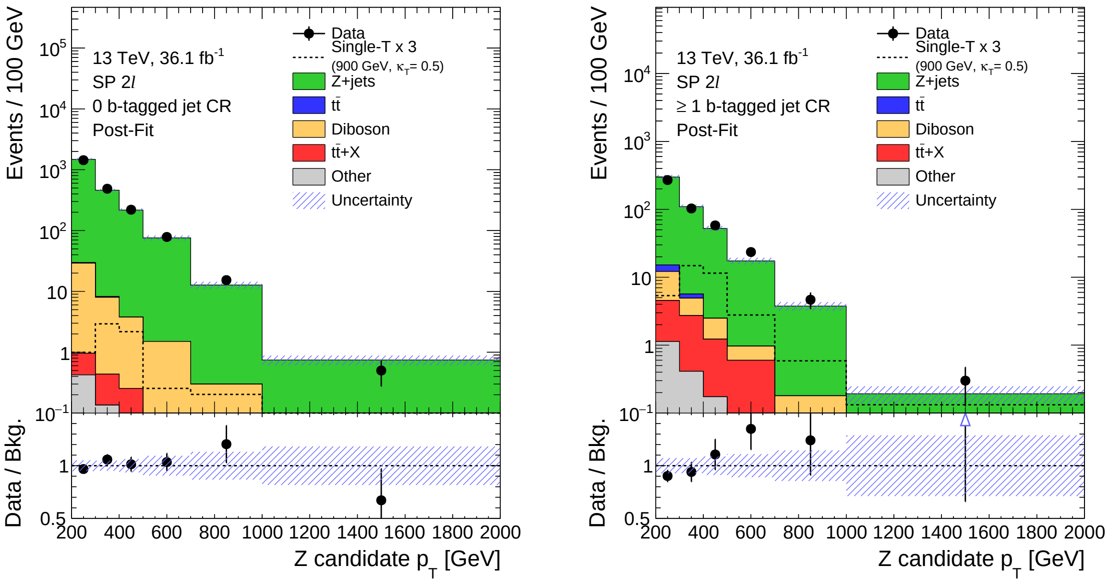

(a) Data/MC comparison in the 0b0t CR

(b) Data/MC comparison in the b0t CR

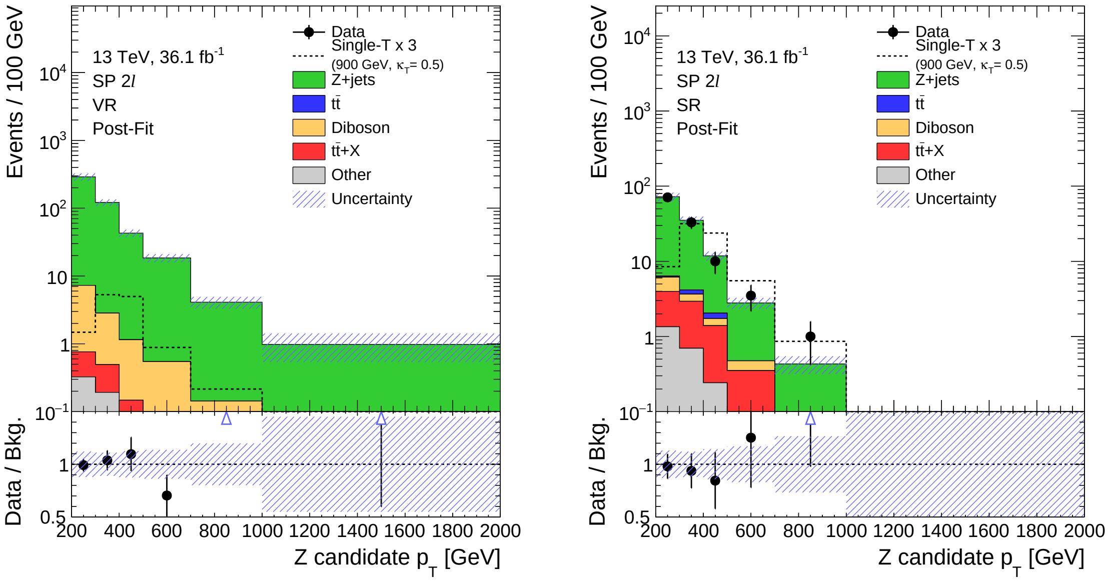

(c) Data/MC comparison in the VR

(d) Data/MC comparison in the SR

Figure B.7: Data/MC comparison(after fitting) of the reconstructed Z p_T distribution in the 0b0t CR(a), b0t CR(b), VR(c), and SR(d).

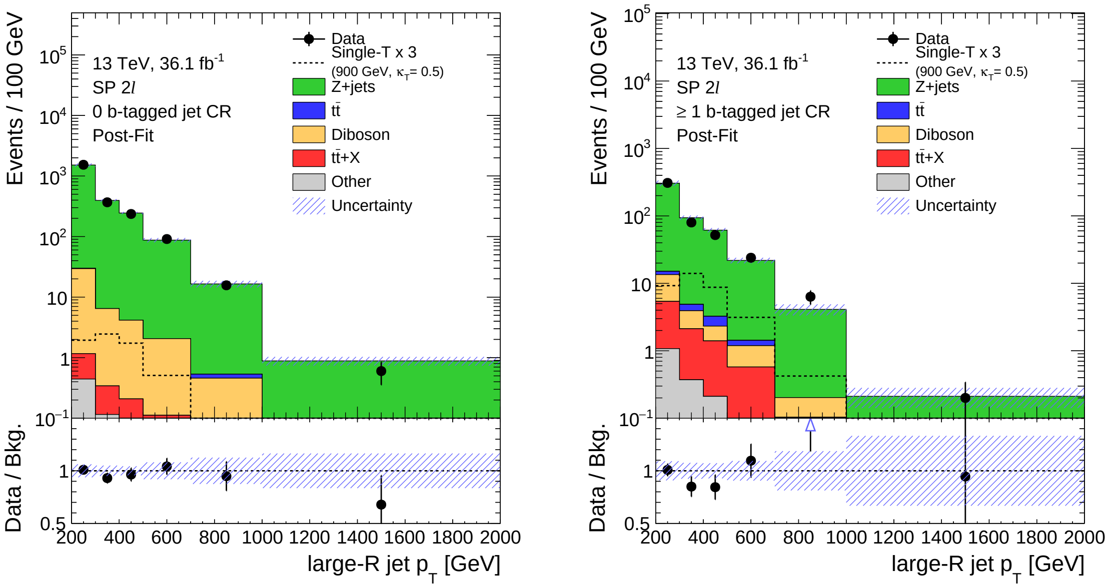

(a) Data/MC comparison in the 0b0t CR

(b) Data/MC comparison in the b0t CR

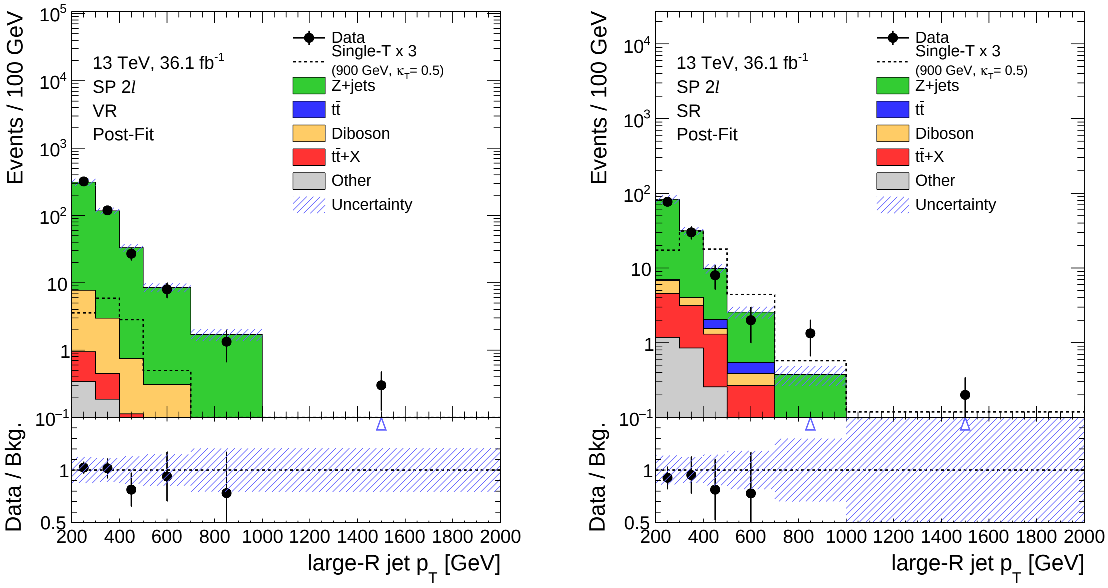

(c) Data/MC comparison in the VR

(d) Data/MC comparison in the SR

Figure B.8: Data/MC comparison(after fitting) of the reconstructed large-R jet p_T distribution in the 0b0t CR(a), b0t CR(b), VR(c), and SR(d).

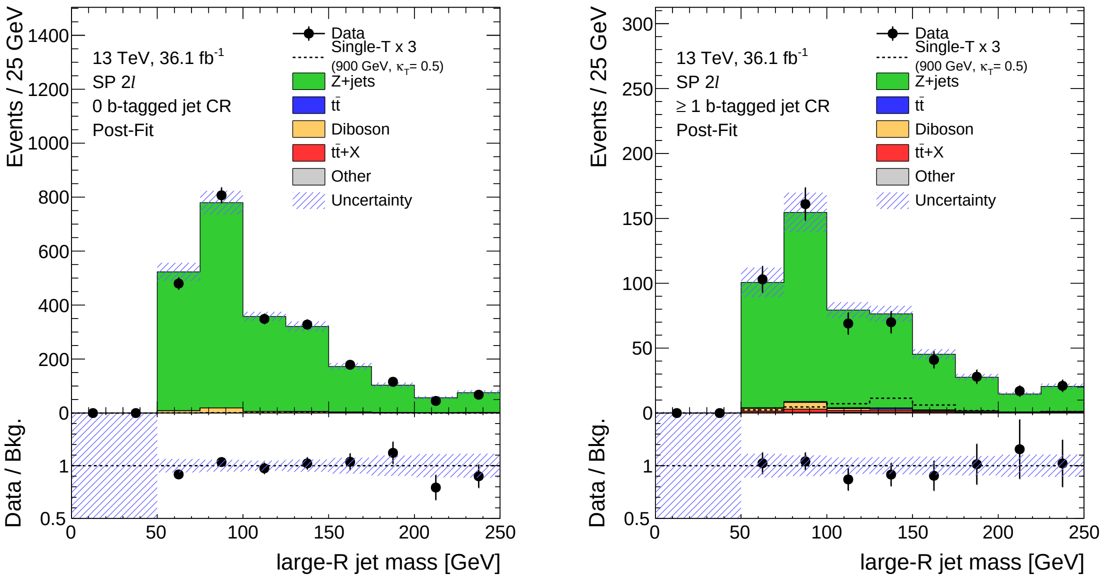

(a) Data/MC comparison in the 0b0t CR

(b) Data/MC comparison in the b0t CR

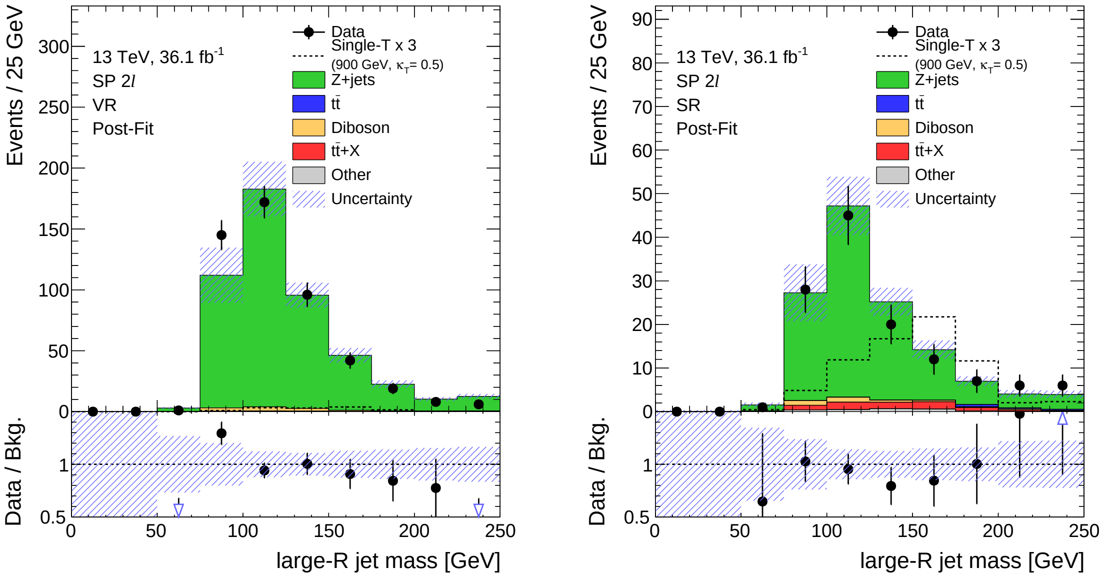

(c) Data/MC comparison in the VR

(d) Data/MC comparison in the SR

Figure B.9: Data/MC comparison(after fitting) of the reconstructed large-R jet mass distribution in the 0b0t CR(a), b0t CR(b), VR(c), and SR(d).

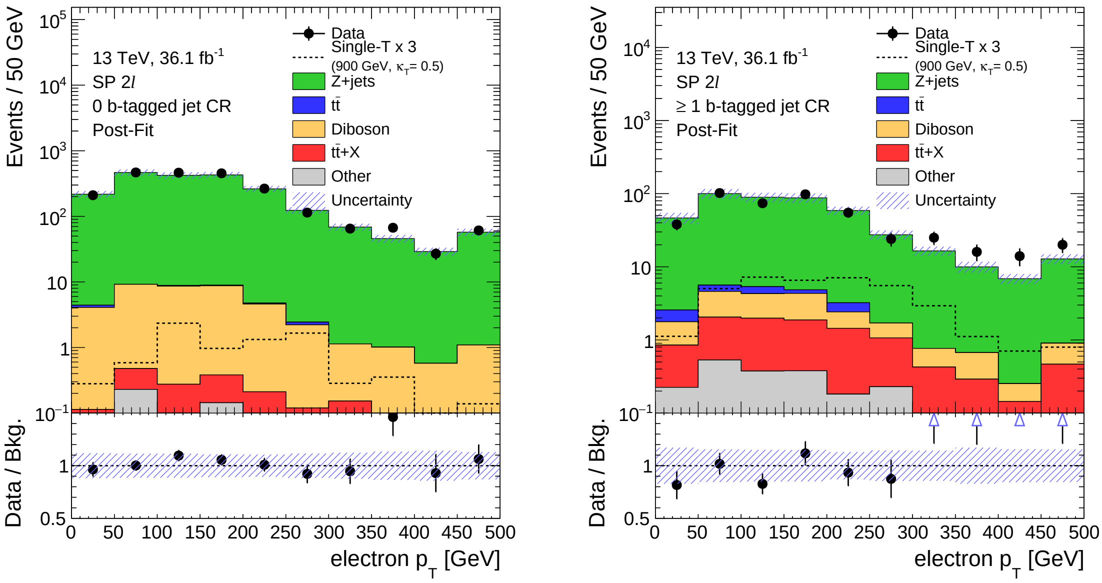

(a) Data/MC comparison in the 0b0t CR (b) Data/MC comparison in the b0t CR

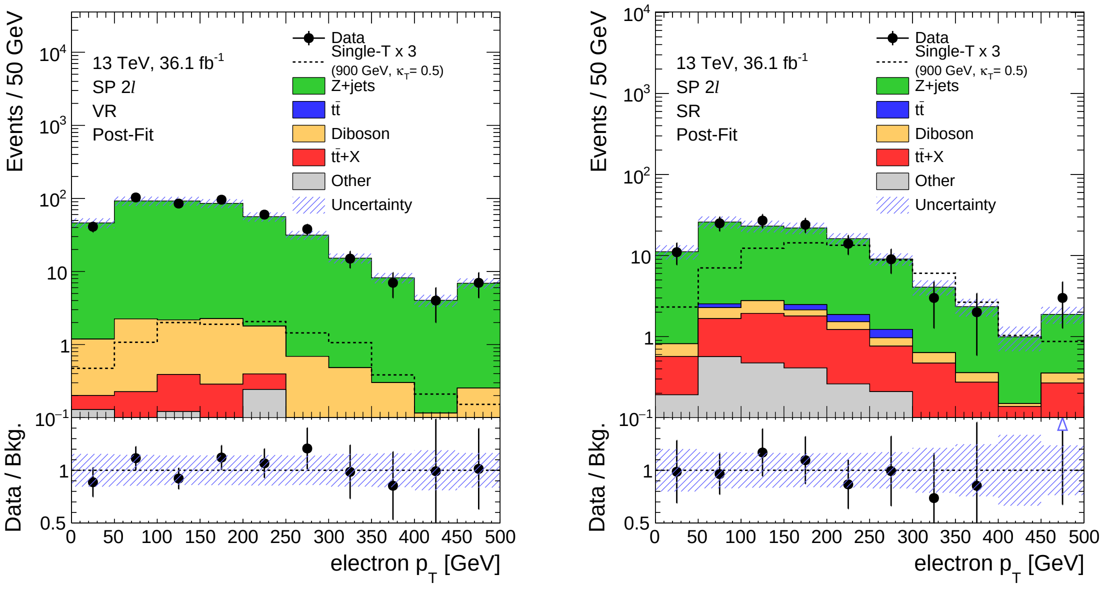

(c) Data/MC comparison in the VR (d) Data/MC comparison in the SR

Figure B.10: Data/MC comparison(after fitting) of the reconstructed electron p_T distribution in the 0b0t CR(a), b0t CR(b), VR(c), and SR(d).

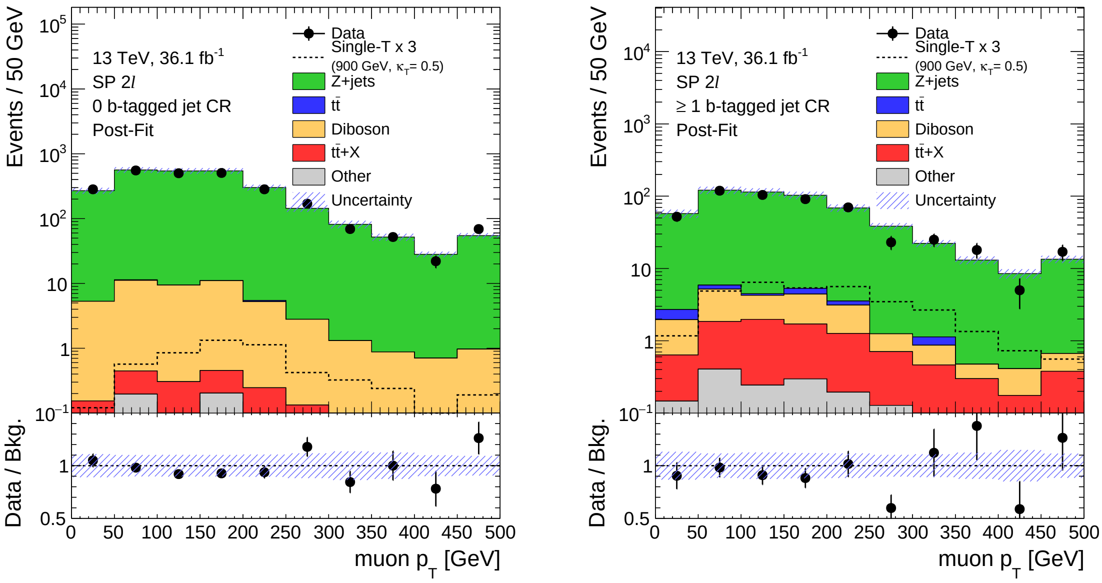

(a) Data/MC comparison in the 0b0t CR

(b) Data/MC comparison in the b0t CR

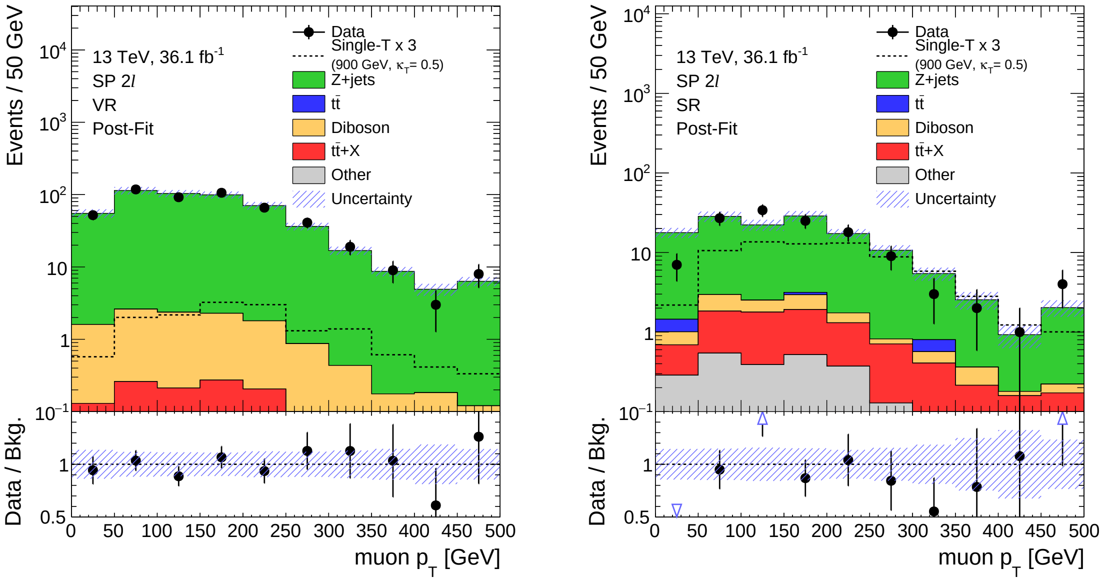

(c) Data/MC comparison in the VR

(d) Data/MC comparison in the SR

Figure B.11: Data/MC comparison(after fitting) of the reconstructed muon p_T distribution in the 0b0t CR(a), b0t CR(b), VR(c), and SR(d).

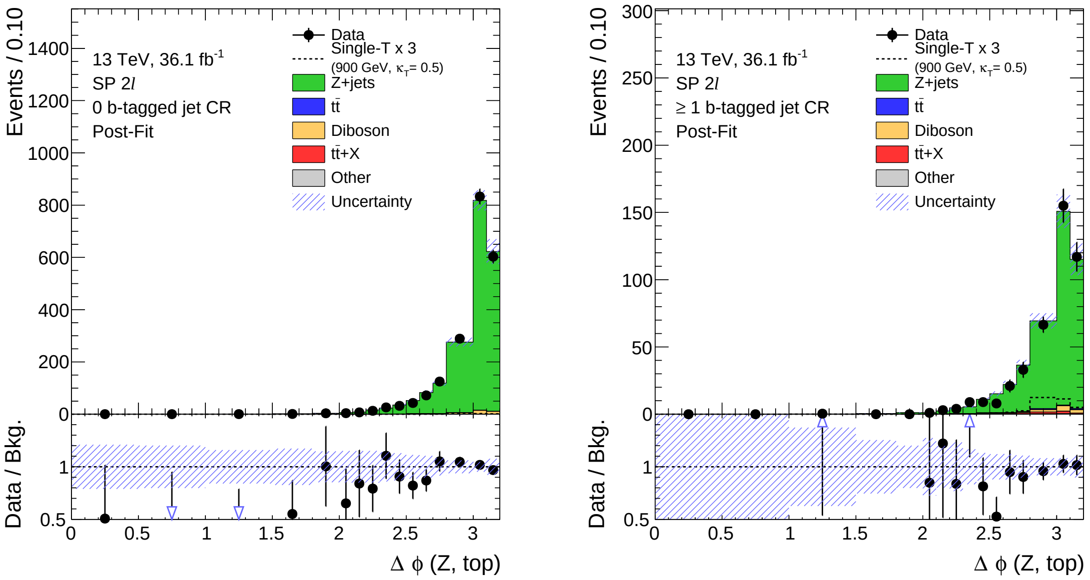

(a) Data/MC comparison in the 0b0t CR (b) Data/MC comparison in the b0t CR

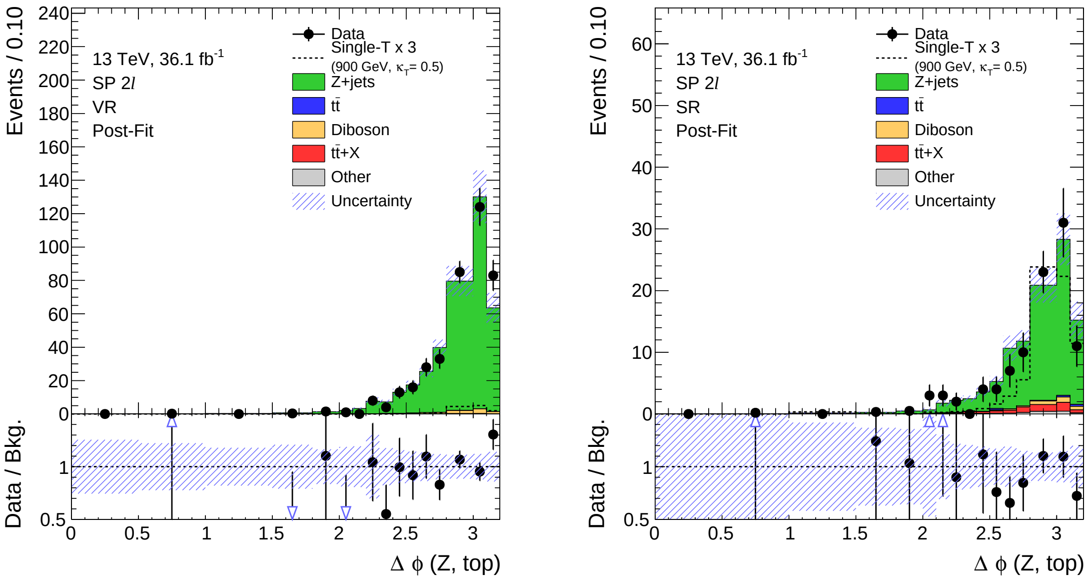

(c) Data/MC comparison in the VR (d) Data/MC comparison in the SR

Figure B.12: Data/MC comparison(after fitting) of $\Delta\phi$ between the reconstructed Z and top candidate distribution in the 0b0t CR(a), b0t CR(b), VR(c), and SR(d).

APPENDIX C

Details of the trilepton channel

C.1 Overview of the analysis strategy

The trilepton channel is designed to search for the single production T decaying into Z and top using the events in which both top and Z decay leptonically. In this channel, two control regions(Diboson CR and $t\bar{t}+V$ CR) and one signal region(SR) are defined. The two CRs are designed to enhance the contribution of diboson and $t\bar{t}+V$ background processes to measure their contribution in SR precisely. The definition of each region is summarized in Table.C.1.

Diboson CR	$t\bar{t}+V$ CR	SR
Preselection		
≥ 3 leptons		
$\|m_{ll} - m_Z\| < 10\text{GeV}$		
–		$p_{T,ll} > 150\text{GeV}$
$= 0$ b-tagged jets	≥ 1 b-tagged jets	
–	$= 0$ forward jets	≥ 1 forward jets
–	$28\text{GeV} < \text{max}p_T^l < 200\text{GeV}$	$\text{max}p_T^l > 200\text{GeV}$
$H_T \times$ (number of small-R jets) ¡ 6 TeV		

Table C.1: Definition of the control regions and the signal region for the trilepton channel.

The fitting procedure described in Section.6.3 is performed to the S_T(scalar sum of small-R jets and leptons p_T) distribution of the CRs and SR to estimate the signal contribution.

C.2 Results

The event yields in each region is summarized in Table.C.2, and the Data/MC comparison plots of the S_T distribution are shown in Fig.C.1.

	Diboson CR	$t\bar{t}$ CR	SR
Z+jets	55 ± 27	11 ± 6	0.17 ± 0.11
$t\bar{t}$	7.3 ± 3.4	15 ± 6	< 0.001
Single top	7.0 ± 3.3	20 ± 10	0.68 ± 0.34
$t\bar{t}$ + X	22 ± 4	110 ± 14	6.2 ± 0.8
Diboson	1060 ± 50	116 ± 25	3.2 ± 0.7
Triboson	6.0 ± 2.5	0.50 ± 0.17	0.031 ± 0.014
Total Bkg.	1160 ± 40	280 ± 20	10.2 ± 1.1
Data	1145	29	14
Data/Bkg.	0.99 ± 0.04	1.01 ± 0.07	1.37 ± 0.14

Table C.2: Observed and expected event yields in each region after fitting.

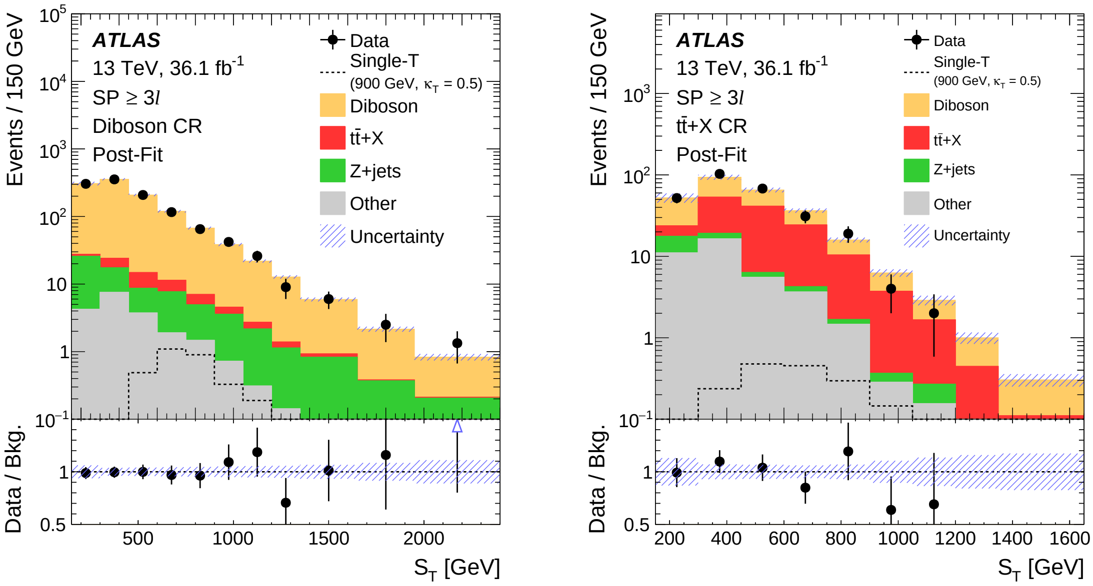

(a) Data/MC comparison in the Diboson CR

(b) Data/MC comparison in the $t\bar{t} + X$ CR

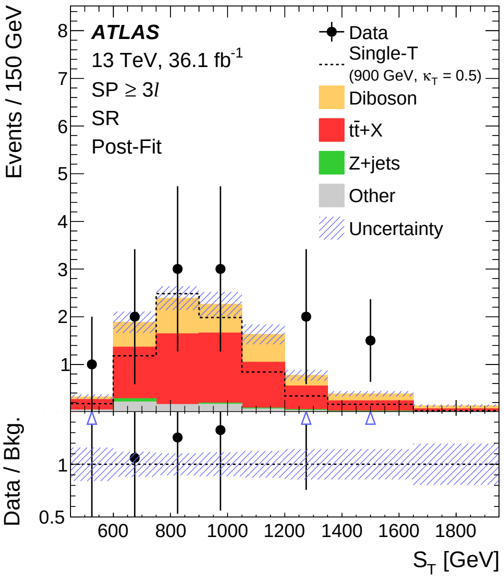

(c) Data/MC comparison in the SR

Figure C.1: Data/MC comparison(after fitting) of the S_T distribution in the Diboson CR(a), $t\bar{t} + X$ CR(b), and SR(c).

APPENDIX D

Observed events with large m_{Zt} in the signal region

In this appendix, the details of the events observed in the SR in the bin for $1600 < m_{Zt} < 1800$ GeV. The event of Event 3425706746 in Run 310691 is already introduced in Section 11.1, so this appendix is focused on the remaining 4 events.

D.1 Run 302053 EventNumber=3425706746

This event was recorded on the 15th June 2016 with the instantaneous luminosity of $5.2 \times 10^{33}\text{cm}^{-2}\text{s}^{-1}$. The event display of this event is shown in Fig. D.1.

The property of the reconstructed objects are listed in Table D.1. Z boson is reconstructed with a pair of $\mu^+\mu^-$ and its mass is 85.2 GeV, p_T is 273.0 GeV. T is reconstructed with Z and top-jet and its mass is 1660.7 GeV and p_T is 166.9 GeV. $\Delta\phi$ between the Z and the top-jet is 2.82, close to the back-to-back topology.

Table D.1: Properties of the reconstructed objects in Run 302053, Event 3425706746.

Object	p_T or E_T [GeV]	η	ϕ	mass [GeV]	other information
μ^+	211,2	-1.39	-3.02	0.11	-
μ^-	74.0	-1.56	2.59	0.11	-
large-R jet	402.7	1.64	0.27	168.5	top-tagged
small-R jet	79.8	1.79	1.18	-	b-tagged
small-R jet	38.4	-3.07	-3.03	-	forward jet
small-R jet	376.8	1.54	0.14	-	-
small-R jet	166.5	-0.80	-2.50	-	-
small-R jet	39.5	0.29	-0.11	-	-
small-R jet	29.8	2.57	0.17	-	-
T	166.9	1.68	0.81	1660.7	-

D.2 Run 309674 EventNumber=1826394116

This event was recorded on the 1st October 2016 with the instantaneous luminosity of $7.7 \times 10^{33}\text{cm}^{-2}\text{s}^{-1}$. The event display of this event is shown in Fig. D.2.

The property of the reconstructed objects are listed in Table D.2. Z boson is reconstructed with a pair of e^+e^- and its mass is 95.1 GeV and p_T is 863.4 GeV. T is reconstructed with

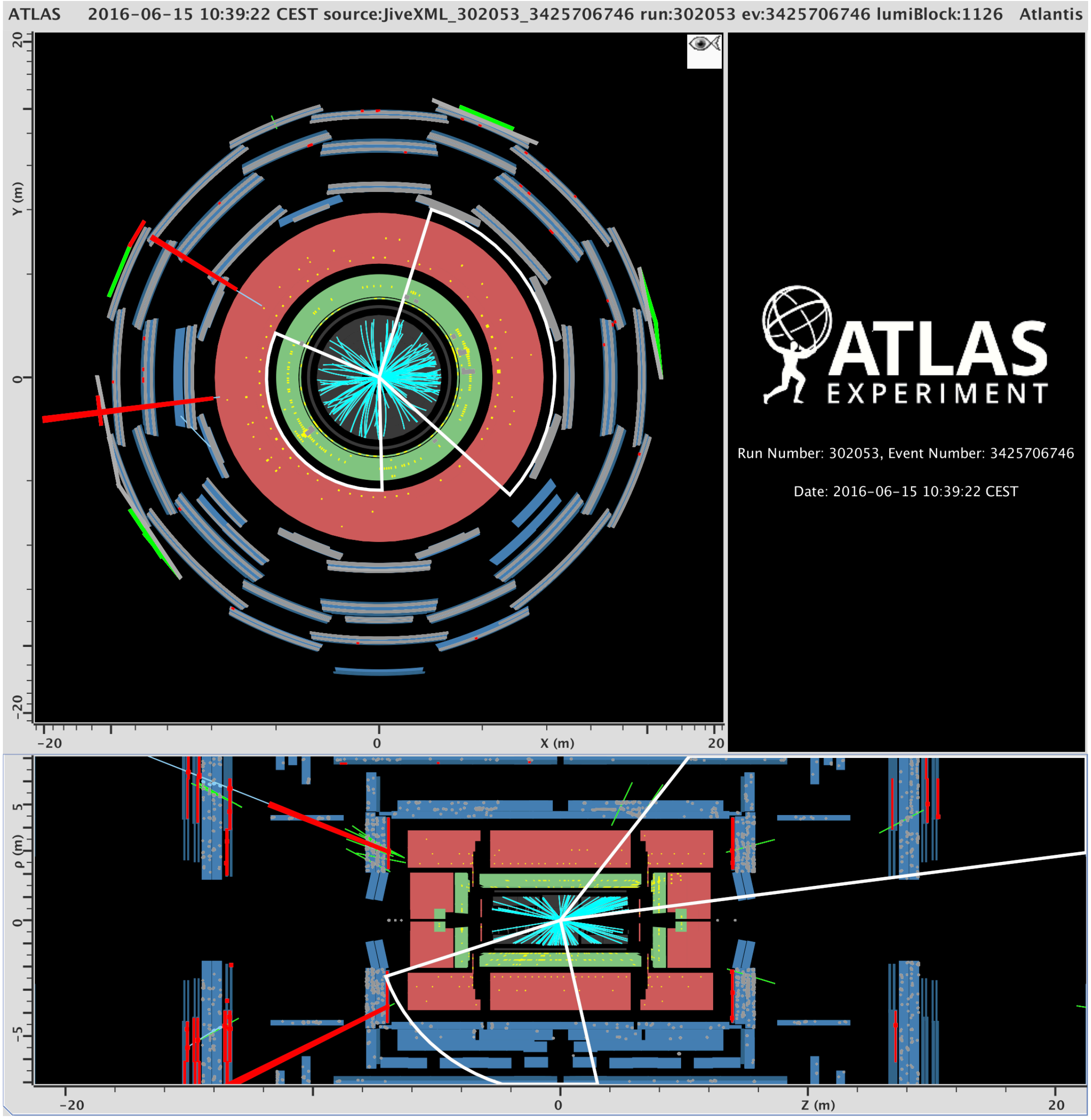

Figure D.1: An event display of Run number 302053, Event Number 3425706746.

Z and top-jet and its mass is 1741.9 GeV and p_T is 84.9 GeV. $\Delta\phi$ between the Z and the top-jet is 3.05, close to the back-to-back topology.

Table D.2: Properties of the reconstructed objects in Run 309674, Event 1826394116.

Object	p_T or E_T [GeV]	η	ϕ	mass [GeV]	other information
e^+	785.0	0.11	0.57	-	-
e^-	83.5	0.06	0.20	-	-
large-R jet	832.7	0.15	-2.7	269.1	top-tagged
small-R jet	446.8	0.42	-2.61	-	b-tagged
small-R jet	737.9	2.55	-0.99	-	forward jet
small-R jet	462.8	-0.13	-2.80	-	
small-R jet	42.0	1.35	-0.92	-	-
small-R jet	27.5	1.61	2.91	-	-
small-R jet	25.5	-1.24	1.87	-	-
T	84.9	1.67	1.69	1741.9	-

D.3 Run 310691 EventNumber=3115231347

This event was recorded on the 16th October 2016 with the instantaneous luminosity of $6.3 \times 10^{33}\text{cm}^{-2}\text{s}^{-1}$. The event display of this event is shown in Fig. D.3.

The property of the reconstructed objects are listed in Table D.3. Z boson is reconstructed with a pair of e^+e^- and its mass is 94.0 GeV and p_T is 262.1 GeV. T is reconstructed with Z and top-jet and its mass is 1698.5 GeV and p_T is 258.1 GeV. $\Delta\phi$ between the Z and the top-jet is 2.10, which is not balanced in this case.

Table D.3: Properties of the reconstructed objects in Run 310691, Event 3115231347.

Object	p_T or E_T [GeV]	η	ϕ	mass [GeV]	other information
e^+	221.3	1.93	-1.10	-	-
e^-	44.3	1.11	-0.66	-	-
large-R jet	255.7	-1.88	1.07	115.7	top-tagged
small-R jet	231.9	-1.87	1.00	-	b-tagged
small-R jet	36.7	-2.56	-2.73	-	forward jet
small-R jet	202.0	0.28	-2.93	-	-
small-R jet	31.6	-1.85	1.88	-	-
T	258.1	-0.05	-0.01	1698.5	-

D.4 Run 311402 EventNumber=914328156

This event was recorded on the 25th October 2016 with the instantaneous luminosity of $10.6 \times 10^{33}\text{cm}^{-2}\text{s}^{-1}$. The event display of this event is shown in Fig. D.4.

The property of the reconstructed objects are listed in Table D.4. Z boson is reconstructed with a pair of $\mu^+\mu^-$ and its mass is 92.1 GeV and p_T is 445.9 GeV. T is reconstructed with Z and top-jet and its mass is 1608.9 GeV and p_T is 84.9 GeV. $\Delta\phi$ between the Z and the top-jet is 2.81, close to the back-to-back topology.

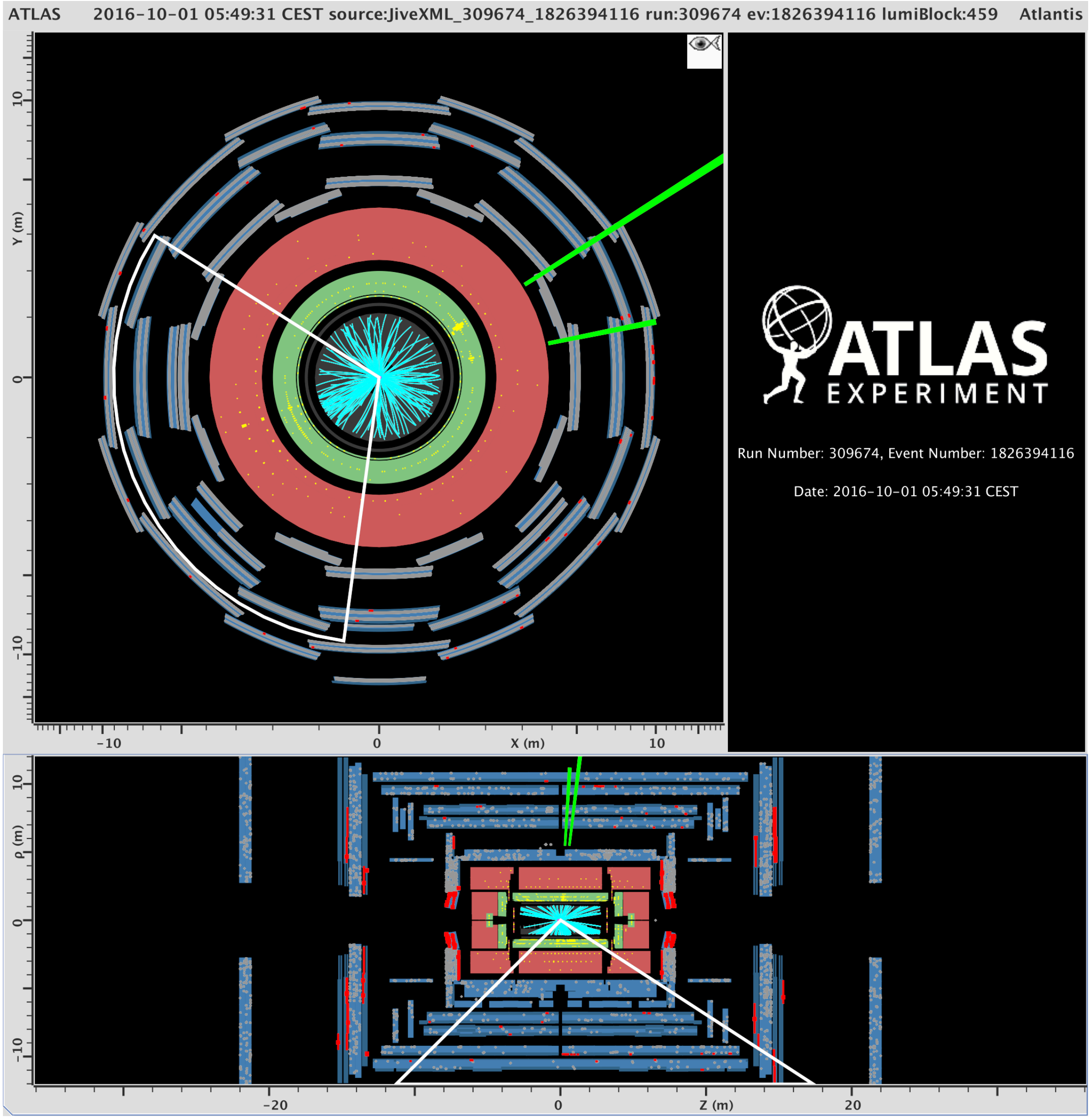

Figure D.2: An event display of Run number 309674, Event Number 1826394116.

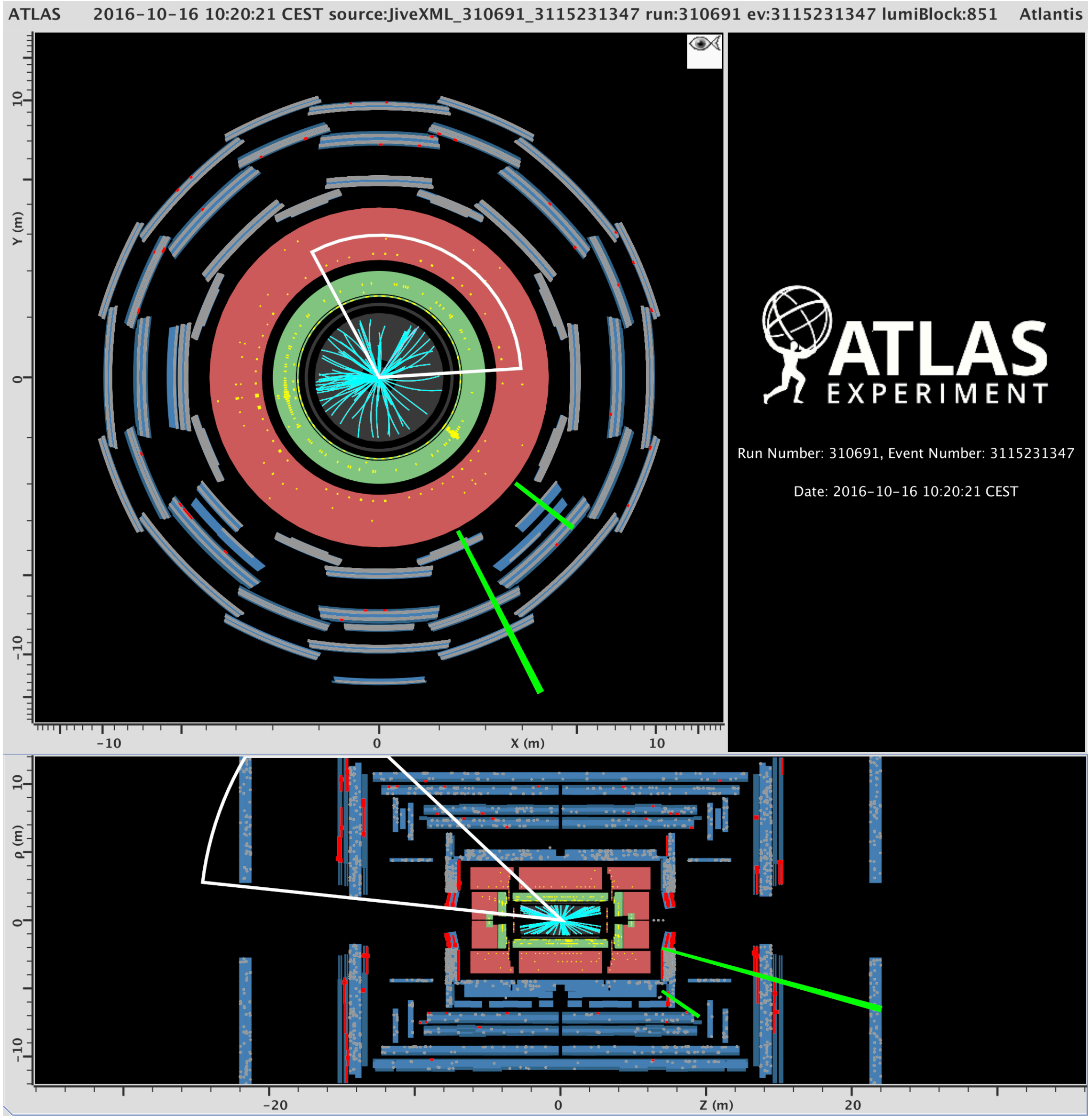

Figure D.3: An event display of Run number 310691, Event Number 3115231347.

Table D.4: Properties of the reconstructed objects in Run 311402, Event 914328156.

Object	p_T or E_T [GeV]	η	ϕ	mass [GeV]	other information
μ^+	232.8	-0.56	2.64	0.11	-
μ^-	220.0	-0.35	2.99	0.11	-
large-R jet	435.4	1.91	-0.14	219.2	top-tagged
small-R jet	261.5	1.81	0.26	-	b-tagged
small-R jet	241.4	1.84	-0.54	-	b-tagged
small-R jet	63.0	3.00	0.74	-	forward jet
small-R jet	70.3	-2.81	-1.70	-	forward jet
small-R jet	56.4	0.27	-2.36	-	-
small-R jet	25.2	0.79	-2.47	-	-
T	84.9	3.36	1.46	1608.9	-

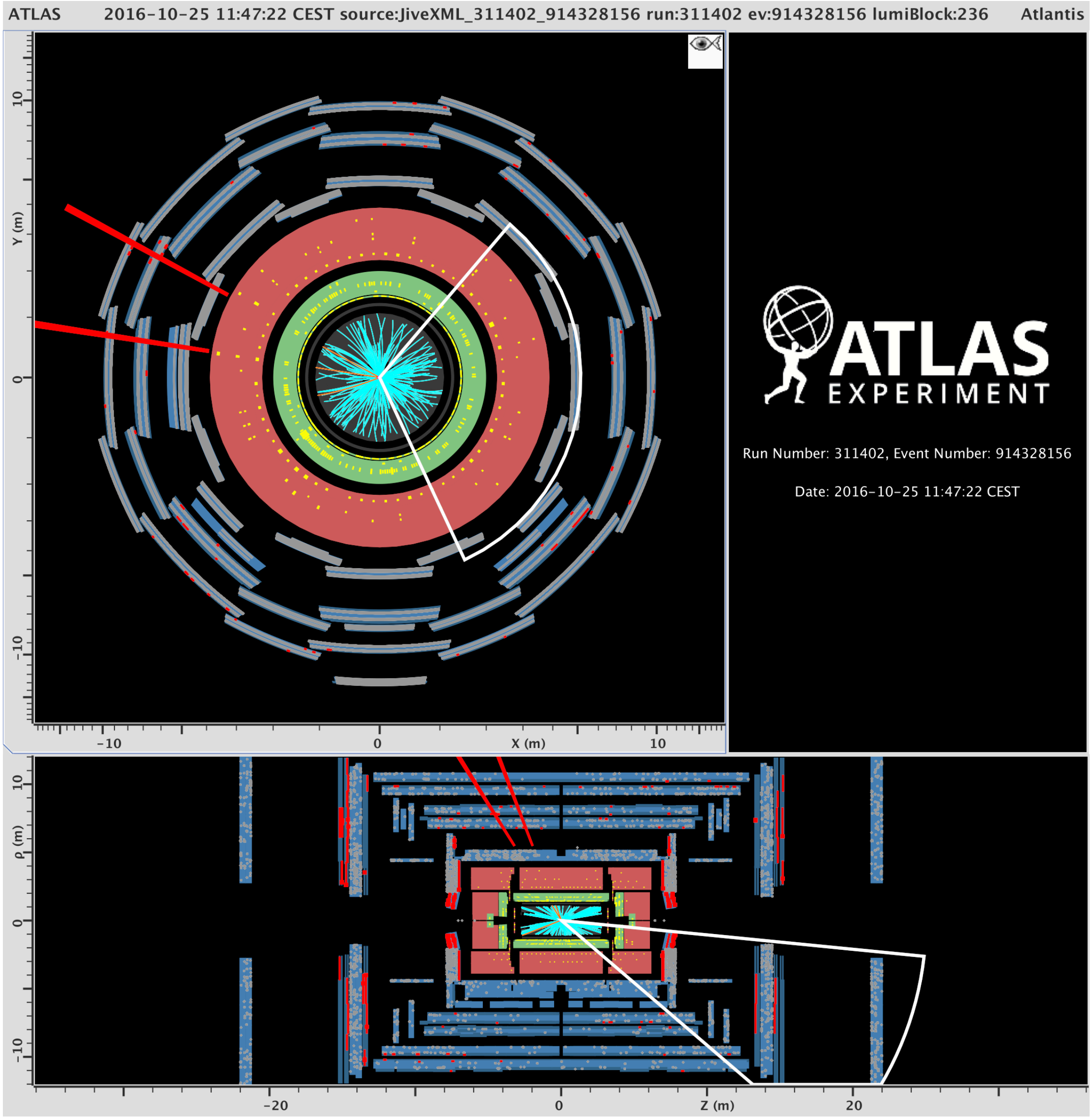

Figure D.4: An event display of Run number 311402, Event Number 914328156.

Acknowledgement

I dedicate this thesis to all the constituents of this kind and gentle world.

This thesis was submitted with the great help of many people. First I really appreciate my wife Sayaka for the kind support. It encouraged me quite a lot in the tough days. This thesis would not be completed without her help.

Masaya Ishino has guided me a lot as a supervisor through my master and Ph.D course. I am very grateful for him and his leadership. I also appreciate Toshi Sumida a lot. He advised me quite lots of things including the experiment, physics theory, computing and so on. The members of Kyoto ATLAS group helped me a lot. The discussion with them reminded me many ideas, which were quite important in pushing on the research. I deeply appreciate Takuto Kunigo, Shunnichi Akatsuka, Yohei Noguchi, Yuta Okazaki, Koichiro Kuniyoshi, Masayuki Hatano, and Yuya Mino. Also, I appreciate Naoyuki Kamo and Ryutaro Monden, who already graduated.

I express a deep gratitude to the ATLAS collaborators. The ATLAS experiment has been operated quite successfully thanks to their hard work. Especially I appreciate the VLQ analysis members. Johannes Erdmann, J.P. Araque, and Nuno Castro drived the difficult analysis among the many channels quite efficiently to publish the paper. Also, Xiaowen Lei, Elena Murielle Freundlich, Tiago Dias Do Vale, Avik Roy, Mesut Unal, Nikiforos Nikiforou, Timothy Robert Andeen worked pretty hard in the analysis. I am pleased and proud that I could complete the analysis with them. I also appreciate the TGC experts, Hiroshi Sakamoro, Osamu Sasaki, Hisaya Kurashige, Makoto Tomoto, Masato Aoki, Junpei Maeda, Yasuyuki Horii, Kentaro Kawade, Yasuyuki Okumura, Tatsuya Masubuchi, Tomoyuki Saito, Chen Ye, Yuta Sano, and Shota Suzuki. They all helped me a lot in the operation of TGC system in my CERN days. The days in Saint-Genis-Pouilly with Katsuya Yamauchi and Chikuma Kato impressed me deeply. I hope we can meet someday again.

My life in the Ph.D course like a sweet dream is full of the beautiful memories with the laboratory members. The fantastic memories will illuminate my life like the full moon in the midnight. I really appreciate Tsuyoshi Nakaya, Atsuko Ichikawa, Osamu Tajima, Wendel Roger, and Tatsuya Kikawa. The laboratory was quite systematically operated with their effort. Also I learned a lot from their guidance. I am grateful to the members of the room 302, Kiseki Nakamura, Ayami Hiramoto, Kazuhiro Nakamora, and Soichiro Kuribayashi. I enjoyed the conversation and discussion with them from the heart. I am also grateful to all the other members, Shunnichi Adachi, Syuhei Obara, Syunsuke Honda, Ichinori Kamiji, Kota Nakagiri, Satoshi Shinohara, Sei Ban, Yosuke Ashida, Shunsuke Tanaka, Masamitsu Mori, Masashi Yoshida, Keisuke Kondo, Junta Komine, Kenji Yasutome, Tomofumi Abe, Takuji Ikemitsu, Takahiro Odagawa, Masanori Tajima. Sometimes the words of the people in the laboratory were cynical, however, I know they are in fact kind and gentle and their spirit is as shiny as a supernova. The discussion and conversation with them always reminded me that life is beautiful.

Finally, I appreciate my family and parents. Their support and understanding encouraged

me.

Everytime I read an ATLAS thesis I would remember the days I spent in CERN and Kyoto. I hope the world is kind and gentle for all the people listed here.

Bibliography

[1] Peter W. Higgs (1964). "Broken Symmetries and the Masses of Gauge Bosons", Physical Review Letters. 13 (16): 508509.

[2] L. Susskind, Dynamics of spontaneous symmetry breaking in the Weinberg-Salam theory, Phys. Rev. D20 (1979) 2619.

[3] N. Arkani-Hamed, A. Cohen, E. Katz and A. Nelson, The littlest Higgs, JHEP 07 (2002) 34,
arXiv: hep-ph/0206021 [hep-ph].

[4] Perelstein, Maxim Prog.Part.Nucl.Phys. 58 (2007) 247-291
arXiv:hep-ph/0512128 [hep-ph].

[5] K. Agashe, R.Contino, A. Pomarol, The minimal composite Higgs model, Nucl. Phys. B 719, 165 (2005),
arXiv: hep-ph/0412089 [hep-ph].

[6] P. Lodone, Vector-like quarks in a ' composite ' Higgs model,
JHEP 12 (2008) 029, arXiv: 0806.1472

[7] J. A. Aguilar-Saavedra, R. Benbrik, S. Heinemeyer and M. Perez-Victoria, Handbook of vectorlike quarks: Mixing and single production,
Phys. Rev. D 88 (2013) 094010, arXiv: 1306.0572

[8] O. Matsedonskyi, G. Panico and A. Wulzer, On the interpretation of Top Partners searches, JHEP 12 (2014) 097, arXiv: 1409.0100 [hep-ph].

[9] CERN, The CERN accelerator complex,
OPEN-PHO-ACCEL-2018-005-1, url: `https://cds.cern.ch/record/2636343`.

[10] LHC design report,
CERN-2004-003, 4 June 2004, url: `https://cds.cern.ch/record/782076`.

[11] LEP Design Report,
CERN-LEP/84-01; June 1984 and CERN-AC/96-01(LEP2), June1996

[12] ATLAS Collaboration, " ATLAS Trigger Performance Status Report ",
CERN/LHCC/98-15 (1998).

[13] ATLAS collaboration (2012). "Observation of a New Particle in the Search for the Standard Model Higgs Boson with the ATLAS Detector at the LHC",
Physics Letters B. 716(1): 129

[14] Howard Baer; Xerxes Tata (2006). "8 - The Minimal Supersymmetric Standard Model". Weak Scale Supersymmetry From Superfields to Scattering Events. Cambridge: Cambridge University Press.p.127.

[15] E. Eichten, K. Lane, and M. Peskin, " New Tests for Quark and Lepton Substructure ", Phys. Rev. Lett. 50 (1983) 811, doi:10.1103/PhysRevLett.50.811.

[16] N. Arkani-Hamed, S. Dimopoulos and G. Dvali, The Hierarchy problem and new dimensions at a millimeter,
Phys. Lett. B 429 (1998) 263272

[17] L. Randall and R. Sundrum, A Large mass hierarchy from a small extra dimension, Phys.Rev.Lett. 83 (1999) 33703373

[18] ATLAS Collaboration," The ATLAS experiment at the CERN Large Hadron Collider ", JINST 3 S08003 (2008).

[19] H.H.J. ten Kate, Superconducting magnet system for the ATLAS detector at CERN, IEEE Trans. Appl. Supercond. 9 (1999) 841.

[20] ATLAS Collaboration, Muon Spectrometer Technical Design Report (Section 10.2.2), CERN/LHCC/97-22 (1997).

[21] ATLAS Collaboration, Study of the material of the ATLAS inner detector for Run 2 of the LHC, JINST 12 (2017) 12009.

[22] ATLAS Collaboration, Insertable B-Layer Technical Design Report
CERN/LHCC/2010-013

[23] G. Aad et al., ATLAS Pixel Detector Electronics and Sensors
2008 JINST 3 P07007.

[24] I. Gorelov et al., A measurement of Lorentz angle and spatial resolution of radiation hard silicon pixel sensors,
Nucl. Instrum. Meth. A 481 (2002) 204.

[25] F. Campabadal et al., Beam tests of ATLAS SCT silicon strip detector modules, Nucl. Instrum. Meth. A 538 (2005) 384.

[26] Karolos Potamianos, The upgraded Pixel detector and the commissioning of the Inner Detector tracking of the ATLAS experiment for Run-2 at the Large Hadron Collider, EPS-HEP2015 (2015) 261

[27] ATLAS Collaboration, Detector amd Physics Performance Technical Design Report, CERN/LHCC/99-14/15 (1999)

[28] ATLAS collaboration, Liquid argon calorimeter technical design report, CERN-LHCC-96-041

[29] M. Aharrouche et al., Response uniformity of the ATLAS liquid argon electromagnetic calorimeter,
Nucl. Instrum. Meth. A 582 (2007) 429.

[30] M. Aharrouche et al., Energy linearity and resolution of the ATLAS electromagnetic barrel calorimeter in an electron test-beam,
Nucl. Instrum. Meth. A 568 (2006) 601.

[31] J. Abdallah et al., Design, construction and installation of the ATLAS hadronic barrel scintillator-tile calorimeter,
ATLAS Note ATL-TILECAL-PUB-20081.

[32] S. Palestini, The muon spectrometer of the ATLAS experiment,
Nucl. Phys. 125 (Proc. Suppl.) (2003) 337.

[33] Arantxa Ruiz Martinez et al., ”The Run-2 ATLAS Trigger System”,
ATLAS Note ATL-DAQ-PROC-2016-003, url: `https://cds.cern.ch/record/2133909`

[34] S. Agostinelli et al., GEANT4—a simulation toolkit, Nucl. Instrum. Meth. A 506 (2003) 250.

[35] C. Degrande, C. Duhr, B. Fuks, D. Grellscheid, O. Mattelaer and T. Re- iter,
Comput. Phys. Commun. 183 (2012) 1201.

[36] J. Alwall, M. Herquet, F. Maltoni, O. Mattelaer and T. Stelzer, MadGraph 5 : Going Beyond,
JHEP 06 (2011) 128, arXiv: 1106.0522.

[37] T. Sjostrand, S. Mrenna and P. Z. Skands, A Brief Introduction to PYTHIA 8.1,
Comput. Phys. Commun. 178 (2008) 852, arXiv: 0710.3820.

[38] R. D. Ball et al., Parton distributions with LHC data, Nucl. Phys. B 867 (2013) 244, arXiv: 1207.1303 [hep-ph].

[39] ATLAS Collaboration, ATLAS Pythia 8 tunes to 7 TeV data, ATL-PHYS-PUB-2014-021, 2014, : `https://cds.cern.ch/record/1966419`.

[40] J. Aguilar-Saavedra, Protos - PROgram for TOp Simulations,
url: `http://jaguilar.web.cern.ch/jaguilar/protos`.

[41] T. Gleisberg, S. Hoche, F. Krauss, M. Schonherr, S. Schumann et al., Event generation with SHERPA 1.1,
JHEP 02 (2009) 007, arXiv: 0811.4622.

[42] P. Nason, A New method for combining NLO QCD with shower Monte Carlo algorithms, JHEP 11 (2004) 040, arXiv: hep-ph/0409146 [hep-ph].

[43] S. Frixione and B. R. Webber, Matching NLO QCD computations and parton shower simulations,
JHEP 06 (2002) 029, arXiv: hep-ph/0204244[hep-ph].

[44] T. Cornelissen et al., The new ATLAS track reconstruction (NEWT),
J. Phys. Conf. Ser. 119 (2008).

[45] ATLAS Collaboration, Tracking and Vertexing with the ATLAS Inner Detector in the LHC Run-2, Springer Proc. Phys. 213 (2018) 400-403 T. Cornelissen et al., The new ATLAS track reconstruction (NEWT),
J. Phys. Conf. Ser. 119 (2008).

[46] ATLAS collaboration (2016). ”Primary vertex reconstruction with the ATLAS detector”, Journal of Instrumentation, Volume 11, December 2016

[47] ATLAS Collaboration, ATL-PHYS-PUB-2015-026, `http://cdsweb.cern.ch/record/2037717`.

[48] ATLAS Collaboration, Muon reconstruction performance of the ATLAS detector in protonproton collision data at $\sqrt{s}$=13 TeV,
Eur. Phys. J. C 76 (2016) 292, arXiv: 1603.05598 [hep-ex].

[49] ATLAS Collaboration, Electron reconstruction and identification efficiency measurements with the ATLAS detector using the 2011 LHC protonproton collision data,
Eur. Phys. J. C 74 (2014) 2941, arXiv: 1404.2240 [hep-ex].

[50] ATLAS Collaboration, Electron efficiency measurements with the ATLAS detector using the 2012 LHC protonproton collision data,
ATLAS-CONF-2014-032, 2014, url: `https://cds.cern.ch/record/1706245`.

[51] ATLAS Collaboration, Improved electron reconstruction in ATLAS using the Gaussian Sum Filter-based model for bremsstrahlung,
ATLAS-CONF-2012-047 url: `https://cdsweb.cern.ch/record/1449796`

[52] ATLAS Collaboration, Electron and photon energy calibration with the ATLAS detector using LHC Run 1 data, Eur. Phys. J. C 74 (2014) 3071, arXiv: 1407.5063 [hep-ex].

[53] ATLAS Collaboration, Electron and photon energy calibration with the ATLAS detector using 2015-2016 LHC proton-proton collision data,
CERN-EP-2018-296, arXiv: 1812.03848 [hep-ex].

[54] M. Cacciari, G. P. Salam and G. Soyez, The anti-kt jet clustering algorithm,
JHEP 04 (2008) 063, arXiv: 0802.1189 [hep-ph].

[55] ATLAS Collaboration, Jet Calibration and Systematic Uncertainties for Jets Reconstructed in the ATLAS Detector at $\sqrt{s}$=13 TeV,
ATL-PHYS-PUB-2015-015, 2015

[56] ATLAS Collaboration, Performance of pile-up mitigation techniques for jets in pp collisions at $\sqrt{s}$=8 TeV using the ATLAS detector,
Eur. Phys. J. C 76 (2016) 581

[57] D. Krohn, J. Thaler and L.-T. Wang, Jet Trimming,
JHEP 02 (2010) 084, arXiv: 0912.1342 [hep-ph].

[58] J. Thaler and K. Van Tilburg, Identifying Boosted Objects with N-subjettiness,
JHEP 03 (2011) 015, arXiv: 1011.2268 [hep-ph].

[59] S. Catani, Y. L. Dokshitzer, M. H. Seymour and B. R. Webber,
Nucl. Phys. B 406, 187 (1993).

[60] ATLAS Collaboration, Performance of b-jet identification in the ATLAS experiment,
JINST 11 (2016) P04008, arXiv: 1512.01094 [hep-ex].

[61] ATLAS Collaboration, Optimisation of the ATLAS b-tagging performance for the 2016 LHC Run,
ATL-PHYS-PUB-2016-012, 2016, url: `https://cds.cern.ch/record/2160731.`

[62] ATLAS Collaboration, Commissioning of the ATLAS high-performance b-tagging algorithms in the 7 TeV collision data, ATLAS-CONF-2011-102. `http://cds.cern.ch/record/1369219`.

[63] ATLAS Collaboration, “ Expected Performance of the ATLAS Experiment Detector, Trigger and Physics. ” CERN-OPEN-2008-020, December, 2008. `http://arxiv.org/abs/0901.0512`.

[64] ATLAS Collaboration, In situ calibration of large-R jet energy and mass in 13 TeV proton-proton collisions with the ATLAS detector, Submitted to Eur.Phys.J. arXiv:1807.09477 [hep-ex], CERN-EP-2018-191

[65] ATLAS Collaboration, Boosted hadronic top identification at ATLAS for early 13 TeV data,
ATL-PHYS-PUB-2015-053, 2015, url: `https://cds.cern.ch/record/2116351`.

[66] T. Junk, Confidence level computation for combining searches with small statistics, Nucl. Instrum. Meth. A 434 (1999) 435, arXiv: hep-ex/9902006 [hep-ex].

[67] A. L. Read, Presentation of search results: the CLs technique, J. Phys. G 28 (2002) 2693.A

[68] S.VanDerMeer,ISR-PO/68-31,KEK68-64

[69] ATLAS Collaboration, Electron efficiency measurements with the ATLAS detector using the 2015 LHC proton-proton collision data, ATLAS-CONF-2016-024, url: `https://cds.cern.ch/record/2157687`.

[70] M. Cacciari, G. P. Salam and G. Soyez, The anti-kt jet clustering algorithm,
JHEP 04 (2008) 063, arXiv: 0802.1189 [hep-ph].

[71] ATLAS Collaboration, Electron and photon energy calibration with the ATLAS detector using data collected in 2015 at $\sqrt{s}$=13 TeV,
ATL-PHYS-PUB-2016-015, 2016,url: `https://cds.cern.ch/record/2203514.`

[72] ATLAS Collaboration, Muon reconstruction performance of the ATLAS detector in protonproton collision data at $\sqrt{s}$=13 TeV,
Eur. Phys. J. C 76 (2016) 292, arXiv: 1603.05598 [hep-ex].

[73] ATLAS Collaboration, Jet energy scale measurements and their systematic uncertainties in protonproton collisions at $\sqrt{s}$=13 TeV with the ATLAS detector,
Phys. Rev. D 96 (2017) 072002, arXiv: 1703.09665 [hep-ex].

[74] ATLAS Collaboration, Jet Calibration and Systematic Uncertainties for Jets Reconstructed in the ATLAS Detector at $\sqrt{s}$=13 TeV,
ATL-PHYS-PUB-2015-015, 2015,url: `https://cds.cern.ch/record/2037613.`

[75] ATLAS Collaboration, Performance of jet substructure techniques for large-R jets in protonproton collisions at $\sqrt{s}$=7 TeV using the ATLAS detector,
JHEP 09 (2013) 076, arXiv: 1306.4945 [hep-ex].

[76] ATLAS Collaboration, In-situ measurements of the ATLAS large-radius jet response in 13 TeV pp collisions,
ATLAS-CONF-2017-063, 2017, url: `https://cds.cern.ch/record/2275655.`

[77] ATLAS Collaboration, Performance of b-jet identification in the ATLAS experiment, JINST 11 (2016) P04008, arXiv: 1512.01094 [hep-ex].

[78] ATLAS Collaboration, Measurements of b-jet tagging efficiency with the ATLAS detector using $t\bar{t}$ events at $\sqrt{s} = 13$ TeV,(2018),
arXiv: 1805.01845 [hep-ex].

[79] ATLAS Collaboration, Monte Carlo Generators for the Production of a W or Z/γ^* Boson in Association with Jets at ATLAS in Run 2,
ATL-PHYS-PUB-2016-003, 2016, url: `https://cds.cern.ch/record/2120133`.

[80] ATLAS Collaboration, Simulation of top-quark production for the ATLAS experiment at $\sqrt{s} = 13$ TeV,
ATL-PHYS-PUB-2016-004, 2016, url: `https://cds.cern.ch/record/2120417.`

[81] ATLAS Collaboration, Multi-Boson Simulation for 13 TeV ATLAS analyses,
ATL-PHYS-PUB-2016-002, 2016, url: `https://cds.cern.ch/record/2120133.`

[82] ATLAS Collaboration, Modelling of the $t\bar{t}$H and $t\bar{t}$V(V=W,Z) processes for $\sqrt{s} = 13$ TeV ATLAS analyses,
ATL-PHYS-PUB-2016-005, 2016, url: `https://cds.cern.ch/record/2120826.`

[83] L. A. Harland-Lang, A. D. Martin, P. Motylinski and R. S. Thorne, Parton distributions in the LHC era:
MMHT 2014 PDFs, Eur. Phys. J. C 75 (2015) 204, arXiv: 1412.3989 [hep-ph].

[84] S. Dulat et al., New parton distribution functions from a global analysis of quantum chromodynamics,
Phys. Rev. D 93 (2016) 033006, arXiv: 1506.07443 [hep-ph].

[85] ATLAS Collaboration, Search for pair and single production of vectorlike quarks in final states with at least one Z boson decaying into a pair of electrons or muons in pp collision data collected with the ATLAS detector at $\sqrt{s} = 13$ TeV:
Phys. Rev. D 98 (2018) 112010, arxiv: 1806.10555 [hep-ex].